

# Investigating in-medium lambda production in pion induced reactions at 1.15 gev/c

---

**Weber, Ivana**

**Doctoral thesis / Disertacija**

**2016**

*Degree Grantor / Ustanova koja je dodijelila akademski / stručni stupanj:* **University of Zagreb, Faculty of Science / Sveučilište u Zagrebu, Prirodoslovno-matematički fakultet**

*Permanent link / Trajna poveznica:* <https://urn.nsk.hr/urn:nbn:hr:217:618475>

*Rights / Prava:* [In copyright](#) / [Zaštićeno autorskim pravom.](#)

*Download date / Datum preuzimanja:* **2025-03-24**



*Repository / Repozitorij:*

[Repository of the Faculty of Science - University of Zagreb](#)





University of Zagreb

Faculty of Science

Ivana Weber

**INVESTIGATING IN-MEDIUM LAMBDA  
PRODUCTION IN PION INDUCED  
REACTIONS AT 1.15 GeV/c**

DOCTORAL THESIS

Zagreb, 2016





University of Zagreb

Faculty of Science

Ivana Weber

**INVESTIGATING IN-MEDIUM LAMBDA  
PRODUCTION IN PION INDUCED  
REACTIONS AT 1.15 GeV/c**

DOCTORAL THESIS

Supervisors:

Prof. Dr. Mile Dželalija

Dr. Paul Bühler

Zagreb, 2016







Sveučilište u Zagrebu  
Prirodoslovno-matematički fakultet

Ivana Weber

**Istraživanje stvaranja lambda čestica u  
nuklearnom mediju pionski induciranim  
reakcijama pri 1.15 GeV/c**

DOKTORSKI RAD

Mentori:

prof. dr. sc. Mile Dželalija

doc. dr. sc. Paul Bühler

Zagreb, 2016.



## Supervisor Information

This PhD thesis by Ivana Weber has been prepared by using the experimental data obtained at the GSI (GSI Helmholtzzentrum für Schwerionenforschung) in Darmstadt, Germany under the supervision of Prof. Dr. Mile Dželalija (University of Split, Faculty of Science, Crosbi profile: <http://bib.irb.hr/lista-radova?autor=172646&period=2007>, [mile@pmfst.hr](mailto:mile@pmfst.hr)) and Dr. Paul Bühler (Stefan Meyer Institute for Subatomic Physics of the Austrian Academy of Sciences, Vienna, <http://orcid.org/0000-0003-2049-1380>, [paul.buehler@oeaw.ac.at](mailto:paul.buehler@oeaw.ac.at)). The study has been a part of the FOPI collaboration at the GSI, particularly under the following research projects: "Higher Energy Physics and GRID application" (177-0000000-3193) lead by Prof. Dr. Mile Dželalija and Croatian-Austrian bilateral project "Studying the In-medium Properties of Strange Particles", lead by Prof. Dr. Mile Dželalija and Dr. Paul Bühler .

Prof. Dr. Mile Dželalija has published over 300 research articles in international journals, more than 200 of which are cited in Current Contents, with more than 20.000 citations. He has been leading and participating in a number of international projects funded by EU, UNESCO, UNDP, and various foreign national funds. He is a member of several international bodies in education and research. Until now, two PhD theses and more than 20 diploma theses were prepared and defended under the supervision of Prof. Dr. Mile Dželalija.

Dr. Paul Bühler is a senior scientist and has published a hundred research articles in Current Contents journals, with over 400 citations. He has 5 invited and more than 20 contributed presentations at international conferences. He is an active member of international collaborations FOPI, PANDA, GO and ALICE. Until now, four PhD theses and two diploma theses were prepared and defended under the co-supervision of Dr. Paul Bühler.



# Acknowledgements

To people who have helped me arrive to where I am now. I am short of words to express all my gratitude, but I shall use the ones I know to express at least a part of it.

First of all, to my supervisors.

To Prof. Dr. Mile Dželalija for giving me the opportunity to work in physics, to explore, to travel, and to meet and collaborate with colleagues around the world, acquiring experiences which have been precious for both my career and private life. I am truly grateful for all his help, support, motivation and understanding. The useful discussions we have had and his advices concerning my study, research and thesis have been exceptionally valuable to me.

To Dr. Paul Bühler for having accepted the responsibility of being my supervisor at a crucial point of my PhD study, for his patience and motivation throughout our research and writing of this thesis. I truly appreciate the time we have spent working together, his unselfish help, the knowledge which he has shared with me, and constructive discussions and ideas for my analysis.

To the FOPI collaboration, and especially to Prof. Dr. Norbert Hermann, for a chance to work and cooperate within this collaboration, to Xavier for his crucial help at the beginning of my FOPI data analysis, and to Dr. Olaf Hartmann for having proposed my PhD topic, for inviting me to work together and for building a great basis for my further research activities. Also to the Croatian FOPI group; Prof. Dr. Zoran Basrak and Prof. Dr. Roman Čaplar for stimulating scientific discussions and for looking after my progress. To Igor for being friendly and supportive. And especially to Mladen, for his substantial technical support and moral backup during all the years of my research.

To all my colleagues from the Department of Physics, for being supportive and cooperative, and for helping me in many different ways over the past ten years of our joint work. Also to Tonći for a really important hardware support which helped to speed up the completion of my thesis. And to Irena, for being a patient listener and motivator on a daily basis.

To my colleagues from the Stefan Meyer Institute, for giving me a chance to work and enjoy with them in Vienna.

To my friends who have always been around, supporting me and making this period fun. To Marija, who has missed only the first month of my life, but has been there for me through all other times.

To my family members who have generously assisted me in various ways, especially during the last, most busy months of my work.

To my father, mother, sister and brother for their unselfish, unconditional and constant support, patience and understanding. Having them with me has made everything easier.

And finally, a very special thanks to my two guys, Toni and Berto. For better or for worse, for love, smiles and hugs... To share joy with them is the top of my world.



# Abstract

The presence of in-medium effects which are manifested in the change of basic hadron properties is one of the central issues in the analysis of nuclear matter. Strange particles are essential probes for studying in-medium effects for hadrons produced in collisions at energies close to the production threshold. The influence of the nuclear medium on the production process of neutral strange particles,  $\Lambda$  hyperons and  $K^0$  mesons, has been studied in pion-induced reactions at 1.15 GeV/c beam momentum with five different target nuclei (C, Al, Cu, Sn and Pb). The FOPI detector at the GSI (Darmstadt, Germany) was used as the experimental environment. The main part of the analysis presented in this work was done for  $\Lambda$  particles. The obtained invariant mass spectra for all five targets used in the experiment are presented. The results of other distributions important for this analysis are shown for reactions on carbon and lead targets. Moreover, relevant distributions gained from experimental data are compared with results produced by simulation, using two different simulation approaches. The reconstruction efficiency is determined and applied as a correction factor in the subsequent analysis and the computation of the invariant cross section. The experimentally determined  $\Lambda$  inclusive cross section and its dependence on the production target size ( $A$ ) is presented for the first time at this energy. The investigation of the inclusive  $\Lambda$  production in the  $\pi^- + A \rightarrow \Lambda + K^0$  reaction in medium should contribute to a better understanding of in-medium effects and the general behaviour of neutral strange particles produced close to the threshold.

**Keywords:** nuclear matter, in-medium effects, strange particles, pion-induced reaction,  $\Lambda$  particle, inclusive cross section





# Sažetak

Jedno od najvažnijih pitanja u proučavanju svojstava nuklearne tvari jest njen utjecaj na hadrone koji se u njoj nalaze, a očituje se kroz promjene njihovih svojstava. Ta pojava poznata je pod nazivom *učinci nuklearnog medija* (engl. *in-medium effects*). Strane čestice prikladne su za proučavanje učinaka nuklearnog medija, budući da uz lagane ( $u$  i  $d$ ) kvarkove ili antikvarkove, sadrže i strani ( $s$ ) kvark te se utjecaj nuklearnog medija upravo na strane čestice može izravno uočiti. Stvaranje neutralnih stranih čestica, s naglaskom stavljenim na  $\Lambda$  česticu, proučavano je u pionski induciranim reakcijama pri 1.15 GeV/c za reakcijske sustave s pet nuklearnih meta (C, Al, Cu, Sn i Pb). Podaci korišteni za analizu prikupljeni su pomoću FOPI detektora koji se nalazi na institutu GSI (Darmstadt, Njemačka).

Glavni cilj ovog istraživanja jest proučavanje stvaranja  $\Lambda$  hiperona u reakciji  $\pi^- + A \rightarrow \Lambda + K^0$  unutar nuklearnog medija ( $A$  je maseni broj mete jezgre). Analizom eksperimentalnih podataka i podataka dobivenih iz korištenih simulacijskih modela određene su ocjene inkluzivnog udarnog presjeka stvaranja  $\Lambda$  hiperona. Po prvi put za ovaj tip elementarnih reakcija to je učinjeno na energiji dostupnoj FOPI eksperimentima (od 1 do 2 AGeV, preciznije za ovaj eksperiment:  $\sqrt{s} = 1.75$  GeV). Proučavanje inkluzivnog stvaranja  $\Lambda$  čestica, usporedba različitih izmjerenih i izračunatih fizikalnih veličina, uključujući i inkluzivni udarni presjek za pet nuklearnih meta čiji se maseni broj kreće od  $A = 12$  (C) do  $A = 208$  (Pb) doprinosi boljem razumijevanju in-medium učinaka i stvaranja stranih čestica unutar nuklearne tvari.

## Uvod

Do sada ne postoji mnogo rezultata teorijskih i eksperimentalnih istraživanja za reakcije tipa  $\pi^- + N \rightarrow Y + K$ , gdje je  $Y$  hiperon, a  $K$  jedan od  $K$  mezona, osobito se to odnosi na  $\Lambda$  čestice na energijama koje su dostupne FOPI eksperimentu (1 - 2 AGeV). U području energija teškoionskog sinkrotrona na GSI-u stvaraju se čestice koje mogu sadržavati i kvarkove veće mase od  $u$  i  $d$  kvarkova. U tim reakcijama postiže se temperatura od oko 70 do 150 MeV i gustoća nuklearne tvari do 2 - 3  $\rho_0$ , pri čemu je  $\rho_0 = 0.17 \text{ fm}^{-3}$  normalna gustoća nuklearne tvari.

Kako bi se bolje razumijeli motivi i ciljevi ovog rada, predstavljeni su osnovni koncepti nuklearne tvari i njenih svojstava te fizika koja stoji iza proučavanja stvaranja stranih čestica u teškoionskim i elementarnim reakcijama poput pionski induciranih reakcija korištenih u ovom

eksperimentu.

Nuklearna tvar je sustav nukleona, sastavnih dijelova atomske jezgre koji međudjeluju jakim nuklearnom silom. U svom osnovnom stanju, nuklearna tvar ponaša se poput fluida, no kako bi se manifestirala neka njena temeljna svojstva, potrebno je to stanje promijeniti. Poznavanje jednadžbe stanja, dane skupom termodinamičkih varijabli ( $p$  - tlak,  $T$  - temperatura,  $\rho$  - gustoća), preduvjet je za opis mogućih stadija promatranog sustava tijekom reakcije. Svojstva nuklearne tvari mogu se istraživati pomoću teškoionskih sudara ili kroz elementarne reakcije kao što su reakcije inducirane pionima. Prednost elementarnih reakcija je stvaranje hadrona u poznatom stanju nuklearne tvari pri  $T = 0$  i  $\rho = \rho_0$ .

Dosadašnja teorijska i eksperimentalna istraživanja pokazala su kako se svojstva elementarnih čestica mogu mijenjati ovisno o gustoći nuklearne tvari (učinci nuklearnog medija). Proučavanje  $\pi^- + A \rightarrow \Lambda + K^0$  reakcije u tim uvjetima potaknuto je sljedećim činjenicama:

- postojanje dokaza za djelomičnu obnovu kiralne simetrije pri normalnoj gustoći nuklearne tvari postignute u elementarnim reakcijama,
- promjene u svojstvima stranih čestica kada se nalaze unutar nuklearne tvari,
- naglašen utjecaj in-medium učinaka na stvaranje stranih čestica blizu ili ispod praga,
- važnost posljedica istraživanja i za ostale grane fizike, npr. astrofiziku.

Posebna svojstva koja imaju strane čestice iziskuju i posebne metode koje se primjenjuju u njihovom proučavanju. Strane čestice nastaju brzo ( $\sim 10^{-23}$  s) kroz jako međudjelovanje koje čuva stranost, dok se raspadaju mnogo sporije ( $\sim 10^{-10}$  s) kroz slabo međudjelovanje. Prednost tog sporog raspada je da kćerke stranih čestica ne mogu biti zasjenjene hadronskim interakcijama. Nadalje, posjedovanje stranog kvarka dozvoljava zauzimanje energijski povoljnijih stanja budući da  $s$  kvark može zauzeti stanja već zauzeta  $u$  i  $d$  kvarkovima.

Dodatno, mjerenja stranih čestica na energijama dostupnim FOPI eksperimentu donose i druge povoljne mogućnosti za ovaj tip istraživanja. Budući da je za reapsorpciju strane čestice potrebna i druga čestica koja sadrži odgovarajući strani kvark (antikvark), a s obzirom na broj stvorenih stranih čestica na ovim energijama (npr.  $\approx 10^{-4} \Lambda$  / događaju), mala je vjerojatnost da se reapsorpcija dogodi. Nadalje, činjenica da su na FOPI energijama strane čestice stvorene ispod ili blizu praga čini ih dobrim probama za procese koji utječu na njihova svojstva. Stoga su strane čestice posebno zanimljive za FOPI eksperimente, bilo da su oni teškoionski ili se odvijaju pomoću elementarnih reakcija.

U uvodu su sažeto predstavljena neka od dosadašnjih eksperimentalnih i teorijskih istraživanja stranih čestica, koja su bila poticajna za ovaj rad.

## S273 FOPI eksperiment

Ime FOPI (engl. FOur PI) naziv je za sustav detektora, za eksperimente koji se pomoću njega ostvaruju te za međunarodnu kolaboraciju koja radi i surađuje na tim eksperimentima. Kako mu i ime sugerira, FOPI detektor konstruiran je tako da pokriva gotovo puni prostorni kut ( $4\pi$ ), a omogućava detekciju nabijenih čestica, dok se neutralne čestice rekonstruiraju preko produkata svojih raspada. Na GSI akceleratorском postrojenju moguće je dobiti primarne snopove kinetičkih energija od 0.1 do 2 AGeV te sekundarne pionske i protonske snopove u rasponu količine gibanja od 0.6 do 2.8 GeV/c.

S273 eksperiment sa sekundarnim pionskim snopom pri 1.15 GeV/c provodio se unutar dva tjedna u kolovozu 2004. godine. Snop negativnih piona sudarao se s ukupno pet nuklearnih meta (C, Al, Cu, Sn i Pb).

Osnovni ciljevi S273 FOPI eksperimenta bili su:

- istraživanje stvaranja stranih čestica u pionski induciranim reakcijama te njihovog ponašanja unutar nuklearnog medija pri normalnoj gustoći nuklearne tvari,
- mjerenje stvaranja stranosti unutar  $\pi^-$  reakcija na pet nuklearnih meta,
- proučavanje  $\pi^- + N \rightarrow \Lambda + K^0$  reakcije u nuklearnom mediju,
- određivanje inkluzivnog udarnog presjeka za reakciju  $\pi^- + N \rightarrow \Lambda + K^0$ ,
- ispitivanje ovisnosti udarnog presjeka stvaranja neutralnih stranih čestica o veličini mete jezgre (masenom broju),
- istraživanje povezanog stvaranja stranosti unutar nuklearnog medija kroz reakciju  $\pi^- + N \rightarrow \Lambda + K^0$  i
- testiranje izvedbe i učinkovitosti dva silicijska detektora u trakama (engl. silicon strip detector) prvi put upotrebljena u ovom eksperimentu.

Primarni snop ugljika energije 2 AGeV na produkcijskoj meti berilija dao je sekundarni pionski snop maksimalnog intenziteta od  $\sim 10^{11}\pi^-$  po mlazu (engl. spill), međutim snop piona koji dođe do mjesta održavanja FOPI eksperimenta (nakon 89 m transporta) imao je intenzitet  $\sim 2 \cdot 10^4\pi^-$  po mlazu. U presjeku je taj snop imao dimenzije  $2 \times 2 \text{ cm}^2$ , stoga su i nuklearne mete bile relativno velike, poprečnog presjeka  $4.5 \times 4.5 \text{ cm}^2$ . Debljine meta kretale su se u rasponu od 4 do 10 mm. Značajna količina podataka prikupljena je u reakcijama na metama ugljika i olova, dok je statistika za reakcije na preostale tri mete relativno mala ponajviše zbog kratkog vremena njihove izloženosti pionskom snopu (npr. meta olova bila je reakcijska meta unutar 117 h, dok je za metu kositra ukupno reakcijsko vrijeme bilo samo 9.5 h).

FOPI eksperimentalni sustav detektora predstavljen je unutar ovog poglavlja, s posebnim naglaskom na CDC (engl. Central Drift Chamber - centralna driftna komora) detektor, čiji su se

rezultati uglavnom koristili u analizi prezentiranoj unutar ovog rada. Za CDC detektor detaljno su opisana njegova tehnička svojstva, proces kalibracije, način na koji se detektira signal, vrši rekonstrukcija udaraca te prati putanja čestica. U sažetom obliku prezentirani su i ostali dijelovi FOPI detektorskog sustava: magnet, startni brojač, halo detektor, scintilacijski detektor snopa, Helitron (radijalna driftna komora), scintilatori Barrel, PLAWA (PLAstic WALL i detektor pri malim kutevima (engl. Zero Degree) te silicijski detektori po prvi put korišteni u S273 FOPI eksperimentu kako bi se poboljšala rezolucija količine gibanja čestica te unaprijedila rekonstrukcija sekundarnog verteksa. Također je prestavljen i sustav okidača (engl. trigger system) koji je poslužio u odabiru povoljnih događaja, tj. eliminaciji onih događaja koji sadržavaju šum (engl. background). Ukratko je opisana i popratna elektronika te proces prikupljanja eksperimentalnih podataka (engl. data acquisition).

S273 FOPI eksperiment korišten je kao baza za prijedlog i realizaciju novog pionskog FOPI eksperimenta održanog u lipnju 2011. godine pri 1.7 GeV/c.

## Analiza podataka

Kako bi se postigli ciljevi spomenuti u uvodnom dijelu, bilo je potrebno provesti detaljnu analizu podataka, koja između ostalog uključuje odabir povoljnih događaja, identifikaciju i rekonstrukciju značajnih čestica te proučavanje skupa fizikalnih veličina koje ih opisuju.

Odabrati relevantne događaje znači identificirati i ukloniti što je moguće više onih događaja koji sadržavaju šum. Dva su osnovna razloga za pozadinsko onečišćenje: događaji koji ne potječu od reakcija s metom i takozvani višestruki događaji kod kojih dva ili više piona dođu na metu gotovo istovremeno. Upotreba sustava okidača, uvođenje ograničenja na informacije dobivene od startnog brojača te ograničenja na položaj verteksa, mogu pomoći u smanjenju obje vrste pozadinskog onečišćenja.

Budući da se uz pomoć FOPI detektora mogu identificirati samo nabijene čestice, neutralne strane čestice poput  $\Lambda$  hiperona i  $K^0$  mezona rekonstruiraju se preko četveroimpulsa produkata njihovog raspada. Kako je  $K^0$  mezon miješano stanje  $K_S^0$  (od engl. short) i  $K_L^0$  (od engl. long) neutralnih kaona, bitno je istaknuti da je samo  $K_S^0$  moguće rekonstruirati pomoću podataka koji se dobiju u FOPI eksperimentu. Tomu je tako budući da je vrijeme života  $K_S^0$  mezona dovoljno kratko da se raspadne unutar područja prihvaćanja detektora. Drugi razlog je taj da konačno stanje  $K_L^0$  mezona uključuje nenabijene čestice, koje je nemoguće detektirati pomoću FOPI detektorskog sustava. Čestice koje može detektirati FOPI detektor identificiraju se preko njihovih masa koje su određene prosječnim gubitkom energije i zakrivljenošću odgovarajućeg traga (tj. količinom gibanja), informacijama koje izravno osigurava CDC detektor.

Kanali raspada  $\Lambda$  i  $K^0$  čestica relevantni za ovu analizu su:  $\Lambda$  čestica raspada se u reakciji  $\Lambda \rightarrow \pi^- + p$ , sa srednjim vremenom života  $2.63 \cdot 10^{-10}$  s i omjerom grananja 63.9%, dok se  $K_S^0$  raspada unutar srednjeg vremena života  $8.93 \cdot 10^{-11}$  s kroz reakciju  $K_S^0 \rightarrow \pi^- + \pi^+$  s omjerom grananja 68.6%.

Kako je već spomenuto, analizirani eksperimentalni podaci uglavnom su prikupljeni iz mjerenja na CDC detektoru. Osnovne veličine koje mjeri taj detektor su: radijus zakrivljenosti traga koji određuje transversalnu količinu gibanja čestice, srednji gubitak energije, najbliža udaljenost primarnog verteksa, brojnost udaraca (engl. multiplicity) i polarni kut. Sve spomenute veličine detaljno su objašnjene i prikazane unutar ovog poglavlja, te je istaknut njihov značaj i navedeni eventualni rezovi (engl. cuts) koji su se na njih primijenili u određenoj fazi postupka analize.

$\Lambda$  i  $K^0$  čestice identificiraju se pomoću metode invarijantne mase nakon što su određeni sekundarni verteksi. Te strane čestice rekonstruiraju se tako da se nađu točke sjecišta putanja parova njihovih kćerki nakon čega slijedi izračunavanje veličina koje ih određuju, poput invarijantne mase, količine gibanja ili rapiditeta.

Korištenjem metode invarijantne mase za identifikaciju stranih čestica dobiju se i kombinacije nekoreliranih čestica koje onda tvore kombinatorni šum. Jedan od načina na koji se taj šum može identificirati i eliminirati je upotreba metode miješanja događaja (engl. event-mixing method). Na primjer, negativni pion iz jednog događaja kombinira se s  $n$  protona (ili pozitivnih piona u slučaju  $K^0$  mezona) iz različitih događaja i kreira se novi spektar invarijantne mase. Nakon što je određen spektar miješanih događaja, integrira se onaj dio oba spektra u kojem se očekuje kombinatorni šum (područje desno i/ili lijevo od vrha koji pokazuje signal). Iz omjera integriranih dijelova izračuna se faktor normiranja (engl. scaling factor), koji služi za normiranje spektra miješanih događaja. Konačno, normirani spektar miješanih događaja oduzme se od izmjerenog spektra invarijantne mase kako bi se dobio željeni signal. Jako je bitno odabrati optimalan skup ograničenja na globalne parametre i parametre koji opisuju čestice, budući da o njima, do neke mjere, ovise i konačni rezultati. U okviru provedene analize učinjeno je mnogo testova na skupove ograničenja relevantnih parametara, a unutar ovog rada (u petom poglavlju) predstavljena su i diskutirana izabrana tri skupa.

## Simulacija i ocjena efikasnosti

Zbog ograničenja detektora, u smislu njegovog geometrijskog prihvatanja i efikasnosti, ali i nesavršenosti procesa identifikacije i rekonstrukcije čestica, prvotno dobivene eksperimentalne rezultate potrebno je korigirati kako bi se dobio stvaran broj stranih čestica u cjelokupnom skupu eksperimentalnih podataka. Za određivanje faktora korekcije efikasnosti korištene su numeričke simulacije eksperimenta. Kako bi se iz eksperimentalnih podataka dobili valjani rezultati, sve fizikalne veličine trebaju se popraviti s obzirom na utjecaj efikasnosti i prostornog prihvatanja detektora.

Za detektor kao što je FOPI, koji je ujedinjeni sustav različitih subdetektora, potrebna je opsežna simulacija koja uključuje sve relevantne fizikalne procese i njihove učinke. U simulaciji detektora, nuklearnih reakcija i prenošenja (engl. transferring) čestica korišten je GEANT 3.21 simulacijski programski paket s CERN-a. Taj simulacijski paket osigurava dobar opis dete-

ktorskog sustava te alate koji pomažu u dizajniranju i optimiziranju sastavnih jedinica detektora, u unapređenju programa korištenih za analizu te razumijevanju eksperimentalnih mjerenja.

GEANT simulacija prihvaća događaje prethodno dobivene pomoću Monte Carlo generatora. Dakle, izlazni podaci (engl. output) generatora događaja su ulazni podaci (engl. input) za iduću fazu simulacije - prijenos (engl. transport) čestica kroz simulirani detektor. Unutar ovog rada ulogu prijenosa čestica preuzima FLUKA (FLUktuierende KAskade) - program koji u sebi sadržava fizikalne i transportne procese za hadrone i leptone, točnije verzija tog programa ugrađena u GEANT - GEANT3-FLUKA.

Dva su tipa simulacija korištena u ovoj analizi. U prvom je kao generator događaja upotrebljen GiBUU (Giessen Boltzmann-Uehling-Uhlenbeck), a transportna faza je izvršena pomoću FLUKA-e. Upotreba GiBUU transportnog modela bila je motivirana određivanjem globalne efikasnosti rekonstrukcije. GiBUU, kao i drugi transportni modeli ima mikroskopski pristup u kojem se dinamička evolucija sustava promatra u malim vremenskim intervalima. Baza svih BUU transportnih modela je BUU transportna jednačica koja daje opis sudara pod utjecajem srednjeg polja okolne nuklearne tvari. Ovaj tip simulacije u tekstu je označen kao TYPE1. U drugom tipu simulacija (u tekstu TYPE2) definira se početna čestica (čestica ulaznog snopa) - pion, preko svoje količine gibanja, te se s obzirom na dimenzije snopa odabire i polazna točka ispred mete, nakon čega nastupa faza transporta, koja se opet obavlja pomoću FLUKA-e. U ovom tipu simulacije, naknadno su dodane lambda čestice, određene svojom količinom gibanja i rapiditetom, kako bi se povećala statistika potrebna za određivanje efikasnosti rekonstrukcije. Nadalje, omjer grananja za kanal raspada strane čestice koji je od interesa u analizi postavljen je na 100 % iz istog razloga. U tom slučaju simulacija TYPE2 označena je kao TYPE2A.

Potpuna definicija detektora uključuje opis geometrije elemenata detektora, njegovih fiksnih dijelova i njihovih međusobnih položaja te logičkih odnosa, korištenih materijala i elektromagnetskih svojstava, njegovog vizualnog identiteta te dodatnih karakteristika pridruženih od strane korisnika. Poseban naglasak unutar ovog rada stavljen je na CDC subdetektor, budući da su se za veći dio provedene analize koristili podaci dobiveni mjerenjima upravo na tom detektoru.

Nakon što je čitav FOPI eksperimentalni sustav, zajedno s odgovarajućom metom, uspješno simuliran, kroz njega se propuštaju čestice i prati se odziv detektora. Sve kinematičke i dinamičke varijable sačuvane su unutar baze podataka (tzv. KINE banka), a konačni (izlazni) podaci imaju oblik ekvivalentan onima dobivenim u eksperimentu. Stoga se u toj završnoj fazi koriste identični programi za analizu kao i kod obrade eksperimentalnih podataka.

Korekcije koje proizlaze iz geometrijskog prihvaćanja i efikasnosti detektora potrebne su kako bi se dobili što precizniji rezultati, odnosno što realnija slika proizašla iz podataka prikupljenih u eksperimentu. Efikasnost rekonstrukcije (globalna efikasnost) određena je omjerom broja detektiranih (rekonstruiranih) čestica i originalnog broja čestica pohranjenih u KINE banci. Rezultati globalne efikasnosti dobiveni su korištenjem prvog tipa simulacije, dok je drugi tip simulacije poslužio za određivanje korekcije lokalne efikasnosti, što je detaljnije objašnjeno u daljnjem tekstu.

Kako bi se odredila prava vrijednost efikasnosti važno je da postoji slaganje među raspodjelama faznog prostora za eksperimentalne i simulirane podatke pod istim uvjetima. Stoga su uspoređeni rezultati svih relevantnih fizikalnih veličina dobivenih iz eksperimenta s onima proizašlim iz simulacija. Prikazani su i diskutirani rezultati dobiveni iz reakcija negativnih piona na metama s najboljom statistikom - mete ugljika i olova.

Rezultati dobiveni prvom metodom, korištenjem GiBUU transportnog modela, u nekim raspodjelama (transverzalna udaljenost od primarnog verteksa  $d_0$  i masa) pokazuju odlično slaganje s eksperimentalnim rezultatima za obje čestice kćerke ( $\pi^-$  i *proton*) u reakcijama na metama ugljika i olova. Međutim, postoje određena neslaganja za longitudinalnu udaljenost od primarnog verteksa  $z_0$  i transverzalne količine gibanja čestica  $p_t$ , osobito za drugu česticu - *proton*. Razlike u raspodjelama za  $z_0$  mogu se objasniti rezolucijom longitudinalne komponente koja je lošija u simulaciji u odnosu na eksperiment za otprilike 20 – 25 %. Također, u slučaju mete olova, opaža se u spektru mase dodatni manji vrh lijevo od nominalne mase protona, koji je posljedica velikog raspona dozvoljenih masa u ovoj fazi analize, a može se lako ukloniti malo oštrijim rezom (dodatnim ograničenjem) na masu. Uspoređene raspodjele relevantnih fizikalnih veličina (transverzalna i longitudinalna najmanja udaljenost od primarnog verteksa ( $d_0$  i  $z_0$ ), transverzalna količina gibanja  $p_t$ , rapiditet  $y_{lab}$ , transverzalna udaljenost od sekundarnog verteksa  $r_t$  i pokazujući kut (engl. pointing angle)  $\Delta\phi$ ) za  $\Lambda$  česticu daju izvrsna slaganja za reakcije na obje mete (C i Pb).

Za drugi tip simulacije raspodjele pokazuju bolje slaganje s onima dobivenima iz eksperimentalnih podataka za  $z_0$  i masu (posebno se to odnosi na *proton*), ali su dobivena veća odstupanja za  $d_0$ . Transverzalne količine gibanja prate jednake trendove, međutim i u slučaju ovog tipa simulacije, odstupanja postoje, osobito za  $\pi^-$ . Kao i kod prvog tipa korištene simulacije i u slučaju simulacije TYPE2 raspodjele za  $\Lambda$  česticu su u izvrsnom slaganju, osim za  $p_t$ , što je očekivana posljedica odstupanja u transverzalnim količinama gibanja čestica kćerki raspada.

Ukoliko se lambda čestice dodaju u simulaciju drugog tipa, zanimljivo je pogledati kako su raspodijeljene unutar faznog prostora. Iz te raspodjele vidljivo je kako efikasnost rekonstrukcije  $\Lambda$  čestica korištenjem CDC detektora nije homogena unutar njegovog prostora prihvatanja, što je poslije potvrdila i daljnja analiza.

Kao što je spomenuto, problemu ocjene efikasnosti pristupilo se na dva načina. U prvom se pretpostavilo kako postoji pouzdan model koji može reproducirati realne raspodjele čestica i stoga je poznata stvarna raspodjela stranih čestica  $N_{prod}(\vec{p})$ . Nakon što se simuliraju događaji s generiranim stranim česticama (lambdama), primjenjuje se analiza podataka, rekonstruiraju se strane čestice i dobiveni broj rekonstruiranih stranih čestica koristi se za određivanje efikasnosti. Drugi način pretpostavlja da ne postoji pouzdan model te da je  $N_{prod}(\vec{p})$  nepoznato. U tom slučaju, fazni prostor  $\Omega$  dijeli se na podprostore  $\Omega_i$  s pretpostavkom da je funkcija  $\varepsilon(\vec{p}_1, \vec{p}_2)$ , koja predstavlja vjerojatnost da se čestica koja je stvorena u  $\vec{p}_2$  rekonstruira u  $\vec{p}_1$ , konstantna za svaki podprostor  $\Omega_i$ . Nakon toga provodi se analiza i rekonstruiraju se strane čestice za svaki od podprostora  $\Omega_i$ . Dobiveni omjeri rekonstruiranih i stvorenih čestica zapisuju se u  $15 \times 15$



matricu efikasnosti  $\Phi$  pomoću koje je onda moguće odrediti broj stranih čestica generiranih u svakom od podprostora.

Dodatno su konačni rezultati korigirani i za faktor omjera grananja  $\Lambda$  čestice za kanal  $\Lambda \rightarrow \pi^- + p$ , 0.639, budući da je u simulaciji taj faktor bio postavljen na 1.

Rezultati dobiveni korištenjem prvog tipa simulacije u analizi provedenoj za mete ugljika i olova dali su sljedeće vrijednosti za efikasnost rekonstrukcije:  $\varepsilon_C = (0.370 \pm 0.010)\%$  i  $\varepsilon_{Pb} = (0.291 \pm 0.008)\%$ . Za mete srednjih masa (Al, Cu i Sn) efikasnost rekonstrukcije aproksimirana je linearnom interpolacijom na izračunate vrijednosti efikasnosti za C i Pb.

Rezultati dobivenih vrijednosti elemenata matrice efikasnosti  $\Phi$ , zajedno s odgovarajućim statističkim pogreškama za svaki od analiziranih podprostora (binova) zapisani su unutar tablice, a dalje su korišteni kako bi se odredila raspodjela udarnog presjeka u različitim  $p_t$  i  $y$  binovima. Te raspodjele prikazane su i diskutirane unutar idućeg poglavlja.

## Eksperimentalni rezultati i rasprava

Jedan od motiva za analizu prezentiranu u sklopu ovog rada bio je još uvijek jako mali broj objavljenih studija za reakcije tipa  $\pi^- + A \rightarrow Y + K^0$  ( $Y$  je hiperon) osobito na energijama  $\sim 1 - 2$  AGeV. Međutim, u smislu usporedbe rezultata s dosadašnjim eksperimentalnim i teorijskim istraživanjima, istovremeno je ta činjenica i ograničavajuća. Stoga bi rad na proučavanju inkluzivnog stvaranja  $\Lambda$  hiperona (i  $K^0$  mezona) unutar reakcije  $\pi^- + A \rightarrow \Lambda + K^0$  trebao doprinijeti boljem razumijevanju stvaranja stranih čestica na FOPI energijama i utjecaju koji na te čestice ima nuklearna tvar. Provedena je opsežna analiza podataka dobivenih u S273 FOPI eksperimentu na svih pet korištenih meta za obje neutralne strane čestice ( $\Lambda$  i  $K^0$ ), ali dodatan značaj je stavljen na  $\Lambda$  česticu, čiji su rezultati detaljno prikazani unutar ovog poglavlja.

Prije same rekonstrukcije stranih čestica napravljeni su brojni testovi na globalnim varijablama i na fizikalnim veličinama koje opisuju sekundarne čestice (kćerke raspada stranih čestica), poput udaljenosti od primarnog verteksa, količine gibanja i mase. Sve raspodjele prikazane su prije i nakon primjene rezova za rezultate dobivene u reakcijama na metama ugljika i olova. Za veličine koje karakteriziraju samu  $\Lambda$  česticu, a relevantne su u daljnjoj analizi ( $d_0$ ,  $z_0$ ,  $p_t$ ,  $y_{lab}$ ,  $r_t$  i  $\Delta\phi$ , kao i u četvrtom poglavlju), načinjena je direktna usporedba među raspodjelama dobivenim za mete ugljika i olova.

Iako je statistika za mete aluminijska, bakra i kositna, u usporedbi s najlakšom metom ugljika i s metom najveće mase - metom olova, značajno manja, u analizi podataka dobivenih iz reakcija na svih pet korištenih meta  $\Lambda$  čestica uspješno je rekonstruirana. U spektrima invarijantne mase vidljiv je naglašen vrh u području  $\pm 2\sigma$  nominalne mase  $m_\Lambda = 1.116$  GeV/c<sup>2</sup>. Rezultati za  $K_S^0$  mezon također pokazuju jasan signal unutar  $\pm 2\sigma$  nominalne mase neutralnog kaona ( $m_{K^0} = 0.494$  GeV/c<sup>2</sup>) u spektrima invarijantne mase za svih pet meta, a prikazani su samo rezultati za mete ugljika i olova. Dobiveni vrh spektra invarijantne mase pomaknut je udesno u odnosu na nominalnu masu neutralnog kaona za 0.01 GeV/c<sup>2</sup>.

Stvaranje strane čestice može se opisati preko izraza koji predstavlja produkt dviju varijabli: amplitude zapisane pomoću matričnog elementa, koja sadrži sve dinamičke veličine, te faktora faznog prostora odgovornog za kinematičke informacije. Iz tog razloga jako je bitno ispitati raspodjele faznog prostora, odnosno relacije između rapiditeta  $y_{lab}$  i transversalne količine gibanja  $p_t$ . Načinjene su i diskutirane usporedbe rezultata dobivenih za reakcije na C i Pb metama.

Raspodjele transversalne količine gibanja pokazuju da za  $p_t$  vrijednosti od  $\approx 200$  MeV/c do  $\approx 400$  MeV/c  $\Lambda$  čestice proizašle iz reakcija na olovu pokazuju veći prirast od onih dobivenih u reakcijama na ugljiku. Za  $p_t$  veći od  $\approx 400$  MeV/c situacija je suprotna, više  $\Lambda$  čestica nastalo je u reakcijama s ugljikom, dok se za  $p_t$  veći od  $\approx 900$  MeV/c raspodjele za obje mete preklapaju. Raspodjela rapiditeta za  $y_{lab}$  manji od  $\approx -0.2$  pokazuje približno jednak broj  $\Lambda$  čestica dobivenih u reakcijama na meti ugljika i meti olova. Za  $y_{lab}$  od  $-0.1$  nešto veći broj  $\Lambda$  čestica opažen je za olovo sve do  $y_{lab} \approx 0.35$  kada  $\Lambda$  čestice nastale u reakcijama na meti ugljika pokazuju veći prirast. Preklapanje rezultata za obje mete nastupa opet za  $y_{lab} > 0.7$ .

Nakon provedene analize faznog prostora te prethodno izračunate korekcije efikasnosti rekonstrukcije pomoću simulacije TYPE1 koja koristi GiBUU transportni model, izračunati su inkluzivni udarni presjeci za  $\Lambda$  česticu za reakcije na svih pet nuklearnih meta:  $\sigma_R(C) = 14.93 \pm 0.62$  mb,  $\sigma_R(Al) = 25.45 \pm 0.46$  mb,  $\sigma_R(Cu) = 60.24 \pm 0.45$  mb,  $\sigma_R(Sn) = 52.89 \pm 0.36$  mb te  $\sigma_R(Pb) = 137.56 \pm 0.40$  mb. Vrijednosti udarnog presjeka za mete ugljika i olova dobivene su uz korekciju efikasnosti određenu upravo za te mete, dok su za mete srednjih masa (Al, Cu i Sn) u izračunavanju udarnog presjeka korekcije efikasnosti aproksimirane linearnom interpolacijom, korištenjem dvije poznate vrijednosti korekcije efikasnosti dobivene za C i Pb. Navedene pogreške su statističke pogreške.

Nadalje, ispitana je zavisnost udarnog presjeka o masenom broju jezgre  $A$ . Nakon što su prikazani rezultati svih pet udarnih presjeka za odgovarajući maseni broj jezgre, provjeravano je preklapanje točaka s tri različite funkcije: linearnom funkcijom koja daje zavisnost  $\sigma_R$  o  $A$  odnosno  $\sigma_R$  o  $A^{2/3}$ , linearnom funkcijom koja ima doprinosi i od  $A$  i od  $A^{2/3}$ :  $(P_1 \cdot A + P_2 \cdot A^{2/3})$  te funkcijom oblika  $\sigma_{eff} \cdot A^\alpha$ . Iz dobivenih rezultata može se zaključiti kako je stvaranje lambda čestice vjerojatnije na površini jezgre nego u njenoj unutrašnjosti. Tome u prilog ide bolja podudarnost na linearnu funkciju ovisnosti udarnog presjeka o  $A^{2/3}$  nego ona dobivena za ovisnost o  $A$ , dominacija  $A^{2/3}$  faktora pri preklapanju s funkcijom koja je kombinacija volumnog i površinskog člana te izračunati parametar  $\alpha$  iz četvrte korištene funkcije ( $\sigma_{eff} \cdot A^\alpha$ ) čija je dobivena vrijednost bliže  $2/3$  nego 1.

Rezultati dobiveni pomoću drugog pristupa određivanja korekcije efikasnosti prikazani su pomoću raspodjela diferencijalnog udarnog presjeka u ovisnosti o rapiditetu za tri  $p_t$  bina ( $p_t \in (0.18, 0.38)$  GeV/c,  $p_t \in (0.38, 0.58)$  GeV/c i  $p_t \in (0.58, 0.78)$  GeV/c). Uspoređeni su rezultati dobiveni za mete ugljika i olova. Potvrđeno je kako se  $\Lambda$  čestice većinom mogu pronaći u prednjem dijelu faznog prostora s rapiditetima većim od 0, pri čemu se maksimalni prirast opaža za  $y \in (0.2, 0.4)$ .

Osim izračunatih statističkih pogrešaka, ocijenjene su i sistematske pogreške provedene analize čiji su glavni doprinosi: metode korištene za identifikaciju i rekonstrukciju čestica i veliki promjer snopa za kojeg je pokazano da utječe na ocjenu efikasnosti, dok zanemariv doprinos ima i prebrojavanje čestica pomoću sustava okidača. Kako bi se ocijenila sistematska pogreška nastala kao posljedica korištenja određene metode za identifikaciju i rekonstrukciju čestica, varirala su se ograničenja na relevantne parametre korištene u analizi podataka. Prikazana su tri skupa ograničenja čijim se korištenjem dobiju različiti rezultati analize. Kako bi se odredila mjera utjecaja veličine snopa na ocjenu efikasnosti, a onda i na izračun ukupnog broja stranih čestica, odnosno udarnih presjeka, analizirani su i uspoređeni podaci položaja i rezolucije primarnog verteksa upotrebom CDC-a i silicijskih detektora. Na temelju relativne razlike u konačnim rezultatima dobivenim korištenjem različitih rezolucija primarnog verteksa određen je doprinos sistematskoj pogrešci. Također, usporedbom rezultata dobivenih za udarne presjeke na svih pet reakcijskih meta za  $K^0$  mezon s već objavljenim rezultatima dobivenim različitim metodom za iste eksperimentalne podatke, izračunata je sistematska pogreška unutar tog dijela analize. Dodatno, u ocjeni korekcije globalne efikasnosti te posljedično izračunatih udarnih presjeka za mete srednjih masa, doprinos sistematskoj pogrešci za te tri mete (Al, Cu i Sn) daje i aproksimacija efikasnosti linearnom interpolacijom vrijednosti dobivenih za C i Pb mete.

## Pregled i zaključci

Glavni cilj ovog istraživanja bio je proučiti inkluzivno stvaranje  $\Lambda$  čestice u pionski induciranim reakcijama pri normalnoj gustoći nuklearne tvari. Po prvi put se u FOPI eksperimentu koristio sekundarni snop negativnih piona količine gibanja 1.15 GeV/c u reakcijama na pet nuklearnih meta (C, Al, Cu, Sn i Pb). Najviše eksperimentalnih podataka pritom je prikupljeno za mete ugljika i olova, dok je statistika za mete srednjih masa značajno lošija.

U sklopu ovog eksperimenta načinjeno je nekoliko promjena u samom sustavu detektora od kojih je najznačajnija ugrađivanje novog silicijskog detektora u svrhu poboljšanja rezolucije količine gibanja te unapređenja rekonstrukcije sekundarnog verteksa čestica. Neke osobine (rezolucija verteksa) tog novog detektora ispitane su unutar provedene analize, a mogućnosti njegove izvedbe korištene su tek u njenim dijelovima. Također, bilo je potrebno razviti i usavršiti programe potrebne za provođenje željene analize podataka. U tom smislu, jedan od doprinosa ovog rada je korištenje rezultata i prednjih dijelova detektora za rekonstrukciju  $\Lambda$  čestice. Pokazano je postojanje jasnog signala u spektru invarijantne mase za proton detektiran u Helitronu, a negativni pion u CDC detektoru.

Nadalje, provedena je detaljna usporedba eksperimentalnih rezultata s onima dobivenima pomoću simulacije kako bi se dobile korekcije efikasnosti potrebne za određivanje udarnih presjeka iz eksperimentalno dobivenih raspodjela. Za simulaciju podataka unutar ove analize korištene su dvije prethodno opisane metode. Pri izračunavanju korekcije globalne efikasnosti rekonstrukcije upotrijebljen je prvi tip simulacije (TYPE1), dok se ocjena lokalne efikasnosti

dobila analizom 15 podprostora faznog prostora  $\Lambda$  čestice te računanjem  $15 \times 15$  matrice efikasnosti  $\Phi$  (simulacija TYPE2).

Prezentirani su rezultati rekonstrukcije  $\Lambda$  čestice metodom invarijantne mase za svih pet meta korištenih u eksperimentu. Uspoređene su raspodjele faznog prostora za mete ugljika i olova.

Inkluzivni udarni presjek određen je za svih pet meta, korištenjem korekcije efikasnosti proizašle iz rezultata simulacije TYPE1, s tim da se za mete srednjih masa koristila aproksimacija efikasnosti rekonstrukcije izračunatih za C i Pb. Ispitana je ovisnost udarnog presjeka o masenom broju jezgre  $A$ , tj. o dimenzijama jezgre. Jedan od motiva tog istraživanja bio je ispitati događa li se stvaranje  $\Lambda$  čestice unutar volumena jezgre ili na njenoj površini. Dobiveni rezultati preklapanja prikazanih ovisnosti s tri različite funkcije (linearnom funkcijom  $\sigma_R = f(A)$  odnosno  $\sigma_R = f(A^{2/3})$ , linearnom funkcijom  $\sigma_R = P_1 \cdot A + P_2 \cdot A^{2/3}$ ) te funkcijom oblika  $\sigma_R = \sigma_{eff} \cdot A^\alpha$ ) pokazali su kako je stvaranje  $\Lambda$  čestice vjerojatnije na površini jezgre nego u njenoj unutrašnjosti. Raspodjela diferencijalnog udarnog presjeka u ovisnosti o rapiditetu za različite binove transversalne količine gibanja dobivena je pomoću korekcija lokalne efikasnosti proizašlih iz simulacije TYPE2 $\Lambda$ . Iz dobivenih rezultata vidljivo je kako je veća vjerojatnost stvaranja  $\Lambda$  čestica u prednjoj hemisferi ( $y > 0$ ), što je potvrdilo teorijska predviđanja.

Provedeno istraživanje planira se proširiti na analizu podataka novijeg pionskog eksperimenta održanog 2011. godine pri većoj količini gibanja (1.7 GeV/c) s metama ugljika, bakra i olova. Tako bi se mogli, osim za reakcijske mete različitih dimenzija, usporediti i rezultati dobiveni na dvije različite energije te eventualno unaprijediti alati i metode korištene unutar ovog istraživanja. Također, za utvrđivanje statističke granice na zajedno stvorene parove  $\Lambda - K^0$  potrebna je veća statistika od one dostupne u ovom eksperimentu, stoga bi se u tom smjeru započeta analiza mogla nastaviti na podacima eksperimenta iz 2011. godine. Nadalje, u reakcijama ovog tipa u sklopu FOPI eksperimenta može se provesti i ekskluzivno mjerenje za neutrealne strane čestice poput  $K^0$  i  $\Lambda$ .

**Ključne riječi:** nuklearna tvar, učinci nuklearne tvari, strane čestice, pionski inducirane reakcije,  $\Lambda$  hiperon, inkluzivni udarni presjek



# Contents

<b>Overview</b>	<b>1</b>
<b>1 Introduction</b>	<b>3</b>
1.1 Properties of Nuclear Matter . . . . .	3
1.1.1 Phases of Nuclear Matter . . . . .	4
1.1.2 Equation of State . . . . .	6
1.1.3 In-Medium Effects . . . . .	7
1.2 Measurements of Strange Particles . . . . .	11
1.2.1 Strange Particles in Heavy Ion Collisions . . . . .	11
1.2.2 Strange Particles in Elementary Reactions . . . . .	15
<b>2 The S273 FOPI Experiment</b>	<b>21</b>
2.1 FOPI in General . . . . .	21
2.2 Basic Characteristics of the S273 Experiment . . . . .	22
2.3 Pion Beam at the GSI . . . . .	22
2.4 Target Properties . . . . .	23
2.5 Experimental Setup . . . . .	24
2.5.1 Magnet . . . . .	25
2.5.2 Start Counter . . . . .	25
2.5.3 Halo Detector . . . . .	25
2.5.4 Beam Scintillator Detector . . . . .	25
2.5.5 Central Drift Chamber (CDC) . . . . .	26
2.5.6 Helitron . . . . .	31
2.5.7 Barrel . . . . .	32
2.5.8 Plastic Wall (PLAWA) . . . . .	33
2.5.9 Zero Degree Detector . . . . .	33
2.5.10 Silicon Strip Detector . . . . .	33
2.5.11 Trigger System . . . . .	34
2.6 Electronics and Data Acquisition . . . . .	36

<b>3</b>	<b>Data Analysis</b>	<b>39</b>
3.1	Event Selection . . . . .	39
3.2	Detector Acceptances . . . . .	42
3.3	Particles Identification and Reconstruction . . . . .	43
3.3.1	Properties of Strange Particles . . . . .	44
3.3.2	Decay Particle Selection . . . . .	45
3.3.3	Reconstruction Methods for $V^0$ Particles . . . . .	50
3.3.4	Determination of the Combinatorial Background . . . . .	53
<b>4</b>	<b>Physics Simulations and Efficiency Correction</b>	<b>59</b>
4.1	GEANT Simulation . . . . .	60
4.1.1	Event Generation . . . . .	60
4.1.2	Simulation of the Detector . . . . .	61
4.2	GiBUU Transport Model . . . . .	66
4.3	Comparison of Simulated and Measured Distributions . . . . .	67
4.3.1	TYPE1 Simulation . . . . .	67
4.3.2	TYPE2 Simulation . . . . .	71
4.4	Acceptance and Efficiency Corrections . . . . .	76
4.4.1	Efficiency Evaluation . . . . .	77
4.4.2	Results of the Efficiency Evaluation . . . . .	82
<b>5</b>	<b>Experimental Results and Discussion</b>	<b>89</b>
5.1	Invariant Mass Spectra . . . . .	89
5.2	$\Lambda$ Particle Phase Space Distributions . . . . .	96
5.3	$\Lambda$ Inclusive Cross Section . . . . .	98
5.3.1	Cross Section as a Function of the System Size . . . . .	100
5.4	Differential Cross Section Distributions . . . . .	102
5.5	Systematic Error Estimation . . . . .	104
<b>6</b>	<b>Summary and Outlook</b>	<b>109</b>
<b>A</b>	<b>The Bethe-Bloch Formula</b>	<b>113</b>
<b>B</b>	<b>Kinematic Variables</b>	<b>115</b>
<b>C</b>	<b>Invariant Cross Section</b>	<b>117</b>
<b>D</b>	<b>BUU Transport Model Equation</b>	<b>119</b>

# List of Figures

1.1	Phase diagram of nuclear matter . . . . .	5
1.2	Dependence of the quark condensate on $T$ and $\rho$ . . . . .	9
1.3	Effective kaon mass as a function of nuclear matter density . . . . .	10
1.4	Subthreshold production of $K^+$ and $K^-$ in heavy ion reactions . . . . .	12
1.5	Differential yield distribution of $K^+$ . . . . .	13
1.6	Transverse momentum dependence of differential flow of $K^+$ . . . . .	14
1.7	$\Lambda$ and $\Xi^-$ production at AGS and SPS . . . . .	14
1.8	Total potential for lambda hyperon and nucleon . . . . .	16
1.9	The invariant amplitude for the $\pi^- + p \rightarrow \Lambda + K^0$ reaction . . . . .	16
1.10	Cross section as a function of invariant collision energy . . . . .	17
1.11	$K^0$ cross section from elementary reactions . . . . .	18
2.1	GSI pion beam . . . . .	23
2.2	FOPI detector system . . . . .	24
2.3	Cross section illustration of the CDC . . . . .	27
2.4	Illustration of the electric field and drift trajectories . . . . .	28
2.5	Regular and mirror tracks in a CDC sector . . . . .	29
2.6	Sketch of time offset calibration . . . . .	30
2.7	Sketch of drift velocity calibration . . . . .	31
2.8	Sketch of Lorentz angle calibration . . . . .	32
2.9	Position of silicon micro-strip detector in S273 experiment . . . . .	34
2.10	Illustration of the trigger system. . . . .	35
2.11	Scheme example of an acquisition system . . . . .	36
3.1	$v_y$ vs $v_x$ CDC vertex distribution . . . . .	40
3.2	$v_z$ vertex distribution . . . . .	41
3.3	Start time and energy loss in the start counter distributions . . . . .	41
3.4	Geometrical acceptance of the FOPI detector. . . . .	42
3.5	Invariant mass spectrum for $\Lambda$ including forward and backward subdetectors. . . . .	43
3.6	Neutral strange particles decay scheme . . . . .	44
3.7	Particle position inside the CDC . . . . .	46



3.8	Energy loss as a function of the momentum per charge . . . . .	47
3.9	CDC mass spectrum . . . . .	48
3.10	Secondary vertex determination for $V^0$ particle . . . . .	51
3.11	Reconstruction of $V^0$ particle . . . . .	52
3.12	An example of the $\Lambda$ invariant mass spectrum used for background determination. . . . .	53
3.13	An example of the $\Lambda$ invariant mass spectrum with signal calculation. . . . .	54
3.14	Background evaluation procedure . . . . .	55
3.15	Background subtraction procedure . . . . .	56
4.1	Spatial $z$ resolution comparison between data and simulation . . . . .	64
4.2	Spatial $xy$ resolution comparison between data and simulation . . . . .	65
4.3	Transverse momentum resolution comparison between data and simulation . . . . .	65
4.4	TYPE1 simulation and experimental data comparison for $\Lambda$ daughters, C target . . . . .	68
4.5	TYPE1 simulation and experimental data comparison for $\Lambda$ daughters, Pb target . . . . .	69
4.6	Simulation TYPE1 and experimental data comparison for $\Lambda$ , C target . . . . .	70
4.7	TYPE1 simulation and experimental data comparison for $\Lambda$ , Pb target . . . . .	71
4.8	TYPE2 simulation and experimental data comparison for $\Lambda$ daughters, C target . . . . .	72
4.9	TYPE2 simulation and experimental data comparison for $\Lambda$ particle, C target . . . . .	74
4.10	$\Lambda$ phase space distribution for C target, TYPE2 $\Lambda$ simulation . . . . .	75
4.11	$\Lambda$ invariant mass spectrum, TYPE2 $\Lambda$ simulation . . . . .	75
4.12	Illustration of phase space division into 24 subspaces . . . . .	79
4.13	One bin phase space distribution, first example . . . . .	79
4.14	Illustration of phase space division into 15 subspaces . . . . .	80
4.15	One bin phase space distribution, second example . . . . .	80
4.16	Illustration of phase space division into 6 subspaces . . . . .	81
4.17	One bin phase space distribution, third example . . . . .	81
4.18	Efficiency versus rapidity for $p_t \in (0.18, 0.38)$ GeV/c . . . . .	87
4.19	Efficiency versus rapidity for $p_t \in (0.38, 0.58)$ GeV/c . . . . .	87
4.20	Efficiency versus rapidity for $p_t \in (0.58, 0.78)$ GeV/c . . . . .	87
5.1	$\Lambda$ daughter particles distributions, C target . . . . .	90
5.2	$\Lambda$ daughter particles distributions, Pb target . . . . .	90
5.3	$\Lambda$ distribution comparisons between C and Pb target . . . . .	91
5.4	$\Lambda$ invariant mass spectrum, C target . . . . .	93
5.5	$\Lambda$ invariant mass spectrum, Al target . . . . .	93
5.6	$\Lambda$ invariant mass spectrum, Cu target . . . . .	94
5.7	$\Lambda$ invariant mass spectrum, Sn target . . . . .	94
5.8	$\Lambda$ invariant mass spectrum, Pb target . . . . .	95
5.9	$K_S^0$ invariant mass spectrum for C and Pb targets . . . . .	95
5.10	$\Lambda$ phase space distribution for C and Pb targets . . . . .	96

5.11	Transverse momentum distribution compared between C and Pb target . . . . .	97
5.12	Rapidity distribution compared between C and Pb target . . . . .	98
5.13	$\Lambda$ production cross section as a function of $A$ , (1) . . . . .	100
5.14	$\Lambda$ production cross section as a function of $A$ , (2) . . . . .	101
5.15	Differential cross section dependence on rapidity, $p_t \in (0.18, 0.38)$ . . . . .	103
5.16	Differential cross section dependence on rapidity, $p_t \in (0.38, 0.58)$ . . . . .	103
5.17	Differential cross section dependence on rapidity, $p_t \in (0.58, 0.78)$ . . . . .	103
5.18	Compared rapidity distribution for C and Pb targets . . . . .	104
5.19	Vertex distribution for the CDC and silicon detectors . . . . .	105
5.20	Efficiency dependence on vertex resolution . . . . .	106



# List of Tables

2.1	Target properties . . . . .	24
3.1	Basic properties of $\Lambda$ and $K_S^0$ . . . . .	45
3.2	Selection cuts for $\Lambda$ particle and its decay products . . . . .	49
3.3	Selection cuts for $K_S^0$ particle and its decay products . . . . .	50
3.4	Additional selection cuts used for the reconstruction of $\Lambda$ and $K_S^0$ . . . . .	52
4.1	$\Lambda$ masses and widths obtained from the data and the simulation TYPE2 $\Lambda$ . . .	76
4.2	Evaluated global efficiencies for the reactions on C and Pb targets . . . . .	82
4.3	Phase space analysis for 15 bins division, C target . . . . .	83
4.4	Phase space analysis for 15 bins division, Pb target . . . . .	85
5.1	Masses and widths for $\Lambda$ produced in five targets reactions . . . . .	92
5.2	Cross section for $K^0$ . . . . .	99
5.3	Reconstructed $\Lambda$ particles and calculated cross sections . . . . .	99
5.4	Sets of cuts used for $\Lambda$ particle analysis . . . . .	107
5.5	$\Lambda$ particle reconstruction with three different sets of cuts . . . . .	108
5.6	Total cross sections with corresponding estimated systematic errors . . . . .	108



# Overview

This thesis presents the results of a measurement for neutral strange particles production in pion-nucleus reaction at 1.15 GeV/c, with special emphasis on the lambda particle. The data analysed in the thesis was obtained by means of the FOPI (FOur PI) detector experiment at the GSI (Gesellschaft für Schwerionenforschung) facility in August 2004.

The outline of the study is presented in the following paragraphs.

In Chapter 1, the main concepts of nuclear matter and its properties are introduced and the phenomenon of in-medium effects is discussed. General physics of strange particle production in heavy-ion and elementary reactions is presented together with examples found in experiments and theoretical models. The motivation for additional investigations in this domain is outlined.

The FOPI experiment is presented in the second chapter. After a short general introduction of FOPI, the main characteristics of the S273 FOPI experiment are described: beam and target properties together with a description of the FOPI experimental setup. All FOPI subdetectors used in this experiment are briefly introduced, along with a more detailed review of the CDC (Central Drift Chamber) subdetector. At the end of the chapter the data acquisition system used in the FOPI experiment is briefly illustrated.

Data analysis, including identification and reconstruction of relevant particles, is summarized in Chapter 3. Technical details of the event selection and the methods used for particle identification and reconstruction are explained.

Chapter 4 presents simulation tools for efficiency evaluation used for the correction of measured yields. The experimental data results are compared with those obtained with the simulations. Two approaches for efficiency determination are described and discussed.

The summary of the results within this study is presented in Chapter 5. Phase space distributions, yields and cross section calculations are given and interpreted. In addition, the obtained results are discussed and compared with some previous experimental investigations and theoretical predictions.

The conclusions and the outlook are provided in the final chapter.



# Chapter 1

## Introduction

This work presents an investigation of strange particle production, with an emphasis on the lambda particle, in elementary pion-induced reaction.

Particles containing strange (or even heavier flavour) quarks, in addition to *up* and *down* quarks, are produced in the range of SIS energies (1 to 2 GeV/nucleon) at the GSI. Mesons such as  $\pi$ ,  $K$ ,  $\rho$ ,  $\phi$  and baryons such as  $\Lambda$  and  $\Sigma$  can be identified or reconstructed. Temperatures of about 70 to 150 MeV and nuclear matter densities up to 2 - 3  $\rho_0$  are reached.

Strange particles represent essential probes for the study of modifications of hadronic properties inside compressed nuclear matter. Nuclear matter and its influence on hadron properties can be investigated using heavy ion collisions and elementary (pion-induced, proton-induced and gamma-induced) reactions. The advantage of elementary reactions is the production of hadrons in a well defined state of nuclear medium with zero temperature and normal nuclear matter density [1].

In this chapter the basic properties of nuclear matter together with its possible phases described by the equation of state (EOS) are introduced. The concept of in-medium effects is explained and some of its experimental evidence is discussed. Afterwards, the available investigations and results of strange particles production are summarized.

### 1.1 Properties of Nuclear Matter

Nuclear matter is a system of nucleons, the strongly interacting constituents of atomic nuclei. Over the past several decades, the study of its properties has prompted great interest both in experimental and theoretical physics [2, 3, 4].

In its ground state, nuclear matter behaves like a fluid, but in order to perceive the manifestation of some of its basic properties, the state of nuclear matter needs to change by, for example, increasing its density by compression. During the compression, a part of the applied energy heats the system and this thermal motion consequently generates new pressure. Therefore, in order to study the properties of nuclear matter, the set of thermodynamic variables ( $p$  -



pressure,  $T$  – temperature,  $\rho$  – density), which provide the description of the observed system, should be known. These variables are related through the equation of state. Knowledge of the EOS parameters is required for a description of possible stages of the system during the reaction evolution.

As a result of the characteristic of nucleon-nucleon interaction, which is attractive at long distances ( $> 1$  fm) and repulsive below 0.5 fm distance, the most stable nuclei have a constant nuclear matter density of  $\sim 0.17 \text{ fm}^{-3}$  (equivalent to  $2.7 \cdot 10^{14} \text{ g/cm}^3$ ), known as normal nuclear matter density  $\rho_0$ .

The properties of nuclear matter can be investigated by means of e.g heavy-ion collisions or by using elementary reactions. The advantage of elementary reactions is the production of hadrons in a well defined state of nuclear matter with  $T = 0$  and  $\rho = \rho_0 = 0.17 \text{ fm}^{-3}$  [1].

### 1.1.1 Phases of Nuclear Matter

Nuclear matter can occur in different phases, usually presented on the phase diagram illustrated in Fig. 1.1, depending on the temperature and density (or equivalent: baryon chemical potential<sup>1</sup>  $\mu_B$ ). Owing to experimental research at different beam energies, some phases of nuclear matter were already approved, i.e. Fermi liquid, hadron gas, quark-gluon plasma, while others are predicted or subjects of further studies, i.e. colour superconductor.

In extreme conditions of low (zero) temperature and baryon chemical potential above 1 GeV, nuclear matter is expected to exist in the cores of cold neutron stars and, at a somewhat higher temperature, in the core-collapse supernovae.

On a temperature scale below 10 MeV and with densities lower or close to the density of normal nuclear matter  $\rho_0$ , there are two nuclear phases coexisting: the Fermi liquid and the cold gas of nucleons and light nuclei [1, 5, 6]. This region is explored by experiments at beam energies from 10 to several hundred MeV/nucleon, e.g. UNILAC (Universal Linear Accelerator, GSI) and GANIL (Grand Accélérateur National d'Ions Lourds). At such low temperatures a solid phase could exist in neutron stars with substantially higher densities.

The so-called hadron gas phase takes place at temperatures below 100 - 150 MeV and baryon chemical potential below 1 GeV. Under these conditions, the nuclear matter essentially behaves like hadron gas which is the consequence of nuclear collisions at relativistic energies. Such conditions can be reached within e.g. SIS and AGS (Alternating Gradient Synchrotron in Brookhaven National Laboratory - BNL) experiments at energies from 1 to 10 AGeV. In the range of SIS energies, available for FOPI experiments (1 - 2 GeV/nucleon), mesons like  $\pi$ ,  $K$ ,  $\rho$ ,  $\phi$  and baryons like  $\Lambda$  and  $\Sigma$  are produced in the collisions of heavy ions. In the performed collisions, a density of up to  $2 - 3\rho_0$  is achieved in the fireball. The fireball is created in the overlap region after the projectile particle has hit the target nucleus and it has a life time of

---

<sup>1</sup>Baryon chemical potential represents a measure of the net baryon density. In general, the chemical potential describes a change in the internal energy associated with a change in the system composition.

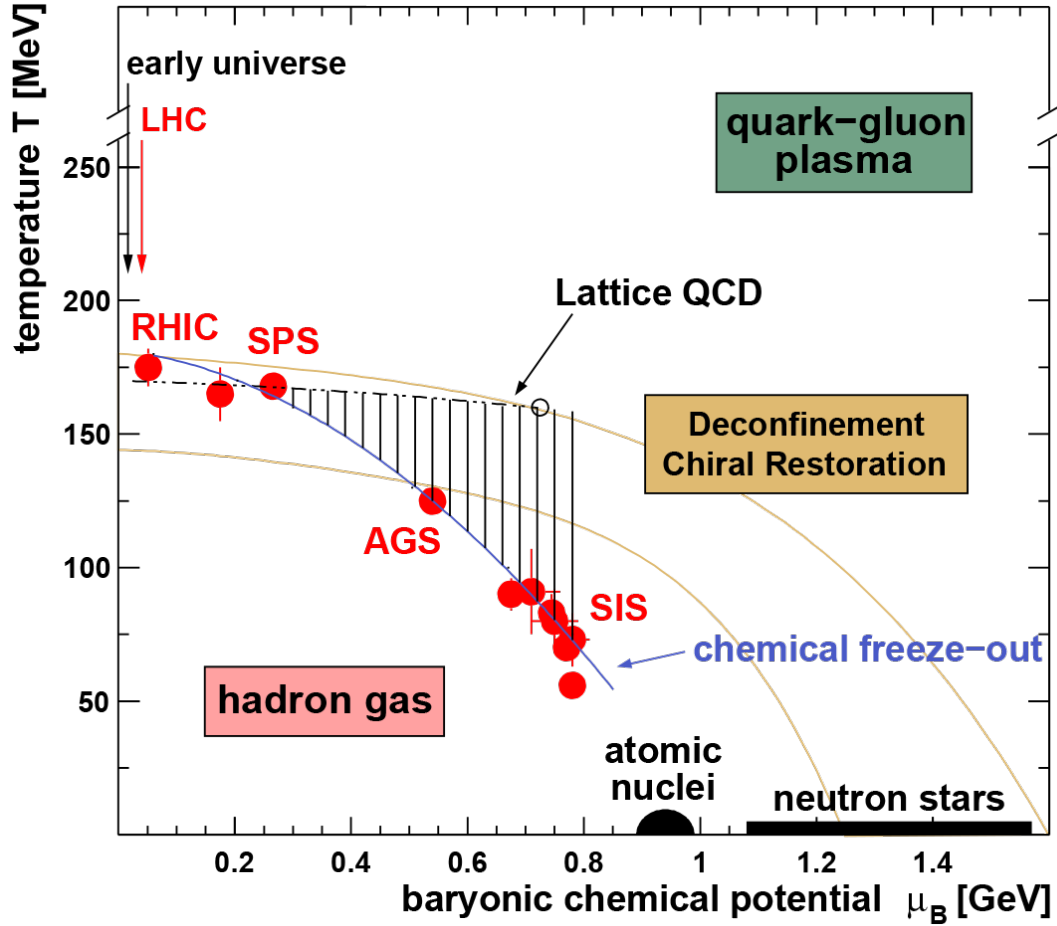


Figure 1.1: Phase diagram of nuclear matter. Depending on the temperature and baryon chemical potential, nuclear matter system occupies a specific state. Red circles indicate experimental data points at the chemical freeze-out curve (blue line), determined by means of a statistical model [12]. The picture is taken from [4].

the order of  $10^{-22}$  s, which is why observations and analyses are possible only after the fireball expansion [7]. At a temperature of about 70 to 150 MeV, nuclear matter can be created within the FOPI experiments. As it was mentioned earlier and indicated by the red circles in Fig. 1.1, in that temperature range nuclear matter is in its "normal" hadronic form.

Theory predicts a phase transition with increasing density towards pion and kaon condensates [8, 9, 10] inside neutron stars originating from a core collapse of type II supernovae [11]. Within the framework of a statistical model which assumes equilibrium, it is possible to determine a chemical freeze-out<sup>2</sup> curve [4, 12]. The red circles in Fig. 1.1 mark the results for different collision energies reached at several accelerators [13, 14, 15]. The chemical freeze-out curve is marked by the blue line.

A further increase of temperature and/or density leads to a phase where quarks and gluons

<sup>2</sup>Chemical freeze-out can be described as a stage at which the abundances of hadrons "freeze" with the memory of the last chemical equilibrium, i.e. the chemical composition of the fireball is fixed.

are no longer confined in hadrons, but they form the so-called quark-gluon plasma, a predicted new state of matter. A phase transition is expected in the shift from hadron gas or atomic nuclei to the deconfined state of quarks and gluons. Characteristics of that transition, as well as its relation to the chiral symmetry restoration [16, 17], are still discussed.

Temperatures above 150 MeV and baryon chemical potential close to zero are reached in the SPS (Super Proton Synchrotron) and LHC (Large Hadron Collider) at CERN and by RHIC (Relativistic Heavy Ion Collider) at BNL, accelerators which perform experiments at energies of 20 AGeV and more.

At low (zero) chemical potential and temperature of several hundred MeV, the early universe conditions are achieved. This region of the phase diagram is indicated by the black arrow in the top left corner of Fig. 1.1.

Theoreticians still discuss the nature of phase transitions, the possibility of critical point, restoration of chiral symmetry, etc. Present and future experiments are aimed at testing their predictions to complete our understanding of the phase diagram.

### 1.1.2 Equation of State

Nuclear matter can be described by the equation of state in situations where a local equilibrium has been reached. As it was mentioned before, in the SIS experiments (1 - 2 AGeV) the fireball lifetime is short enough not to allow observation of the particles inside, but only after the expansion of the fireball. The experiment has shown that the global chemical equilibrium has not been reached [18], but that a local one could be present at smaller time scales, which allows nuclear matter depiction in terms of EOS. [7] The EOS is a relation between thermodynamic variables, and in the case of nuclear matter they are the following: internal energy  $E$ , temperature  $T$  and density  $\rho$ . Usually, the energy is decomposed into thermal ( $E_{th}$ ) and compressional ( $E_c$ ) [7]:

$$E(\rho, T) = E_{th}(\rho, T) + E_c(\rho, T = 0) + E_0, \quad (1.1)$$

$E_0$  is the ground state energy (the binding energy for the infinite nuclear matter at  $\rho = \rho_0$  and  $T = 0$ ). The pressure of nuclear matter can be derived from:

$$p = - \left( \frac{\partial E}{\partial v} \right)_s = \rho^2 \left( \frac{\partial E}{\partial \rho} \right)_s, \quad (1.2)$$

where  $v$  is the volume and  $s$  the entropy per nucleon. Infinite nuclear matter at zero temperature and zero pressure has  $\rho_0 = 0.17 \text{ fm}^{-3}$  density. For this infinite nuclear system, the energy has to reach its minimum exactly at  $\rho = \rho_0$  (the condition of stability), and the value of that minimum is  $E_0 = -16 \text{ MeV/nucleon}$  due to the neglected effects of Coulomb force and absence of surface effects (infinite volume). For the sake of comparison, the average binding energy of regular nuclei according to the Bethe-Weizsäcker relation is about  $-8 \text{ MeV/nucleon}$ .

Thermal energy is used for thermal excitation and particle production. The compressional energy is defined at  $T = 0$ . If nuclear matter is compressed, the fraction of energy needed for the system compression is determined by the incompressibility:

$$\kappa_{\infty} = 9\rho_0^2 \left[ \frac{\partial^2 E_c}{\partial \rho^2} \right]_{\rho=\rho_0}. \quad (1.3)$$

The  $\kappa$  factor of about 200 MeV implies the EOS which is referred to as *soft* while higher values ( $\kappa \geq 250$  MeV) imply the EOS which is referred to as *stiff*.

There are several ways to determine incompressibility: heavy ion experiments, astrophysical observations or giant monopole resonance (GMR)<sup>3</sup> studies. Different investigations result in different values of  $\kappa$ .

Frequency measurements of GMR indicate that  $\kappa$  ranges between 200 and 300 MeV [19, 20], but in those investigations the change in nuclear density is less than 10%, so the EOS cannot be easily extrapolated to higher densities.

The study of transverse and elliptic flow in the Au+Au reaction at the AGS (at energies from 1 to 2 AGeV and densities from 2 to 5  $\rho_0$ ) provided the lower (167 MeV) and upper (380 MeV)  $\kappa$  limit [21]. In the same reaction, at SIS energies a  $\kappa$  value of 230 MeV was obtained by using the elliptic flow of charged particles, which indicates a soft EOS [22].

Subthreshold production of  $K^+$  was proposed as a probe for the EOS, and the difference in assuming diverse types (soft or stiff) of EOS at energies below threshold in the example of the  $K^+$  production probability [23] has been shown. The evidence for the soft EOS was found in the measurements of the KaoS collaboration in Au+Au and C+C collisions at different beam energies near threshold [24]. They showed that with an incompressibility value of 200 MeV, QMD (Quantum Molecular Dynamics) calculations are able to reproduce the observations [25].

### 1.1.3 In-Medium Effects

Research has shown that the properties of elementary particles may change depending on the density of their surrounding environment (nuclear medium). This phenomenon is called *in-medium effect*. The presence of in-medium effects which are manifested through the change of basic hadron properties is one of the central issues in the analysis of the properties of nuclear matter [26, 27, 28].

In a hot and dense nuclear matter chiral symmetry can be partially restored [29, 30, 31]. The in-medium effects concept can be considered as a consequence of such a partial chiral symmetry restoration. Therefore, the study of such nuclear matter behaviour is an essential part of this work. The region of deconfinement and chiral restoration is marked in the phase diagram in Fig. 1.1.

---

<sup>3</sup>Giant monopole resonance is a so-called "breathing mode" of giant nuclear resonance since nuclear volume expands and compresses symmetrically around the equilibrium volume. The frequency of the monopole vibration is directly related to the compressibility of the nuclear matter.

This symmetry is broken due to a non-zero value of the quark (chiral) condensate  $\langle \bar{q}q \rangle$  with the effective quark masses of the order of several hundred MeV. In the region of (partially) restored chiral symmetry, the effective quark masses are reduced to  $\sim 12$  MeV for the sum of *up* and *down* quarks and to  $\sim 150$  MeV for the *strange* quark [32] which makes the production of  $\bar{q}q$  pairs energetically much easier.

The evidence of a spontaneous breaking of chiral symmetry exists in low energy hadron phenomenology and in lattice QCD (quantum chromodynamics) [31]. The quark condensate (or correspondingly, the decay constant  $f_i$ ,  $i$  stands for particle identification) is a measure of spontaneous chiral symmetry breaking [33]. A change of the quark condensate value implies a change in hadron properties, so it can be said that light hadron masses and coupling constants are controlled by chiral symmetry [1, 34]. The GOR (Gell-Mann, Oakes and Renner) expression [35] provides the relation between quark condensate, changed quark mass and corresponding hadron mass and decay constant. For pions, the said relation predicts the following:

$$m_\pi^2 f_\pi^2 = -(m_u^0 + m_d^0) \langle \bar{q}q \rangle + O(m_{u,d}^2), \quad (1.4)$$

$f_\pi$  is the pion decay constant ( $\approx 92.4$  MeV) and  $m_u^0$  and  $m_d^0$  refer to the current masses of *up* and *down* quark respectively. This mass modification will influence the production of particles in hot and dense nuclear matter as well as their further propagation. Hence, experiments with particles yields and collective effects measurements, can provide arguments for changes in hadronic properties.

The mass of  $K$  meson in vacuum is also associated with the quark condensate through the GOR relation:

$$m_K^2 f_K^2 = -\frac{1}{2}(m_u^0 + m_s^0) \langle \bar{u}u + \bar{s}s \rangle + O(m_s^2), \quad (1.5)$$

$f_K$  is the kaon pseudo-scalar decay constant ( $\approx 114$  MeV),  $m_s^0$  is the current mass of a strange quark. But one has to bear in mind that the explicit chiral symmetry breaking is significantly larger than in the case of a pion due to kaon mass ( $\approx 495$  MeV/c<sup>2</sup>) and that strange particle behaviour in nuclear matter is different. As was presented in [10], a strongly attractive interaction between kaons and baryons leads to the effective kaon mass drop in dense baryonic matter and the charged kaon condensation at 2 - 3 normal nuclear densities was predicted. That study represented a strong motivation for new investigations of kaons, and strange particles in general, in the surrounding nuclear medium.

The  $\langle \bar{q}q \rangle$  changes under different pressures (densities) and temperatures, which is why it is important to be familiar with such behaviour. The derivative of the pressure  $p$  with respect to the quark mass  $m_q$  produces the in-medium quark condensate in an assumingly homogeneous nuclear medium. Thermal expectation value as a function of temperature and density is given in the following formula:

$$\frac{\langle \bar{q}q \rangle_{T,\rho}}{\langle \bar{q}q \rangle_0} = 1 + \frac{1}{f_\pi^2} \frac{dp(T, \mu_B)}{dm_\pi^2}, \quad (1.6)$$

where  $\langle \bar{q}q \rangle_0$  is the quark condensate at  $T = 0$  and  $\rho = 0$  ( $|\langle \bar{q}q \rangle_0| = (-240 \text{ MeV})^3$ ) and  $p(T, \mu_B)$  is the pressure for the temperature  $T$  and baryon chemical potential  $\mu_B$  [33].

As it was mentioned above, the change of  $\langle \bar{q}q \rangle_{T,\rho}$  is connected with the decay constant which has a different  $f_\pi^*$  value, e.g for pions in medium. A strong argument for the partial restoration of chiral symmetry at normal nuclear matter density was provided in [36]. The measurement of  $f_\pi^*(\rho)^2/f_\pi^2$  ratio using deeply bound state  $1s$  of  $\pi^-$  in  $^{115,119,123}\text{Sn}$  showed a reduction of the chiral order parameter  $f_\pi^*(\rho)^2/f_\pi^2$  to the value of  $\approx 0.64$ .

Nambu-Jona-Lasinio model [37, 38] calculations predict a reduction of the quark condensate [33] in case of an increased temperature and/or density of nuclear matter. That behaviour is shown in Fig. 1.2.

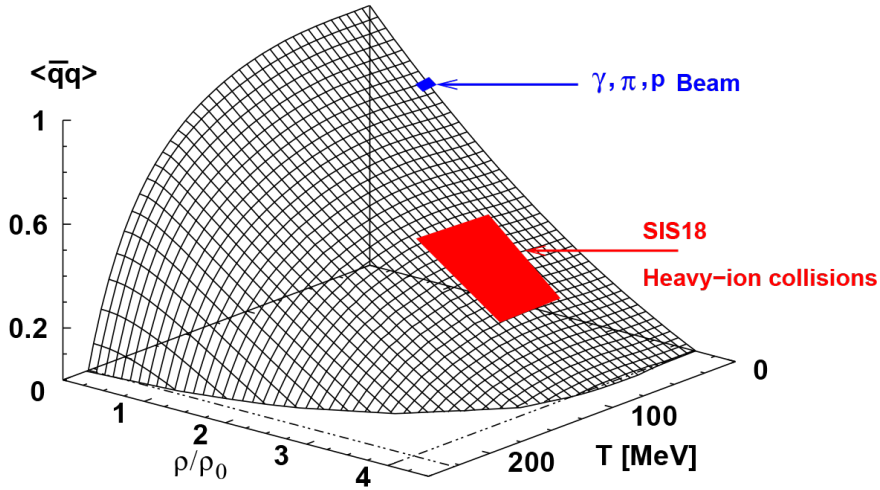


Figure 1.2: Dependence of the quark condensate  $\langle \bar{q}q \rangle$  on temperature  $T$  and nuclear matter density  $\rho$ . The figure is taken from [33] and adapted in [1].

As indicated in Fig. 1.2, it can be calculated that for the density of 2 - 3  $\rho_0$  and the temperature of 70 - 150 MeV reached at the SIS energies of 1 - 2 GeV, the magnitude of  $\langle \bar{q}q \rangle$  can be reduced by  $\approx 80\%$  (indicated by the red area), whereas for the elementary reactions at normal nuclear matter density  $\langle \bar{q}q \rangle$  magnitude is predicted to be reduced by  $\approx 30\%$  [30, 33].

There are different experimental approaches to probe in-medium effects. Among them, experiments with vector mesons decaying into dilepton pairs are interesting because the characteristics of their decay products are not influenced by the hadronic environment [39, 40]. Strange particles also represent a good probe for in-medium effects. At SIS energies they are usually produced below the production threshold. In that region, in-medium effects have an emphasised impact on particle production yields.

Several examples of evidence for the nuclear matter influence on the hadron properties are provided within sections of this chapter. The example below indicates theoretical predictions of the effective  $K^+$  and  $K^-$  masses which depend on nuclear matter density.

That can be seen in Fig. 1.3 which shows that  $K^+$  mass increases slowly with an increase in

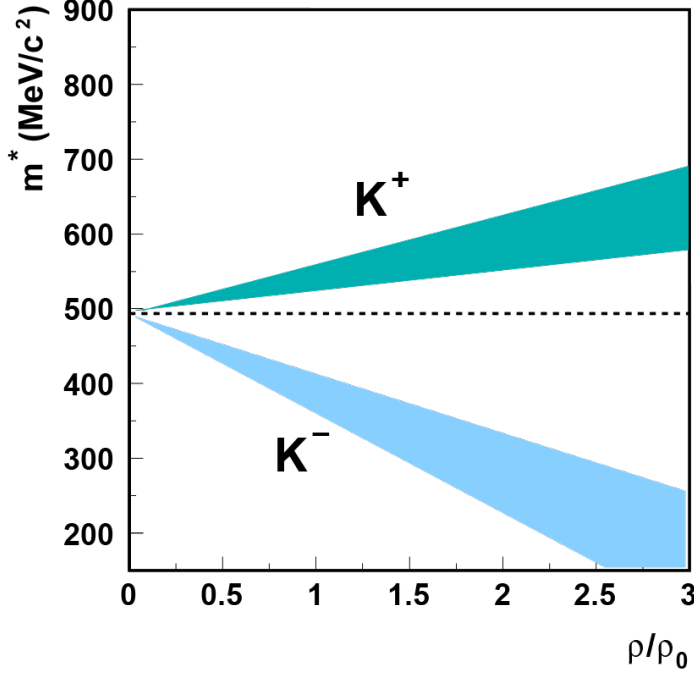


Figure 1.3: Effective mass of  $K^+$  and  $K^-$  as a function of relative nuclear matter density ( $\rho/\rho_0$ ). The mass of  $K^+$  meson demonstrates a slow increase proportional to nuclear density, but the  $K^-$  mass strongly decreases as the density increases. This trend was predicted by the theoretical calculation mentioned in the text. The figure is taken from [4].

density, while  $K^-$  mass steeply decreases. Several theoretical calculations predicted the same trend for kaons at rest [41, 42, 43].

The in-medium modifications of kaon properties are introduced through kaon-nucleon potentials inside transport models. Both,  $K^+$  and  $K^-$  are influenced by an attractive scalar  $KN$  potential and  $K^+$  effects are modelled with a repulsive vector potential, while for the  $K^-$  effects an attractive vector potential is used.

The consequences of in-medium effects which change hadron properties affect astrophysical investigations as well. For example, at large density,  $K^-$  condensates in nuclear matter [10] can soften the EOS which would prefer the formation of a black hole instead of a neutron star after a supernova explosion [11, 44, 45].

The investigation of the  $\pi^- + N \rightarrow \Lambda + K^0$  reaction in a nuclear medium, which is the central part of this thesis, could be motivated by the following arguments:

- the available evidence for a partial restoration of chiral symmetry at normal nuclear matter density [36] which is achieved in elementary reaction, such as a pion-induced reaction used in the S273 FOPI experiment,
- changes in the properties of strange particles when they are surrounded by nuclear matter,
- strange particle production close or below the threshold where in-medium effects have a pronounced influence on particle production,
- the consequences in other branches of physics, like astrophysics.

## 1.2 Measurements of Strange Particles

The special properties of strange particles dictate the nature of investigation and the methods applied.

They are produced via a strong interaction which conserves strangeness, which is why a strange quark  $s$  is always produced along with an  $\bar{s}$  antiquark. Their production is fast,  $\sim 10^{-23}$  s, but they decay much more slowly via weak interaction,  $\sim 10^{-10}$  s. The advantage of such a slow disintegration is that the decay products of strange particles cannot be “overshadowed” by hadronic interactions, because strange particles already exit the collision zone during that time.

In addition, one of the strange particle constituents, the strange quark (antiquark), is allowed to occupy states unavailable to lighter ( $u$  and  $d$ ) quarks which can be energetically more favourable than having additional lighter quarks.

Moreover, measurements of strange particles in the SIS energy range are of special interest for the following two reasons:

1. Reabsorption of a strange particle is not very likely to happen. The process of reabsorption in the fireball requires the other particle which carries the proper quark or antiquark, which is a rare occurrence in this energy range.
2. Strange particles are produced below or close to the free nucleon-nucleon threshold which makes them sensitive probes for the processes which influence their properties.

Research done by means of the FOPI detector at SIS energies can answer some of the still open issues concerning hadrons in medium. Comparisons of model predictions and experimental data should include as many particles of interest as possible in order to obtain a more complete description of the influence of in-medium effects on hadron properties. As the following examples will explain, charged kaons are interesting particles to study in this context. Neutral strange particles, as  $\Lambda$  baryon and  $K^0$  meson, are also good candidates. For example, the existing results obtained for  $K^+$  meson can be examined by  $K^0$  investigations with the advantage that neutral kaons are not affected by the Coulomb force. Extra measurements of the neutral  $\Lambda$  hyperon may provide an answer to the question whether the  $K^-$  yield is connected to the yield of  $\Lambda^0$  via the reaction  $\pi^- \Lambda^0 \rightarrow K^- N$  [4].

Strange particles are very interesting probes in FOPI experiments, in both heavy ion and elementary reactions. For this reason a summary of the previously obtained results on this topic are presented in the following sections.

### 1.2.1 Strange Particles in Heavy Ion Collisions

Heavy ion collisions provide us with numerous opportunities for experimental investigations of hot and dense nuclear matter. Scientists gathered around different accelerator facilities perform experiments in a broad energy range, from several MeV up to the order of 10 TeV. Some of



them are the so-called fixed target experiments (SIS, AGS, SPS accelerators), while others are using colliding beams (LHC at CERN). In those studies, various aspects of nuclear matter properties are observed, e.g. in-medium effects, the equation of state and search of new phases, compressibility of nuclear matter and other. The importance of the results obtained within heavy ion collision experiments and their subsequent analyses do not only affect the area of nuclear and particle physics, but also have an important role in other branches of physics and computer engineering. For example, properties of nuclear matter determine the dynamics of supernova explosions, neutron star properties or the process of matter formation immediately after the big bang.

Strange particles represent unique probes for investigating nuclear matter properties in heavy ion collisions [4, 46, 47]. That uniqueness is manifested through several properties specific to those particles. A strange quark ( $s$ ) is always produced along with the corresponding antiquark ( $\bar{s}$ ) because the strong interaction responsible for the creation of strange particles conserves the strangeness. On the other hand, reabsorption of a strange particle inside a fireball has to be carried out with another strange particle containing corresponding quark or antiquark required for the annihilation. In the energy regime available for FOPI experiments strange particles are rare, and hence the possibility of reabsorption is small. Another interesting characteristic for the strange particles yield at SIS energies is that the production occurs close to or even below the free nucleon-nucleon threshold. They decay via weak interaction, i.e.  $10^{12}$  times slower than they appear. Due to this feature, their decay products cannot be “overshadowed” by hadronic reactions.

Several examples of strange particle creation and behaviour during heavy ion collision processes will be introduced in the following lines.

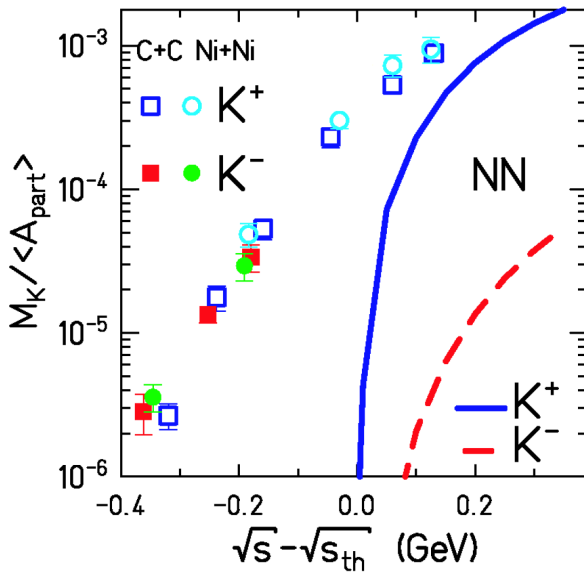


Figure 1.4: Subthreshold production of  $K^+$  and  $K^-$  in C+C and Ni+Ni reactions measured in the KaoS experiment [48, 49]. Empty circles and squares indicate  $K^+$ , while full circles and squares indicate  $K^-$  multiplicity. The lines represent model calculations of  $K^+$  and  $K^-$  multiplicities in nucleon-nucleon collisions.

As it was already mentioned in the previous section, the effective mass of  $K^+$  and  $K^-$  changes inside nuclear matter (increasing slowly for  $K^+$  and decreasing relatively quickly for

$K^-$ ), and comparisons between these two mesons are often used as a probe for in-medium effects. Measurements of the  $K^-/K^+$  ratio are of particular interest because it is estimated that this ratio is more sensitive to in-medium effects. Moreover, by using the ratio many systematic uncertainties are cancelled.

The example of  $K$  mesons production (far) below the threshold is provided by the KaoS collaboration experiment [48, 49] which was performed for C+C and Ni+Ni collisions at different energies. The results are presented in Fig. 1.4 and compared with expectations for nucleon-nucleon ( $NN$ ) collisions in which the production of kaons is only possible above the threshold (indicated with solid and dashed lines). The multiplicity per average number of nucleons as a function of the energy above the threshold ( $\sqrt{s} - \sqrt{s_{th}}$ ) in the  $NN$  system is shown. The  $K^+$  and  $K^-$  multiplicities in nucleus-nucleus collisions are approximately the same, but in  $NN$  reactions the  $K^+$  yield is larger by 1 - 2 orders of magnitude.

Figure 1.5 represents the differential yield distribution of  $K^+$  mesons measured in KaoS [50] and FOPI [51] experiments at the same energy of 1.93 AGeV in Ni+Ni collisions. There is a nice agreement between data sets from the two different experiments. The comparison with model (IQMD - Isospin QMD [52] and RBUU - Relativistic BUU [53]) predictions was done for the cases with and without in-medium effects, which is indicated in the figure by the solid and dashed lines respectively. When the same set of cross sections is used, calculations of both models match.

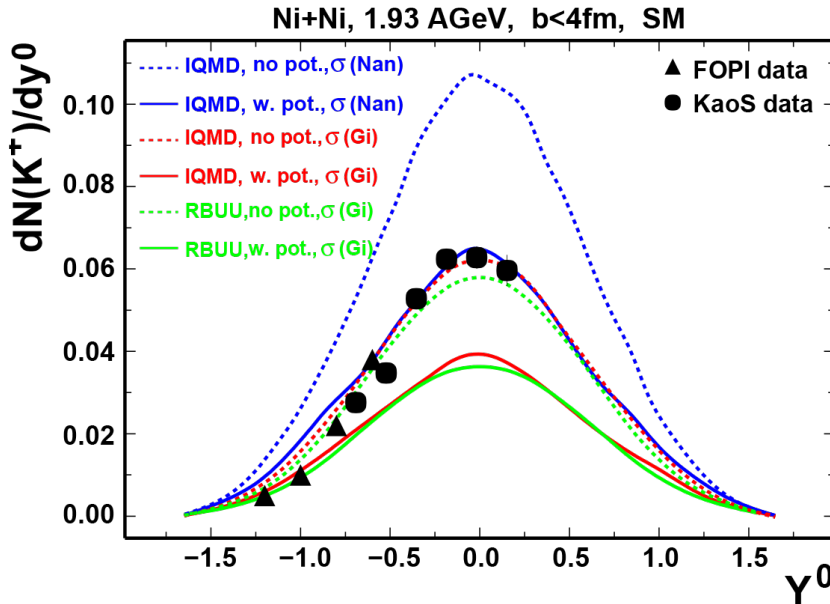


Figure 1.5: Differential yield distribution of  $K^+$  mesons from KaoS [50] and FOPI [51] experiments at 1.93 AGeV in Ni+Ni reactions. The lines indicate IQMD and RBUU model predictions with (solid line) and without (dashed line) the influence of in-medium effects. The plot is taken from [54].

In the SIS energies regime the kaon flow is suggested as an observable sensitive to the KN (kaon-nucleon) potential [1]. The study of  $K^+$  flow was conducted by the FOPI collaboration in Ni+Ni and Ru+Ru reactions at 1.93 AGeV and 1.69 AGeV respectively and published in [55]. The results are compiled in Fig. 1.6. Proton and  $K^+$  sideward flow ( $v_1 = \langle p_x/p_t \rangle$ ) measurements are plotted as a function of transverse momentum  $p_t$ . The presented measurements have

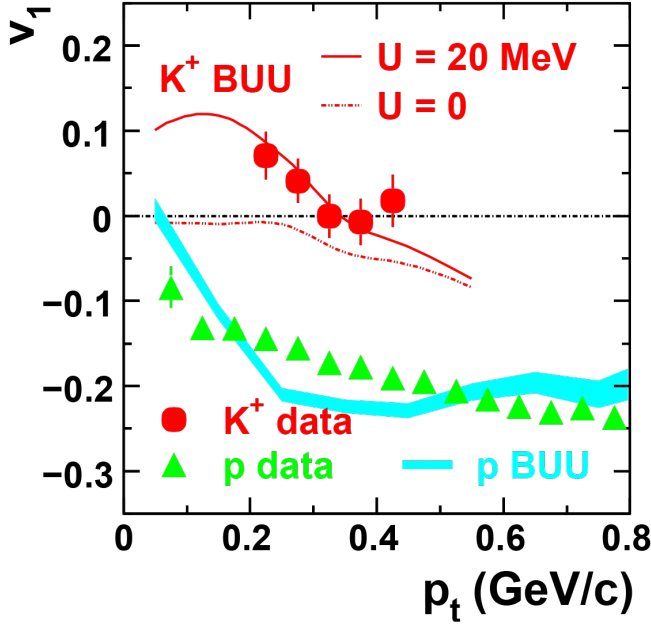


Figure 1.6: Transverse momentum dependence of sideward flow of  $K^+$  (circles) measured in Ni+Ni collisions at 1.93 AGeV by the FOPI experiment [55]. The experimental flow of protons is marked by triangles and its RBUU model prediction is presented by the turquoise area. The lines indicate model predictions for different  $K^+N$  potentials.

been carried out in the rapidity range of  $-1.2$  to  $-0.65$ . It is shown that protons have a negative flow for the whole  $p_t$  range, while  $K^+$  mesons have a positive flow of low momentum particles. The lines indicate the results of the RBUU model prediction. An agreement between the data and the model is achieved when a repulsive KN potential of 20 MeV (solid line) is used. The resulting anti-correlation between  $K^+$  and proton flow can afterwards be explained by a repulsion between these two particles. Additional checks should be performed because of the repulsive Coulomb interaction between a  $K^+$  and a proton.

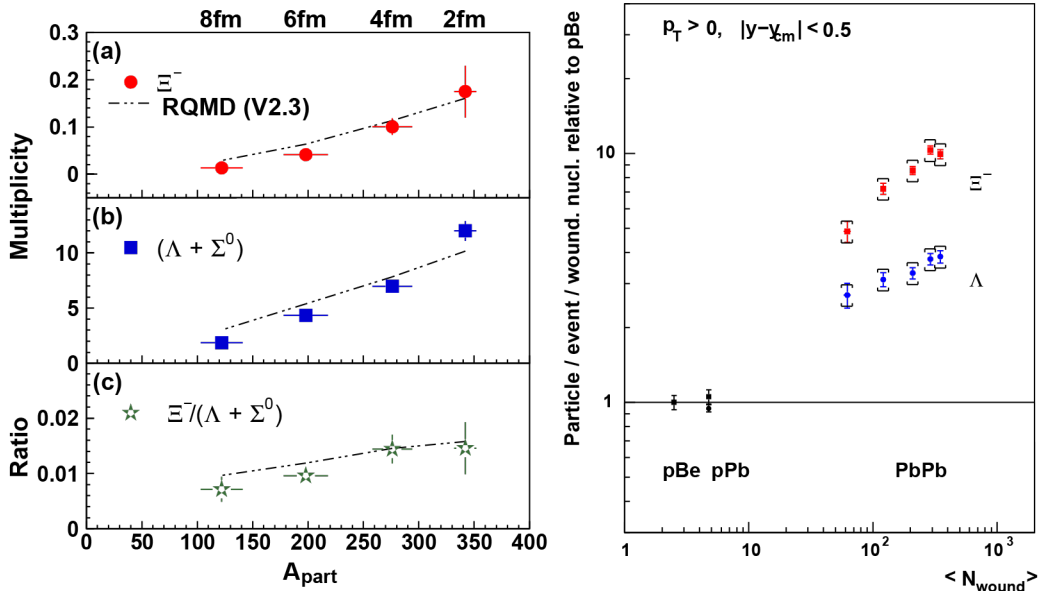


Figure 1.7: Results of  $\Lambda$  and  $\Xi^-$  particle production from measurements conducted by the E895 collaboration [56] at AGS (left) and NA57 collaboration [57] at SPS (right).

At higher energies, production of strange particles can be sensitive to the quark-gluon

plasma presence which is indeed demonstrated by the experimental results of AGS, SPS and RHIC. The production of  $s\bar{s}$  pairs is more probable in this region, because it is energetically more favourable; thus, an increment of strangeness production could imply the formation of quark-gluon plasma in heavy ion collisions. Particles like  $\Xi^-$  or  $\Omega^-$ , which are multi-strange baryons are especially interesting for research in this energy region, but studies of the  $\Lambda$  particle are performed as well.

The results of measurements of  $\Lambda$  and  $\Xi^-$  particle production by the E895 experiment at the AGS are presented in the left panel, while those by the NA57 experiment at the SPS are presented in the right panel of Fig. 1.7. The outcome of the E895 experiment at 6 AGeV in Au+Au collisions shows that the particle yield is in agreement with statistical and transport model calculations, which implies that the multi-strange hadron production approaches chemical equilibrium already at these collision energies [4].

The NA57 experimental results are obtained from Pb+Pb collisions and proton-induced reactions and they are plotted as  $\Lambda$  and  $\Xi^-$  yields per wounded nucleon relative to  $p$ +Be as a function of collision centrality. An up-trend of strangeness production can be observed for the hyperon containing more strange (anti)quarks.

The last example, which includes the elementary proton-induced reaction, demonstrates the importance of such studies and is a motivation for further research on that topic.

## 1.2.2 Strange Particles in Elementary Reactions

Investigations of neutral strange particles in elementary reactions, such as pion-induced reactions performed in the S273 FOPI experiment, are still rare. This refers particularly to lambda particles, whereas for the  $K^0$  the situation is slightly better. The great advantage of elementary reactions is the production of particles in the nuclear medium for which the nuclear density is well defined. In this way it is possible to avoid some consequences of interactions with nuclear matter, like the dependency of KN potential on the nuclear density, varying strongly over time for heavy ion reactions. Interesting results, which motivated this analysis as well, were obtained within the investigation of Tsushima et al. [28]. They studied strangeness production deriving from  $\pi N$  collisions inside nuclear matter, and they also analysed the  $\pi + N \rightarrow Y + K$  reaction, where  $K$  is one of the  $K$  mesons and  $Y$  stands for a hyperon.

They used the *quark-meson coupling (QMC) model* [58] which yielded very successful results in the studies of meson and hyperon properties inside a nuclear medium. The scalar and vector potentials were determined on the basis of the QMC model:

$$U_s^h \equiv U_s = m_h^* - m_h, \quad (1.7)$$

$$U_v^h = (n_q - n_{\bar{q}}) \cdot V_\omega^q - I_3 \cdot V_\rho^q. \quad (1.8)$$

$U_s^h$  stands for scalar potential and  $U_v^h$  stands for vector potential felt by hadron  $h$  in nuclear

matter,  $m_h^*$  is effective mass,  $V_\omega^q$  and  $V_\rho^q$  are the mean field potentials and  $I_3$  is the third component of isospin projection of the hadron  $h$ . Within the approximation that the mean-field potentials are momentum independent, the four-momentum of the hadron is modified to  $p_h = \left( \sqrt{\vec{p}^2 + m_h^{*2}} + U_v^h, \vec{p} \right)$ , which apart from kinematic factors such as the flux and the phase space also modifies the reaction amplitudes and hence the reaction thresholds, which are changed in nuclear matter and now depend on baryon density.

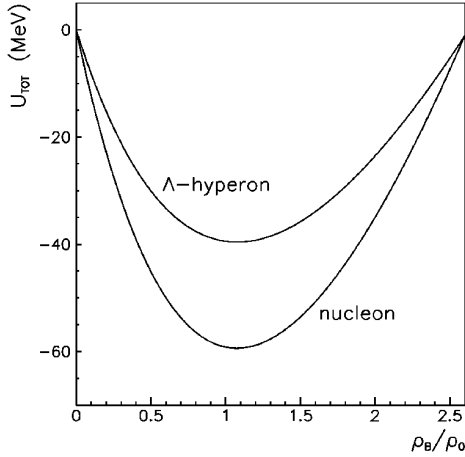


Figure 1.8: Total potential for  $\Lambda$  hyperon and nucleon as a function of baryon density  $\rho_B$  in units of nuclear matter saturation density  $\rho_0 = 0.15 \text{ fm}^{-3}$ . [28]

The total nucleon and  $\Lambda$  potential ( $U_{tot}$ ) at zero momenta as a function of baryon density are presented in Fig. 1.8. The figure indicates that both potentials approach minima around normal nuclear matter density, which is the consequence of the fact that the energy density of nuclear matter is minimized around  $\rho_0$ . [28]

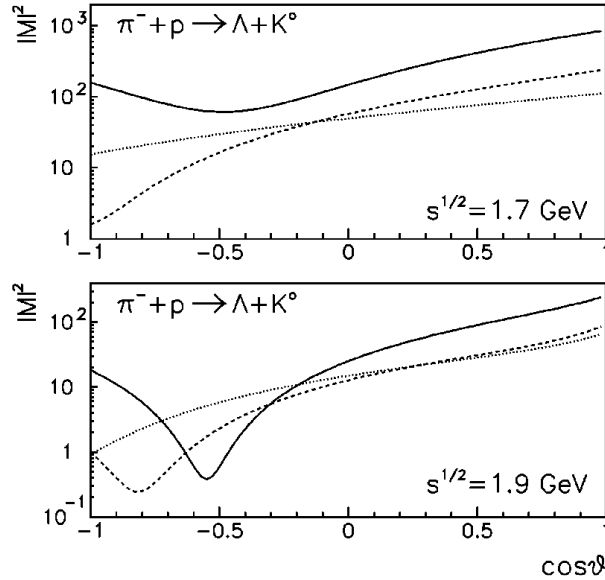


Figure 1.9: The dimensionless invariant amplitude square for the  $\pi^- + p \rightarrow \Lambda + K^0$  reaction, as a function of  $\cos\vartheta$ ,  $\vartheta$  is the K meson emission angle in the centre of mass system. The amplitude is calculated for the  $\sqrt{s} = 1.7 \text{ GeV}$  (upper plot) and  $\sqrt{s} = 1.9 \text{ GeV}$  (lower plot) invariant collision energies. The lines indicate model calculations for free space (solid line), for nuclear matter at  $\rho_B = \rho_0$  (dashed line) and  $\rho_B = 2\rho_0$  (dotted line). [28]

The dependence of the total cross section on energy for the  $\pi + N \rightarrow Y + K$  reaction can be very well explained by means of *resonance model* [59, 60, 61] which was extended in this investigation study by including medium modifications of hadron properties. The in-medium reaction amplitudes were calculated for  $\pi^- + p \rightarrow \Lambda + K^0$  by applying that model. The results in nuclear matter differ significantly from the free space results at the used energies ( $\sqrt{s} = 1.7$  GeV and  $\sqrt{s} = 1.9$  GeV). Moreover, dependence on baryon density is clearly indicated. The results are shown in Fig. 1.9.

Cross section of the  $\pi^- + p \rightarrow \Lambda + K^0$  reaction, as a function of the invariant incident energy  $\sqrt{s}$  for different densities, is presented in Fig. 1.10. The expected dependence on the baryon density is unquestionably observed. Lines on the plot indicate three model prediction results for: free space  $\rho_B = 0$ , normal nuclear matter density  $\rho_B = \rho_0$  and double normal nuclear matter density  $\rho_B = 2\rho_0$ . Model calculations are compared with the experimental data outcome measured in bubble chambers and published in [62], marked with circles in the figure.

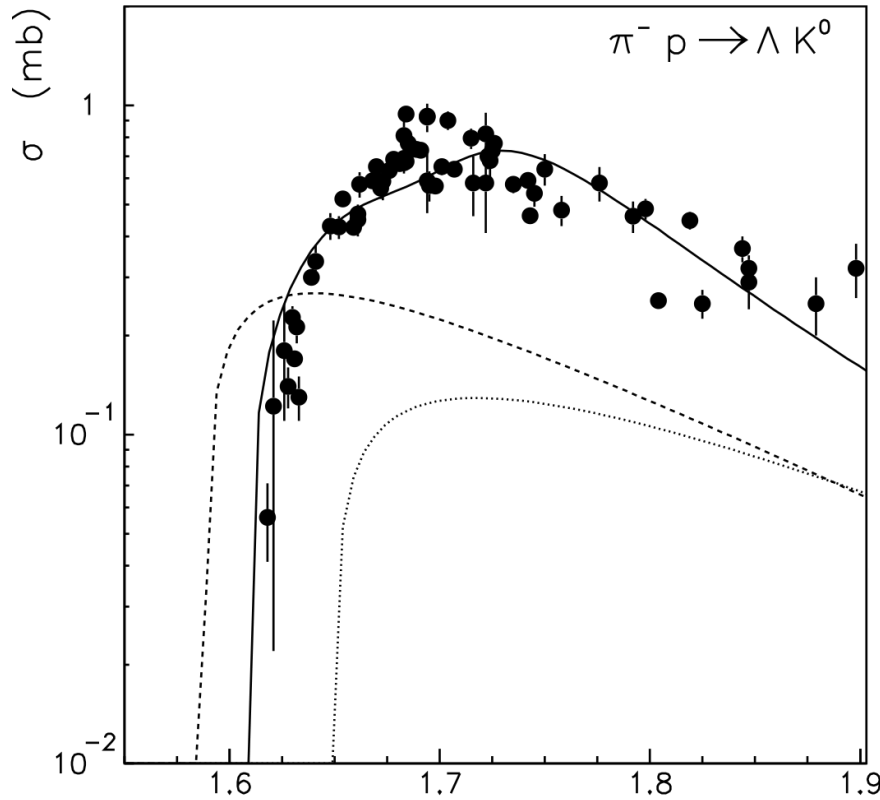


Figure 1.10: Total cross section of the represented reaction as a function of invariant collision energy  $\sqrt{s}$  at different baryon densities. The circles indicate the data in free space ( $\rho_B = 0$ ), and lines indicate the results of model calculations: full line for the free space, dashed line for the normal nuclear matter density,  $\rho_B = \rho_0$ , and dotted line for  $\rho_B = 2\rho_0$ . The figure is taken from [28].

The model calculation for free space (full line) is in a good agreement with the compared experimental data over the entire  $\sqrt{s}$  range. For the calculation at normal nuclear matter density (dashed line), a shift to the left (to lower  $\sqrt{s}$ ) in the reaction threshold with respect to the threshold in free space  $\sqrt{s} = 1.63$  GeV is observed. On the other hand, the reaction threshold is shifted to the right (to higher  $\sqrt{s}$ ) for the result obtained at double normal nuclear matter density (dotted line).

Just for the sake of comparison, the S273 FOPI experiment used  $\sqrt{s} = 1.75$  GeV invariant

incident energy.

The first results on the kaon production cross section in pion-induced elementary reactions inside nuclear matter were obtained by the  $K^0$  meson analysis of the S273 experiment. Kaons are reconstructed from the measured daughter particles by the CDC of the FOPI detector (this technique will be explained in more detail in the following chapters). The investigation mainly done by M. L. Benabderrahmane, is explained in detail in [1] and published in [63].

Figure 1.11 presents the ratio of  $K^0$  yield produced by pions on Pb and C targets as a function of the  $K^0$  momentum in a laboratory system. The data are compared with the results for  $K^+$ , measured in proton-induced reactions on Au and C targets by ANKE collaboration (marked with circles), and with HSD (Hadron String Dynamics) transport model calculations for different values of the KN potential:  $U = 0$  MeV (solid line),  $U = 20$  MeV (dashed red line) and  $U = 10$  and  $30$  MeV (dotted blue line).

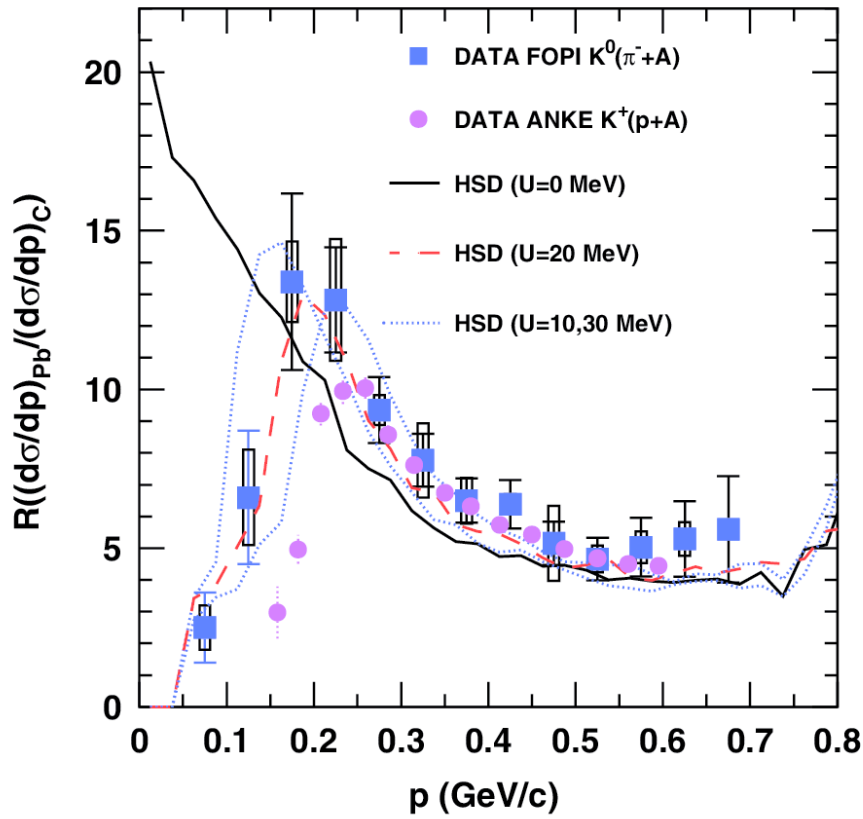


Figure 1.11: The ratio of cross sections obtained from elementary reactions on heavy and light targets as a function of kaon momentum. The experimental results are compared with HSD calculations with different KN potential. The squares indicate the yield ratio of  $K^0$  produced on Pb and C targets in the FOPI S273 experiment. The figure is published in [63].

A decrease of  $K^0$  production at low momenta ( $p < 170$  MeV/c) on a heavy target nucleus (Pb) compared to the light one (C) was shown by the comparison between the ratio of yields as a function of the momentum of  $K^0$  mesons. Furthermore, the HSD (Hadron String Dynamics) transport model [26, 64] suggests a repulsive KN potential ( $20 \pm 5$  MeV) at normal nuclear

matter density due to  $K^0$  interactions with the nuclear medium. [63]

Several physical aspects related to the subject matter of this study have been introduced within this chapter. In the following presentation and discussion of experimental results obtained by FOPI within the SIS energy range at the corresponding conditions of nuclear matter (temperature and density, indicated in the phase diagram of Fig. 1.1), focus will be placed on the production of neutral strange particles ( $\Lambda$  and  $K^0$ ) in nuclear medium, using an elementary pion-induced reaction.





# Chapter 2

## The S273 FOPI Experiment

The FOPI experimental setup is a system of subdetectors unified in one, principally heavy-ion, detector assembled at the SIS (Schwer-Ionen-Synchrotron) accelerator at the GSI (full name: GSI Helmholtzzentrum für Schwerionenforschung) in Darmstadt, Germany [65]. The SIS facility provides ion beams with kinetic energies from 0.1 to 2 AGeV and secondary proton and pion beams in the momentum range from 0.6 to 2.8 GeV/c.

The S273 experiment was performed in August 2004 with a secondary pion beam at 1.15 GeV/c hitting five different targets from carbon ( $A = 12$ ) to lead ( $A = 208$ ).

After the short introduction about FOPI in general, the following sections describe the S273 FOPI experiment whose data is investigated within this inquiry, together with properties of the pion beam and nuclear targets used in the experiment. The short overview of the FOPI experimental setup is presented. At the end of the chapter, electronics and data acquisition are briefly introduced.

### 2.1 FOPI in General

FOPI stands for the detector system built within the SIS facility at the GSI, but also for the international collaboration of scientists who work and cooperate on the detector experiments.

As suggested by its name, the FOPI detector is constructed in a way that covers almost full solid angle ( $4\pi$ ) for the measurements of charged reaction products. It is designed for detection of particles like light mesons, protons, deuterons, tritons and intermediate mass charged fragments. The more detailed description of the FOPI detector with all its major components will be presented in Section 2.5.

The international collaboration of scientists from about twenty institutions around the world, gathered together in 1990, improved the detector setup and therefore extended the investigations. The main physics issues inside the FOPI collaboration have been the study of nuclear fragmentation [66, 67], the pion production [68, 69, 70], the production of strange particles [71, 72], strangeness studies [1, 4, 73, 74, 75] and investigations of flow [76, 77, 78].

## 2.2 Basic Characteristics of the S273 Experiment

The FOPI experiment, named S273 experiment, with a secondary pion beam of 1.15 GeV/c momentum, which corresponds to the energy of about 1.75 GeV in the system of  $\pi^-$  mesons colliding with protons at rest, was performed in August 2004 by the FOPI collaboration at the GSI facility. The leading motive for the pion beam usage was to investigate the hadron properties under the well known state of nuclear matter at normal density. The beam was running for 14 days from the production target (beryllium) to the cave B of the FOPI experiment. Five different nuclear targets (C, Al, Cu, Sn and Pb) were used in this experiment.

The main goals of the S273 experiment can be summarized as follows:

- to investigate the pion-induced strange particles production and propagation in nuclear medium at normal nuclear matter density,
- to measure the strangeness production in  $\pi^-$  reactions on the five nuclear targets,
- to study the  $\pi^- + A \rightarrow \Lambda + K^0$  reaction in medium,
- to measure the in-medium inclusive cross section for the  $\pi^- + N \rightarrow \Lambda + K_S^0$  reaction,
- to inspect the total production cross section dependence on target size,
- to investigate in-medium modifications of associated strangeness production through the  $\pi^- + N \rightarrow \Lambda + K_S^0$  reaction and
- to test the performances of two silicon strip detectors used in this experiment for the first time.

This experiment was afterwards used as an inducement and a proposal criterion for the preparation of the new FOPI pion experiment in June 2011 at higher momentum value of 1.7 GeV/c.

## 2.3 Pion Beam at the GSI

The SIS facility provides ion beams in the energy range from 0.1 to 2 AGeV and also secondary pion and proton beams. In that environment is possible to produce a secondary pion beam in the momentum range from 0.6 to 2.8 GeV/c [79].

The primary beam of carbon at the SIS maximum energy of 2 AGeV provided pions with maximum intensity  $\sim 10^{11} \pi^-/\text{spill}$  at momentum of 1.0 GeV/c with resolution of 0.5%. This momentum range ensures the lowest level of the beam electron contamination (the  $e^-/\pi^-$  ratio is about 3/95). But the final pion beam (the one which impinges the target) intensity was  $\sim 2 \cdot 10^4 \pi^-/\text{spill}$ , as a result of the 89 m transportation length to the cave B and the beam line acceptance.

In 1998, the pion beam was set at the SIS facility for the first time, in order to extend the contemporary research. The main goal of using this kind of beam was to have the well known environment at normal nuclear matter density and zero temperature for hadron property studies. Figure 2.1 shows the scheme of the pion production target and transport of the beam to different experiments of the GSI. The FOPI experiment is situated at cave B indicated in the scheme. The pion production beryllium target was located in the main beam line coming from the synchrotron.

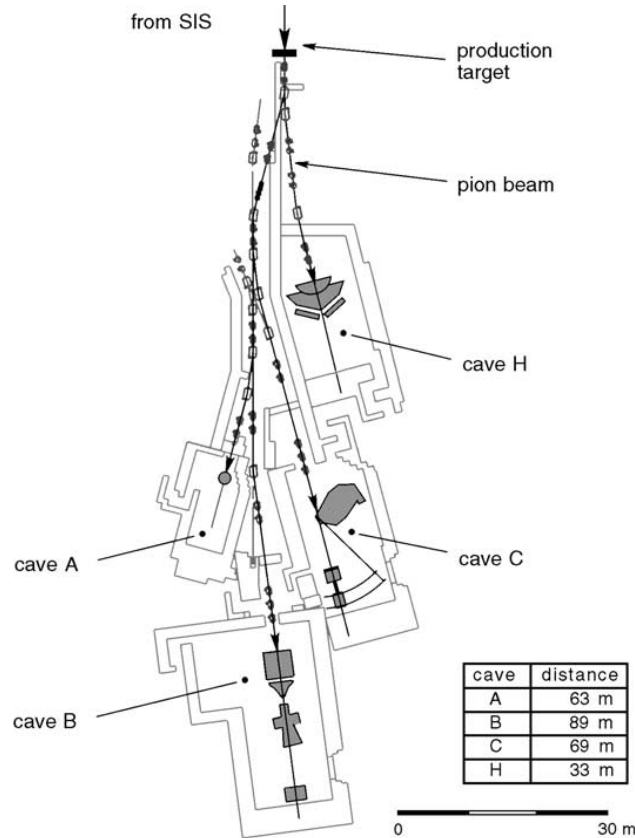


Figure 2.1: GSI pion beam

## 2.4 Target Properties

As it was already mentioned, the systematics of five nuclear targets: C, Al, Cu, Sn and Pb, was used in the S273 experiment, in order to get an extensive overview of the production probability and phase space distribution of all observed particles in performed pion-induced reactions. A considerable amount of data was obtained only for C and Pb targets, while for the intermediate mass targets (Al, Cu, Sn) the statistics was low due to the very short beam time usage. All targets and their main properties are given in Table 2.1. The sizes of the targets were chosen according to the beam spot, which was approximately  $2 \times 2 \text{ cm}^2$  wide, so all of them have the cross section size of  $4.5 \times 4.5 \text{ cm}^2$ . The target thickness ranges from 4 to 10 mm. The beam

time for the reactions on the specific target is presented in the last column of the table.

Table 2.1: Target properties

target	$\rho \cdot d$ [g/cm <sup>2</sup> ]	thickness [mm]	beam time [h]
C	1.87	10	95
Al	1.56	6	13
Cu	4.41	5	17
Sn	2.83	4	9.5
Pb	5.76	5	117

## 2.5 Experimental Setup

A suitable detector for primary central heavy ion collisions with huge number of charged products distributed over the full solid angle was designed and constructed at the SIS facility at GSI in 1990s. Precursors of such a kind of  $4\pi$  detector were Plastic Ball and the Streamer Chamber at Berkeley and the DIOGENE system at Saclay [80]. The FOPI detector setup, which has rotational symmetry around the beam axis, is presented in Fig. 2.2.

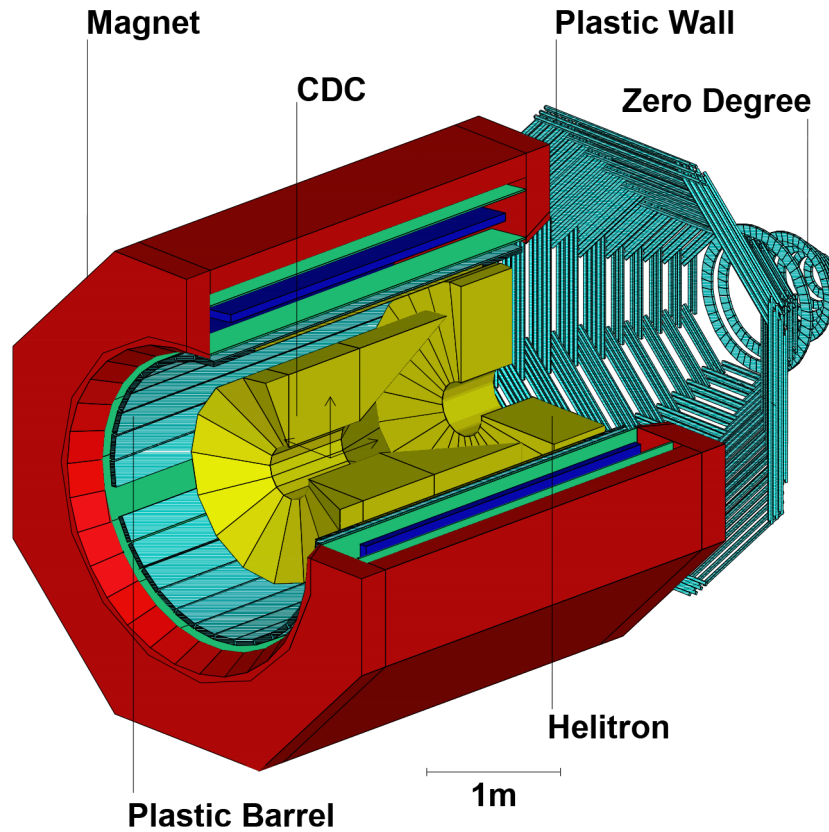


Figure 2.2: Schematic drawing of the FOPI detector system coming from the FOPI GEANT (see Chapter 4) environment.

In this section the whole experimental detection setup will be briefly described, with special focus on the CDC detector whose data has been mostly used for the particles reconstruction in this study.

### **2.5.1 Magnet**

Three major subdetectors of the FOPI setup (CDC, Barrel and Helitron) are placed inside the superconducting magnet which produces a homogeneous solenoidal field parallel to the beam axis. The magnet has a diameter of 2.4 m and a length of 3.3 m. The nominal magnetic field of 0.6 T is achieved with the 720 A current. Charged particles pass through the field along helical trajectories and the information about their curvatures in  $xy$  plane and the polar angle ( $\vartheta$ ) are used for the transverse and total momenta determination.

### **2.5.2 Start Counter**

This detector is used to define the reference time (start time) for all detectors in the FOPI setup and to count incoming particles. It consists of a scintillator foil tilted by  $45^\circ$  around the vertical axis and it is placed at about 2.5 m in front of the target. The signal produced by the beam particles passing through the scintillator is detected by two photomultipliers placed perpendicular to the beam line. The provided information are the deposited energy and the arrival time of the particle, measured with a time resolution of 160 ps.

### **2.5.3 Halo Detector**

There are two halo detectors which monitor the beam quality. *Halo 1* is 5 mm thick and it is placed in front of the start counter. It is a veto counter which is used to allocate the beam spot. *Halo 2* is 2 mm thick with a cylindrical hole in the middle, placed closer to the target as an additional veto detector. Those two halo detectors are in anti-coincidence with the start counter in order to reject all the beam particles which are not focused on the target. They work in the way that they provide a veto signal whenever a beam particle passes them.

### **2.5.4 Beam Scintillator Detector**

The role of this detector is to control the focusing of the beam as the supplement to halo detectors. In this experiment it has an important role due to the wide spot of the pion beam. Its position is at 30 cm in front of the target. It is 2 mm thick and  $35 \times 35 \text{ mm}^2$  in cross section surface.

### 2.5.5 Central Drift Chamber (CDC)

The central drift chamber of the FOPI detector is a cylindrical jet chamber. In chambers like this, the signal wires are placed axial, forming the sector shaped unit with electric drift field perpendicular to the beam axis.

This type of chamber was designed and used for the first time in the JADE experiment at PETRA (DESY) [81] in the early 1980s and then later on in the OPAL experiment at LEP (Large Electron-Positron Collider at CERN) [82, 83].

The drift paths of this drift chamber are short, e.g. for the FOPI CDC their lengths are between 5 and 15 cm, hence electron drift times are of the order of several  $\mu\text{s}$  and the chamber can operate at high event rates. The other nice outcome is that events with a high local track density can be recorded with a good double track resolution and particles can be identified in nearly  $4\pi$  solid angle range.

#### Technical Details

The CDC is placed inside a homogeneous magnetic field with a precision of better than 1%. The geometrical acceptance of the polar angle of the CDC goes from  $23^\circ$  to  $113^\circ$  while the azimuthal coverage is complete.

The active volume of the chamber has a cylindrical shape about 2 m long and with radius size of 80 cm. It is azimuthally divided into 16 identical sectors and each sector consists of 252 wires (125  $\mu\text{m}$  in diameter) placed parallel to the beam direction. Those wires produce electrical drift field perpendicular to the beam axis (see Fig. 2.4, upper left). The anode (sense) plane in the middle of sectors includes 61 potential wires (125  $\mu\text{m}$  in diameter) and 60 sense wires (20  $\mu\text{m}$  in diameter). They are placed alternately at distances of 0.5 cm, parallel to the beam axis. The lengths of wires vary between 86 and 196 cm, depending on its radial position. The anode plane is not sited radially, but it is inclined by  $8^\circ$  (see Fig. 2.3). That placement helps in distinguishing between real and mirror tracks. The other option for figuring out the left-right uncertainty is to displace the sense wires by  $\pm 200 \mu\text{m}$  (so-called staggering) with respect to the anode plane.

The nominal drift voltage of  $-15 \text{ keV}$ , distributed to the wires by a voltage divider chain, generates a homogeneous field of approximately 800 V/cm. By applying a voltage of  $-1275 \text{ V}$  to the each potential wire, the electric field for the charge multiplication is provided (see Fig. 2.4, upper right). The electric field around the sense wires decreases with  $r$ .

The CDC volume is filled with argon (88%), iso-butane (10%) and methane (2%) gas mixture, chosen in a way that drift velocity is nearly independent of the drift electric field.

#### Signal Detection, Hit Reconstruction, Tracking

When a charged particle passes through the CDC volume it ionizes atoms or molecules of the gas mixture and loses a fraction of its energy. The mean energy loss is described by the

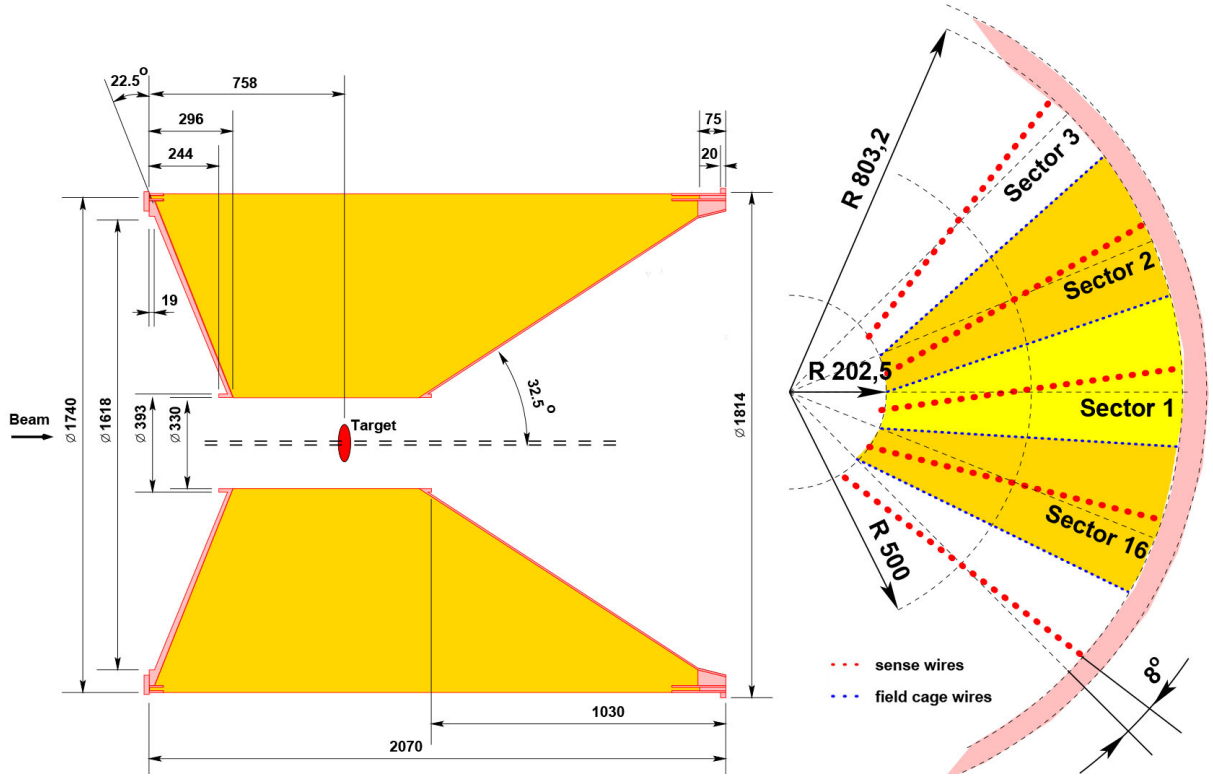


Figure 2.3: Longitudinal (left) and transverse (right) cross section of the CDC.

Bethe-Bloch formula (see Appendix A). After the ionization, created electrons are accelerated towards the sense wires in the anode plane and the positive ions are accelerated towards the field cage. On their way they undergo collisions with atoms or molecules of the gas. Consequently, the particles acquire the drift velocity  $v_D$ . Its magnitude is approximately  $4.5 \text{ cm}/\mu\text{s}$  and its direction is defined with magnetic and electric field. As it is shown in the illustration of Fig. 2.4 (lower left), a drift cell<sup>1</sup> is now tilted by the Lorentz angle  $\alpha_L$  to the electric field. In a constant electric and magnetic field, the electrons will drift along a straight line at an Lorentz angle with respect to electric field lines.

Lorentz angle and drift velocity are related by equations:

$$v_D = \frac{\frac{eE\tau}{2m_e}}{\sqrt{1 + \left(\frac{eB\tau}{m_e}\right)^2}}, \alpha_L = \arctg\left(\frac{eB\tau}{m_e}\right). \quad (2.1)$$

The quantities used in Eq. (2.1) are:  $e$  is electron charge,  $m_e$  is electron mass,  $\tau$  is the mean time between two collisions, and  $E$  and  $B$  are strengths of electric and magnetic field respectively.

The value of the Lorentz angle for the CDC is around  $42^\circ$  to  $45^\circ$  and it depends on the gas mixture, the pressure and both, electric and magnetic, fields. As it was already mentioned in the introduction of this subsection the lengths of drift paths of the CDC are short and electron drift

<sup>1</sup>The drift cell is defined as an area within the active volume of a sector for which all electrons created inside will end up on the sense wire that specific drift cell is assigned to.



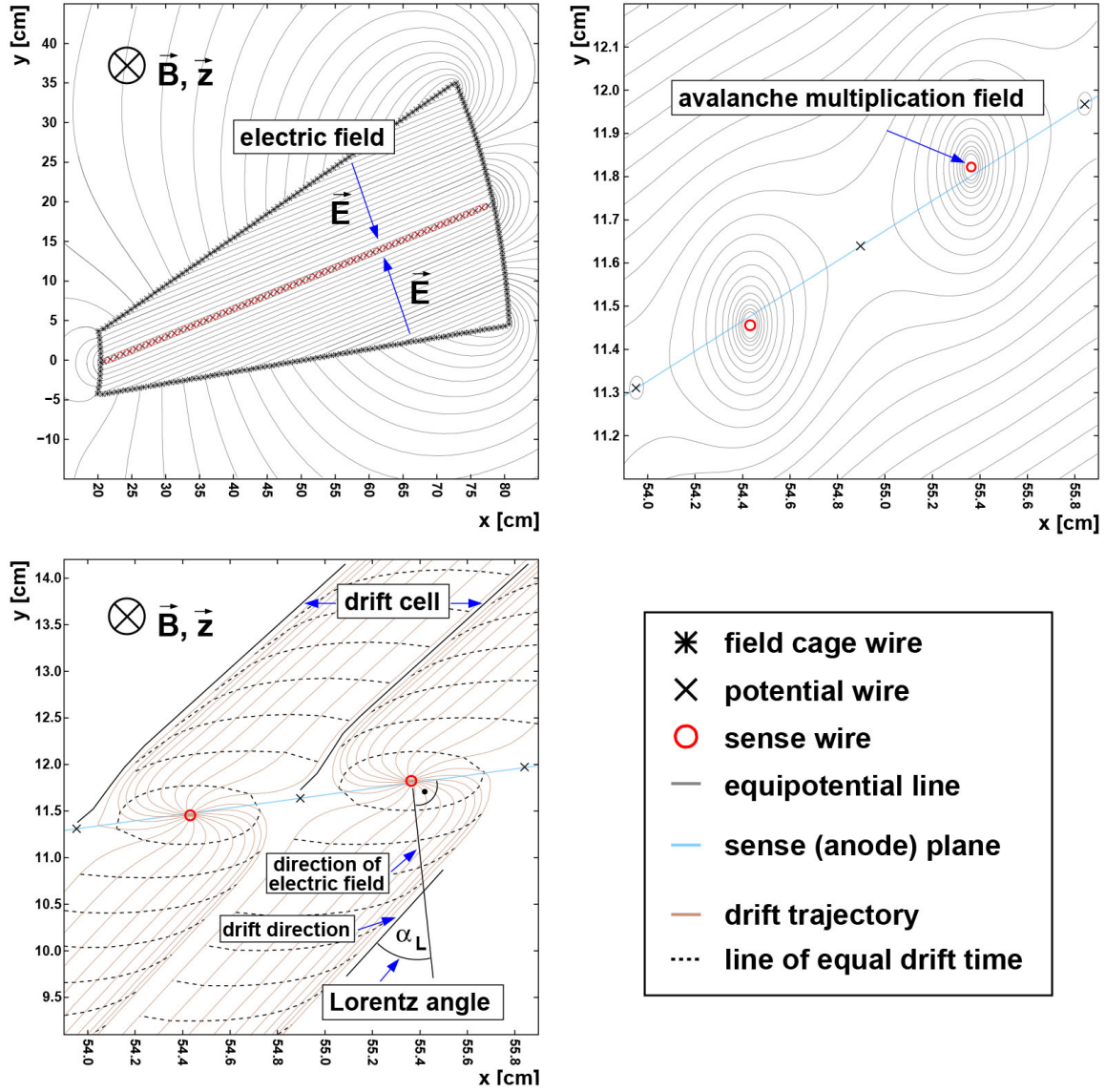


Figure 2.4: Illustration of a CDC sector: electric field (upper left), the avalanche multiplication field (upper right) and the drift trajectories of electrons in  $xy$  plane (lower left). The interpretation of used symbols is presented in lower right panel. The plots are generated with GARFIELD program [84].

times are of the order of several  $\mu\text{s}$ . The longest drift path is about 22 cm which corresponds to a maximum drift time of about 5  $\mu\text{s}$ .

After drift time  $t_D$  electrons come close to the sense wires, starting to feel a strong inhomogeneous electric field (at a radial distance around 0.5 cm from a wire) and avalanches start (see Fig. 2.4, upper right). Therefore, the total charge collected on a sense wire is orders of magnitude larger than charge initially produced in the ionization process. For the CDC specific gas mixture and the configuration of the field around the sense wire, the factor for which primary charge is increased is about  $10^4$  to  $10^5$ .

An avalanche detected on a sense wire by measuring its charge is called a hit [4]. To start with a track reconstruction, the positions of the primary ionizations, i.e. the origins of hits, have to be determined. That is done in the  $xy$  plane by extrapolating back from the well known wire position. The Lorentz angle, drift velocity and drift time should be taken into account. The procedure of the hit reconstruction is explained in detail in [85, 86]. The hit position in the  $xy$  plane is given in equations:

$$x = x_w \pm \cos \alpha_L \cdot v_D \cdot (t_D - t_w - t_0), \quad (2.2)$$

$$y = y_w \pm \sin \alpha_L \cdot v_D \cdot (t_D - t_w - t_0), \quad (2.3)$$

where  $x, y$  are the coordinates of the hit position,  $x_w, y_w$  coordinates of the assigned sense wire,  $t_D$  is the electron drift time,  $t_w$  is a wire dependent time offset (time needed for the collected charge to travel from the wire to the FADC - explained in Section 2.5) and  $t_0$  is the total time offset (the reference time in the clocks of the FADCs). The position resolution is less than  $500 \mu\text{m}$  in the  $xy$  direction and for the  $z$  direction it is around 5 to 7 cm.

After the hit positions are obtained, one can proceed with the tracking. The tracking procedure is done by complex algorithms which can roughly be divided in two groups depending on their operation. If an algorithm is acting on all hits, it is called *global* and if it is acting only on a subset of hits at a time, it is called *local*. The track finding algorithm used for the tracking procedure in the S273 experiment is a local one [87, 88]. Only tracks with high momentum, i.e. small curvature in the  $xy$  plane are reconstructed [1].

The electrons created by ionization can drift towards the sense plane from two directions (see Fig. 2.4, upper left). That is why an ambiguity for the hit position in the  $xy$  plane arises. It is important to discard "mirror tracks".

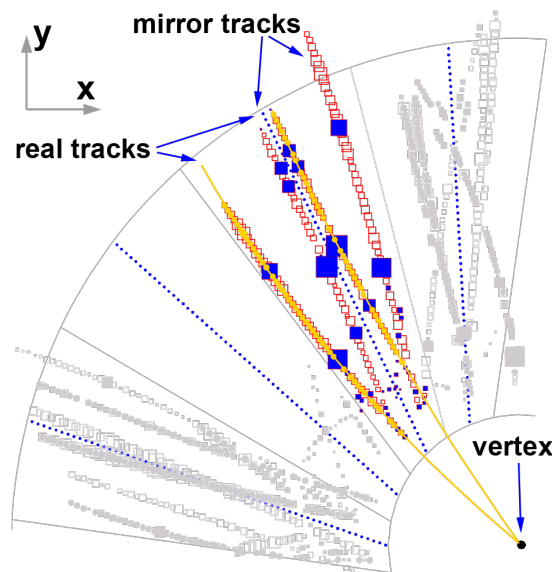


Figure 2.5: Illustration of choosing right tracks in a CDC sector. Figure is taken from [4].

As it was already explained, there are technical features that help to attenuate this problem. As a result of the tilting of the sense plane, mirror tracks never originate from the event vertex but miss it by a distance of several centimetres. The staggering of the sense wires leads to a better fit quality for the real track in comparison to the mirror track. Here it can be added that, because of the Lorentz angle value, mirror tracks include hits with positions outside the active volume of the CDC. The illustration of real (yellow) and mirror (empty red squares) tracks is given in Fig. 2.5. It can be seen that the real tracks originate from the primary vertex and their mirror images don't and they may have hits outside the active volume of the CDC. [4]

## Calibration

To be sure that good calibration is obtained the process of a hit reconstruction, tracking and calibrating three parameters: total time offset  $t_0$  (needed for the calculation of the drift time  $t_D$ ), drift velocity  $v_D$  and Lorentz angle  $\alpha_L$  should be repeated several times. The calibration is done through the procedure in which tracks which either cross a sector border (specified by  $v_D$  and  $\alpha_L$ ) or the sense plane (specified by  $t_0$  and  $\alpha_L$ ) are selected and then the parameters are adjusted in a way there are no discontinuities in the track left.

The calibration of three global parameters begins by gauging a total time offset. The results of the procedure are shown in Fig. 2.6. The same event is presented in (a) and (b) panels of the figure, a track before calibration (it can be observed that the track is split while crossing sector border) and after correction of  $t_0$  (split parts of the track are merged) respectively.

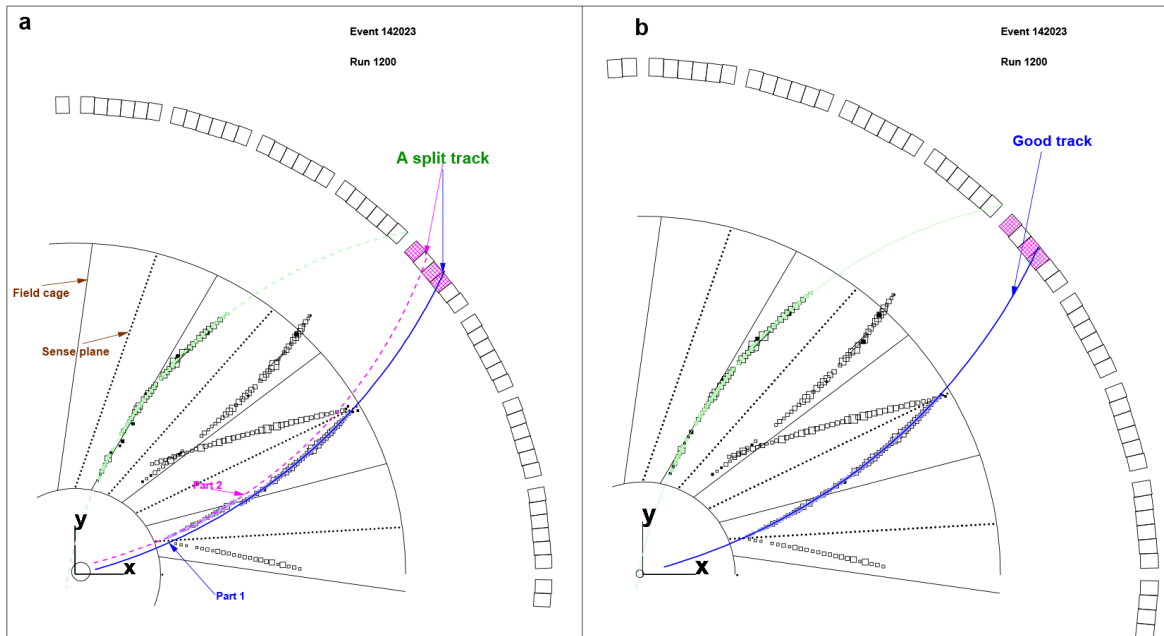


Figure 2.6: Time offset calibration. (a) An event with wrong total time offset, before the calibration. (b) The same event after calibration. Figure is taken from [1].

After the time offset is set properly it is possible to proceed with two other parameters

calibration. Figure 2.7 in panel (a) shows that the track is broken when crosses the sector border with not corrected drift velocity. The track after drift velocity is calibrated is shown in panel (b) of the same figure.

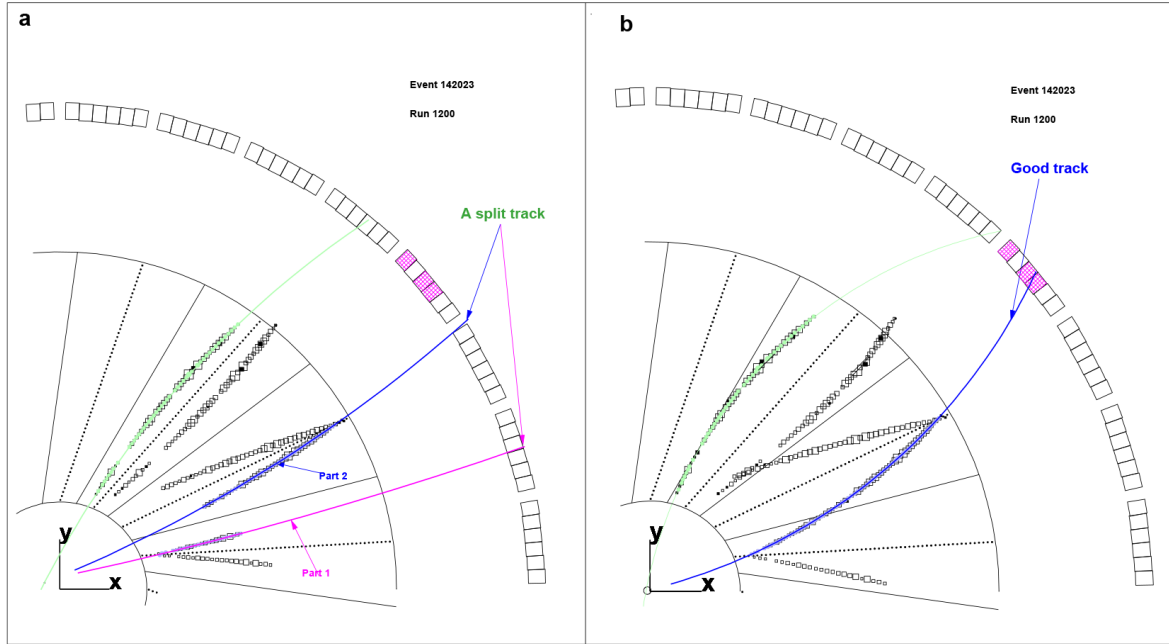


Figure 2.7: Drift velocity calibration. (a) An event before drift velocity calibration. (b) The same event with corrected drift velocity. Figure is taken from [1].

A similar situation happens with Lorentz angle calibration (see Fig. 2.8).

Once when the global parameters are calibrated, the  $z$  coordinate and the energy loss calibration procedures are applied. A charge division method is adopted in the determination of the  $z$  coordinate of a hit along a sense wire [1, 89]. For the energy loss calibration, the fact that the total energy loss of a particle passing through the active volume of the CDC is proportional to the collected charge in each drift cell is used. Then the factor of the proportionality, which takes into account the gas gain and the amplification factors of the preamplifiers at both ends of each wire, has to be calibrated. The detailed procedure of  $z$  and  $\Delta E$  calibration is presented in [1].

## 2.5.6 Helitron

This detector is a radial drift chamber which provides information about momentum and energy loss of charged particles (charged particles are identified via their energy loss in the sensitive volume and their track curvature). It covers the full azimuthal angle and its polar angle acceptance spreads from  $7^\circ$  to  $30^\circ$ . It is filled with the exactly same gas mixture like the CDC. The chamber is divided into 24 sectors and the middle of each of it has 53 potential and 54 sense wires. Those wires extend radially between inner and outer radius of the detector. Sense wires detect the signal of the electron multiplication as a result of the electric field produced by po-

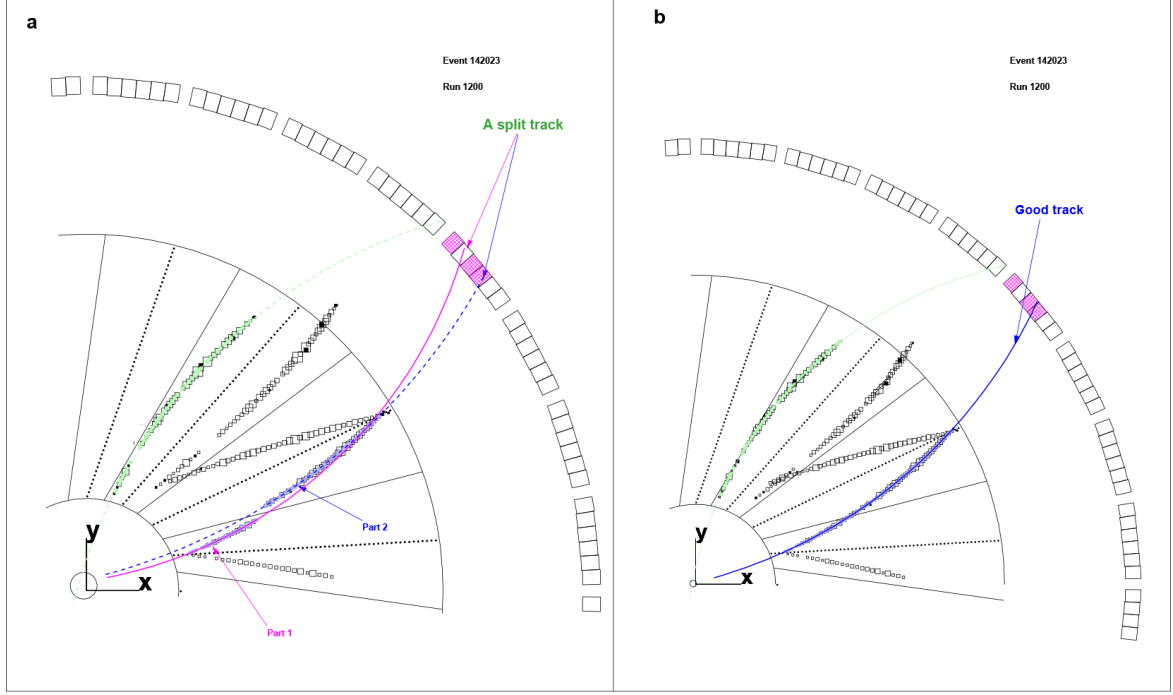


Figure 2.8: Lorentz angle calibration. (a) Split track of an event before Lorentz angle is calibrated. (b) The same event after Lorentz angle calibration. Figure is taken from [1].

tential wires. Helitron is fitted in a place where the magnetic field is known with an accuracy of 0.5%. So, due to inhomogeneity of the magnetic field the azimuthal angle of the particles in the transverse plane has to be corrected according to formula:

$$\phi_{new} = \phi + \frac{12^\circ}{p}, \quad (2.4)$$

$\phi_{new}$  is corrected and  $\phi$  is measured azimuthal angle, while  $p$  is total momentum of the detected particle measured in GeV/c.

### 2.5.7 Barrel

The Barrel scintillator provides information about the energy loss, the time of flight and the position. It surrounds the CDC at the distance of 111 cm and covers polar angles from  $27^\circ$  to  $57^\circ$  and about 85% of the azimuthal angle. It is made out of 180 plastic scintillator bars. Each bar is 150 cm long and has a cross section of  $4 \times 3 \text{ cm}^2$ . Barrel has the position resolution around 7 cm and its time resolution is about 300 ps. The light produced in the bar is detected by a photomultiplier tube at both ends of the bar. In that way the information about the hit position of a charged particle along the beam axis, as well as its time of flight, are gained. A privilege of usage of the Barrel information (velocity) in the combination of the data measured by other subdetector (CDC's momentum) leads to a better particles identification possibilities.

### 2.5.8 Plastic Wall (PLAWA)

PLAWA is the outer part of the forward wall of the FOPI setup. This scintillator, like Barrel, measures the energy loss and the time of flight and also gives the information about the position along a strip (via the angular position of the strip which scintillated). PLAWA covers the polar angles from  $7^\circ$  to  $30^\circ$ . It consists of 512 plastic scintillator strips arranged in 8 sectors and at both ends of the each strip the produced light is detected by photomultipliers. Hence, every strip provides two energy and two time information and then the energy loss ( $\propto \sqrt{E_1 \cdot E_2}$ ) and the time of flight ( $\propto (t_1 + t_2)/2$ ) are calculated. The active length of the strips is from 45 cm in the inner sector to 165 cm in the outer sector of PLAWA and that is the reason that the time resolution varies from 80 to 120 ps for the inner to the outer part respectively. The hit position resolution is measured in the range from 1.2 to 2.0 cm [80, 90]. It is suitable to combine the momentum obtained from Helitron and velocity from PLAWA to achieve the better particle identification.

### 2.5.9 Zero Degree Detector

This detector is the inner part of the forward wall and it measures energy loss and time of flight of the particles. It covers polar angles from  $1.2^\circ$  to  $7.0^\circ$  and it is built out of 252 trapezoid plastic scintillator strips arranged in 7 concentric rings. The signal at each strip is read out by one photomultiplier. The time resolution of this detector is about 200 ps.

### 2.5.10 Silicon Strip Detector

Two silicon strip detectors were used in the S273 FOPI experiment, sitting directly in the beam before the target at the distance chosen such that the beam particles (negative pions) are tracked with a precision in the order of mm. The so achieved information on the primary vertex should provide an improvement of the momentum resolution and the reconstruction of secondary vertices.

Each silicon micro-strip detector is double sided, it has a cross section of  $3.2 \times 3.2 \text{ cm}^2$  and it is 300  $\mu\text{m}$  thick. The resistivity of detector is 6 - 10 k $\Omega\text{m}$  and the operating voltage of each silicon strip detector is 50 - 60 V. Each side of the detector consists of 1280 strips with a pitch of 25  $\mu\text{m}$  and strips of one side of the detector are perpendicular to the strips of the other side, but only strips at 50  $\mu\text{m}$  are read out to reduce the number of the output channels [91]. To get an information about the position of the particle, the centre of gravity of the charges collected at several readout strips should be calculated. The position of the silicon detectors during this pion experiment are sketched in Fig. 2.9 in relation with the CDC (and target) position, but also with other smaller subdetectors which are not introduced in the figure of the FOPI setup (Fig. 2.2).

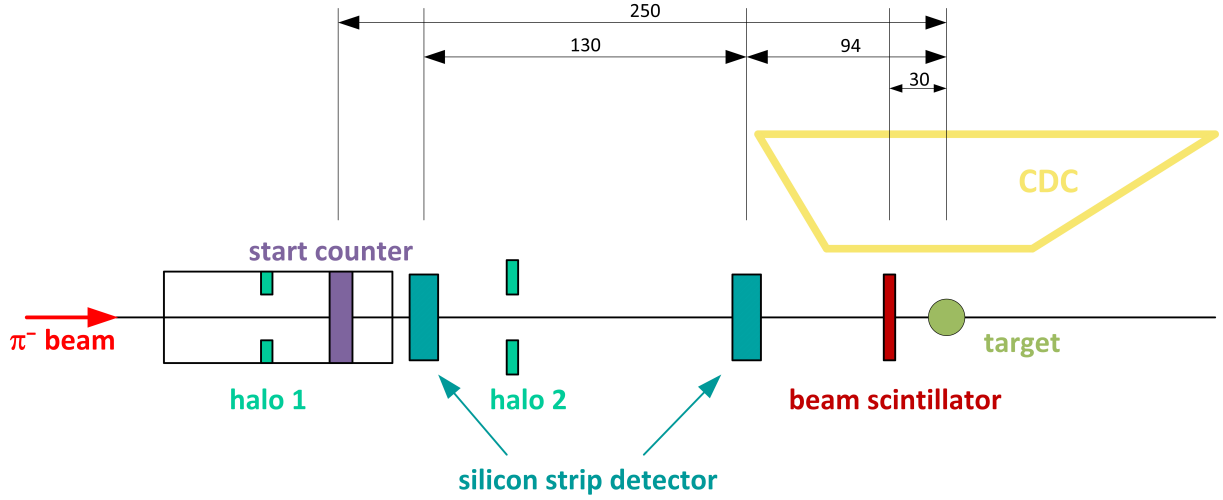


Figure 2.9: Illustration of silicon micro-strip detector position in the FOPI setup in respect with target and CDC position during the S273 experiment. Positions of other smaller subdetectors: start counter, two halo detectors and beam scintillator are marked too. The sizes of subdetectors are not realistic. All indicated distances are in centimetres.

### 2.5.11 Trigger System

To select the events of interest, i.e. to reduce the background events, the trigger system is used, which ultimately results in stored data quantity decrement. The start and halo detectors represent a "pre-trigger" setup, so if no veto signals are produced a possible event can be accepted by the trigger. First of all, the incident particles are counted by the start detector. Then the halo detectors monitor the beam quality (its adjustment and focusing). According to those beam quality requests, as well as the information of subdetectors, different types of events are imposed. To enhance the number of favourable events comparing to the others, so-called *down-scale factors* ( $ds$ ) are applied (see Eq. (2.5)). In that way the number of some (unfavourable) events are reduced.

$$ds_{tot} = \frac{N_{inh}}{N_{raw}}, \quad ds_{trig} = \frac{N_{acc}}{N_{inh}}, \quad (2.5)$$

where  $ds_{tot}$  stands for dead-time induced downscale factor and  $ds_{trig}$  is hardware downscale factor. The numbers counted by LeCroy 4434 32-fold 32 bit CAMAC scalers which are used for determination of the inclusive cross section for the reaction  $\pi^- + N \rightarrow Y + K$  are:

- $N_{raw}$  stands for the total number of events, i.e. the number of beam particles which pass the trigger box.
- $N_{inh}$  is inhibited number of events which fulfil the trigger condition. It is derived as  $N_{inh} = \epsilon_{dead} \cdot N_{beam}$ , where  $\epsilon_{dead}$  is a number calculated from the number of total and



accepted events and also takes into account the dead time of the detector ( $t_{dead}$ ). Hence, it represents the number of events outside the dead time of the detector.

- $N_{acc}$  is the number of accepted events, fulfilling a trigger called *Fast Clear*, which means that an event will be rejected or deleted if the number of hits detected by the CDC is not large enough.

A very simplified illustration of events selection through the trigger system used in the S273 experiment is given in Fig. 2.10.

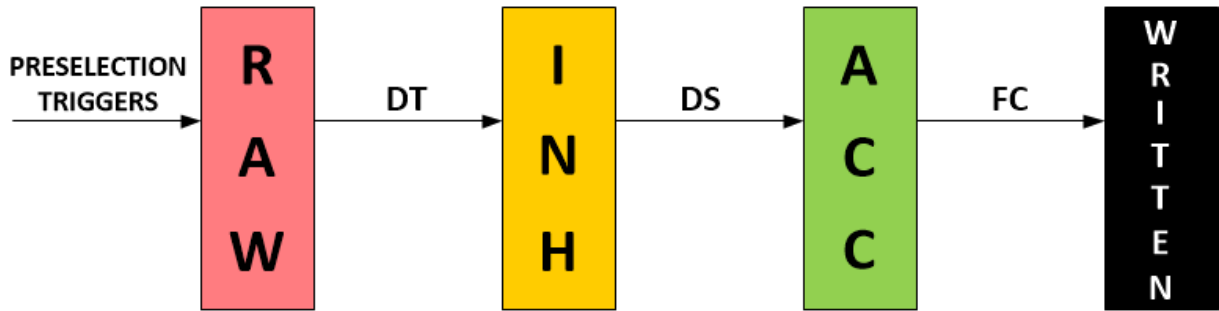


Figure 2.10: Illustration of the event selection through the trigger system in the S273 experiment. RAW indicates events which passed preselection triggers and could result as accepted (ACC) and finally be written to a computer (WRITTEN). INH stands for inhibited number of particles (explained in the text). DT is dead time, DS downscale factor and FC stands for fast clear which can be activated in a case of pile-up events or no hits inside the CDC.

By using the explained trigger system, the experimental cross section can be calculated from the following equations. The experimental cross section for a given trigger type is determined as:

$$\sigma_{exp, trig} = \frac{1}{N_{beam} n_{targ}} \frac{N_{trig}}{ds_{tot} ds_{trig}}, \quad (2.6)$$

and then the total cross section is then calculated using the relation:

$$\sigma_{tot} = \frac{1}{N_{beam} n_{targ}} \sum_{trig} \frac{N_{trig}}{ds_{tot} ds_{trig}}, \quad (2.7)$$

where  $N_{beam}$  stands for the number of beam particles ( $\pi^-$ ) passing through the start counter without hitting the halo detector,  $n_{target}$  stands for the number of target nuclei per  $\text{cm}^2$  and  $N_{trig}$  is the number of events for a given trigger per second. The results of the cross section determination will be presented in Chapter 5.



## 2.6 Electronics and Data Acquisition

The data acquisition, together with associated electronic equipment, is used for collecting, (pre)processing and storing data from subdetectors of the FOPI system. The CDC and the Helitron produce the largest amount of all data (80 to 90%), each of them in average 2 MB per event, so for the efficient transfer and data storage it is important that preprocessing procedure is effective.

In this section the DAQ system is shortly introduced and more detailed overview may be found in for example [4, 65]. As an example, Fig. 2.11 shows the data acquisition system for the FOPI S261 experiment held in 2003. Almost the same setup was used in the S273 experiment.

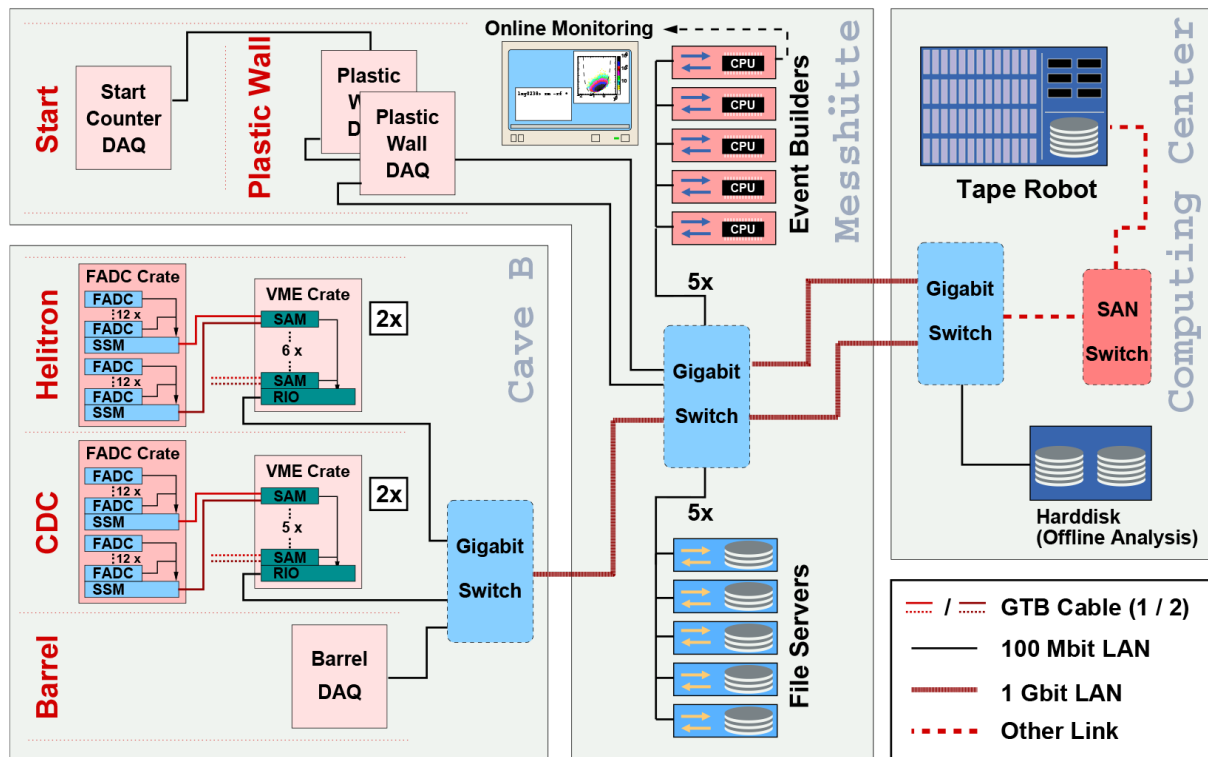


Figure 2.11: A scheme example of an acquisition system the FOPI S261 experiment held in 2003. Figure is taken from [4].

The main parts of data acquisition system are listed and described below.

**Flash Analogue-to-Digital Converters (FADC).** After a hit on a wire is selected, the signal pulse has to be digitized for further analysis. The FOPI experiment operates with FADCs of 100 MHz sampling frequency. The provided time resolution is 10 ns with a dynamic range of 8 bit (effectively extended to 10 bit due to the nonlinear characteristics of FADC's internal preamplifier). The digitized values are stored in a ring buffer with a depth of 1024 samples which corresponds to a maximum time range of 10.24  $\mu$ s. Since drift velocity

values range from 4 to 5 cm/ $\mu$ s and maximum drift path length is 25 cm, a time range of 500 to 600  $\mu$ s is sufficient for digitization of all hits. FADC has 24 modules, arranged in two groups inside so-called crate. The crate ensures the cooling system, the power supply and the data bus for the readout. For example, the CDC readout needs 10 crates which equals 240 FADCs. Each FADC module has 8 independent inputs, so it can process the data from four wires read out on both ends. Each group of FADC modules is assigned to one SSM module.

**Scanning and Sampling Module (SSM).** After the sampling of the FADCs is stopped, which means that the valid trigger signal is received, the data is collected by the SSMs. Each modul reads the data form 12 different FADCs. At this stage a first step of reducing the data is accomplished. A data reduction of about a factor 5 to 10 can be achieved. That factor depends on the number of hits and the noise on each wire. Sample values smaller than a defined threshold are rejected. The clock frequency of the SSM can be chosen between 20 to 40 MHz. The combined FADC data is transferred from the SSM to the SAM via a so-called GTB3 (form German: GeräTeBus) cable. Data rates of 20 MB/s can be achieved due to a 16 bit wide bus with 10 MHz frequency. Two different modes of data transmission can be provided by the SSM. Slow mode is used for calibrating FADC pedestals and initializing the SSM at the startup of the DAQ. The other mode operates in the total bus speed and is used during the experiment while transferring zero-suppressed FADC data from the SSM to the SAM.

**Control and Selection Module (SAM - from German: Steuerungs- und Auslese-Modul).**

It is the hardware component needed for the online data reduction in the second, more complex, step. Each module in the drift chamber DAQ receives the data collected by two SSMs via the GTB cables. The data is then processed by two DSPs (Digital Signal Processor - fast CPU with a pipelined architecture) and stored in an external memory for further processing. [4, 92]

**RIO3.** RIO3 is a power-PC real time computer. In the FOPI experiments it is used to collect data after its reduction is finished by SAM. After that, the data is sent to the event builders. The calibration of the FADC modules and initialization of the SSM at the start of the data acquisition is also done by RIO3. In addition, RIO3 is used for loading the data reduction code into the DSP memory and it is responsible for the processor start working after initializing the other modules. [93]

**Event builders.** The so-called event builders function is to combine the data delivered by all subdeterctors into "full events". Each event builder is allocated to one of five file servers.

**File servers.** File servers provide 200 GB disk space. They are used for buffering the raw data files from the experiment before they are written to the tape robot.

**Tape Robot.** The space of more than 100 TB in LTO2 (Linear Tape-Open magnetic tape data storage of second generation) cartridges with a capacity of 100 GB per volume is available at the tape robot. 535 raw data files were written during the S273 beam time.

# Chapter 3

## Data Analysis

One of the main goals of the FOPI S273 experiment and of this investigation, was to measure the in-medium inclusive cross section for the  $\pi^- + A \rightarrow \Lambda + K^0$  reaction. The analysis procedure, presented in this chapter, consists of the selection of the favourable events, the elimination of the background, particle identification and reconstruction.

The FOPI detector system is made for the detection of charged particles. The strange particles of interest ( $\Lambda$  and  $K^0$ ) are reconstructed from 4-momenta of the identified decay products with the invariant mass method. Daughter particles are identified via their masses determined from mean energy loss and momentum of the associated track. In general, one has to be careful with elimination of non-target reactions and possible multiple events, as well as with detector acceptance which has to be taken into account.

In this chapter the event selection procedure is presented with the main accent to rejection of the background events. To do the proper data analysis it is important to consider the acceptance of the detector used in the experiment. After that the detailed overview of particles identification and reconstruction is explained.

### 3.1 Event Selection

The accumulated events are contaminated by so-called background events which one needs to identify and eliminate from the analysed data set. There are two main sources of these background events. The first category are the events which do not originate from the target and the second one comes from so-called multiple or pileup events (when two or more pions reach the target at almost the same time). In order to reject those cases and to minimise the background contamination, several triggers were applied. The scheme of the S273 experiment trigger system has been presented in Fig. 2.10 of Section 2.5.

The spot of the pion beam was  $2 \times 2 \text{ cm}^2$  wide, so due to the large beam spot dimensions there are events in which there was no interaction with target before the pion hit the detector, but instead the pion interacted with different parts of the detector system. Those events are

considered as a background contamination and they are rejected with help of dedicated trigger combinations.

The trigger called *Good beam* provides the information based on the signal from start and halo detectors. It operates in a way that the event is rejected whenever a halo detector is hit by an incident particle (pion). An additional trigger input, called *Better Beam*, has been provided by a scintillator counter which was placed at a distance of 30 cm in front of the target. It provided information of beam particles hitting detector parts in the space between the start counter and the target.

Introducing constraints to the start counter information, but also to the CDC vertex position, can help to reduce both types of the background. The vertex position of an event  $(v_x, v_y, v_z)$  represents the mean values of track intersections and it is determined by extrapolating the measured tracks towards the target. Due to the fact that pions can hit the whole target surface ( $4.5 \times 4.5 \text{ cm}^2$ ), there are no restrictions on the vertex in the  $xy$  plane, which is demonstrated in Fig. 3.1.

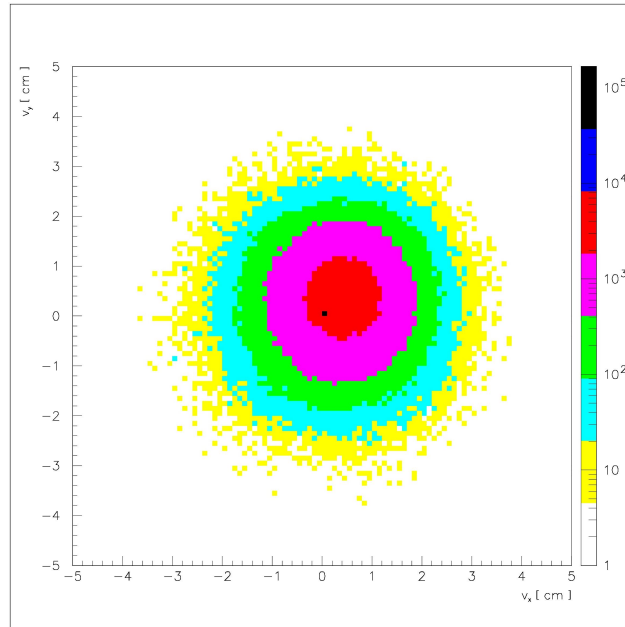


Figure 3.1: The experimental CDC vertex distribution in the transverse plane,  $v_y$  vs  $v_x$ . The circular beam spot is not exactly centred at  $(0, 0)$ .

Hence, the background constraints should be applied on the  $z$  coordinate (along the beam direction) of the event vertex. Figure 3.2 shows the vertex position in the  $z$  direction in the range of 1 m in front to 0.5 m behind the target. Two pronounced peaks are visible. One at the nominal target position (0 cm) and one at around  $-30$  cm. The second peak is caused by beam particles interacting within the exit window of the beam pipe. In order to suppress these background events, only events with a reconstructed vertex position in the range of  $\pm 3\sigma$  ( $\pm 12$  cm) around the nominal position of the target are accepted (the resolution  $\sigma$  of the  $v_z$  is about 4 cm).

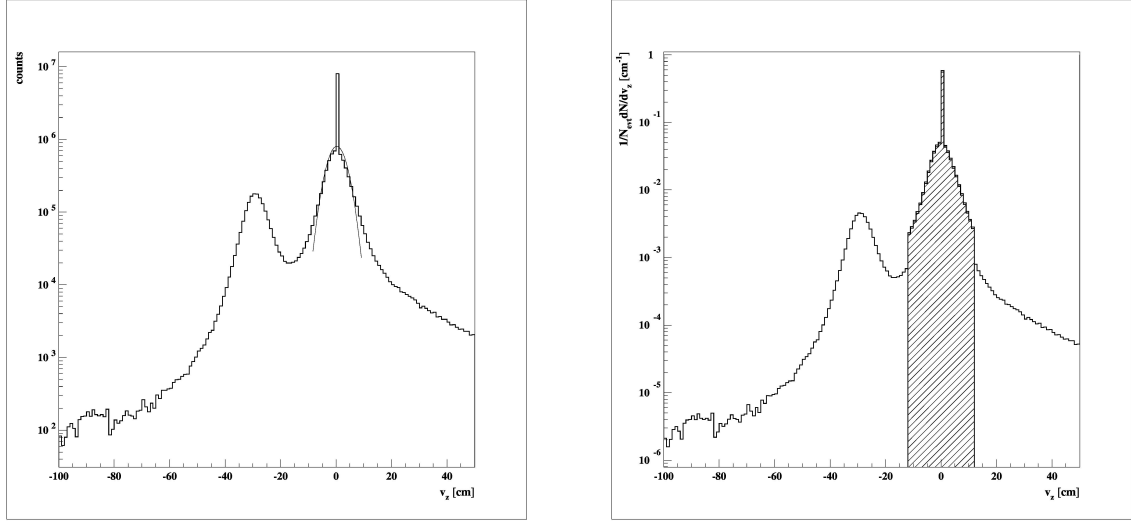


Figure 3.2: The distribution of the  $z$  component of the event vertex ( $v_z$ ) before the cuts were applied. In the left panel solid line around the maximum indicates the fitting to a Gaussian-like function for the range close to the nominal target position. In the right panel dashed area represents the range of the accepted  $v_z$  values used in the further analysis.

The term *multiple events* is used for cases in which two or more pions that arrive at the start counter in a time interval less than the counter time resolution (for this study that means less than 100 ns - the time interval of the start counter gate). Of course, in such cases it is impossible to distinguish the multiple interactions. In this particular experiment, multiple events were very rare because the mean beam intensity was about 3000 to 5000  $\pi^-$  per second, which means that

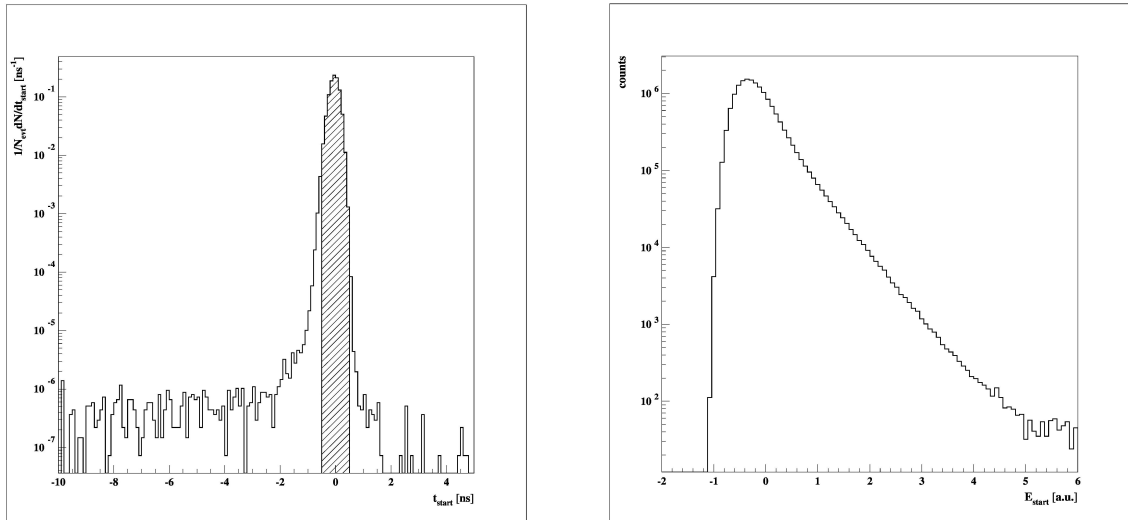


Figure 3.3: The distribution of the start time ( $t_{start}$ ) in the left panel and energy deposited in the start counter component ( $E_{start}$ ) in the right panel. Cuts applied to these two quantities are explained in the text.

in average one pion interacted with target every 250  $\mu\text{s}$ .

The information gained from the start counter helps to reduce background events with constraints set to start time and energy loss. The distributions of these two quantities, before applying preselection cuts, are presented in Fig. 3.3, the left panel shows  $t_{start}$  and the right panel  $E_{start}$ . The start time  $t_{start}$  of a good event should be close to 0. Strong deviation of the start time from 0 is an indication for multiple events. The distribution of  $t_{start}$  has a pronounced peak around 0 with long tails. To eliminate the tails and potential multiple events, only events with  $-0.5 \text{ ns} < t_{start} < 0.5 \text{ ns}$  are selected. The distribution of the deposited energy of pions which pass through the start counter is smooth, especially for  $E_{start} < 5$ . It does not have a multiple peak structure which would indicate multiple events. Therefore, only an upper limit is set to 5 and no additional cuts are applied on this parameter.

## 3.2 Detector Acceptances

Some features of the detector acceptance have already been introduced in Chapter 2. In the following lines it will be explained how they affect on particle identification and reconstruction.

Each detector has a limited acceptance owing to its geometry and kinematic constraints. That property must be considered in the determination and interpretation of the results. In this analysis this concerns mostly the FOPI CDC subdetector, since it has been mainly used for the particle identification. The geometrical acceptance of the CDC together with PLAWA of the FOPI detector is shown in Fig. 3.4.

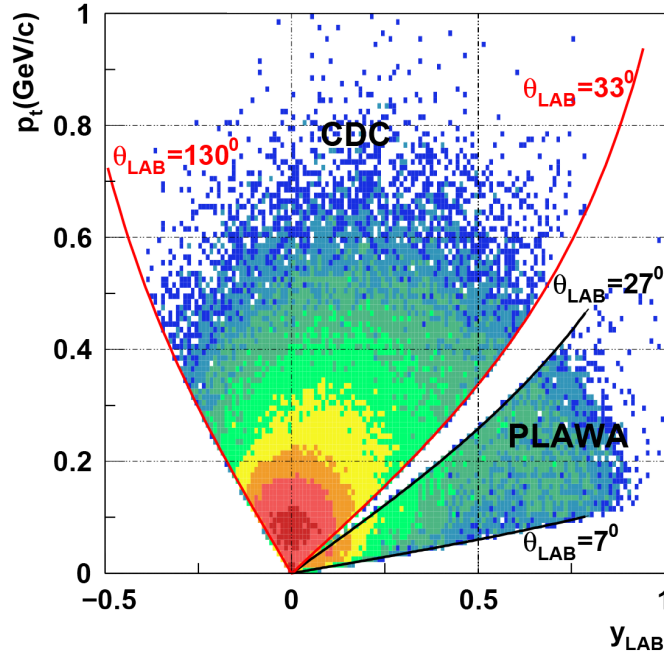


Figure 3.4: Geometrical acceptance of the FOPI detector. Polar angles covered with the CDC and PLAWA are indicated by the red and blue lines respectively.

The CDC covers the full azimuthal angle and the polar angle between  $23^\circ$  and  $113^\circ$  which corresponds to a geometrical acceptance of about 70%.

It has been shown that the reaction such as  $\pi + N \rightarrow K + Y$ , where  $K$  is one of the  $K$  mesons and  $Y$  is a hyperon (e.g.  $\Lambda$  or  $\Sigma$ ) is not isotropic [28], but there is a preferential emission of hyperons in forward direction. So the identification and subsequent reconstruction of the hyperon ( $\Lambda$ ) should include the data from the forward parts of the FOPI detector as well. One of the examples showing the invariant mass spectrum of reconstructed  $\Lambda$  particles is given in Fig. 3.5, where negative pion is detected in the CDC and proton in Helitron.

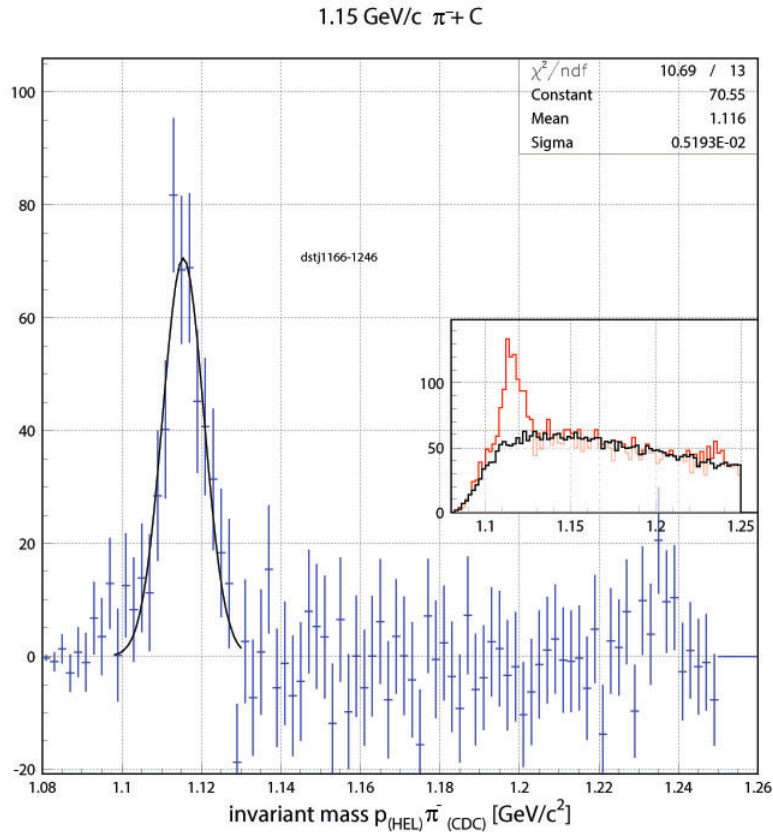


Figure 3.5: Invariant mass spectrum of the Lambda particle for  $\Lambda \rightarrow \pi^- + p$  channel, including forward and backward subdetectors.  $\pi^-$  was identified in the CDC and  $p$  in Helitron of the FOPI detector. The plot was published in [94].

### 3.3 Particles Identification and Reconstruction

Particles which can be detected by the FOPI detector (like  $\pi^-$  and proton) are identified via their masses. The mass is determined from the quantities taken from the obtained detector information: mean energy loss and curvature (momentum) of the corresponding track.

Neutral strange particles, such as  $\Lambda$  and  $K^0$ , have to be reconstructed from their decay products. The strange particles are identified by the invariant mass method after secondary



vertices were found by combining all selected decay particles present in the event. Using that method, combinations of uncorrelated particles create a background contribution to the invariant mass distribution. Within this study this type of background is estimated by combining particles from different events (the *event-mixing* method). The scaled background is then subtracted from the invariant mass distribution and the resulting signal distribution is used to derive the physical properties of the strange particle.

In this section decay properties of strange particles, their decay products and cuts applied for their selection are presented. The procedure for neutral strange particles reconstruction is explained. The event-mixing method used for the combinatorial background determination is described, together with the procedure used to subtract the background from the measured invariant mass spectrum. After all, everything is corroborated with adequate examples.

### 3.3.1 Properties of Strange Particles

Due to the V shape formed by the traces which their daughter particles made when they were discovered, and their neutrality, both, the  $\Lambda$  hyperon and the  $K^0$  meson are denoted as  $V^0$  particles.

Strange particles arise relatively fast ( $\sim 10^{-23}$  s) in a strong interaction process. The strong interaction conserves the strangeness, so in the reaction of the pion beam with the nuclear target, an associated production of strange particles is expected. On the other hand, strange particles decay slowly via weak interaction, which means with a decay time of approximately  $10^{-10}$  s. These characteristics of strange particles are, of course, very important in correlation with geometry, dimensions and technical possibilities of the FOPI detector system, for the analysis of the experimental data. A schematic illustration of neutral strange particles decay channels used in this study is given in Fig. 3.6.

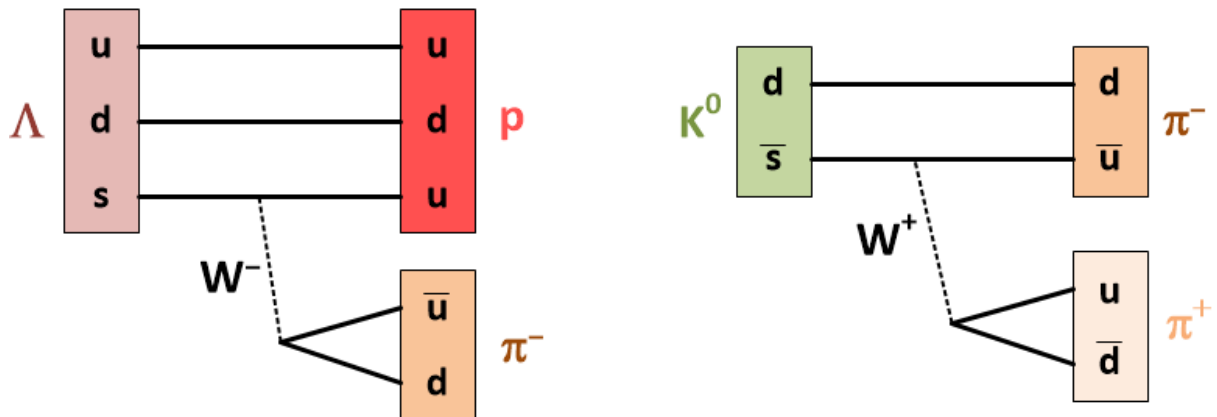


Figure 3.6: A scheme of  $\Lambda$  and  $K^0$  decay channels relevant in this study. Both particles decay via weak interaction inside single process with two charged daughter particles.

$K^0$  meson is a mixed state of short ( $K_S^0$ ) and long ( $K_L^0$ ) neutral kaon, but only  $K_S^0$  can be detected by the FOPI detector system. The reasons for that are the following:

- the life time of  $K_S^0$  is short enough to decay in the detector acceptance, the path it travels within the mean lifetime is about 2.67 cm, while the decay time of  $K_L^0$  is longer and the flight path within the mean lifetime is about 15.51 m,
- the final state of  $K_L^0$  includes uncharged particles ( $\pi^0$ ) which are not measurable with the FOPI detector.

The topology of the decay of  $\Lambda$  or  $K_S^0$  is characterized by two daughter particles emanating from a secondary vertex.

$\Lambda$  decays in the reaction:

$$\Lambda \rightarrow \pi^- + p, \quad (3.1)$$

with the mean life time of  $2.63 \cdot 10^{-10}$  s and 63.9% branching ratio.  $K_S^0$  decays with the mean life time  $8.93 \cdot 10^{-11}$  s and 68.6% branching ratio via reaction:

$$K_S^0 \rightarrow \pi^- + \pi^+. \quad (3.2)$$

Some basic properties of strange particles suitable for the FOPI experiment reconstruction are summarized in Table 3.1: mass ( $m$ ), the product of speed of light  $c$  and mean lifetime  $\tau$  which gives a typical value of the distance between primary and secondary vertex ( $c \cdot \tau$ ), decay mode and branching ratio ( $BR$ ). The values are taken from [95].

Table 3.1: Basic properties of neutral strange particles,  $\Lambda$  and  $K_S^0$ .

particle	$m$ [GeV/ $c^2$ ]	$c \cdot \tau$ [cm]	decay mode	BR
$\Lambda$	1.116	7.89	$\Lambda \rightarrow \pi^- + p$	63.9 %
$K_S^0$	0.497	2.68	$K_S^0 \rightarrow \pi^- + \pi^+$	68.6 %

The analysis for the  $K^0$  channel, measured by the CDC of the FOPI detector, together with the results for calculated  $K^0$  inclusive cross section are published by M. L. Benabderrahmane for the FOPI collaboration [63].

### 3.3.2 Decay Particle Selection

There are several factors which influence the reconstruction efficiency of lambdas and neutral kaons. The branching ratio into the analysed decay channels should be large. The observed decaying particles should survive long enough to produce a secondary vertex which is clearly separated from the primary vertex. That condition is satisfied for the strange particles such as  $\Lambda$

and  $K_S^0$ , which decay via weak interaction with life times of order  $10^{-10}$  s. As weakly decaying particles have long life times (small widths), they produce a pronounced peak in the invariant mass spectrum, which makes them candidates that can be easily identified.

As it was emphasised before, to reconstruct a neutral strange particle (e.g.  $\Lambda$ ), first of all, products of its decay (e.g.  $\pi^-$  and *proton*) should be selected. The selection of the particles from the collected CDC data is described in the following lines.

The information obtained from the CDC for each track is:

- radius of track's curvature  $r_c$  which determines the transverse momentum of a particle,
- the mean energy loss  $\langle dE/dx \rangle$ , together with an information of momentum per unit charge, which is used for a particle mass calculation,
- the closest approach to the primary vertex  $d_0$  in the transverse plane (and in beam direction  $z_0$ ),
- hit multiplicity, i.e. the number of hits per a track and
- polar angle  $\vartheta$ .

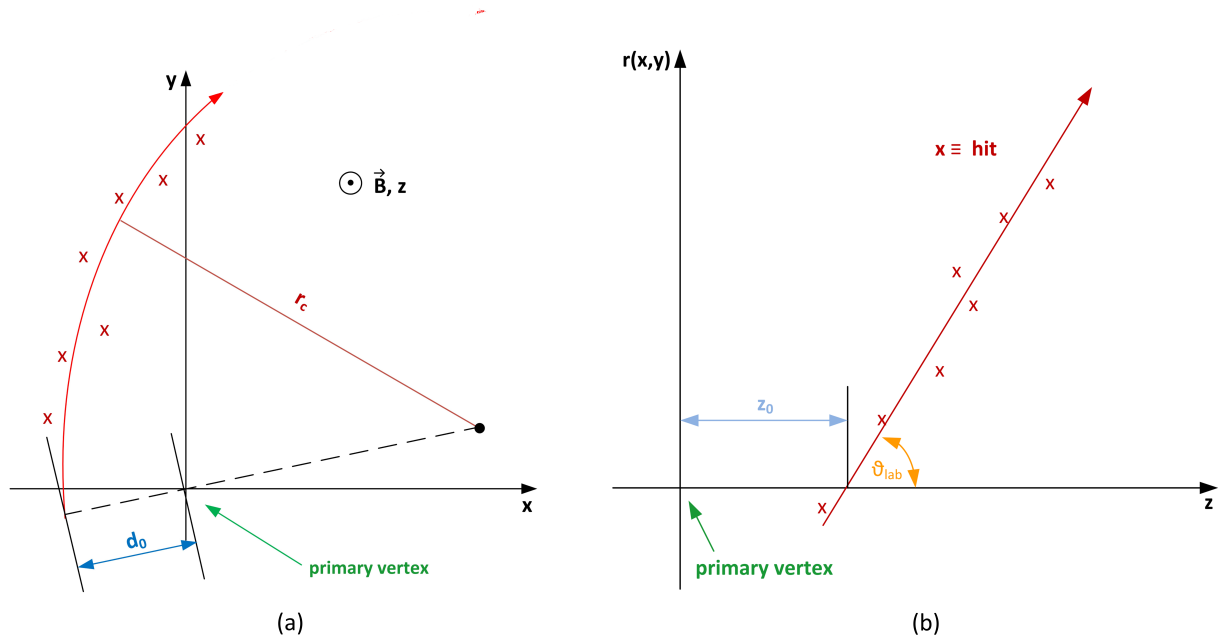


Figure 3.7: Quantities determining particle position inside the CDC detector, in transverse plane (a) and in beam direction (b). The primary vertex is set in the origin of both coordinate systems, as indicated in the illustrations.

A schematic drawing of quantities determining particle track inside the CDC is shown in Fig. 3.7. The left panel (a) represents the track of the particle in the  $xy$  plane perpendicular to the magnetic field  $B$  and beam axis  $z$ . The radius of curvature  $r_c$  and the transverse distance

to the primary vertex  $d_0$  are also indicated in the scheme. The tracks of secondary particles (daughters of  $V^0$  particles) are not supposed to pass through the primary vertex and thus are supposed to have larger  $d_0$  values than tracks from particles created in the primary vertex (e.g.  $V^0$ ). The right panel of Fig. 3.7 shows the important quantities in the  $rz$  plane: distance of the track to the primary vertex  $z_0$  and polar angle (angle between the track and the beam axis).

The curvature of the track ( $r_c$ ), obtained from the CDC, provides the transverse momentum ( $p_t$ ) of a particle. A minimum transverse momentum, about 80 MeV/c for pions and 100 MeV/c for protons, is requested to discard all particles doing spiral rotations in the CDC due to their low momenta, and also to ensure that the particles reach the outer radius of the CDC. That corresponds to a track's curvature of about 44.4 cm for pions and 55.5 cm for protons.

The total momentum  $p$  can be calculated from the transverse momentum  $p_t$  and the polar angle  $\vartheta$  ( $p = p_t / \sin \vartheta$ ), where the transverse momentum of the particle is obtained from the measured quantities using the relation:

$$\frac{p_t}{|q|} = 0.3 \cdot |r_c| \cdot B, [GeV/c]. \quad (3.3)$$

$B$  is the magnetic field of the magnitude 0.6 T and factor 0.3 is arriving from light speed in vacuum  $c \approx 3 \cdot 10^{10}$  cm/s.

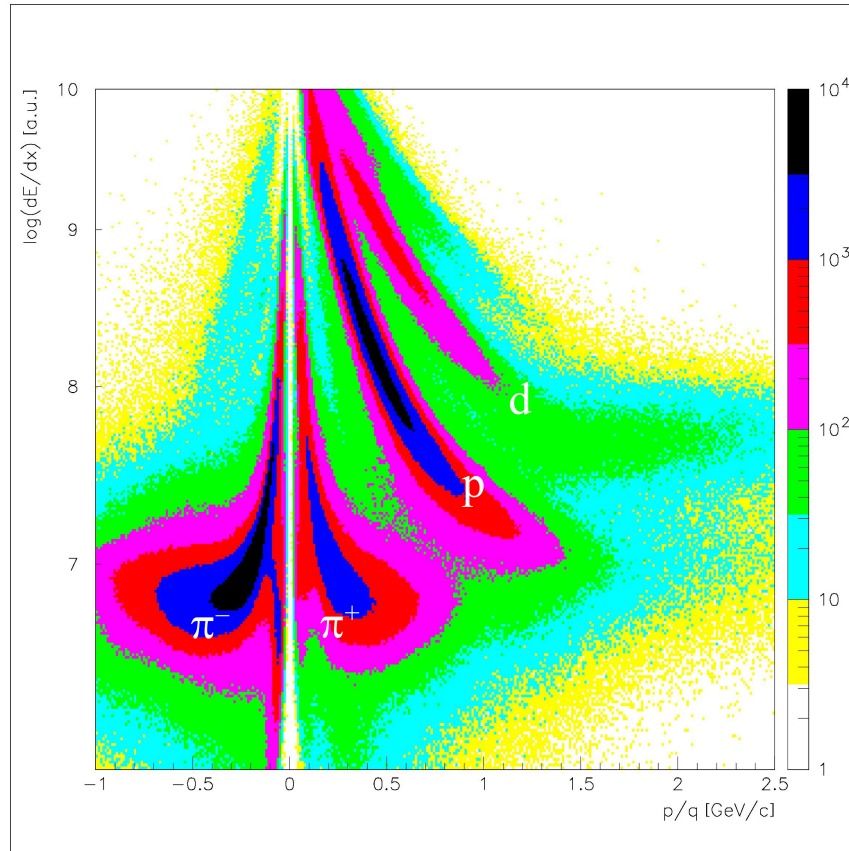


Figure 3.8: Energy loss as a function of the momentum per charge of the particles in the CDC.

By using the Bethe-Bloch parametrization (explained in Appendix A) the mass of the particle can be calculated from the mean energy loss  $\langle dE/dx \rangle$  and the momentum per unit charge  $p/q$ . In Fig. 3.8 the logarithm of energy loss in the CDC as a function of the particle momentum per charge is presented. All recognized particles are marked in the figure. The CDC mass spectrum extracted with the Bethe-Bloch formula is given in Fig. 3.9. Negative and positive pion, proton and deuteron are recognized particles indicated in the plot. It is shown that in this experiment heavier particles like deuterons are observed and distinguished from protons. A clear separation of particle masses is the result of good calibration quality of the detector.

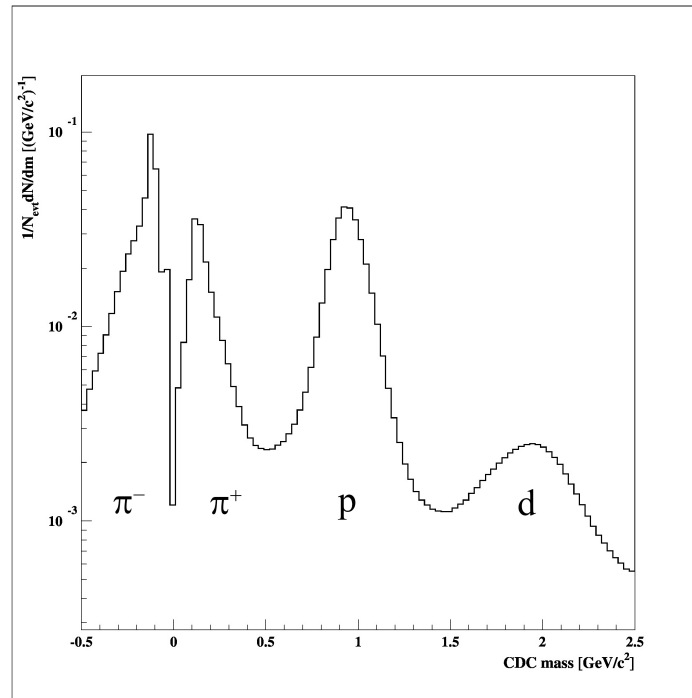


Figure 3.9: Mass spectrum of the particles detected inside the CDC of the FOPI detector. Data is taken from the reactions of the negative pion beam with the carbon target in the S273 FOPI experiment.

The mass distribution shown in Fig. 3.9 is used to select pions and protons. To select negative pions a mass window of  $[0.05, 0.5] \text{ GeV}/c^2$  is used and for proton a mass window of  $[0.5, 1.3] \text{ GeV}/c^2$  is used.

Since the event vertex is determined, the distance between its position and each track is calculated in the transverse and longitudinal direction and the cuts applied on those parameters are presented in Table 3.2.

Table 3.2: Selection cuts for  $\Lambda$  particle and its decay products

particle	quantity [unit]	meaning	cut
$\pi^-$	$ d_0 $ [cm]	distance to vertex in $xy$	$1.2 < \dots < 9.5$
	$m$ [GeV/c <sup>2</sup> ]	particle mass	$0.05 < \dots < 0.50$
	$p_t$ [GeV/c]	transverse momentum	$> 0.08$
	$ z_0 $ [cm]	distance to vertex in $rz$	$< 20$
	$N_{hit}$	number of hits per track	$> 24$
<i>proton</i>	$ d_0 $ [cm]	distance to vertex in $xy$	$0.8 < \dots < 5.5$
	$m$ [GeV/c <sup>2</sup> ]	particle mass	$0.5 < \dots < 1.3$
	$p_t$ [GeV/c]	transverse momentum	$> 0.1$
	$ z_0 $ [cm]	distance to vertex in $rz$	$< 20$
	$N_{hit}$	number of hits per track	$> 24$
$\Lambda$	$ d_0 $ [cm]	distance to vertex in $xy$	$< 5$
	$m$ [GeV/c <sup>2</sup> ]	particle mass	$1.00 < \dots < 1.25$
	$p_t$ [GeV/c]	transverse momentum	$> 0.18$
	$r_t$ [cm]	transverse flight path	$1 < \dots < 10$
	$ \Delta\Phi  [^\circ]$	pointing angle	$< 15$

The hit multiplicity ( $N_{hit}$ ) is the number of hits in a track. A minimum track multiplicity required in this analysis is set to 24 and it is applied to reject "broken" or short tracks and to choose the right ones.

In a schematic view of Fig. 3.7, all quantities important for the particle selection and reconstruction are indicated. Cuts for these quantities, together with other important analysis cuts, are summarized in Table 3.2 for  $\Lambda$  and its decay particles ( $\pi^-$  and *proton*) and in Table 3.3 for  $K_S^0$  and product particles of its decay ( $\pi^-$  and  $\pi^+$ ). The cuts used in the main analysis are displayed for: transverse and longitudinal distance to the primary vertex ( $d_0$  and  $z_0$ ), particle mass ( $m$ ) and transverse momentum ( $p_t$ ), hit multiplicity ( $N_{hit}$ ), transverse flight path of a strange particle ( $r_t$ ) and pointing angle ( $\Delta\Phi$ ).

Table 3.3: Selection cuts for  $K_S^0$  particle and its decay products

particle	quantity [unit]	meaning	cut
$\pi^-$	$ d_0 $ [cm]	distance to vertex in $xy$	$1.1 < \dots < 16.5$
	$m$ [GeV/c <sup>2</sup> ]	particle mass	$0.05 < \dots < 0.45$
	$p_t$ [GeV/c]	transverse momentum	$> 0.08$
	$ z_0 $ [cm]	distance to vertex in $rz$	$< 45$
	$N_{hit}$	number of hits per track	$> 24$
$\pi^+$	$ d_0 $ [cm]	distance to vertex in $xy$	$1.1 < \dots < 16.5$
	$m$ [GeV/c <sup>2</sup> ]	particle mass	$0.05 < \dots < 0.45$
	$p_t$ [GeV/c]	transverse momentum	$> 0.08$
	$ z_0 $ [cm]	distance to vertex in $rz$	$< 45$
	$N_{hit}$	number of hits per track	$> 24$
$K_S^0$	$ d_0 $ [cm]	distance to vertex in $xy$	$< 2.2$
	$m$ [GeV/c <sup>2</sup> ]	particle mass	$0.4 < \dots < 0.7$
	$p_t$ [GeV/c]	transverse momentum	$> 0.05$
	$r_t$ [cm]	transverse flight path	$1 < \dots < 17$
	$ \Delta\Phi $ [°]	pointing angle	$< 30$

### 3.3.3 Reconstruction Methods for $V^0$ Particles

A first step in the reconstruction of strange particles with a candidate pair of daughter particles ( $\pi^-$  and  $p$  of  $\Lambda$  or  $\pi^-$  and  $\pi^+$  of  $K^0$ ), is to evaluate the intersection point of the two daughter particle tracks. If the two tracks are found to intersect, quantities that specify a certain strange particle, such as its invariant mass or total momentum, can be calculated from daughter particle 4-momenta.

The procedure for reconstruction of a secondary vertex is explained in the lines below and illustrated in Fig. 3.10.

In the  $xy$  plane the tracks of two particles are given by the centres  $C_1$  and  $C_2$  and the radii  $r_1$  and  $r_2$  of the circular tracks. The distance between two circle centres is denoted as  $d_{21}$ . If  $d_{21} > r_1 + r_2$ , the two tracks do not intersect and the pair of tracks is excluded from the further analysis. If  $d_{21} \leq r_1 + r_2$ , there is at least one intersection point. Only the case of two intersection points is relevant for the further analysis. In those cases the intersection points are parametrized with the angle  $\alpha$  and the coordinates of the intersection points in the transverse plane are calculated.

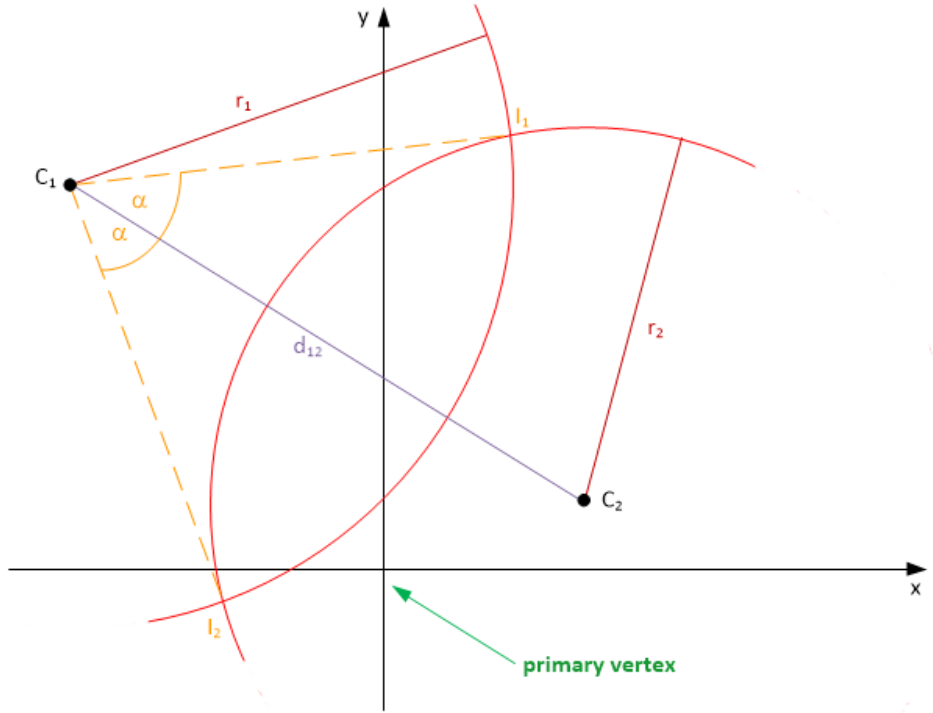


Figure 3.10: Secondary vertex determination for  $V^0$  particle

The next thing to do is to determine the quantities and properties of strange particle candidates and their associated cuts, which should be done for each intersection point. The reconstruction of the  $V^0$  particle is presented in Fig. 3.11. The procedure in the  $xy$  plane (left), as well as in the  $rz$  plane (right), is illustrated. To calculate the transverse distance from the secondary to the primary vertex  $r_t$  the determined coordinates of the secondary vertex  $(x_s, y_s)$  are used. A lower and upper limits are applied on  $r_t$ . In that way, the background coming from primary particles is reduced and secondary vertices far away from the primary vertex are also discarded. At this step of analysis the longitudinal positions of the two tracks  $(z_1, z_2)$  relative to the secondary vertex are calculated too. Track pairs with a large distance in the  $z$  direction are eliminated by applying a cut on  $\Delta z$  quantity.

The azimuthal angle  $\varphi_t$  is also determined and is used, together with the track curvature and the polar angle, to calculate the 4-momenta of the decay particles at the secondary vertex position. Finally, the total and transverse momentum of the  $V^0$  particle are derived and from that information other quantities describing the neutral strange particle, such as: the azimuthal and polar angles ( $\varphi_{V^0}$  and  $\vartheta_{V^0}$ ), the pointing angle ( $\Delta\phi$ ) and the shortest distances to the primary vertex ( $d_0$  and  $z_0$ ) are derived.

Finally, the invariant mass  $M_{inv}$  of the neutral strange particle is calculated using the relation:

$$M_{inv} = \sqrt{(E_1 + E_2)^2 - (\vec{p}_1 + \vec{p}_2)^2} = \sqrt{E^2 - \vec{p}^2}. \quad (3.4)$$

$E_1$  and  $E_2$  are the energies of the first and the second decay particle,  $\vec{p}_1$  and  $\vec{p}_2$  are the mo-



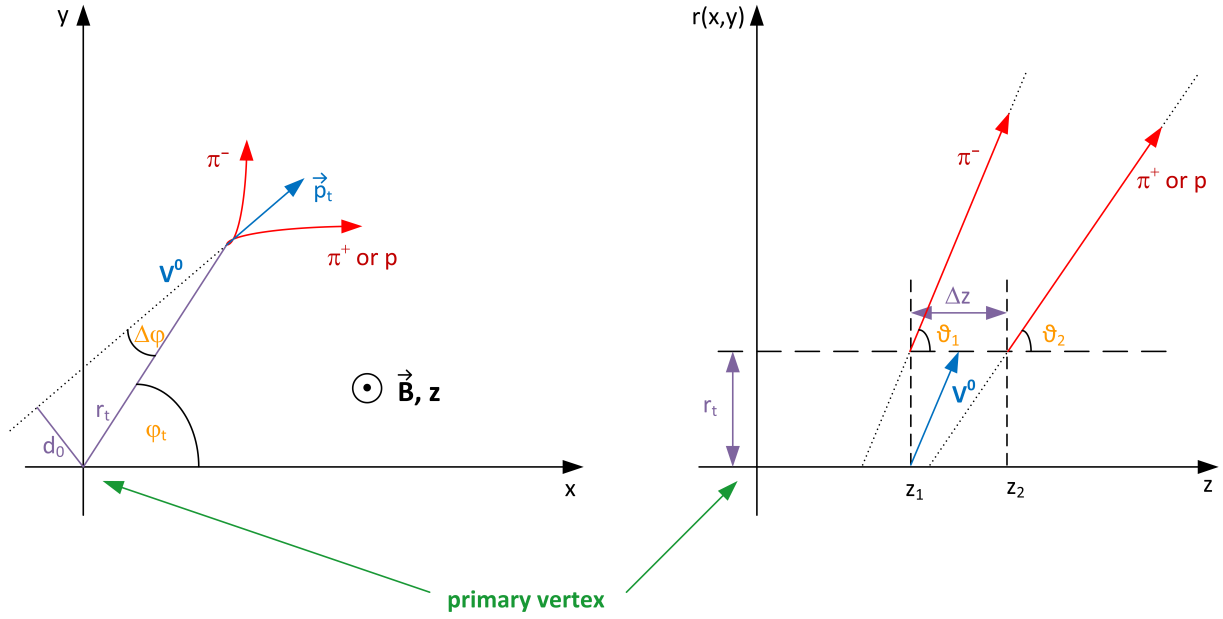


Figure 3.11: Illustration of the reconstruction of  $V^0$  particle in  $xy$  and  $rz$  plane. Quantities used for the particle selection and reconstruction are indicated in the plots. The reconstruction procedure is explained in the text.

menta of corresponding decay particles and  $E$  and  $\vec{p}$  are the total energy and the momentum respectively.

Table 3.4: Additional selection cuts used for the reconstruction of  $\Lambda$  and  $K_S^0$ .

cut	particle	
	$\Lambda$	$K_S^0$
$r_t$ [cm]	$1.0 < \dots < 10.0$	$1.5 < \dots < 17.0$
$ \Delta z $ [cm]	$< 40$	$< 35$
$ \Delta\phi $ [°]	$< 20$	$< 30$
$ d_0 $ [cm]	$< 5.0$	$< 2.2$
$ z_0 $ [cm]	$< 100$	$< 100$
$M_{inv}$ [GeV/c <sup>2</sup> ]	$1.00 < \dots < 1.25$	$0.40 < \dots < 0.70$

The following cuts are applied to select "good"  $\Lambda/K^0$  candidates:

- an upper threshold for  $|\Delta\phi| = |\varphi_{V^0} - \varphi_t|$  to reject particles that are not pointing to the primary vertex,
- an upper cut for  $|d_0|$  ( $|z_0|$ ) to be sure that the strange particle is originating from the primary vertex and

- lower and upper cut for  $M_{inv}$  to choose the right candidate of  $V^0$  particle.

These additional cuts for  $\Lambda$  and  $K_S^0$  particles are presented inside Table 3.4.

Some important kinematic variables, derived from the quantities mentioned above, and their mutual relations are explained in Appendix B.

### 3.3.4 Determination of the Combinatorial Background

As it was already mentioned, to find a strange particle of interest the reconstructing procedure is applied to all pairs of identified decay particles in an event. Among the selected particles there are those which are not correlated, i.e. there are pairs of particle tracks in which one or both particles don't come from a strange particle decay. Such track pairs, which nevertheless pass the selection for "good" events, contribute to the invariant mass spectrum and form the so-called *combinatorial background*.

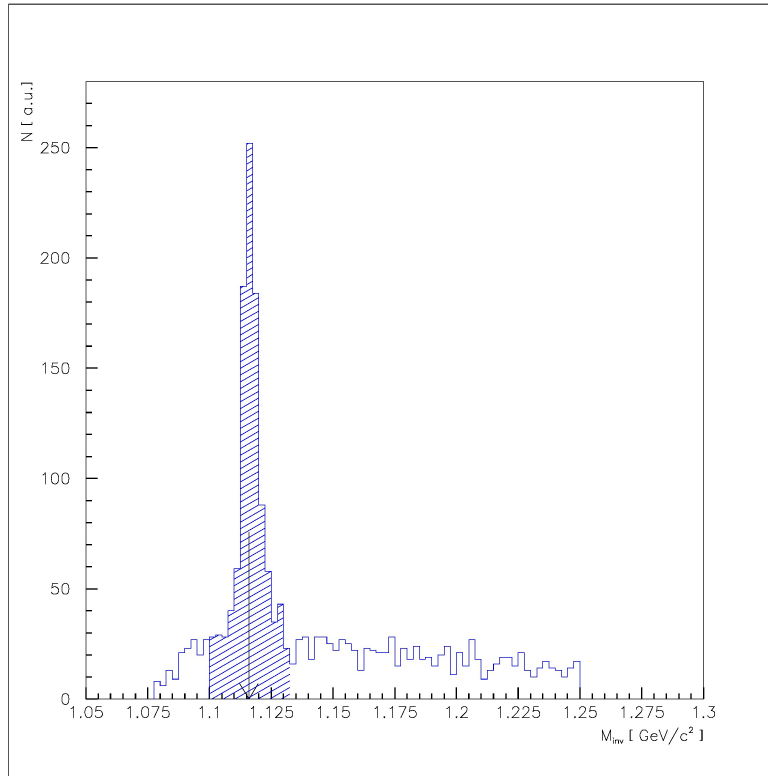


Figure 3.12: An example of the  $\Lambda$  invariant mass spectrum,  $\Lambda \rightarrow \pi^- + p$ , for the  $\pi^- + C$  reactions at  $\sqrt{s} = 1.75$  GeV of the S273 FOPI experiment. The arrow at the plot is pointing to the nominal  $\Lambda$  mass.

As an example Fig. 3.12 shows the invariant mass spectrum of  $\Lambda$  particle reconstructed from the reactions with carbon target in the S273 experiment. The peak around a nominal  $\Lambda$

mass ( $1.116 \text{ GeV}/c^2$ ) can be clearly seen. The part of the spectrum indicated as filled area is afterwards fitted with a Gaussian-type function to calculate the number of  $\Lambda$  particles under the peak after the whole procedure described below is done.

The sum of entries in a mass range of  $\pm 2\sigma$  ( $\sigma$  stands for mass width) after subtracting the *background* represents the evaluated number of  $\Lambda$  particles, i.e. the *signal*. The quality of the evaluated signal is described with *signal over background ratio* ( $S/B$ ) and *significance* defined with:

$$sign \equiv \frac{S}{\sqrt{S+B}}, \quad (3.5)$$

$S$  stands for signal counts and  $B$  for background counts. The significance value larger than 3 is required for a clear signal [96]. The same example of the invariant mass spectrum for  $\Lambda$  particle, but with determined signal, significance and signal-to-background ratio, is presented in Fig. 3.13.

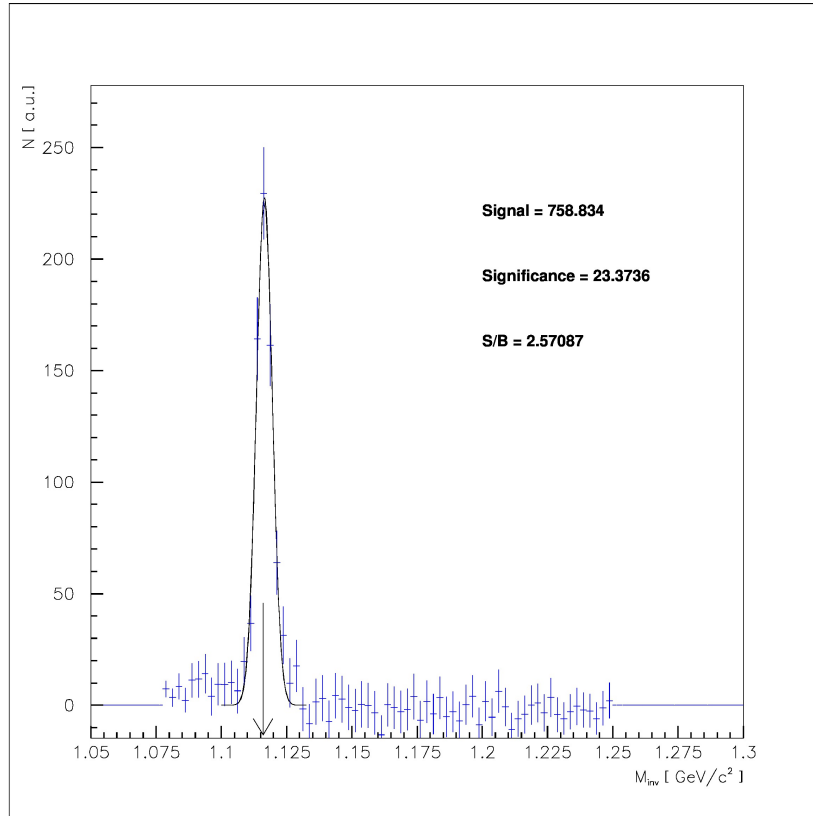


Figure 3.13: An example of the  $\Lambda$  invariant mass spectrum,  $\Lambda \rightarrow \pi^- + p$ , for the  $\pi^- + C$  reactions at  $\sqrt{s} = 1.75 \text{ GeV}$ , with calculated signal, significance and signal-to-background ratio. The measured spectrum is fitted with a Gaussian-like function. The arrow on the plot is pointing to the nominal  $\Lambda$  mass.

A combinatorial invariant mass spectrum for the  $\Lambda$  particle, obtained from the carbon data of the S273 FOPI experiment, is shown in the left panel of Fig. 3.14. A continuous combi-

natorial background is observed below the peak from about  $1.078 \text{ GeV}/c^2$ , which is the sum value of pion and proton mass. Hatched area indicated in the plot is used for the calculation of normalization (scale) factor in the further background evaluation procedure. There are two ways to describe and subtract the combinatorial background, it is possible to fit it with a polynomial or exponential function (depending on the shape of the background) or the event-mixing method [96, 97] can be used. The first way is applicable only if a very good signal over background ratio exists, but sometimes the situation is more complicated and more complex procedure is needed. Hence, in this inquiry the event-mixing method is applied and it will be described in the next lines.

Decay particles coming from two different events are combined (as they were coming from the same event) and the equivalent reconstruction procedure is applied. For example, one  $\pi^-$  coming from one event is combined with  $n$  protons (or  $\pi^+$ ) from different events and new invariant mass spectrum is produced. It is required that these two combined events have similar properties in order to discard only desired correlations. In this analysis it is also requested that at least one valid particle candidate of each daughter particle exists in the event. As two potential daughter particles are not correlated with strange particle decay, the associated invariant mass spectrum is not showing the strange particle mass peak as it can be seen in the right panel of Fig 3.14 (the mixed-events spectrum).

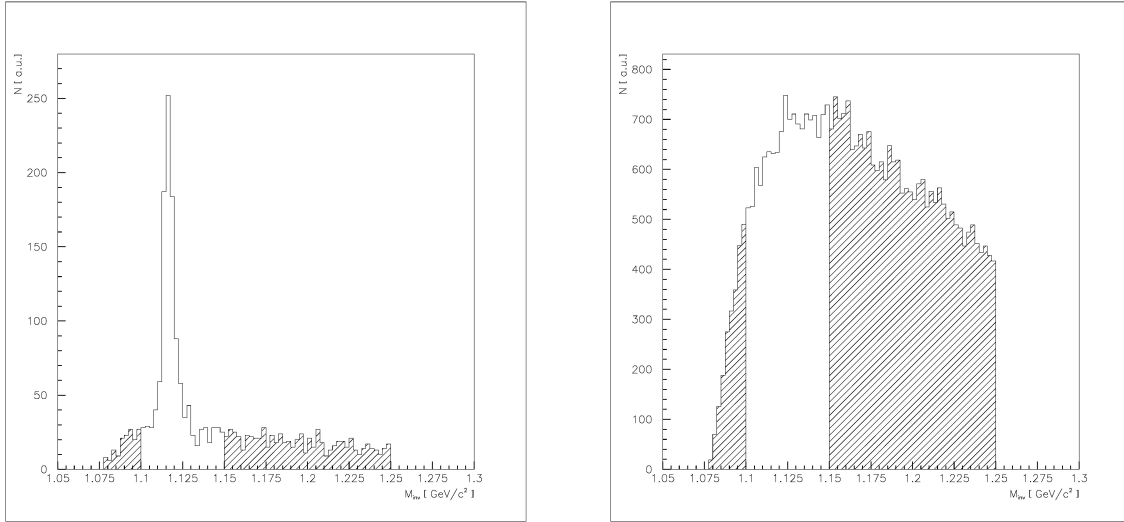


Figure 3.14: Background evaluation procedure for  $\Lambda$  particle ( $\Lambda \rightarrow \pi^- + p$ ). Left panel shows the combinatorial background and right panel shows the mixed-events background.

After the mixed-events mass spectrum is determined, both, the measured invariant mass spectrum and mixed-events spectrum are integrated over a mass range which is well outside of the signal region. In this example case two regions to the left and the right of the signal are

selected (hatched areas in Fig. 3.14). Then a scaling factor, used for the mixed-events spectrum normalization, is calculated from the ratio between the two integrals. That step of the procedure is depicted in the upper panel of Fig. 3.15. The blue histogram represents the measured spectrum and the red histogram represents the normalized mixed-events spectrum. The hatched area in this figure shows the range in which the signal is evaluated.

At the end, the normalized mixed-events spectrum is subtracted from the measured invariant mass spectrum and final number of  $\Lambda$  particles is calculated.

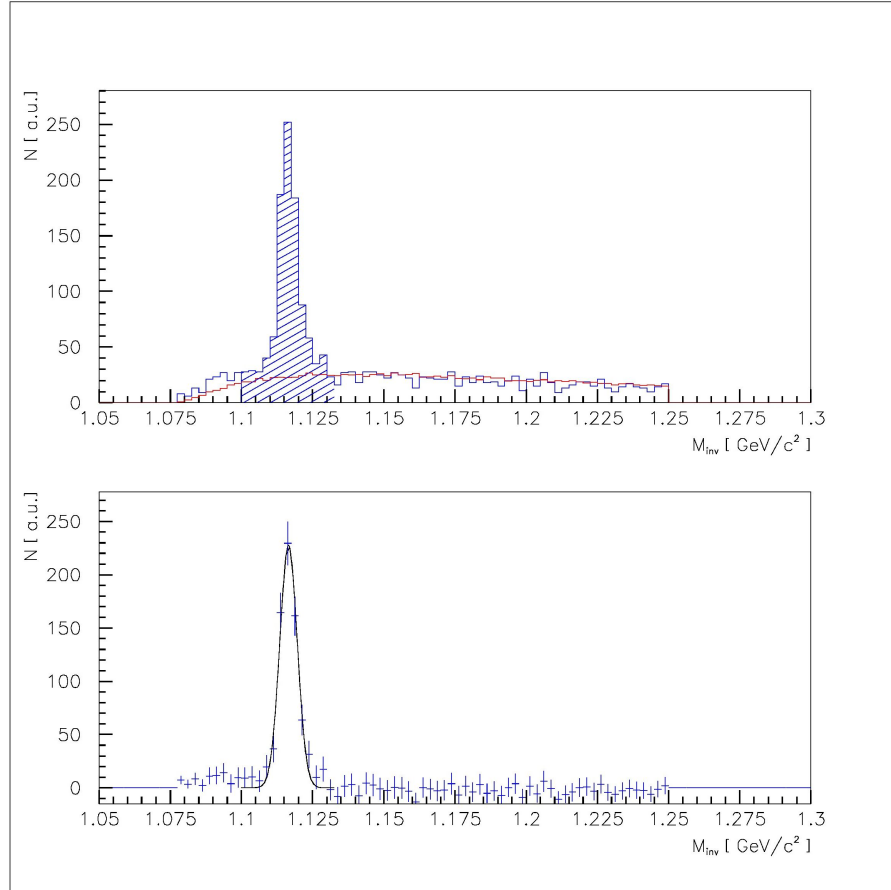


Figure 3.15: Background subtraction procedure for  $\Lambda$  particle. Upper panel represents combinatorial and scaled mixed-events background. Corrected  $\Lambda$  invariant mass spectrum after subtraction is shown in the lower panel. Both plots are obtained for  $\Lambda \rightarrow \pi^- + p$  channel, observed within the  $\pi^- + C$  reactions at  $\sqrt{s} = 1.75$  GeV.

The lower panel of Fig. 3.15 shows  $\Lambda$  invariant mass spectrum after subtraction of the estimated background. The example shows that the used event-mixing method provides a good estimation of the combinatorial background in the measured spectrum.

The other quantities describing  $\Lambda$  or  $K_S^0$  can be derived in a similar way.

What is very important for the applicability of this method is to choose an appropriate set of constraints for the selection of the involved particles. In that way the background can be

well estimated with the mixing-events method and the difference between the original data and mixed-events distribution does only originate from the resonance. Different sets of cuts can however give slightly different results. So it is important to consider the influence of the cuts on any derived results. This will be further discussed in Chapter 5.



# Chapter 4

## Physics Simulations and Efficiency Correction

In general, the detector and the reconstruction procedure are not ideal, which is why the number of reconstructed particles has to be efficiency corrected to obtain the true number of lambdas or neutral kaons contained in the data set. To determine the efficiency correction factor, numerical simulations of the experiment are used. The majority of the corrections come out from the geometrical acceptance of the FOPI detector, but also other issues of possible detector inefficiencies must be considered. In order to extract valid results from experimental data all quantities should be adjusted regarding acceptance and efficiency impacts. For a detector like FOPI, which is composed of several subdetectors, extensive simulation, including all relevant physical processes and effects, is needed. For this purpose, the GEANT 3.21 simulation package from CERN is used.

For the main part of this work only the CDC subdetector has been used. For the implementation of the simulations it is therefore important to understand all the details and characteristics of particle detection in the CDC.

Pion-induced (and proton-induced) reactions are essential reactions for testing transport models. On the other hand, reliable models are required as an input for simulations for the further analysis and efficiency estimation. For that purpose the results obtained by using the GiBUU (Giessen Boltzmann–Uehling–Uhlenbeck) hadron transport model are considered within this study.

All the introduced issues of the simulation of the detector and transport models are explained in detail in the next sections. After that, the comparison of the distributions of certain cut quantities needed for the particle selection and reconstruction obtained from the experimental and simulation data are discussed. And finally, methods and results for the reconstruction efficiency evaluation and corrections are presented.



## 4.1 GEANT Simulation

The GEANT simulation package is a detector description and simulation tool that helps in designing and optimizing detector facilities, improving analysis programs and understanding and explaining the experimental data [98]. The first version of GEANT was written in 1974 and specific FOPI detector properties were implemented in 1997 when the upgrade of the detector was made.

After the simulation of the whole FOPI detector system with the appropriate target (the geometry, volumes and materials implementation), particles are propagated through the experimental setup and in that way it is possible to determine the detector response effect. While propagating the particles through the detector, kinematic and dynamic variables and all vertices of particles are saved in data base structure called the KINE bank. The output data of the simulation has the equivalent format as the data measured in the experiment, so the same analysis software can be used in the final phase.

The GEANT program arrangement accepts events obtained by Monte Carlo generators which are shortly discussed in this chapter. The main GEANT tools are introduced and described. The application of the GEANT for efficiency estimations and comparison with experimental data analysis results for the S273 experiment are presented.

Within this work the GEANT 3.21 version from CERN has been used.

### 4.1.1 Event Generation

Event generation is the first step of the simulation process. It provides the 4-momentum vectors of generated particles. There are several event generators applicable in this (heavy-ion, hadronic) branch of physics at the SIS energy range.

The main purpose of an event generator is to provide the correct distributions and kinematic properties of all particles produced in a observed reaction. This is used for many purposes such as the prediction of possible types and rates of certain events that can be found in an investigated reaction, estimating detector acceptance corrections, helping in designing, constructing and upgrading detectors for optimal performance and also helping in developing analysis methods and implementations for the treatment of a real data.

The output of an event generator are events with almost the same average characteristics and behaviour as experimental data events. Usually it is written as a sequence of particles observed in a final state and associated quantities as their charge, mass, momentum and energy. That list represents, of course, an ideal situation which could be perceived with an ideal detector. Monte Carlo methods are used for the selection of relevant variables for requested distributions, including needful randomness to the computations.

The output of the event generator (event with corresponding produced particles) is the input for the transport phase of the simulation process. In this study the role of the transportation of particles is taken over by FLUKA (FLUktuierende KAskade) or more precisely its version

embedded in GEANT, known as GEANT3-FLUKA. FLUKA is standalone code which contains transport and physical processes for hadrons and leptons, together with tools for geometrical description [99, 100, 101]. Parts of the code, which deal with hadronic elastic and inelastic interactions, have been included into GEANT since GEANT's version 3.15 [98].

In this inquiry, as it was mentioned in the introductory part of this chapter, two approaches to physics simulation are adopted:

1. GiBUU (described in Section 4.2) is used as an event generator. The particles which are the result of GiBUU simulations are placed at a selected vertex position and the transport phase of simulation is done by FLUKA.
2. The initial particle (pion) is defined with its momentum in  $z$  direction. A starting point in front of the target is selected according to the beam spot diameter. After that, the transportation part of the simulation process is done by FLUKA. In addition,  $\Lambda$  particles, specified with their transverse momenta and rapidities, can be embedded in the simulation events in order to increase the statistics for the reconstruction efficiency evaluation. For the same reason, the branching ratio for the decay channel of interest (explained in Section 3.3) is set to 100 %.

In the further text, the first approach will be denoted as TYPE1 and the second one as TYPE2. If additionally lambdas are inserted in the simulation of TYPE2, this will be indicated by TYPE2 $\Lambda$ .

## 4.1.2 Simulation of the Detector

The GEANT simulation tools enable to build a three dimensional model of the detector including all subdetectors and the magnet, with usage of different materials actually existing in the experimental setup, as it has been shown in Fig. 2.2. In the simulation, particles are propagated through the detector and undergo all corresponding interactions, scatterings and decays, so at the end the output should be equivalent to the one produced in the experiment, and analysed with the same program as experimental data. For the complex detector system, the response of all subcomponents to the particles traversing should be modelled.

Some basic terms important for understanding and dealing with GEANT simulation, which will be used further in the text, are:

- **run** - the largest unit of simulation which consists of a sequence of events (within one run all detector properties and the physics processes should be unchanged),
- **event** - element of the run which gives the information about primary vertex, primary particles and their trajectories, the collection of hits generated by sensitive detectors as well as the collection of the digits generated by digitizer modules,

- **hit** - snapshot of the physical interaction of a track in the sensitive region of detector (user-defined information recorded at tracking time to keep track of interaction between one particle and a given detector, necessary to compute digitisations later),
- **tracking** - following the propagation of particles,
- **detector response** - the physical signal in the sensitive detector element (got from the relation between incident energy and pulse height),
- **digitisation (digit)** - user-defined information simulating the response of a given detector element, usually estimated after tracking a complete event,
- **gain** - adjustable factor that the detector (CDC) electric drift field is replaced with.

As it was mentioned in the introductory part of this chapter, in this work only the CDC subdetector results were included in the analysis of the simulated data and its comparison with experimental measurements. The complete detector definition requires the geometrical representation of detector elements (solid parts, their spatial positions and their logical relations one to another), their materials and electronics properties, together with visualization attributes and user defined properties [102]. So, the main tasks for a user are to specify materials, to specify particles and their range threshold and finally to assign physics properties which define the interaction of particles and materials.

## The CDC Digitizer

The main function of the CDC digitizer is to model detector response and propagation of the energy deposited by a hit inside the gas of the detector through the front-end electronic. The result is a digitized information written into files of similar format as experimental data files.

While tracking particles through matter the number of steps per track is calculated by GEANT automatically. The magnetic field has to be included for tracking particles inside the active volume of the CDC. Calculation of hits per tracks is done including all relevant physical processes inside the active volume of the CDC. After hits are identified, the equivalent charge is assigned for each hit. In addition, the deposited energy is recorded within each step. The deposited energy (the energy loss) per hit in each drift cell (i.e. for each sense wire) is then multiplied by the gain factor which has to be modelled in a way that properly simulates the effect obtained with the potential wire voltage in the gas volume of the CDC (explained in Chapter 2, see Eq. (2.4)). The procedure of the simulation of electrons transport inside a gas in electric field gets more complicated if the field is inhomogeneous, as it is case in the CDC of the FOPI detector [1].

The procedure of charges digitizing (done using FADC 100 MHz clock) is shortly described in the next lines. The drift time of each hit is derived from drift velocity information (obtained from electric drift field and gas properties of the CDC) and the distance of each hit to the closest

drift cell in the  $xy$  plane. The drift cell is a sense wire surrounded by two potential wires at a distance of 0.5 cm each. Then the fraction of charge on the left and on the right side (to the total charge) is determined and written as a fraction of charges:

$$R_{L,R} = 0.5 \cdot \left( 1 \pm 2 \cdot \frac{z_{mw} - z_{hit}}{l_{eff}} \right) \equiv \frac{Q_{L,R}}{Q_L + Q_R}, \quad (4.1)$$

$R_{L,R}$  is the charge fraction left or right (to the total charge),  $z_{mw}$  represents the middle of the wire and  $l_{eff}$  is the effective length of the wire. The Gaussian-like signal is given by:

$$S_{L,R} = E \cdot R_{L,R} \left( \frac{1}{\sqrt{2\pi}\sigma} \cdot \exp \left( \frac{1}{2} \cdot \left( \frac{t_d - t_m}{\sigma} \right)^2 \right) \right), \quad (4.2)$$

$S_{L,R}$  stands for the collected signal from left or right end of the wire,  $E$  is the deposited energy per step,  $\sigma$  is the width of the drift time distribution (about 10 ns),  $t_d$  is the drift time associated with the distance between the hit position and the drift cell and  $t_m$  is the mean drift time.

To study and implement the hit resolution several preparation steps need to be done.

### Drift Path, Drift Time

The appropriate drift distance of each hit in GEANT with respect to each drift cell has to be calculated. Knowing the hit and wire positions and the Lorentz angle  $\alpha_L$  it is possible to derive the drift path and the drift time of the hit. The drift path inside the drift cell is determined as:

$$s_{drift} = D_x - L. \quad (4.3)$$

If  $(x_h, y_h)$  are coordinates of the hit position,  $(x_w, y_w)$  coordinates of the wire and  $R$  its radius,  $D_x$  and  $L$  are given by:

$$D_x = \sqrt{(x_h - x_w)^2 + (y_h - y_w)^2} \cdot \cos \alpha_L, \quad (4.4)$$

$$L = \sqrt{R^2 - D_y^2}, \quad D_y = \sqrt{(x_h - x_w)^2 + (y_h - y_w)^2} \cdot \sin \alpha_L. \quad (4.5)$$

### Energy and Spatial Resolution, Momentum Resolution

Just like the hit position at the  $z$  axis and the energy deposited by the hit are related by:

$$E = Q_L + Q_R, \quad (4.6)$$

$$z = \frac{Q_L - Q_R}{Q_L + Q_R} = \frac{Q_L - Q_R}{E}, \quad (4.7)$$

their resolutions ( $\sigma_z$  and  $\sigma_{\Delta E}$ ) are correlated as well. The dependence is given in the expression:

$$\frac{\sigma_z}{z} = \frac{2 \cdot Q_L}{|Q_L - Q_R|} \cdot \frac{\sigma_{\Delta E}}{E} . \quad (4.8)$$

The resolution of the hit position in the  $xy$  plane is mainly relating to the time resolution of the electronics. With a time resolution of 10 ns and drift velocity of 4 cm/ $\mu$ s, the calculated  $(x, y)$  resolution ( $\sigma_{xy}$ ) is 400  $\mu$ m.

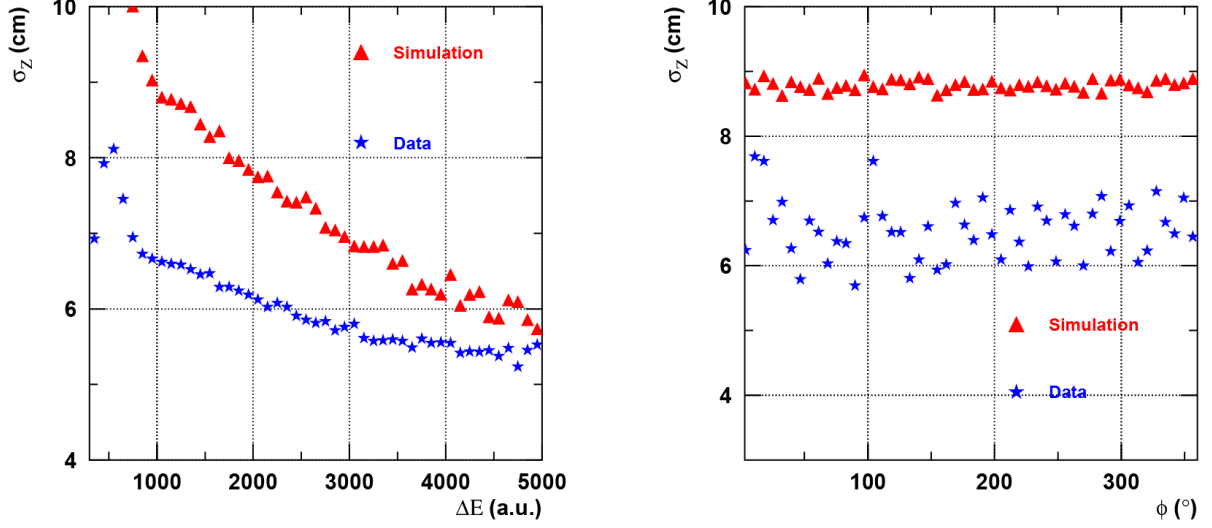


Figure 4.1: Comparison of the spatial  $z$  resolution between experimental and GEANT simulation data as function of deposited energy (left) and azimuthal angle (right). The figure is taken from [1].

The investigation of the energy and spatial resolution for the S273 FOPI experiment was done in [1] and that study shows the discrepancy between experimental and GEANT data. The energy resolution of the experimental data is worse by a factor 2 and for the position in the  $z$  direction the resolution is worse by 20 – 25 % for GEANT data. It is explained that the possible reasons for not so good matching is that the energy loss distributions (or  $z$  since they are correlated) in a drift cell is not modelled properly in GEANT. The comparison of the spatial resolution for the  $z$  direction is presented in Fig. 4.1. Two approaches were used,  $\sigma_z$  as function of deposited energy  $\Delta E$  and as function of azimuthal angle  $\phi$ . In both plots, blue stars indicate experimental data and red triangles simulation results. It is notable that the trends are mainly similar, but on both plots showing a "gap" between experimental and simulation results.

The resolution for the  $(x, y)$  position obtained with GEANT is in a good accordance with one got from experimental data, it is about 400  $\mu$ m as expected and it is constant over all CDC sectors. Figure 4.2 shows comparisons of the  $\sigma_{xy}$  between the measured and simulated data in dependence of deposited energy  $\Delta E$  and azimuthal angle  $\phi$ . As in the previous figure, blue stars indicate the results obtained from experimental data and red triangles the simulation results.

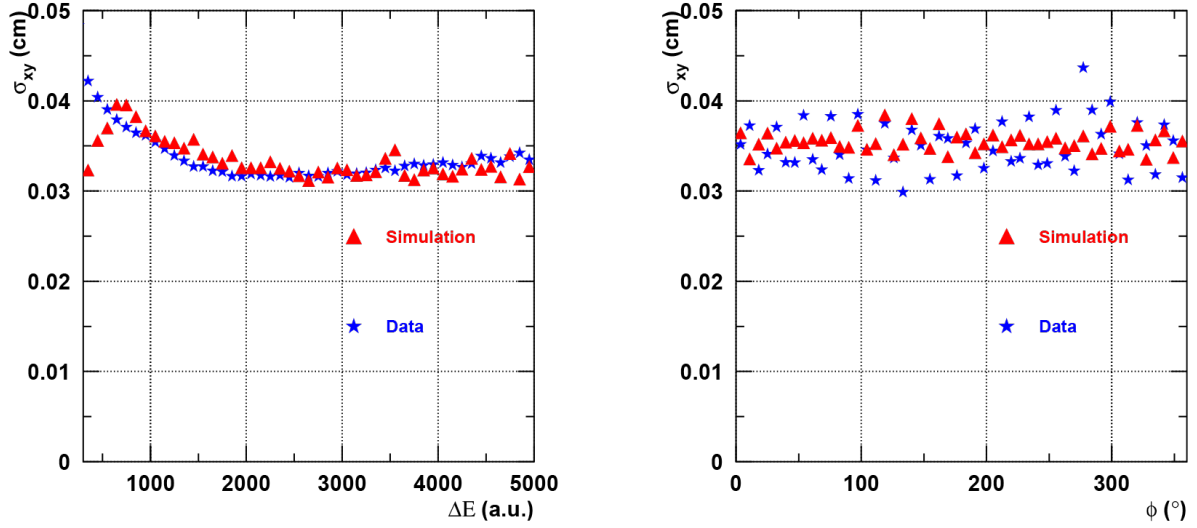


Figure 4.2: Comparison of the spatial  $xy$  resolution between experimental and GEANT simulation data as function of deposited energy (left) and azimuthal angle (right). [1]

The expression for the transverse momentum derived from the CDC information is given in Chapter 3 (see Eq. (3.3)). The momentum resolution is influenced by multiple scattering and track resolution in space, so it should be determined as the sum of these two contributions. It has been shown that below the transverse momenta of 0.2 GeV/c the resolution is governed by the multiple scattering and for the transverse momenta above 0.2 GeV/c it is governed by the position resolution in the  $xy$  plane. Transverse momentum resolution as a function of transverse momentum is shown in Fig. 4.3.

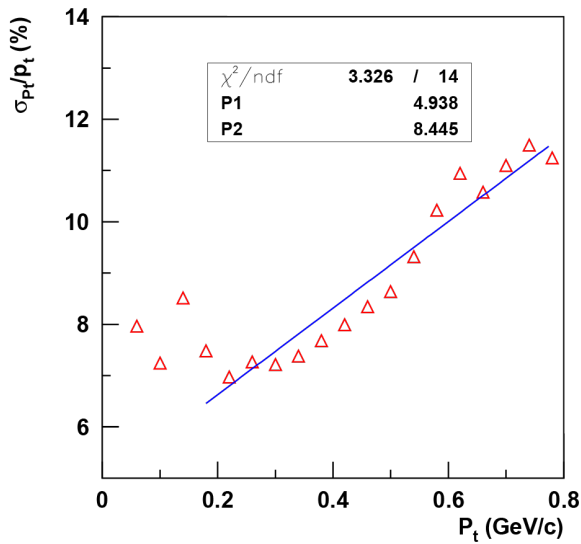


Figure 4.3: Transverse momentum resolution of GEANT simulation data as function of transverse momentum. The blue line represents the fit in the transverse momentum range above 0.2 GeV/c. The plot is a result of the investigation presented in [1].

Once the spatial, energy and momentum resolutions are fixed in GEANT, one can proceed with simulation data analysis.

## 4.2 GiBUU Transport Model

The main motivation to use a transport model calculation, as a part of this study, has been the reconstruction efficiency evaluation of investigated strange particles produced inside elementary pion-induced reactions.

A common attribute of all transport models is completely microscopic approach in which the dynamical evolution of a collision system is observed in small time intervals. Determining the way system evolves scattering cross sections, particle production and different potentials are considered.

In the regime of the SIS energies BUU - Boltzmann-Uehling-Uhlenbeck (as GiBUU - Giessen BUU) and QMD - Quantum Molecular Dynamics (IQMD - Isospin QMD and UrQMD - Ultra-relativistic QMD) models are mostly used. The basis of BUU models is the BUU transport equation describing collisions under the influence of a mean field originating from the surrounding nuclear matter (see Appendix D).

As it is described in [103], the GiBUU project has been developed at the Institute for Theoretical Physics of the Justus Liebig University in Giessen, Germany. It can be applied for the simulation of the elementary reactions (like pion – nucleon interactions) and for the heavy-ion collisions in the MeV and GeV energy regimes. The flow of particles is modelled within a BUU framework. The GiBUU code has been written in Fortran 2003 and ensures the user's control over the complete evolution phase. The results obtain by the GiBUU model, besides the inspection of different physical quantities calculated from the experimental data, are expected to be important for the total efficiency determination, which is needed for the reaction cross section determination.

The GiBUU code started primarily with an application in heavy-ion reactions, taking into account the hadronic potentials effects on propagation of particles and also the equation of state of nuclear matter. While many heavy-ion applicable transport models were developed and widely applied, few attempts including transport theoretical models for inclusive or semi-inclusive reactions on nuclei with elementary projectiles existed. The first work with usage of transport theoretical methods in such a process was a study of inclusive pion-nuclear reactions in an Monte Carlo calculation [104]. Inside the BUU theory the first test on that type of reaction is done by the Giessen group for pion and  $\eta$  photoproduction off nuclei [105]. Those first inspections were done with the same code used for heavy-ion reactions.

Today the GiBUU transport model refers to a method and a simulation code for photon-, hadron-, electron-, neutrino- and heavy-ion-induced reactions on nuclei. The basis of the model is the set of semi-classical kinetic equations which give the description of the system's dynamics inside the phase space and time. The initial state of the system is built directly from the experimental conditions for heavy ion collisions and reactions of mesons and hadrons on nuclei. For the other elementary reactions on nuclei the initial state is obtained by some external models. The aim of this model is to unify theoretical transport methods in one framework in

the energy range from 10 MeV to more than 100 GeV. The main features of GiBUU transport model are: the fundamental parameters (particle properties and elementary cross sections) assume the same common values for all reactions types which allows to validate the model over an extensive spectrum of phenomena, detailed comparisons with lot of diverse experimental results provide a sense about inherent systematic uncertainties of the model and many options concerning different reaction and surrounding settings are available. [103]

The whole code is available under the public licence at [106].

## 4.3 Comparison of Simulated and Measured Distributions

It is important to verify that the simulation provides relevant results for the physical quantities of identified particles. Hence, some spectra important for the lambda particle reconstruction from measured and simulated data are compared in order to inspect the agreement between distributions from the simulation and the real experiment. Comparison of cut quantities have been done for all five targets, but the results only for two targets with the highest available statistics are discussed below.

### 4.3.1 TYPE1 Simulation

As it was already indicated in previous sections of this chapter and will be discussed later, the first idea for efficiency estimation method was the usage of a reliable transport model as an event generator. Many inspections and comparisons between the simulation results, obtained by using the transport model (GiBUU), and the experimental data results were done. Some of them are presented here.

Figure 4.4 presents the comparison of some parameter distributions between the real data and the simulation for the pion-induced reactions on the carbon target. Four precut quantities of negative pions and protons, the daughter particles of lambdas, are presented: transverse and longitudinal closest distances to the primary vertex  $d_0$  and  $z_0$ , transverse momentum  $p_t$  and  $mass$  gained from the CDC. The comparison is done without using any additional cuts. Experimental data distributions are indicated by the red and simulation results by the blue lines.

The results obtained for the same precut quantity distributions, but for lead target, are shown in Fig. 4.5.

Almost the same behaviour can be observed for the distributions of distances to primary vertex,  $d_0$  and  $z_0$ , for the results on the carbon and lead target reactions. The differences in the  $z_0$  experimental and simulation distributions originate from differences in the  $z$  resolution between experimental and simulated data. It has been shown that  $z$  resolution is worse for the simulation by 20 - 25 % compared to the experimental measurement. The  $p_t$  distribution for the first particle ( $\pi^-$ ) shows a little bit better comparison result between the experimental data and the simulation in the case of the carbon target, but still  $p_t$  distributions of both particles for both



inspected targets show discrepancies when the data and simulation results are compared. The peak for the  $p_t$  distribution is shifted to the left in the simulation results with a maximum around 0.2 GeV/c. In case of the Pb target the mass distribution for protons shows an extra peak left from the nominal proton mass and from the main peak of the distribution. That peak is easily removed with a slightly tighter mass cut. At this stage of the analysis the mass window is left wide open, as it has been explained in the previous chapter.

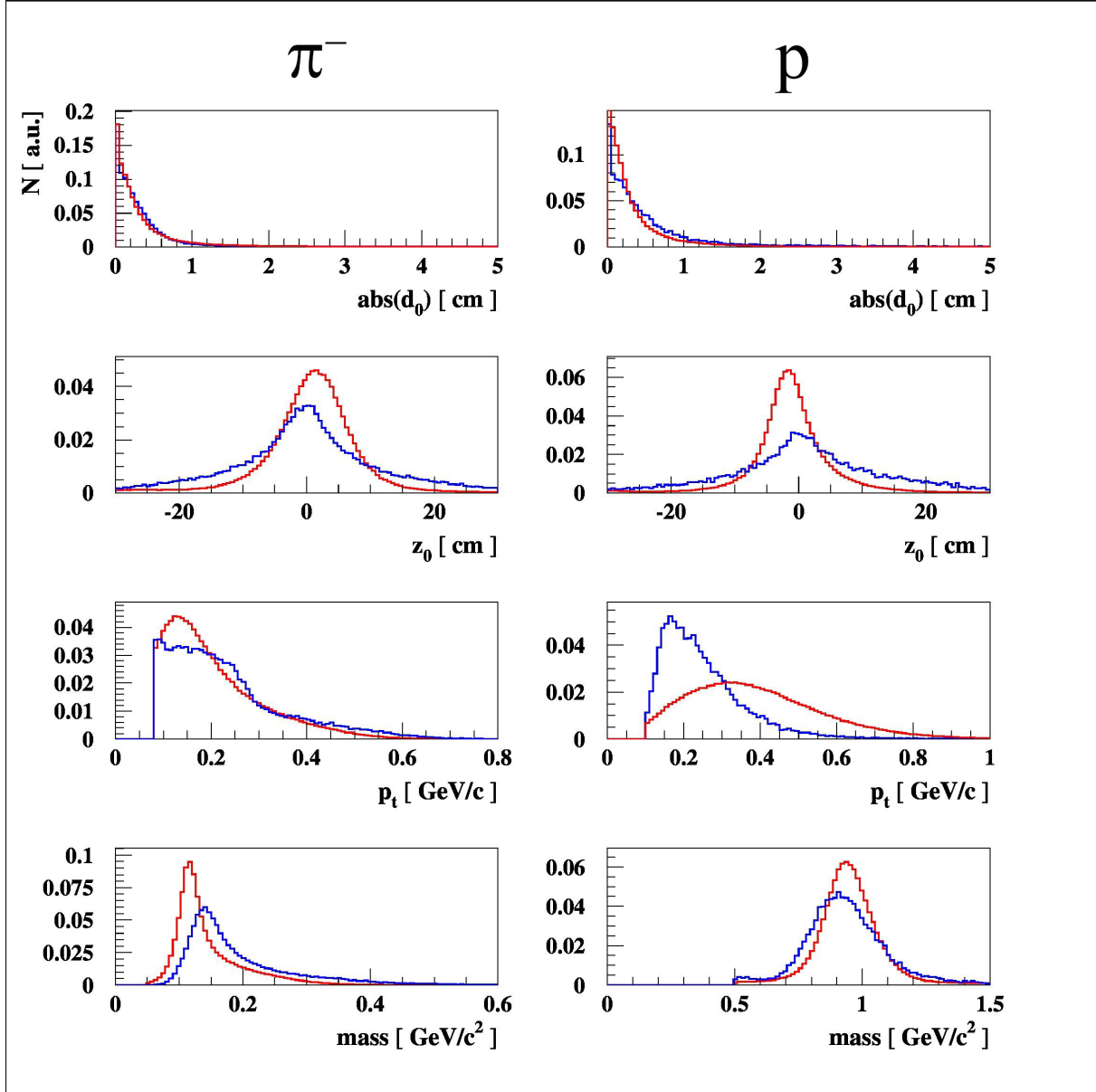


Figure 4.4: Precut distributions for  $\Lambda$  daughters compared between experimental data (red) and simulation (blue) obtained by using the GiBUU transport model for the reactions on C target. Transverse and longitudinal closest distances to the primary vertex  $d_0$  and  $z_0$ , transverse momentum  $p_t$  and  $\text{mass}$  are compared for  $\pi^-$  (left panel) and  $\text{proton}$  (right panel).

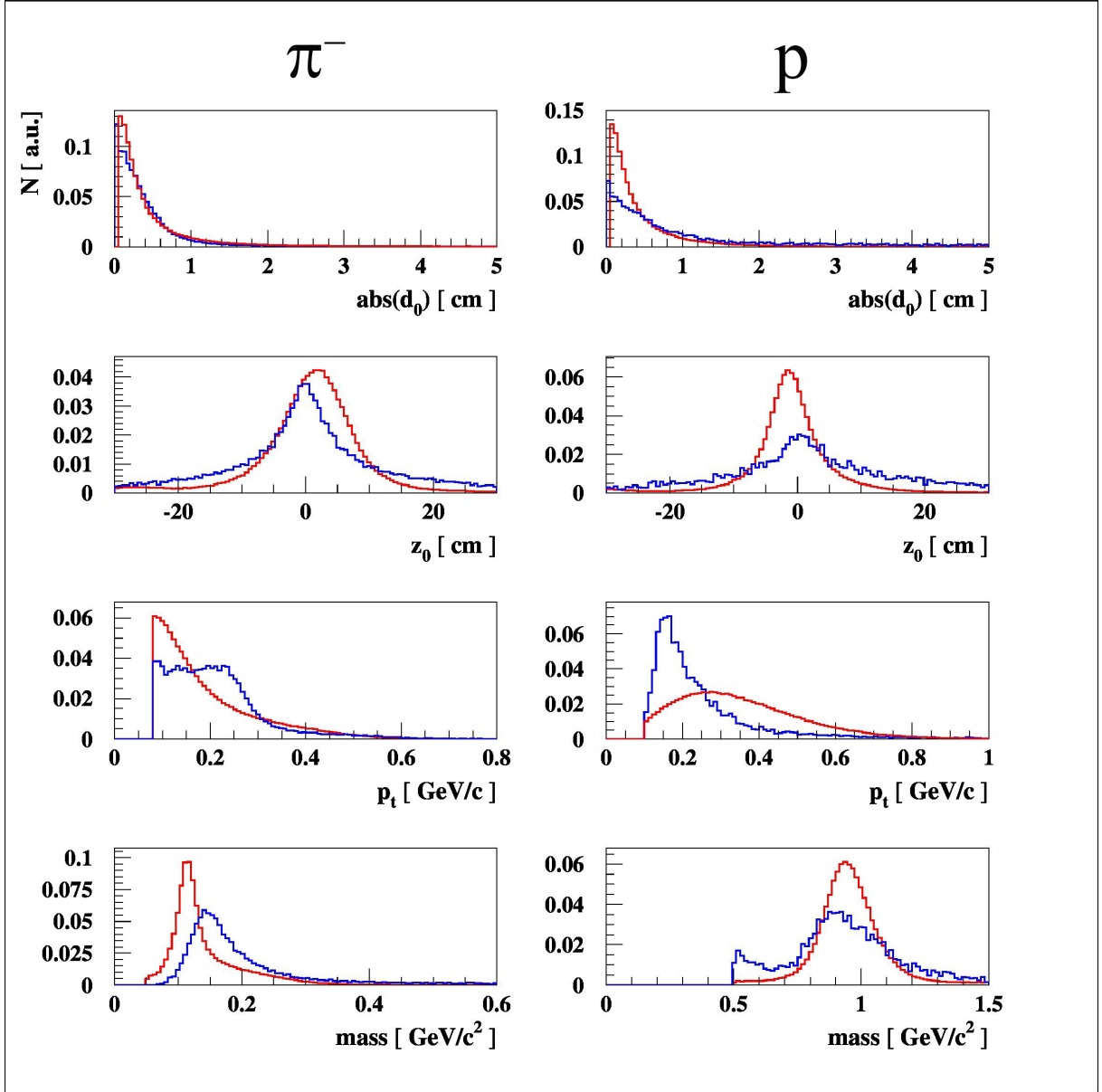


Figure 4.5: Precut distributions for  $\Lambda$  daughters compared between experimental data (red) and simulation (blue) obtained by using the GiBUU transport model for the reactions on Pb target. Transverse and longitudinal closest distances to the primary vertex  $d_0$  and  $z_0$ , transverse momentum  $p_t$  and  $mass$  are compared for  $\pi^-$  (left panel) and  $proton$  (right panel).

By using this simulation type the comparison of the basic observables characterizing lambda particle, between the data and simulation results, is provided as well, in Fig. 4.6 for the carbon and in Fig. 4.7 for the lead target reactions. The quantities displayed in the figures are the following: transverse and longitudinal closest distance to the primary vertex  $d_0$  and  $z_0$ , transverse momentum  $p_t$ , rapidity in the laboratory  $y_{lab}$ , transverse distance to the secondary vertex  $r_t$  and pointing angle  $\Delta\phi$ .

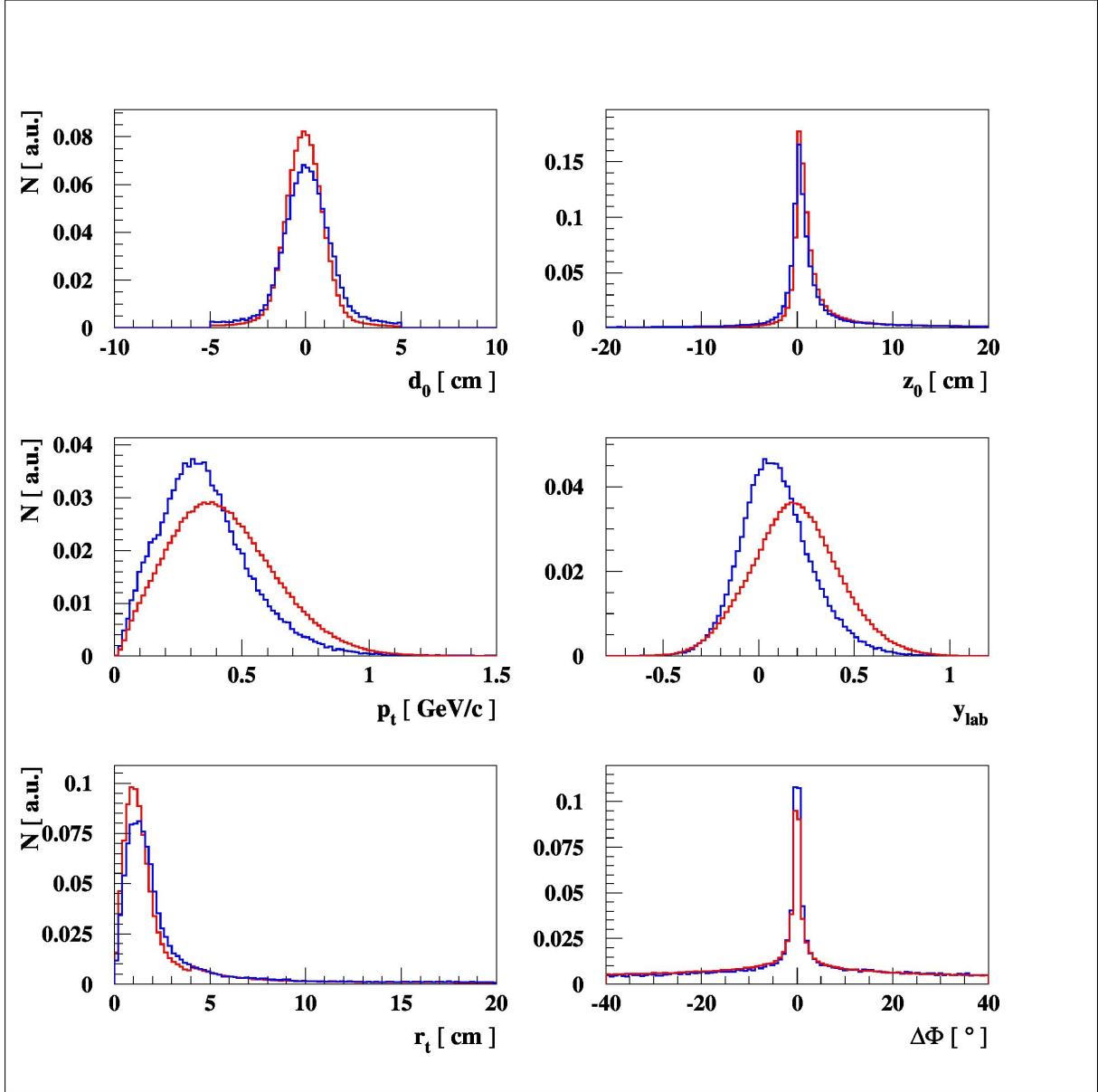


Figure 4.6: Precut distributions for  $\Lambda$  compared between the experimental data (red) and the TYPE1 simulation (blue) for the reactions on C target. The distributions of transverse and longitudinal closest distance to the primary vertex  $d_0$  and  $z_0$ , transverse momentum  $p_t$ , rapidity in the laboratory  $y_{lab}$ , transverse distance to the secondary vertex  $r_t$  and pointing angle  $\Delta\phi$  are represented in six plots in the figure.

The choice of presented variables is made according to the importance of the related cuts for the further analysis.

A reasonable agreement between experimental and simulated data is gained for all shown quantities. Some differences can be seen in the distributions of  $p_t$  and  $y_{lab}$ , especially for the results obtained for lead target.

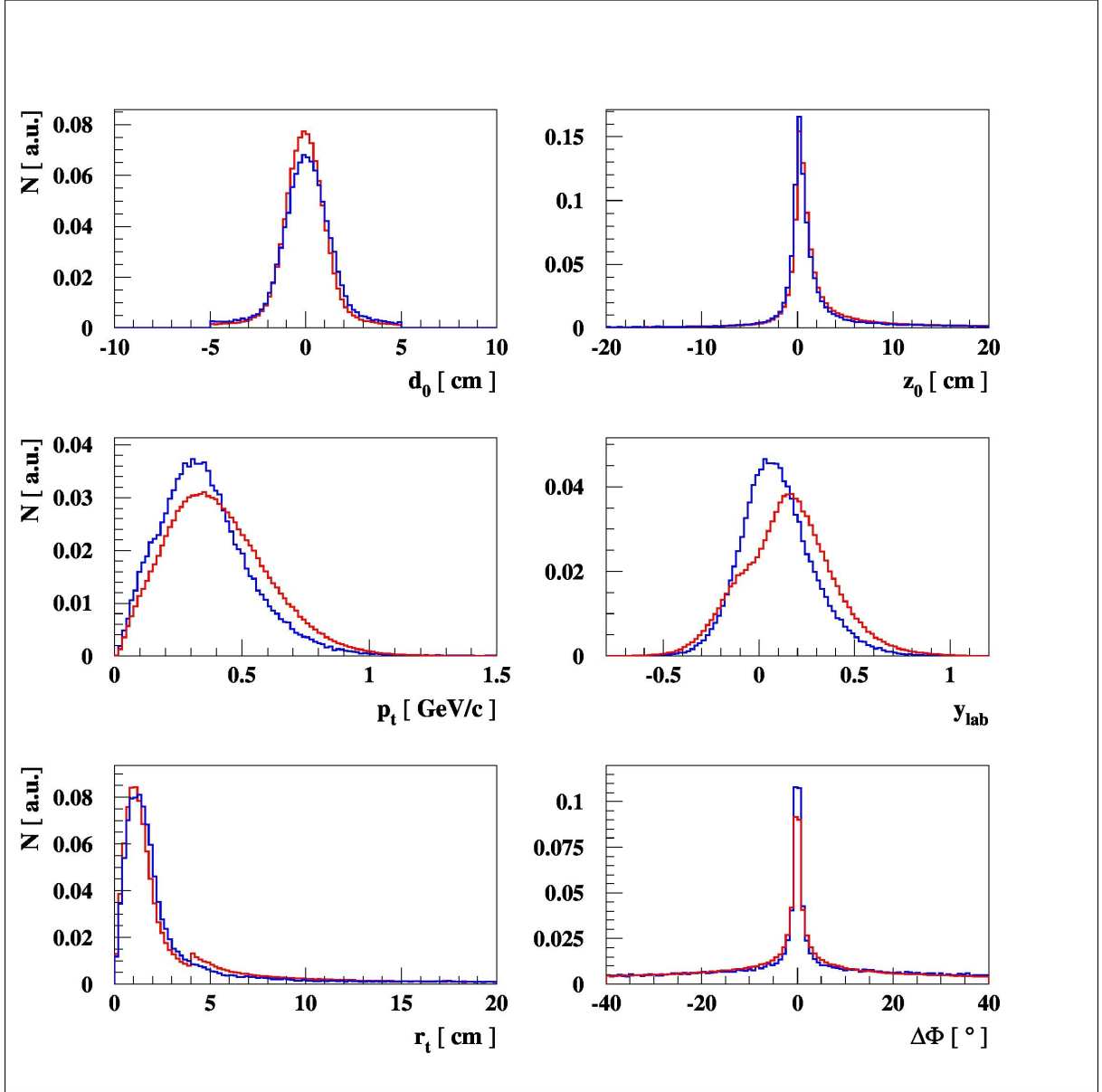


Figure 4.7: Precut distributions for  $\Lambda$  compared between experimental data (red) and the TYPE1 simulation (blue) for the reactions on Pb target. The distributions of transverse and longitudinal closest distance to the primary vertex  $d_0$  and  $z_0$ , transverse momentum  $p_t$ , rapidity in the laboratory  $y_{lab}$ , transverse distance to the secondary vertex  $r_t$  and pointing angle  $\Delta\phi$  are presented.

### 4.3.2 TYPE2 Simulation

As it was described in Section 4.1, in the simulation named TYPE2 the beam particle, negative pion, is defined and an initial point in front of the target is selected for the start of the simulation process. Here, the results obtained by this simulation method are presented.

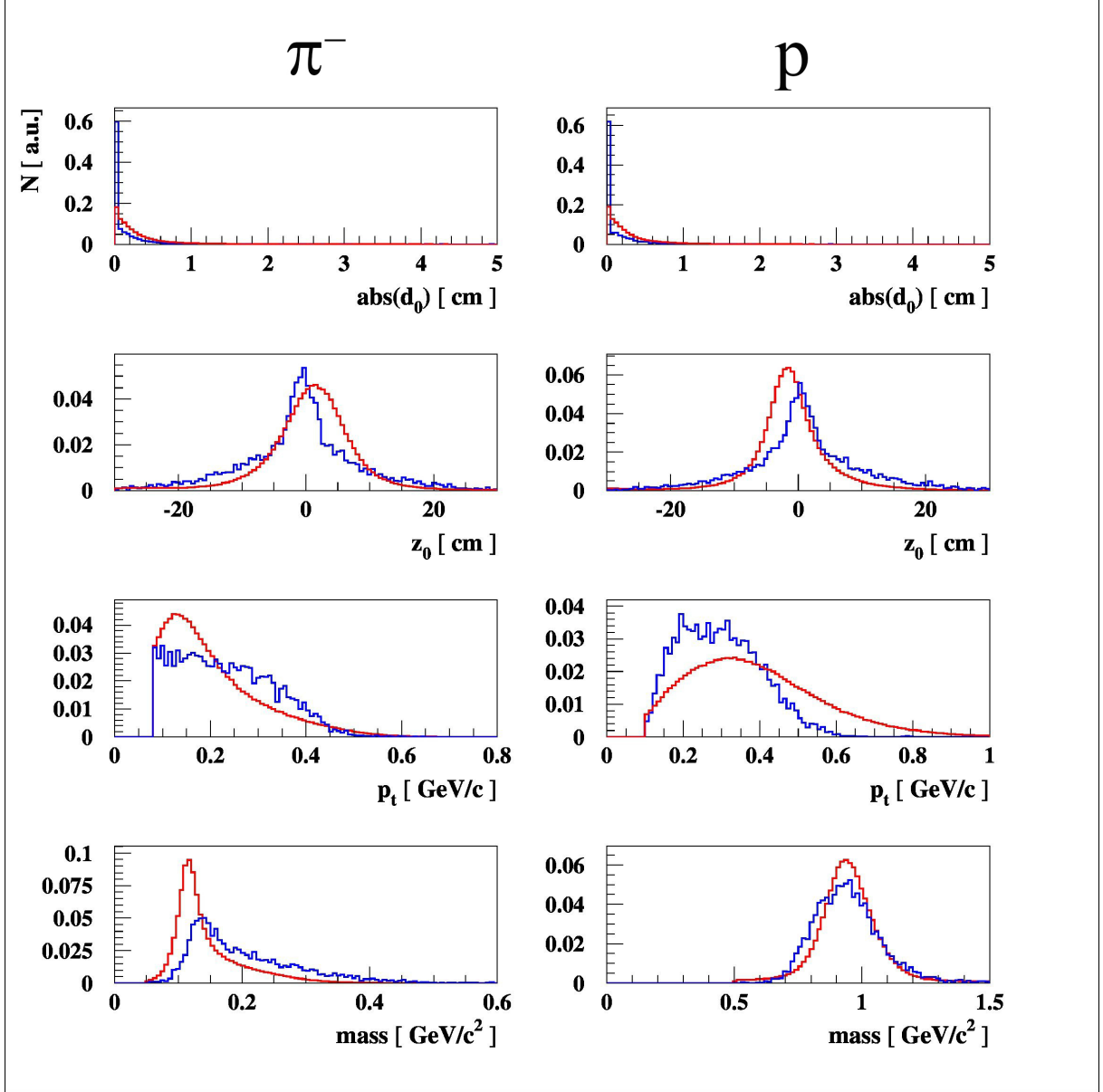


Figure 4.8: Precut distributions for  $\Lambda$  daughters compared between the experimental data (red) and the simulation (blue) for the reactions on C target. Transverse and longitudinal closest distances to the primary vertex  $d_0$  and  $z_0$ , transverse momentum  $p_t$  and  $mass$  are compared for  $\pi^-$  (left) and  $proton$  (right). The TYPE2 simulation is used to get the displayed distributions.

A comparison of quantities related to the lambda daughter particles,  $\pi^-$  and  $proton$ , obtained from the reactions on carbon target are presented in Fig. 4.8. As before (for the simulation TYPE1), precut quantities for both particles, shown in the figure, are the following: transverse and longitudinal closest distances to the primary vertex  $d_0$  and  $z_0$ , transverse momentum  $p_t$  and  $mass$  gained from the CDC. Experimental data distributions are indicated by the red and simulation results by the blue lines. This comparison is also done without using any additional cuts.

The closest distance to the primary vertex  $d_0$  shows a good agreement between the data and the simulation, except there are much more particles with  $d_0 = 0$  in the simulation results. Comparison of the longitudinal distance  $z_0$  slightly differs between the experimental data and the simulation for both daughter particles. The mean simulation value is slightly shifted compared to the mean value obtained from the data results, which is centred at zero. The peak is more pronounced, but the rest of the distribution is a bit broader for the simulation. As it was mentioned before, that can be understood in view of the results for the  $z$  resolution which is shown to be worse for the simulation by 20 - 25 % than for the experimental data. The transverse momentum  $p_t$  shows less agreement than other compared quantities. The trends of experimental and simulated data are similar, but for the second particle, the distribution of simulation data is slightly shifted to smaller values. While the proton mass shows great agreement between data and simulation, the pion mass peak is slightly shifted to higher mass values for the experimental results compared to the simulation and to nominal pion mass ( $m_\pi = 0.1396$  GeV/c<sup>2</sup>). The reason is the open mass window in preselection criterion for all the particles due to the detector resolution, as it has been previously explained (Section 3.3).

Figure 4.9 presents the comparison of some basic observables characterizing the lambda particles, between the simulated and experimental reactions with the carbon target.

The displayed quantities are the following: transverse and longitudinal closest distance to the primary vertex  $d_0$  and  $z_0$ , transverse momentum  $p_t$ , rapidity in the laboratory  $y_{lab}$ , transverse distance to the secondary vertex  $r_t$  and pointing angle  $\Delta\phi$ . As it was already mentioned when the results gained by the TYPE1 simulation were presented, here it is also important to emphasize that all the represented variables are relevant for the cuts applied in the further analysis. The importance of cuts used on rapidity and transverse momentum is great for the efficiency evaluation method which is used and presented in the next section.

All the distributions of quantities which describe  $\Lambda$  particle show excellent agreement between experimental and simulation results. Only for the transverse momentum there are discrepancies due to differences in the  $p_t$  distribution of the lambda decay particles demonstrated and discussed above.

It can be concluded that in general, the agreement between the data and simulation distributions of quantities characterizing  $\pi^-$  and proton is good enough to proceed with the further analysis, to apply the appropriate cuts on presented quantities and to use the obtained results in the efficiency correction determination.

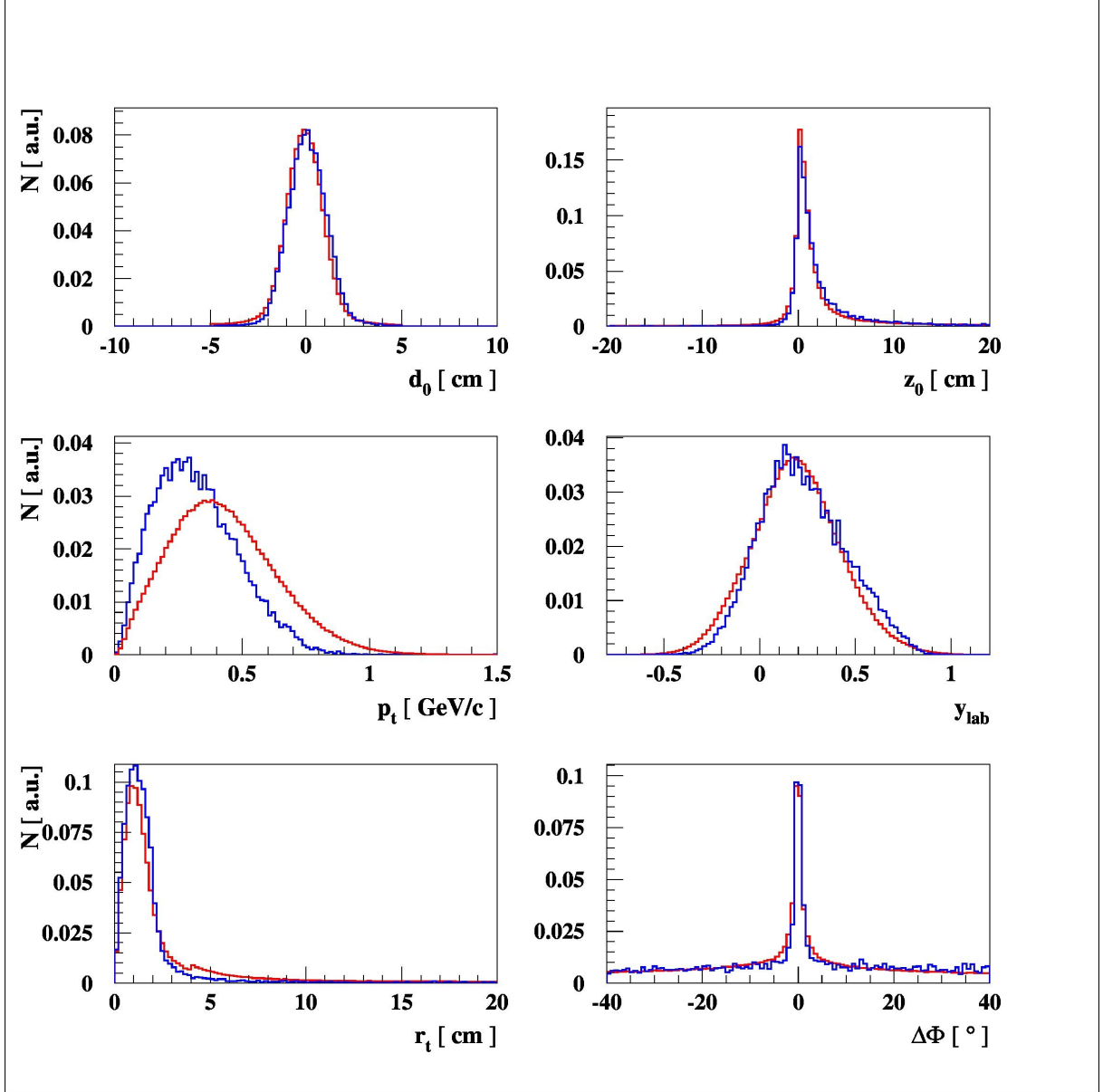


Figure 4.9: Precuts distributions for  $\Lambda$  compared between the experimental data (red) and the simulation (blue) for the reactions on C target. The distributions of transverse and longitudinal closest distance to the primary vertex  $d_0$  and  $z_0$ , transverse momentum  $p_t$ , rapidity in the laboratory  $y_{lab}$ , transverse distance to the secondary vertex  $r_t$  and pointing angle  $\Delta\phi$  are represented in six plots in the figure. The TYPE2 simulation is used to obtain the displayed plots.

As mentioned before, using the TYPE2 simulation,  $\Lambda$  particles can be embedded in the simulation events in order to increase the statistics. In the example shown in Fig. 4.10 the added lambdas were equally distributed within the phase space characterized by the transverse momentum  $p_t \in (0., 1.2)$  and the rapidity  $y_{lab} \in (-1, 1)$ . The left panel of the figure shows the distribution of the lambda candidates after the application of precuts and the right panel shows the distribution after the application of full cuts.

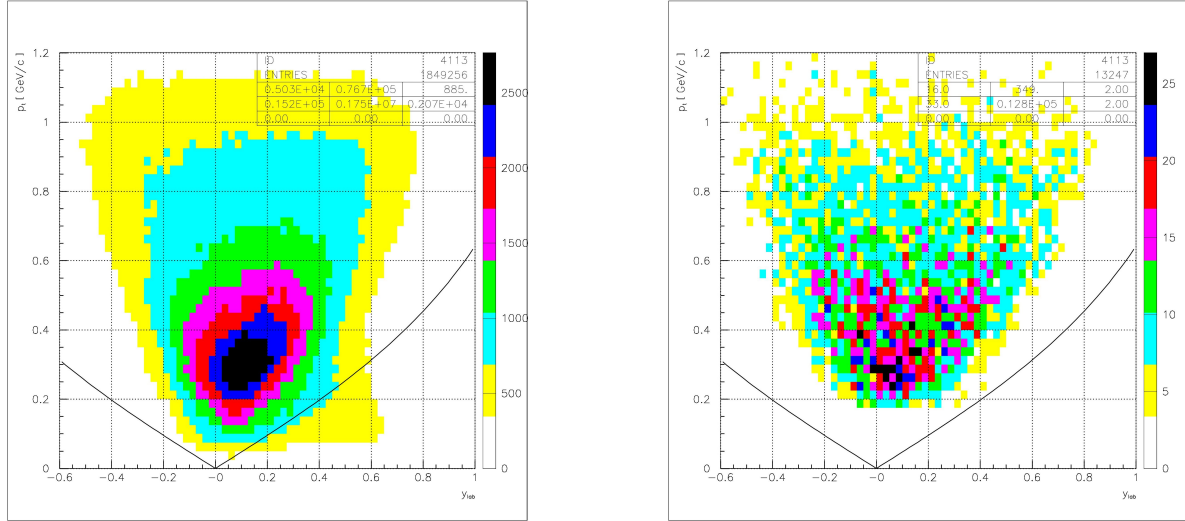


Figure 4.10:  $\Lambda$  phase space distribution for C target obtained from the TYPE2 $\Lambda$  simulation. The left panel shows  $p_t$  versus  $y_{lab}$  distribution of generated  $\Lambda$  particles and the right panel shows the same distribution obtained after the cuts were applied. The full lines indicate the geometrical acceptance of the CDC.

The solid lines indicate the geometrical acceptance of the CDC. The figure demonstrates that the reconstruction efficiency of  $\Lambda$  particles with the CDC is not at all homogeneous over the whole CDC acceptance.

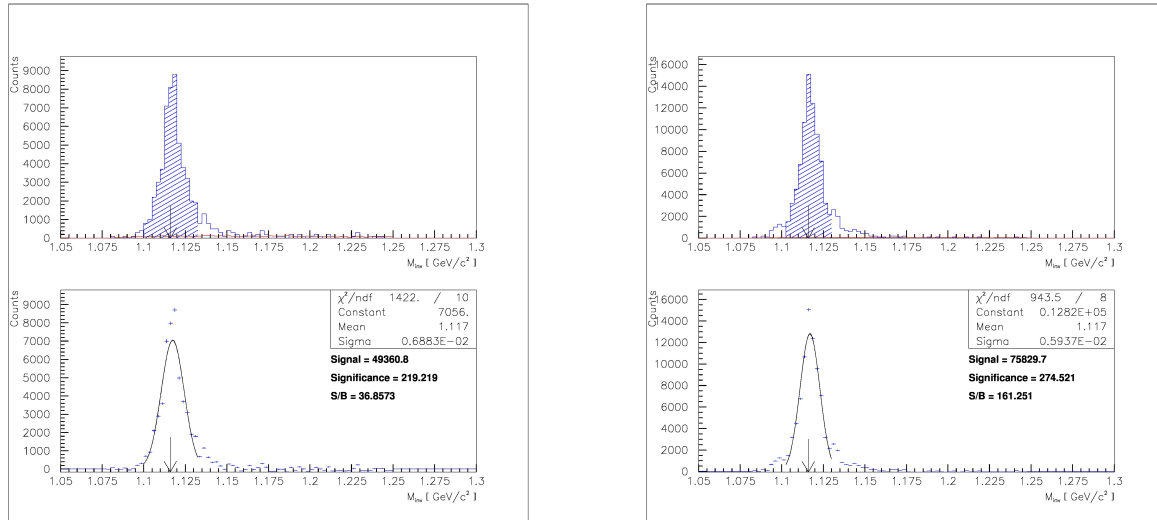


Figure 4.11:  $\Lambda$  invariant mass spectrum,  $\Lambda \rightarrow \pi^- + p$ , obtained from the TYPE2 $\Lambda$  simulation in GEANT for the  $\pi^- + C$  (left panel) and  $\pi^- + Pb$  reactions (right panel). The mass values together with corresponding widths are indicated in the plots. The arrow points to the nominal  $\Lambda$  mass.

The invariant mass spectra of reconstructed  $\Lambda$  particles for the carbon and lead targets are



presented in Fig. 4.11. These spectra are obtained from  $\approx 10^7$  simulated events in GEANT by using the TYPE2 $\Lambda$  simulation, where lambdas are generated with  $p_t \in (0., 1.2)$  and  $y_{lab} \in (-1, 1)$ . The invariant mass spectrum of reconstructed  $\Lambda$  particles for the carbon target is displayed in the left panel of the figure. The spectrum for the lead target is shown in the right panel of the figure. To obtain shown spectra, the same technique, as has been used for the experimental data, is applied. A Gaussian fit is used to extract the mass peak position and its width.

The comparison between lambda masses and corresponding widths obtained from the data and the TYPE2 $\Lambda$  simulation is given in Table 4.1.

Table 4.1:  $\Lambda$  masses and widths obtained from the data and the TYPE2 $\Lambda$  simulation. The nominal  $\Lambda$  mass is 1115.68 MeV/c<sup>2</sup>.

target	C		Pb	
	data	simulation	data	simulation
$mass$ [MeV/c <sup>2</sup> ]	$1116.40 \pm 0.17$	$1117.10 \pm 0.04$	$1116.70 \pm 0.10$	$1116.90 \pm 0.04$
$\sigma$ [MeV/c <sup>2</sup> ]	$2.31 \pm 0.13$	$6.88 \pm 0.10$	$3.18 \pm 0.13$	$5.94 \pm 0.09$

## 4.4 Acceptance and Efficiency Corrections

The corrections due to the limited geometrical acceptance and efficiency of the detector have to be applied to the results obtained with the experimental data. A method used for the correction determination is to simulate the relevant physical situation. The CDC of the FOPI detector has a geometrical acceptance of about 70 % of the full solid angle  $4\pi$ . Its efficiency is determined by the track finding, the fraction of the particles arriving from the target in the active volumes of the detector and particle identification possibilities.

Global or reconstruction efficiency is determined in simulations by the number of reconstructed (detected) particles in the detector acceptance divided by the original number of particles stored in the KINE bank. To get the real value of the global efficiency, an agreement between phase space distributions for simulated and experimental data under the same conditions is very important.

For the determination of the differential cross section for  $\Lambda$  particles, a model independent local efficiency correction is applied.

Both cases are explained and discussed below and the obtained results are presented.

#### 4.4.1 Efficiency Evaluation

After the particle identifications, the analysed experimental data is compared with the results obtained from the simulation. As it was already emphasized, for the further investigation, as well as the efficiency estimation, it has been important to check whether the simulated distributions which describe particle properties, used for the invariant mass reconstruction of  $\Lambda$  ( $K_S^0$ ), agree with the distributions obtained from the experimental data. In the previous subsection the comparison for the carbon and lead targets has been presented and discussed and now these results are used to estimate the efficiency correction.

The detection efficiency  $\varepsilon$  is defined by:

$$\varepsilon = \frac{N_{rec}}{N_{prod}}, \quad (4.9)$$

where  $N_{rec}$  stands for the number of reconstructed and  $N_{prod}$  stands for the number of produced particles (lambdas). Generally, the detection efficiency depends on the particle dynamical properties, so it is possible to write:

$$\varepsilon = \frac{\int_{\Omega} d\vec{p}_1 \int_{\Omega} d\vec{p}_2 \cdot \varepsilon(\vec{p}_1, \vec{p}_2) \cdot N_{prod}(\vec{p}_2)}{N_{prod}}, \quad (4.10)$$

$\Omega$  represents full phase space volume,  $N_{prod}(\vec{p})$  is the distribution function of produced strange particles and  $\varepsilon(\vec{p}_1, \vec{p}_2)$  is a characteristic function of the detector properties and reconstruction procedure, which represents the probability to reconstruct a strange particle at  $\vec{p}_1$  if it was produced in  $\vec{p}_2$ .

Two approaches in efficiency estimation have been applied. In the first one it is exploited that there is a confident model which reproduces the real distribution of particles and the true strange particle distribution  $N_{prod}(\vec{p})$  is known. The simulation is done in a way that  $N_{prod}^{sim}$  particles with a distribution  $N_{prod}^{sim}(\vec{p})$  are produced. After data analysis is applied, the strange particles are reconstructed and  $N_{rec}^{sim}$  is determined, Eq. (4.9) is used to compute efficiency  $\varepsilon_{sim}$ . If  $N_{prod}^{sim}(\vec{p}) = N_{prod}(\vec{p})$ , i.e. if we trust the simulation model, the obtained efficiency equals  $\varepsilon$ . To evaluate the reconstruction efficiency with this approach, the TYPE1 simulation is used, where the GiBUU hadron transport model [103] is assumed to be a confident model which reproduces the real distribution of particles.

The other way for the efficiency estimation is used if  $N_{prod}(\vec{p})$  is not known and no reliable model is available. Then the phase space  $\Omega$  is divided into subspaces  $\Omega_i$  with the assumption that  $\varepsilon(\vec{p}_1, \vec{p}_2)$  is constant in each  $\Omega_i$ . The accuracy of the approximation depends on the shape of the function  $\varepsilon(\vec{p}_1, \vec{p}_2)$  and on the size of the subspaces  $\Omega_i$ . In this case it is valid to write:

$$N_{rec}^j = \alpha_j \cdot \sum_i \varepsilon(j, i) \cdot N_{prod}^i, \quad (4.11)$$

where  $N_{rec}^j$  stands for the number of particles reconstructed in the subspace  $\Omega_j$ ,  $N_{prod}^i$  is the

number of particles produced in the subspace  $\Omega_i$ ,  $\alpha_j$  is the volume of subspace  $\Omega_j$  and  $\varepsilon(j, i)$  is the other way to write  $\varepsilon(\vec{p}_1, \vec{p}_2)$  if  $\vec{p}_1 \in \Omega_j$  and  $\vec{p}_2 \in \Omega_i$ . Or in the matrix notation:

$$\vec{N}_{rec} = \Phi \cdot \vec{N}_{prod} , \quad (4.12)$$

where  $\Phi$  is a matrix with matrix elements  $\Phi(j, i) = \alpha_j \cdot \varepsilon(j, i)$ . When the  $\Phi$  matrix and the vector of reconstructed lambdas  $N_{rec}$  are determined, it is possible to invert Eq. (4.12) and to calculate the number of produced particles in each subspace.

In order to determine the  $\Phi$  matrix, TYPE2 $\Lambda$  simulations are used.

A convenient circumstance would be if it could be assumed that the  $\Phi$  matrix is a diagonal matrix, which would simplify the further procedure. That would indicate that strange particles produced inside subspace  $\Omega_i$  are exclusively reconstructed in the same subspace  $\Omega_i$ . After studying the relation between produced and reconstructed strange particles in the same subspace, the following can be concluded:

- Between 64 – 66 % (mostly depending on refit parameters used in the simulation) of  $\Lambda$  particles are reconstructed in the same subspace where they were created. That means that the assumption of purely diagonal  $\Phi$  matrix is not valid.
- If only the " $p_t$  direction" is considered, the number of strange particles reconstructed in the same subspace in which they were created increases up to 89 – 90 %. For the " $y_{lab}$  direction" that percentage is lower and with larger dependence on the subspace position and size. It ranges from 63 to 73 %.
- The total phase space can be divided into subspaces in a way that the number of bins in " $p_t$  direction" is smaller compared to the number of divisions in " $y_{lab}$  direction".
- According to previous comments, it has been decided that for the strange particles produced in one subspace the reconstruction will be done for that particular subspace, but also for neighbouring bins in the left and the right side across  $y_{lab}$  axis.

There have been more attempts to chose the optimal subspace division of the total phase space. The priorities are to keep the approximation as accurate as possible, i.e. not to choose too large subspaces, and to have the constant efficiency inside one subspace which again leads to division into larger number of small bins. On the other hand, bins should not be selected too small in order to be sure that statistically significant number of  $\Lambda$  particles gained from the experimental data is contained inside. Furthermore, due to limited computing resources, the phase space should not be divided in too many subspaces.

The complete determination of the efficiency matrix  $\Phi$  includes the inspection of global variables and quantities describing  $\Lambda$  and its daughter particles,  $\Lambda$  particle invariant mass calculation for all subspaces and their neighbouring subspaces.

0.78 - 0.98 GeV/c	b19	b20	b21	b22	b23	b24
0.58 - 0.78 GeV/c	b13	b14	b15	b16	b17	b18
0.38 - 0.58 GeV/c	b7	b8	b9	b10	b11	b12
0.18 - 0.38 GeV/c	b1	b2	b3	b4	b5	b6
$p_t$ \ $y_{lab}$	-0.6 - (-0.4)	-0.4 - (-0.2)	-0.2 - 0.	0. - 0.2	0.2 - 0.4	0.2 - 0.6

Figure 4.12: Phase space division into 24 subspaces. Six bins were chosen in  $y_{lab}$  and four in  $p_t$  direction with ranges shown in the figure.

Three examples of the procedure including subspace division of the total phase space are presented in the following lines and figures.

Figure 4.13 shows an example of a subspace within the phase space division as indicated in Fig. 4.12 (into 24 subspaces). For the demonstration the subspace defined with  $y_{lab} \in (0., 0.2)$  and  $p_t \in (0.18, 0.38)$  GeV/c is taken to represent a "production" bin (bin in which all lambdas are created). In the left panel  $p_t$  versus  $y_{lab}$  distribution is shown before the final cuts used in the analysis are applied. The same distribution after the cuts are applied is shown in the right panel.

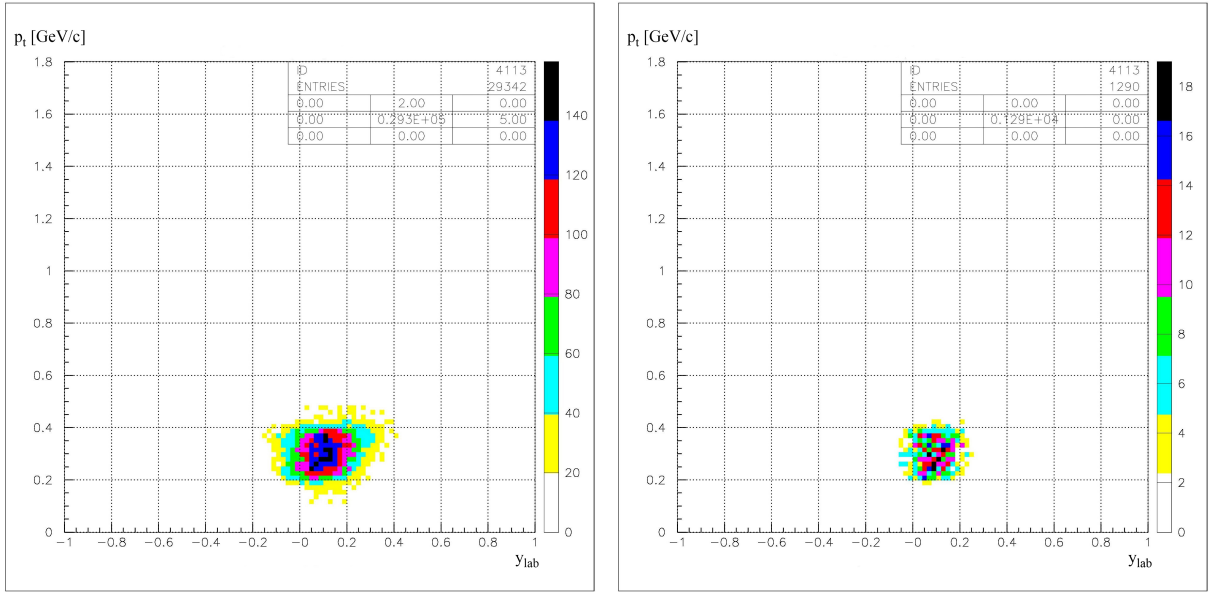


Figure 4.13:  $\Lambda$  phase space division in subspaces for the C target obtained from simulation. Left panel shows  $p_t$  versus  $y_{lab}$  distribution of  $\Lambda$  particles generated in the subspace with  $y_{lab}$  from 0. to 0.2 and  $p_t$  from 0.18 to 0.38 GeV/c and right panel shows the same distribution after the cuts are applied. These distributions are obtained after the phase space is divided into 24 subspaces.

After the complete analysis, described above, was carried out, it has been concluded that in the border bins in  $p_t$  direction, which means with  $y_{lab} \in (-0.6, -0.4)$  over entire  $p_t$  range, only few lambdas were reconstructed. The same is true for the whole rapidity range when  $p_t \in (0.78, 0.98)$  GeV/c. Hence, nine subspaces were omitted from the next step of the analysis, which resulted in the division shown in Fig. 4.14.

0.58 - 0.78 GeV/c	<b>b11</b>	<b>b12</b>	<b>b13</b>	<b>b14</b>	<b>b15</b>
0.38 - 0.58 GeV/c	<b>b6</b>	<b>b7</b>	<b>b8</b>	<b>b9</b>	<b>b10</b>
0.18 - 0.38 GeV/c	<b>b1</b>	<b>b2</b>	<b>b3</b>	<b>b4</b>	<b>b5</b>
$p_t$ $y_{lab}$	-0.4 - (-0.2)	-0.2 - 0.	0. - 0.2	0.2 - 0.4	0.2 - 0.6

Figure 4.14: Phase space division into 15 subspaces. Five bins are chosen in  $y_{lab}$  and three in  $p_t$  direction. The range of each subspace is indicated in the figure.

An example of the phase space division into 15 subspaces is shown in Fig. 4.15. In this case lambdas were produced in the subspace defined by  $y_{lab} \in (0.2, 0.4)$  and  $p_t \in (0.38, 0.58)$  GeV/c. The figure shows  $p_t$  versus  $y_{lab}$  distribution of the reconstructed lambdas before (left panel) and after (right panel) the final cuts used in the analysis are applied.

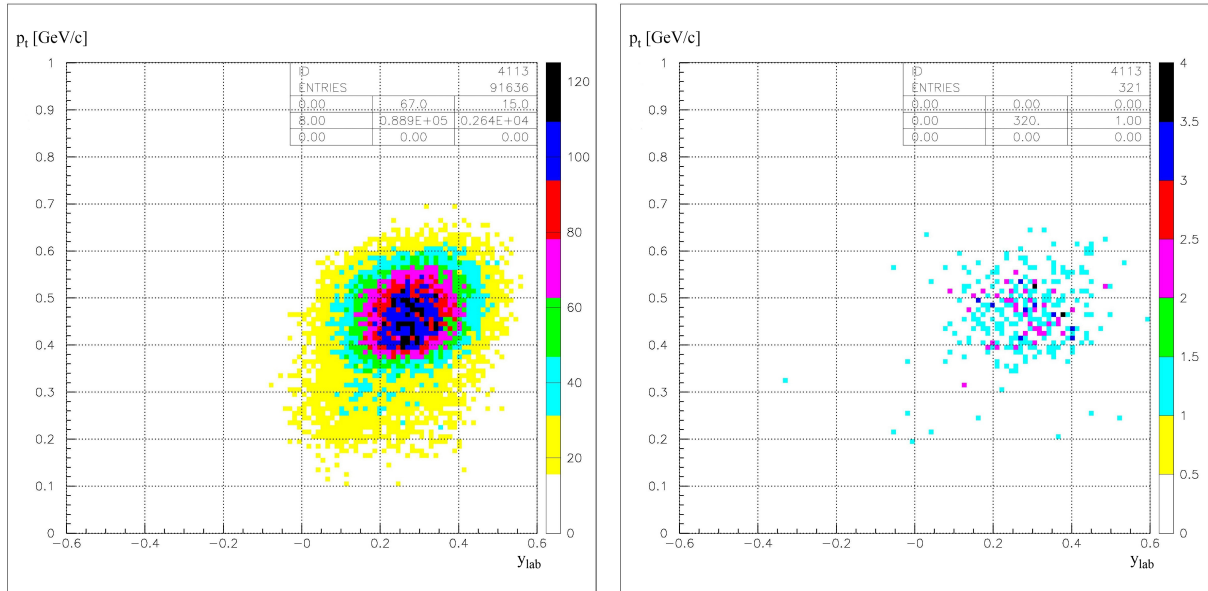


Figure 4.15:  $\Lambda$  phase space division in subspaces for the C target obtained from simulation. Left panel shows  $p_t$  versus  $y_{lab}$  distribution of  $\Lambda$  particles generated in the subspace with  $y_{lab}$  from 0.2 to 0.4 and  $p_t$  from 0.38 to 0.58 GeV/c and right panel shows the same distribution gained after the cuts are applied. These distributions are obtained within the phase space division into 15 subspaces.

In the first (the simplest) approximation it has been assumed that the efficiency changes over the considered  $p_t$  range is small and that the phase space can be divided only over  $y_{lab}$  bins. For that case division in six subspaces is done for  $y_{lab} \in (-0.6, 0.6)$  and  $p_t \in (0., 1.2)$  GeV/c, as shown in Fig. 4.16.

0. - 1.2 GeV/c	b1	b2	b3	b4	b5	b6
$p_t$ $y_{lab}$	-0.6 - (-0.4)	-0.4 - (-0.2)	-0.2 - 0.	0. - 0.2	0.2 - 0.4	0.2 - 0.6

Figure 4.16: Phase space division into 6 subspaces. Six bins are chosen in  $y_{lab}$  and the whole simulated range in  $p_t$  direction. The range of each subspace is indicated in the figure.

Figure 4.17 shows one of the subspaces in this simplified division of the phase space. The transverse momentum is taken over the whole simulated range from 0. to 1.2 GeV/c and rapidity bin chosen for illustration is  $y_{lab} \in (0.2, 0.4)$ .

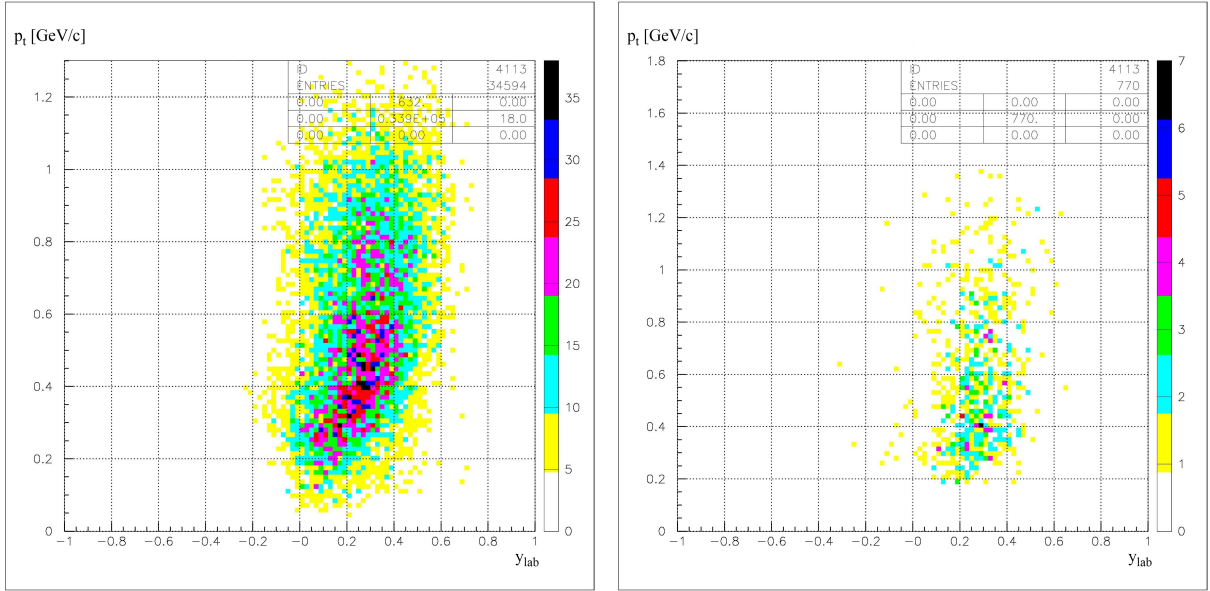


Figure 4.17:  $\Lambda$  phase space division in subspaces for the C target obtained from simulation. Left panel shows  $p_t$  versus  $y_{lab}$  distribution of  $\Lambda$  particles generated in the subspace with  $y_{lab}$  from 0.2 to 0.4 and  $p_t$  from 0. to 1.2 GeV/c and right panel shows the same distribution after the application of cuts. These distributions are obtained within the phase space division into 6 subspaces.

After tests applied on several sets of subspaces covering almost the whole phase space, it was decided that complete analysis will be done and presented for the 15 subspace division. That choice has been made according to previously described criteria.

#### 4.4.2 Results of the Efficiency Evaluation

Here, the results of the efficiency evaluation, assigned to two different methods described above, are presented.

Evaluated reconstruction efficiencies with corresponding errors, obtained from the TYPE1 simulation are summarized in Table 4.2.

Since the TYPE1 simulation has been performed for the reactions on carbon and lead targets only, the efficiency corrections for middle mass targets, required for the subsequent analysis, are approximated using linear interpolation between determined C and Pb values. The obtained results are:  $\varepsilon_{Al} \approx 0.364 \%$ ,  $\varepsilon_{Cu} \approx 0.327 \%$  and  $\varepsilon_{Sn} \approx 0.327\%$ .

Table 4.2: Evaluated efficiencies from the TYPE1 simulation for the reactions on C and Pb targets.

target	number of produced $\Lambda$	number of reconstructed $\Lambda$	efficiency (%)
<b>C</b>	70194	259	$0.370 \pm 0.010$
<b>Pb</b>	89456	260	$0.291 \pm 0.008$

The error estimates given in Table 4.2 are statistical only, gained with standard error propagation, where the number of simulated (produced)  $\Lambda$  particles has been specified exactly, so the assigned error value from that contribution is zero.

As it was explained before, in an other approach to the efficiency evaluation, the relevant part of the  $\Lambda$  phase space is divided into 15 subspaces. The conducted investigations have shown that  $\Lambda$  particles produced in one of the subspaces, defined with the transverse momentum  $p_t$  and the rapidity  $y$ , will be reconstructed in that particular subspace or one of its neighbours. Hence, the determined  $15 \times 15$  efficiency matrix  $\Phi$ , which contains the efficiency values per each bin, has non zero values on the main diagonal, its subdiagonal and superdiagonal.

The results obtained from the reactions with carbon target are presented in Table 4.3 and the results obtained from the reactions with lead target are summarized in Table 4.4. Both sets of results are included in the further analysis and will be discussed within the next chapter.

In these two tables, the subspace in which lambdas are produced is indicated by  $b_i$  and the subspace in which lambdas are reconstructed is indicated by  $b_j$ ,  $i, j = 1, \dots, 15$ . The new notation for the subspace (instead of  $\Omega_{i,j}$ ) is used here to emphasize the fact that the sum of chosen subspaces does not equal total phase space. The obtained numbers of produced  $N_{prod}$  and reconstructed  $N_{rec}$  lambdas in each bin are shown in the second and in the fourth column of the table respectively. The last column represents a matrix element  $\varepsilon(j, i) \equiv \varepsilon_{ji}$  of the efficiency matrix  $\Phi$ , i.e. the local efficiency with the statistical error estimates obtained by standard error propagation.

Empty cells in the table indicate that  $b_i$  subspace is boundary with no neighbour bin on its left or right side, as it is outlined in Fig. 4.14.

Table 4.3: Phase space analysis for 15 bins division. The data is obtained from the TYPE2 $\Lambda$  simulation for reactions with the carbon target. From the left: name of the bin in which lambdas are produced, number of produced lambdas, name of the bin in which lambdas are reconstructed, number of reconstructed lambdas and efficiency matrix element  $\varepsilon_{ji}$  as explained in the text.

$\text{bin}_{\text{prod}} \equiv b_i$	$N_{\text{prod}}$	$\text{bin}_{\text{rec}} \equiv b_j$	$N_{\text{rec}}$	$\varepsilon_{ji}$
<b>b1</b>	81139	—	—	—
		<i>b1</i>	119	$0.00147 \pm 0.00013$
		<i>b2</i>	129	$0.00161 \pm 0.00019$
<b>b2</b>	80275	<i>b1</i>	23	$0.00028 \pm 0.00010$
		<i>b2</i>	879	$0.01096 \pm 0.00039$
		<i>b3</i>	262	$0.00325 \pm 0.00026$
<b>b3</b>	80546	<i>b2</i>	115	$0.00143 \pm 0.00013$
		<i>b3</i>	1180	$0.01466 \pm 0.00048$
		<i>b4</i>	81	$0.00108 \pm 0.00015$
<b>b4</b>	75805	<i>b3</i>	261	$0.00324 \pm 0.00027$
		<i>b4</i>	599	$0.00790 \pm 0.00036$
		<i>b5</i>	35	$0.00046 \pm 0.00009$
<b>b5</b>	76063	<i>b4</i>	39	$0.00052 \pm 0.00014$
		<i>b5</i>	50	$0.00066 \pm 0.00011$
		—	—	—



$\text{bin}_{\text{prod}} \equiv \mathbf{b}_i$	$N_{\text{prod}}$	$\text{bin}_{\text{rec}} \equiv \mathbf{b}_j$	$N_{\text{rec}}$	$\varepsilon_{ji}$
<b>b6</b>	85165	—	—	—
		<i>b6</i>	691	$0.00811 \pm 0.00032$
		<i>b7</i>	311	$0.00384 \pm 0.00023$
<b>b7</b>	81208	<i>b6</i>	115	$0.00135 \pm 0.00014$
		<i>b7</i>	982	$0.01210 \pm 0.00041$
		<i>b8</i>	308	$0.00387 \pm 0.00024$
<b>b8</b>	79720	<i>b7</i>	187	$0.00230 \pm 0.00017$
		<i>b8</i>	1037	$0.01301 \pm 0.00043$
		<i>b9</i>	213	$0.00261 \pm 0.00020$
<b>b9</b>	81725	<i>b8</i>	279	$0.00350 \pm 0.00023$
		<i>b9</i>	998	$0.01222 \pm 0.00041$
		<i>b10</i>	141	$0.00169 \pm 0.00016$
<b>b10</b>	83414	<i>b9</i>	281	$0.00344 \pm 0.00021$
		<i>b10</i>	698	$0.00837 \pm 0.00033$
		—	—	—
<b>b11</b>	85435	—	—	—
		<i>b11</i>	565	$0.00662 \pm 0.00030$
		<i>b12</i>	278	$0.00320 \pm 0.00021$
<b>b12</b>	87033	<i>b11</i>	123	$0.00144 \pm 0.00013$
		<i>b12</i>	609	$0.00700 \pm 0.00031$
		<i>b13</i>	258	$0.00310 \pm 0.00021$
<b>b13</b>	83397	<i>b12</i>	144	$0.00166 \pm 0.00015$
		<i>b13</i>	585	$0.00701 \pm 0.00029$
		<i>b14</i>	175	$0.00207 \pm 0.00017$
<b>b14</b>	84998	<i>b13</i>	203	$0.00243 \pm 0.00018$
		<i>b14</i>	609	$0.00716 \pm 0.00031$
		<i>b15</i>	129	$0.00147 \pm 0.00014$
<b>b15</b>	87705	<i>b14</i>	226	$0.00266 \pm 0.00019$
		<i>b15</i>	643	$0.00733 \pm 0.00031$
		—	—	—

Table 4.4: Phase space analysis for 15 bins division done for the reactions with the lead target. The data is obtained from the TYPE2Λ simulation.

$\text{bin}_{\text{prod}} \equiv \mathbf{b_i}$	$N_{\text{prod}}$	$\text{bin}_{\text{rec}} \equiv \mathbf{b_j}$	$N_{\text{rec}}$	$\varepsilon_{\text{ji}}$
<b>b1</b>	80048	—	—	—
		<i>b1</i>	161	$0.00201 \pm 0.00016$
		<i>b2</i>	192	$0.00247 \pm 0.00020$
<b>b2</b>	77865	<i>b1</i>	42	$0.00052 \pm 0.00008$
		<i>b2</i>	1252	$0.01606 \pm 0.00048$
		<i>b3</i>	359	$0.00455 \pm 0.00024$
<b>b3</b>	78888	<i>b2</i>	172	$0.00221 \pm 0.00017$
		<i>b3</i>	1470	$0.01863 \pm 0.00055$
		<i>b4</i>	140	$0.00181 \pm 0.00015$
<b>b4</b>	77200	<i>b3</i>	361	$0.00458 \pm 0.00024$
		<i>b4</i>	965	$0.00125 \pm 0.00040$
		<i>b5</i>	43	$0.00061 \pm 0.00009$
<b>b5</b>	70328	<i>b4</i>	58	$0.00075 \pm 0.00010$
		<i>b5</i>	43	$0.00061 \pm 0.00009$
		—	—	—
<b>b6</b>	81833	—	—	—
		<i>b6</i>	987	$0.01206 \pm 0.00040$
		<i>b7</i>	461	$0.00554 \pm 0.00029$
<b>b7</b>	83291	<i>b6</i>	161	$0.00197 \pm 0.00016$
		<i>b7</i>	1532	$0.01839 \pm 0.00049$
		<i>b8</i>	443	$0.00540 \pm 0.00028$
<b>b8</b>	82032	<i>b7</i>	248	$0.00298 \pm 0.00019$
		<i>b8</i>	1480	$0.018041 \pm 0.00050$
		<i>b9</i>	353	$0.00430 \pm 0.00023$
<b>b9</b>	82161	<i>b8</i>	419	$0.00511 \pm 0.00027$
		<i>b9</i>	1519	$0.01849 \pm 0.00050$
		<i>b10</i>	207	$0.00252 \pm 0.00018$
<b>b10</b>	82229	<i>b9</i>	411	$0.00500 \pm 0.00026$
		<i>b10</i>	1012	$0.01231 \pm 0.00040$
		—	—	—

$\text{bin}_{\text{prod}} \equiv b_i$	$N_{\text{prod}}$	$\text{bin}_{\text{rec}} \equiv b_j$	$N_{\text{rec}}$	$\varepsilon_{ji}$
<b>b11</b>	86395	—	—	—
		$b11$	925	$0.01071 \pm 0.00035$
		$b12$	459	$0.00553 \pm 0.00028$
<b>b12</b>	83040	$b11$	183	$0.00212 \pm 0.00017$
		$b12$	865	$0.01042 \pm 0.00037$
		$b13$	388	$0.0047 \pm 0.00025$
<b>b13</b>	82712	$b12$	204	$0.00246 \pm 0.00017$
		$b13$	898	$0.01086 \pm 0.00037$
		$b14$	297	$0.00366 \pm 0.00023$
<b>b14</b>	81401	$b13$	269	$0.00325 \pm 0.00022$
		$b14$	884	$0.01086 \pm 0.00038$
		$b15$	213	$0.00242 \pm 0.00017$
<b>b15</b>	87972	$b14$	373	$0.00459 \pm 0.00025$
		$b15$	949	$0.01079 \pm 0.00037$
		—	—	—

The efficiency dependence on rapidity in three different  $p_t$  bins is presented in Fig. 4.18, Fig. 4.19 and Fig. 4.20.

The distributions in these figures are done for the 15 subspaces in which  $\Lambda$  particles are, both, produced and reconstructed. If these distributions are compared with  $\Lambda$  phase space distribution shown in Fig. 4.10, it is clearly seen that for the smaller  $p_t$  values the middle rapidity bins should give the larger efficiency values than those bins with  $y < -0.2$  and  $y > 0.4$ . On the other hand, in the case of the larger  $p_t$  values ( $p_t > 0.58$ ) the probability of the  $\Lambda$  reconstruction is almost equal for the entire observed rapidity range ( $y \in (-0.4, 0.6)$ ). That is well demonstrated in Fig. 4.20, where the efficiency is almost constant for all rapidity values.

The obtained results are further used to determine the numbers of experimentally produced particles in each production subspace  $b_i$ , which will be demonstrated and discussed in Chapter 5. In addition, the obtained cross section distributions in different  $p_t$  and  $y$  bins will be presented as well.

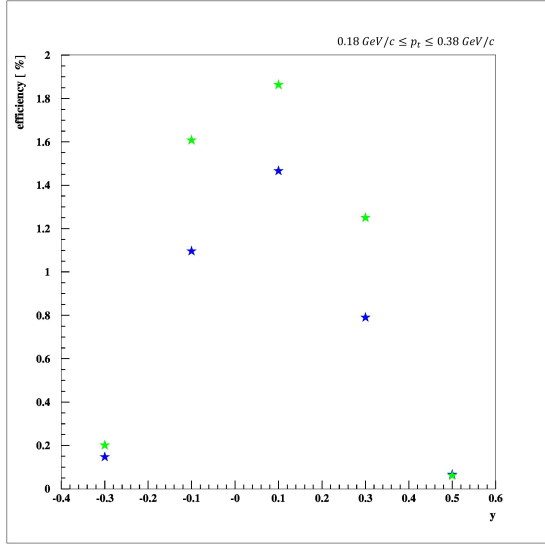


Figure 4.18: Efficiency (in %) versus rapidity for  $p_t \in (0.18, 0.38)$  GeV/c. The results obtained from the data with reactions on C (blue stars) and Pb (green stars) targets are compared.

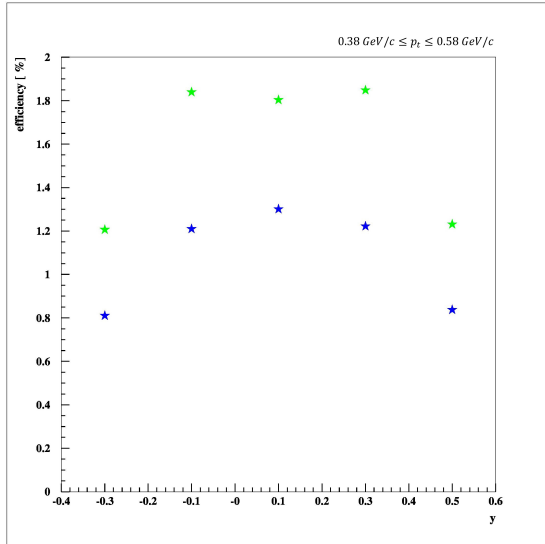


Figure 4.19: Efficiency (in %) versus rapidity for  $p_t \in (0.38, 0.58)$  GeV/c. The plot represents the comparison of the carbon and lead target results, indicated by the blue and the green stars respectively.

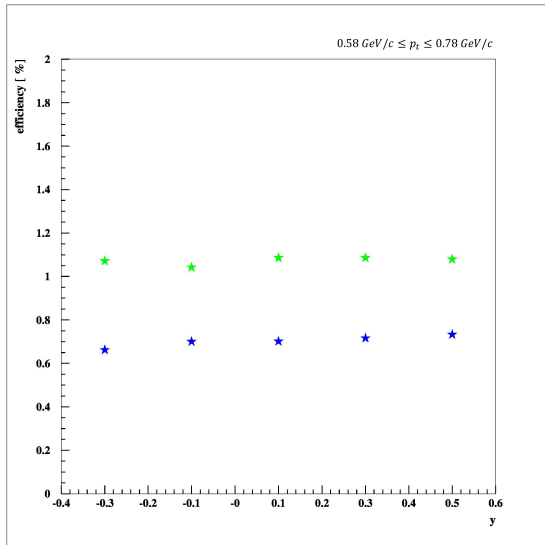


Figure 4.20: Efficiency (in %) versus rapidity for  $p_t \in (0.58, 0.78)$  GeV/c. The results obtained from the data with reactions on C and Pb targets are compared. The blue stars indicate the C and the green stars indicate the Pb results.



# Chapter 5

## Experimental Results and Discussion

As it was already discussed in previous chapters, strange particles, such as  $\Lambda$  hyperons and  $K$  mesons, represent good probes to study in-medium effects for hadrons. To obtain a precise image of the prevailing in-medium conditions, the accurate and complete measurement of all reaction and decay products is required.  $\Lambda$  and  $K_S^0$  particles, whose results will be presented in this chapter, are reconstructed by the identification of their charged daughters, as it was previously explained.

The strong motivation for this analysis was a lack of information for the reactions like  $\pi^- + N \rightarrow Y + K^0$  ( $N$  – nucleon,  $Y$  – hyperon). But at the same time, that fact limits the possibilities for comparison of the results with prior experimental and theoretical investigations. Anyhow, the study of inclusive production of the  $\Lambda$  hyperon in the  $\pi^- + N \rightarrow \Lambda + K^0$  reaction in medium should contribute to better understanding of in-medium impacts with potential benefit of extra constraints to transport model parameters.

The invariant mass spectra of reconstructed  $\Lambda$  particles in the CDC acceptance is presented for all five targets used in the experiment. The complete analysis is shown only for the C and Pb target reactions since the statistics for Al, Cu and Sn targets has been significantly more scarce. The obtained results for the evaluated efficiency, described in the previous chapter, are used for the invariant total and differential cross section calculations. The complete analysis together with phase space distributions and cross section dependence on nucleus size is presented.

### 5.1 Invariant Mass Spectra

Some of the preparatory steps preceding the determination of a strange particle invariant mass spectrum have been already explained in Chapter 3 and Chapter 4. At this point, quantities which describe candidates and selected daughter particles of  $\Lambda$  are presented for the  $\pi^- + C$  and  $\pi^- + Pb$  experimental data at  $\sqrt{s} = 1.75$  GeV, in the  $\Lambda \rightarrow \pi^- + p$  decay channel.

Transverse and longitudinal closest distances to the primary vertex ( $d_0$  and  $z_0$ ), transverse momentum ( $p_t$ ) and CDC mass ( $mass$ ) for daughters of  $\Lambda$  particle,  $\pi^-$  and *proton*, are pre-

sented in Fig. 5.1 and Fig. 5.2 for carbon and lead experimental data respectively. The left panels of both figures show the distributions of the above mentioned quantities before cuts were applied. The same distributions, but with final cuts applied, are shown in the right panels of the figures.

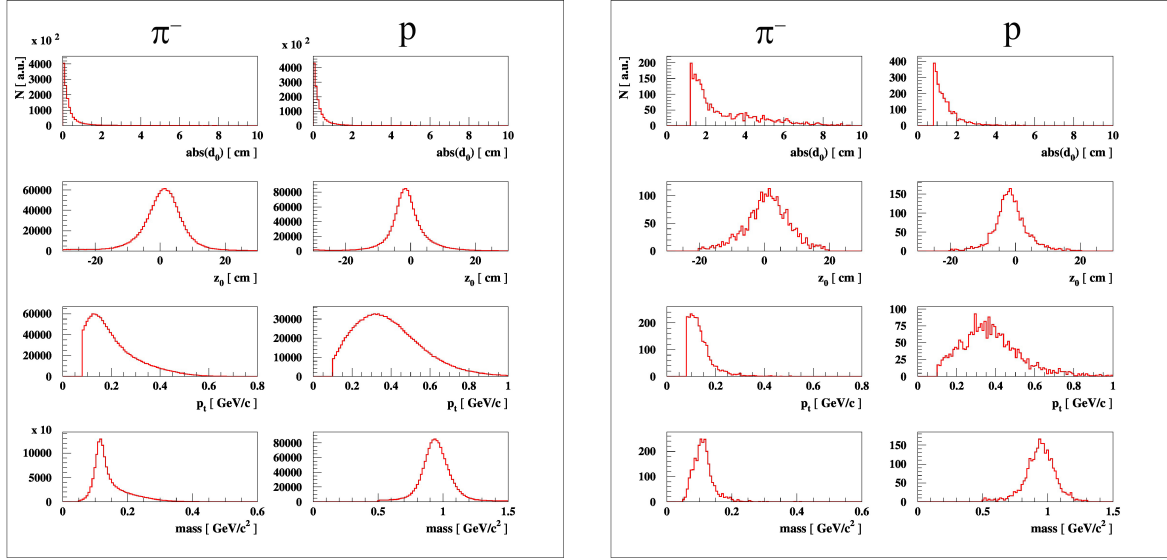


Figure 5.1:  $\pi^-$  and *proton* distributions for the  $\pi^- + C$  reactions at  $\sqrt{s} = 1.75$  GeV, before (left panel) and after (right panel) final cuts were applied: transverse and longitudinal closest distances to the primary vertex ( $d_0$  and  $z_0$ ), transverse momentum ( $p_t$ ) and CDC mass (*mass*).

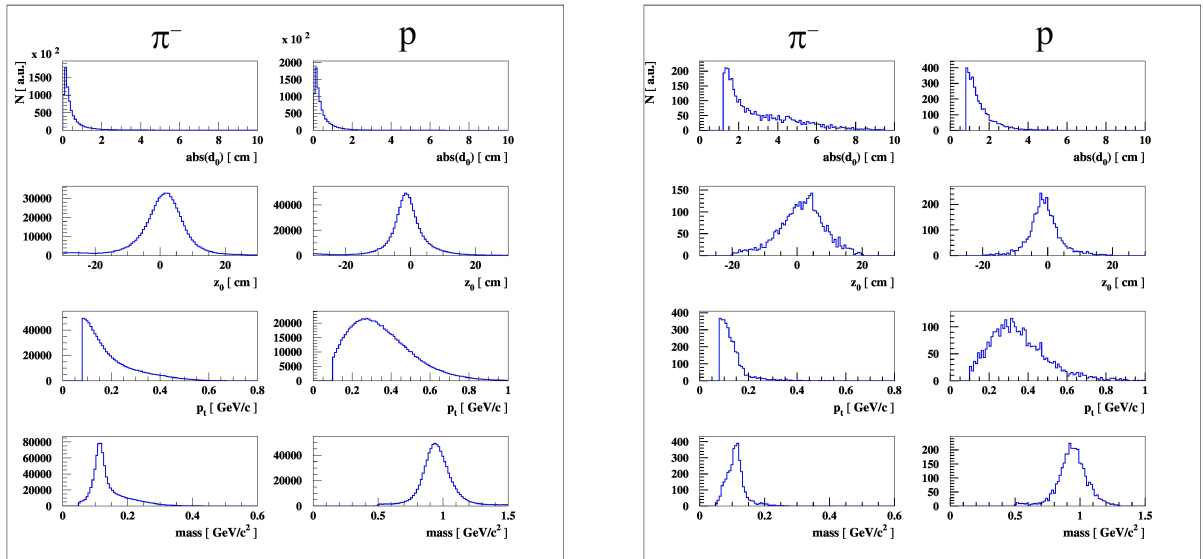


Figure 5.2:  $\pi^-$  and *proton* distributions for the  $\pi^- + Pb$  reactions at  $\sqrt{s} = 1.75$  GeV, before (left panel) and after (right panel) final cuts were applied.

The lower cuts are applied to the closest approach to the primary vertex to ensure that daughter particles are not coming from the primary vertex. As it was already mentioned, the mass values were taken in a very wide range at the first stage of the analysis, but the extra cuts were applied afterwards to get a properly reconstructed  $\Lambda$  particle as it is indicated in Table 3.2 or Table 5.4. No upper limits are applied on the transverse momenta of secondary particles and lower cuts are set to 0.08 GeV/c for  $\pi^-$  and 0.1 GeV/c for proton, as it has been discussed before.

Several relevant quantities describing  $\Lambda$  particle itself are presented in Fig. 5.3: transverse and longitudinal closest distances to the primary vertex ( $d_0$  and  $z_0$ ), transverse momentum ( $p_t$ ), rapidity in the laboratory system ( $y_{lab}$ ), transverse distance to the secondary vertex ( $r_t$ ) and pointing angle ( $\Delta\phi$ ). Normalized distributions are shown as a comparison between results gained from the reactions on carbon (indicated by the red colour) and lead (indicated by the blue colour) targets.

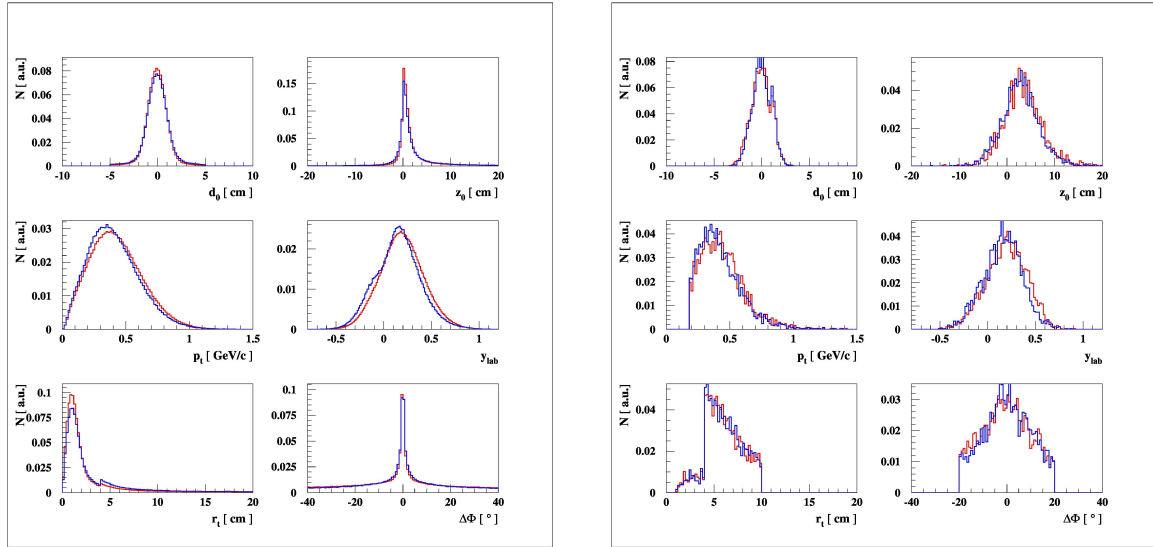


Figure 5.3: Normalized distributions describing  $\Lambda$  particle compared between the experimental results of  $\pi^- + C$  (red) and  $\pi^- + Pb$  (blue) reactions at  $\sqrt{s} = 1.75$  GeV: transverse and longitudinal closest distances to the primary vertex ( $d_0$  and  $z_0$ ), transverse momentum ( $p_t$ ), rapidity in the laboratory system ( $y_{lab}$ ), transverse distance to the secondary vertex ( $r_t$ ) and pointing angle ( $\Delta\phi$ ). The left panel shows the distributions before and the right panel after the final cuts were applied.  $\Lambda$  is reconstructed within the  $\Lambda \rightarrow \pi^- + p$  channel.

The left panel in the figure shows the experimental data comparison between the two target results before cuts were applied. It can be observed that the obtained distributions show almost the same behaviour for both targets. As expected, that is also observed for the distributions compared after the final cuts were applied. The outcome of that comparison is displayed in the right panel of the same figure.

The obtained results for the  $\Lambda$  invariant mass spectra for the  $\Lambda \rightarrow \pi^- + p$  channel obtained from the experimental data of the pion-induced reactions at  $\sqrt{s} = 1.75$  GeV with five nuclear



targets: C, Al, Cu, Sn and Pb, are presented in the following five figures. As it was mentioned in the introductory part of this chapter, the statistic is much better for the C and Pb targets than for the middle mass targets (Al, Cu and Sn) due to the longer acquisition time. Nevertheless, a clear  $\Lambda$  signal is found for each target. All the spectra are obtained with the same invariant mass method, as it was described in Section 3.3, together with quantities describing the signal, its quality and significance. The final distributions are fitted to a Gaussian function and the arrow in each plot indicates the nominal mass of the  $\Lambda$  particle ( $m_\Lambda = 1.116 \text{ GeV}/c^2$ ).

The  $\Lambda$  invariant mass spectrum for the carbon target is shown in Fig. 5.4. The measurements and the analysis are done for 178 runs with approximately  $10^7$  events. The obtained number of reconstructed lambdas is  $861 \pm 29$  with a signal to background ratio  $S/B = 6.30$ .

For the next heavier target, aluminium, 28 runs with  $\approx 6.6 \cdot 10^5$  events are available.  $84 \pm 9$  lambdas are reconstructed with a  $S/B = 4.11$  and a significance of 9.2, which, as was previously explained, is enough to have a clear signal. The invariant mass spectrum of the lambda particle for Al target is shown in Fig. 5.5.

Figure 5.6 represents the outcome of 43 runs ( $\approx 10^6$  events) from the reactions with the copper target. The clear signal of  $251 \pm 16$  reconstructed lambdas with a  $S/B = 5.99$  is indicated in the plot.

The tin target had the shortest exposure to the pion beam, only 18 runs with  $\approx 9.8 \cdot 10^5$  events. The corresponding invariant mass spectrum is presented in Fig. 5.7 with the calculated number of  $99 \pm 10$  reconstructed lambdas and a  $S/B = 6.56$ .

Finally, the result obtained for the heaviest lead target is shown in Fig. 5.8. That spectrum is gained from the experimental data collected in 234 runs with  $\approx 1.2 \cdot 10^7$  events in total. As expected, the largest number of reconstructed lambdas is evaluated for the reactions with this target:  $1457 \pm 38$  lambdas are reconstructed with a  $S/B = 8.92$ .

The mass of the  $\Lambda$  particle is well determined for all five targets. The mean and sigma values are indicated in the statistic box at top right corner of each explained figure and they are summarized in Table 5.1.

Table 5.1: Calculated experimental masses with corresponding widths for the  $\Lambda$  particle.

target	mass [MeV/c <sup>2</sup> ]	$\sigma$ [MeV/c <sup>2</sup> ]
<b>C</b>	$1116.40 \pm 0.17$	$3.24 \pm 0.22$
<b>Al</b>	$1115.90 \pm 0.49$	$2.91 \pm 0.79$
<b>Cu</b>	$1116.60 \pm 0.35$	$3.32 \pm 0.40$
<b>Sn</b>	$1116.30 \pm 0.29$	$2.78 \pm 0.51$
<b>Pb</b>	$1116.70 \pm 0.11$	$3.08 \pm 0.14$

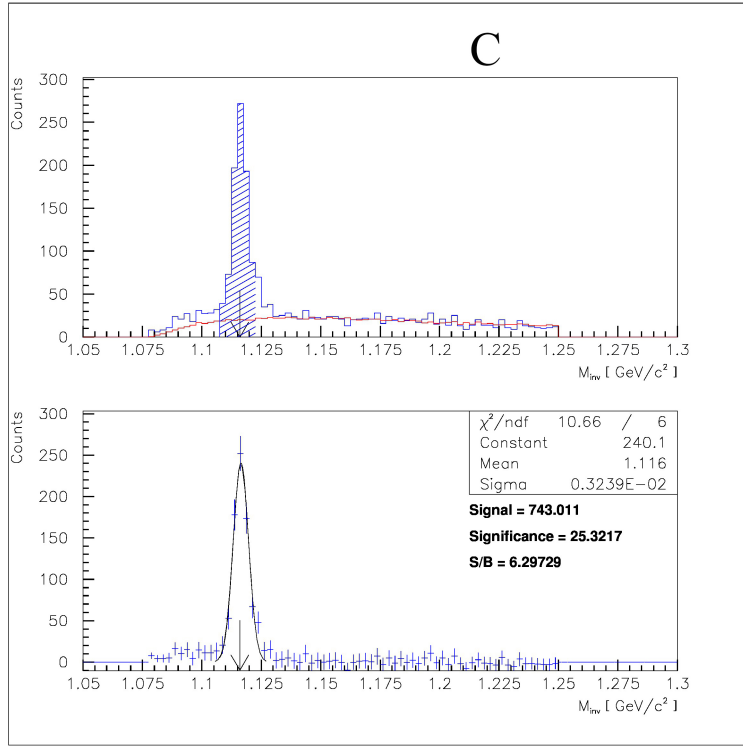


Figure 5.4:  $\Lambda$  invariant mass spectrum,  $\Lambda \rightarrow \pi^- + p$ , for the  $\pi^- + C$  reactions at  $\sqrt{s} = 1.75$  GeV. Number of analysed runs: 178, number of events:  $\approx 10^7$ .

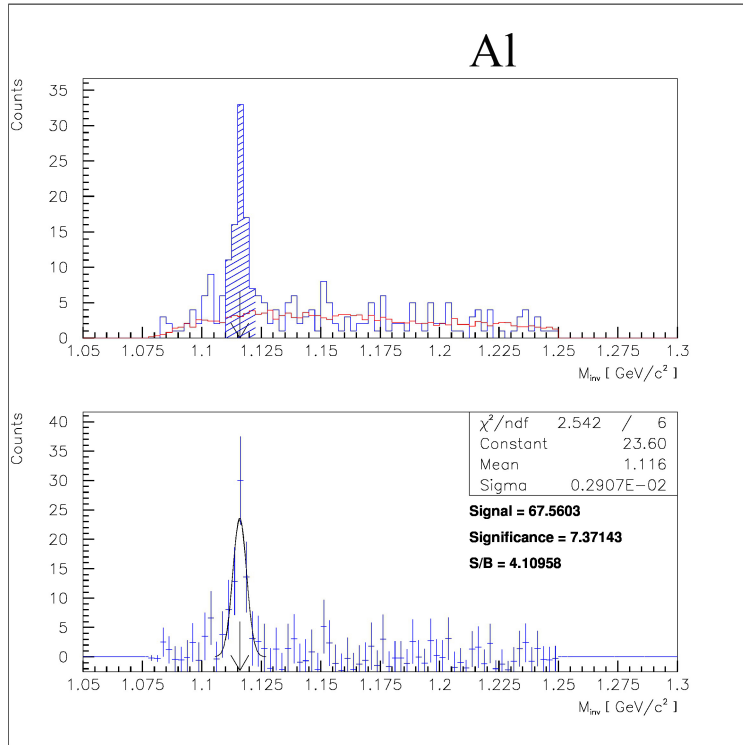


Figure 5.5:  $\Lambda$  invariant mass spectrum,  $\Lambda \rightarrow \pi^- + p$ , for the  $\pi^- + Al$  reactions at  $\sqrt{s} = 1.75$  GeV. Number of analysed runs: 28, number of events:  $\approx 6.6 \cdot 10^5$ .

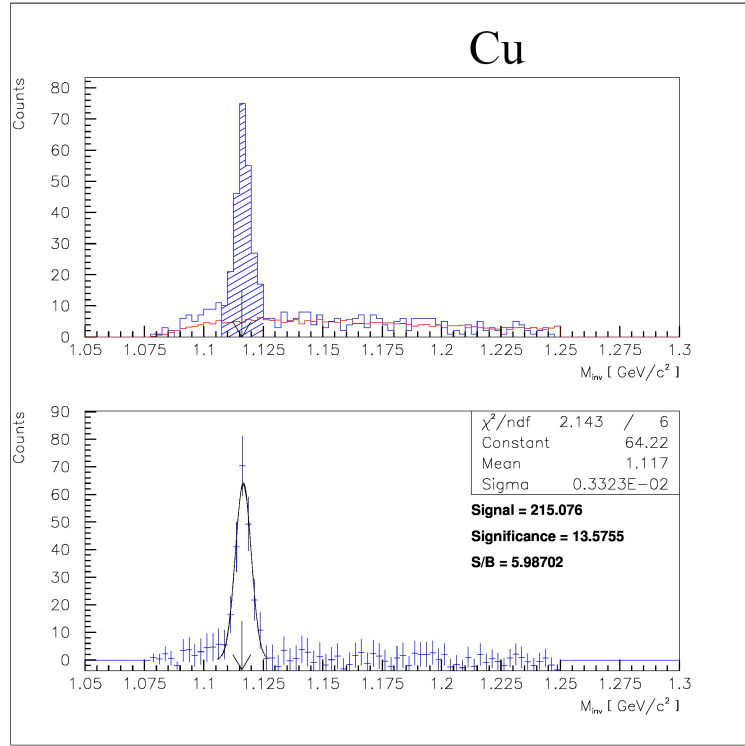


Figure 5.6:  $\Lambda$  invariant mass spectrum,  $\Lambda \rightarrow \pi^- + p$ , for the  $\pi^- + Cu$  reactions at  $\sqrt{s} = 1.75$  GeV. Number of analysed runs: 43, number of events:  $\approx 10^6$ .

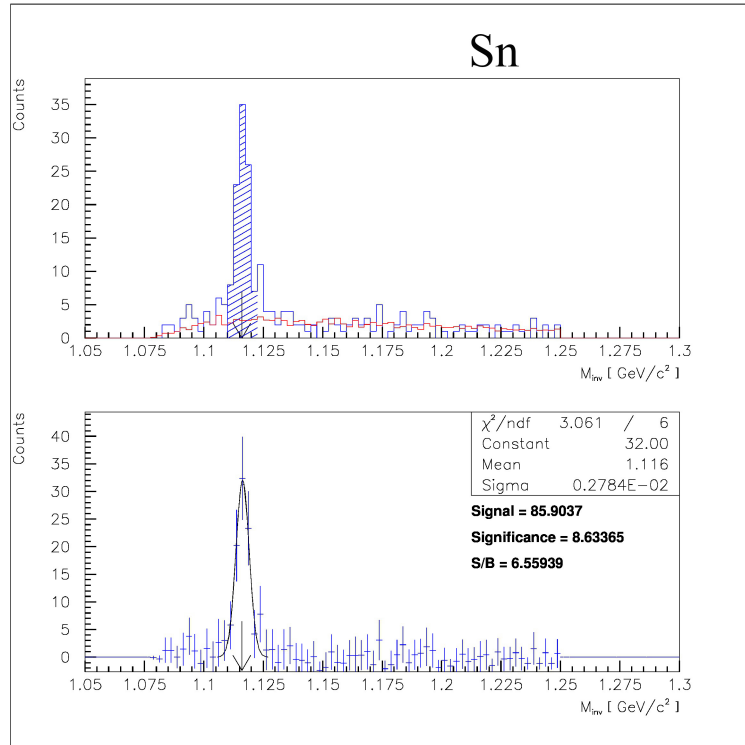


Figure 5.7:  $\Lambda$  invariant mass spectrum,  $\Lambda \rightarrow \pi^- + p$ , for the  $\pi^- + Sn$  reactions at  $\sqrt{s} = 1.75$  GeV. Number of analysed runs: 18, number of events:  $\approx 9.8 \cdot 10^5$ .

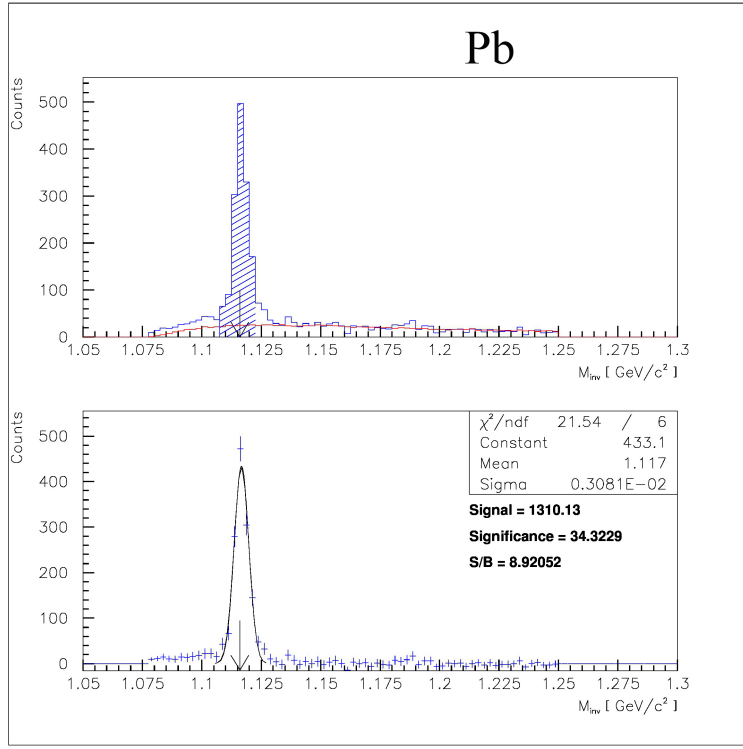


Figure 5.8:  $\Lambda$  invariant mass spectrum,  $\Lambda \rightarrow \pi^- + p$ , for the  $\pi^- + \text{Pb}$  reactions at  $\sqrt{s} = 1.75$  GeV. Number of analysed runs: 234, number of events:  $\approx 1.2 \cdot 10^7$ .

As mentioned before, almost the whole analysis which was performed for  $\Lambda$  was also carried out for  $K_S^0$  particle. For a demonstration, the invariant mass spectra of  $K_S^0$  meson for C and Pb targets are presented in the left and right panel of Fig. 5.9 respectively.

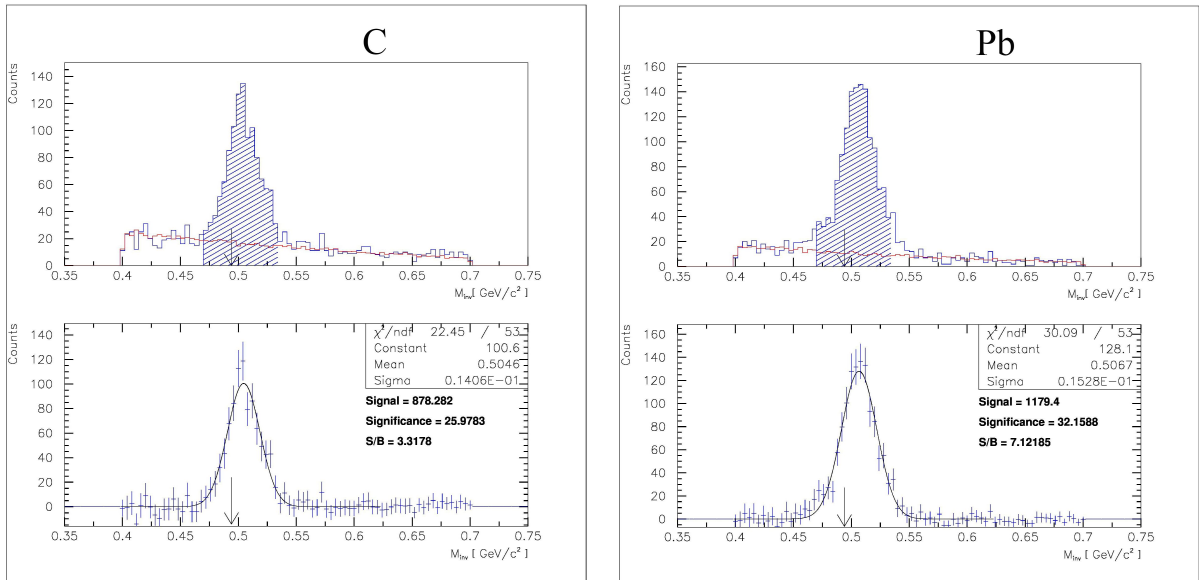


Figure 5.9:  $K_S^0$  invariant mass spectrum,  $K_S^0 \rightarrow \pi^- + \pi^+$ , for pion-induced reactions at  $\sqrt{s} = 1.75$  GeV on carbon target (left panel) and on lead target (right panel). Number of analysed runs: 178 for C and 234 for Pb target, number of events:  $\approx 10^7$  for C and  $\approx 1.2 \cdot 10^7$  for Pb target.

A clear signal is obtained for all five targets. A shift of the peak position to higher masses, compared to the nominal  $K^0$  mass ( $m_{K^0} = 0.494 \text{ GeV}/c^2$ ), which is indicated by the arrow, is observed in both presented spectra.

## 5.2 $\Lambda$ Particle Phase Space Distributions

The production of a strange particle ( $\Lambda$  or  $K^0$ ) can be expressed as a product of the two following variables: amplitude written as matrix element which includes all dynamic quantities and phase space factor which contains the available kinematic information. The detailed description and corresponding expressions are given in Appendix C.

Hence, it is of great importance to examine the phase space distributions, i.e. rapidity and transverse momentum relations.

Figure 5.10 represents the comparison between phase space distributions of the  $\Lambda$  particle produced in two reaction systems. The left panel shows the results in transverse momentum ( $p_t$ ) versus rapidity ( $y_{lab}$ ) plot for the  $\Lambda$  produced in the  $\pi^- + C$  reactions and the right panel shows the same distribution for the  $\pi^- + Pb$  reactions. The number of lambdas per  $(y_{lab}, p_t)$  bin is indicated by the colour map at the right side of each plot. The geometrical acceptance of the CDC is marked by the full lines.

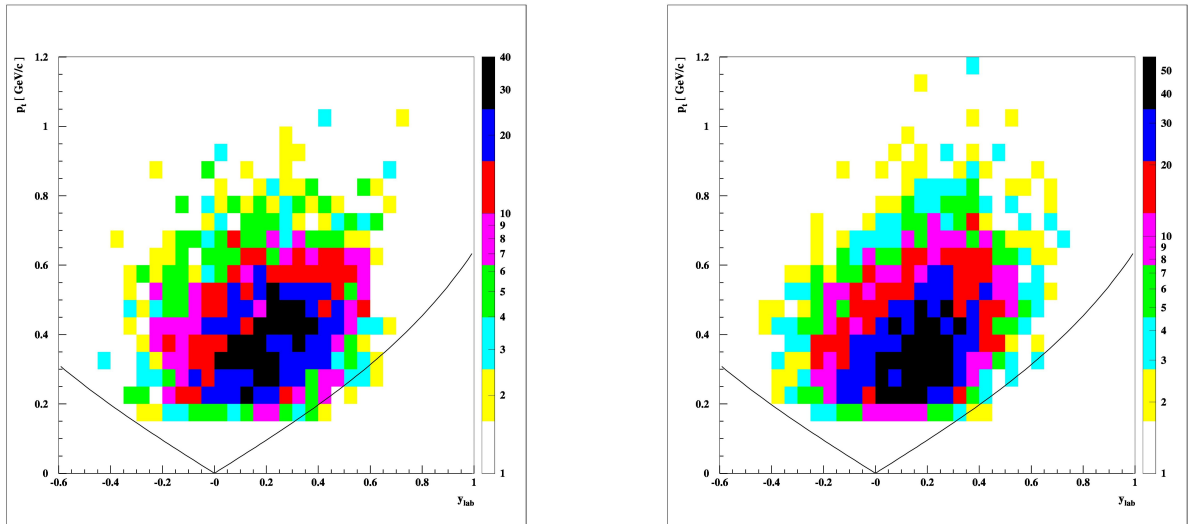


Figure 5.10:  $\Lambda$  phase space distribution. The left panel shows the phase space distribution of  $\Lambda$  particles for the  $\pi^- + C$  reactions and the right panel shows the same distribution for the  $\pi^- + Pb$  reactions, both at  $\sqrt{s} = 1.75 \text{ GeV}$ . The full lines indicate the CDC geometrical acceptance.

The comparison of the  $\Lambda$  particle  $p_t$  distribution for reactions on carbon and lead target is presented in Fig. 5.11. The distributions are normalized and not efficiency corrected. The red circles indicate carbon and the blue squares indicate lead data. At  $p_t$  values from  $\approx 200 \text{ MeV}/c$  to  $\approx 400 \text{ MeV}/c$   $\Lambda$  particles coming from the reactions on lead demonstrate higher yield than

those coming from carbon reactions. For  $p_t$  above  $\approx 400$  MeV/c the situation is opposite, yield for the carbon is higher than for the lead reactions. At  $p_t$  above 900 MeV/c two distributions almost overlap.

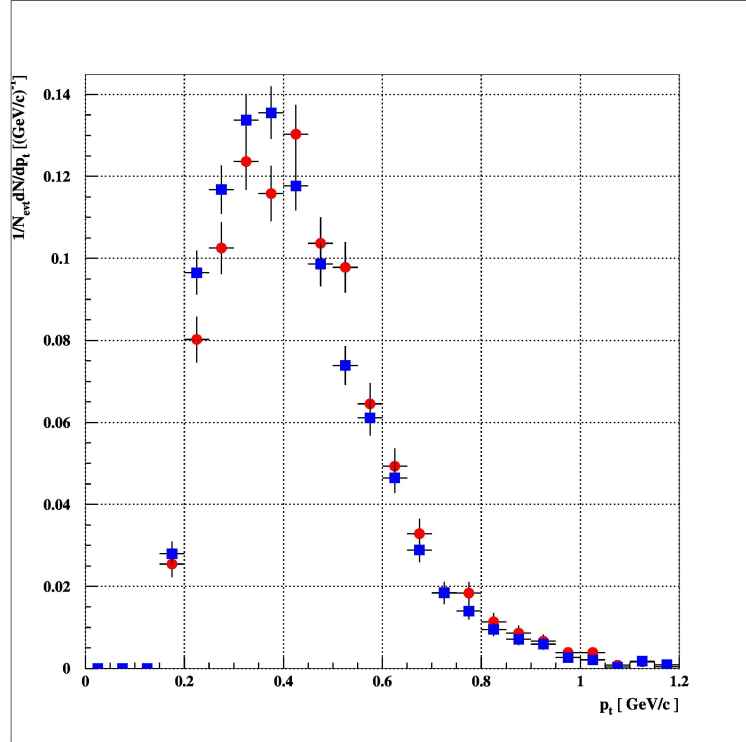


Figure 5.11: Transverse momentum distributions of the  $\Lambda$  particle compared between the results obtained from the  $\pi^- + C$  (red circles) and  $\pi^- + Pb$  (blue squares) reactions, both at  $\sqrt{s} = 1.75$  GeV. The plot is not efficiency corrected.

The normalized rapidity distributions of the  $\Lambda$  particle for the  $\pi^- + C$  and  $\pi^- + Pb$  systems are displayed in Fig. 5.12. The displayed distributions are not efficiency corrected.

As in the case of the  $p_t$  distribution, the red circles indicate carbon and the blue squares lead data. For rapidities lower than  $\approx -0.3$  both systems show almost the same yields. At  $y_{lab}$  above  $-0.2$  the number of lambdas produced in the lead reactions is slightly higher than the one obtained in carbon reactions (especially around  $0.1 - 0.2$ ) till  $y_{lab}$  reaches  $\approx 0.35$  where the situation is reversed and  $\Lambda$  coming from the carbon reactions exhibit higher yield, but again not of a great importance. The overlapping of distributions of carbon and lead data reappears for the rapidities above  $0.7$ .

The possible reason for these small differences in represented distributions for the  $\Lambda$  production in C and Pb target reactions is that the  $\Lambda$  particle produced in the Pb target has to experience more scattering than the one produced in the C target due to larger number of nucleons in the Pb nucleus.

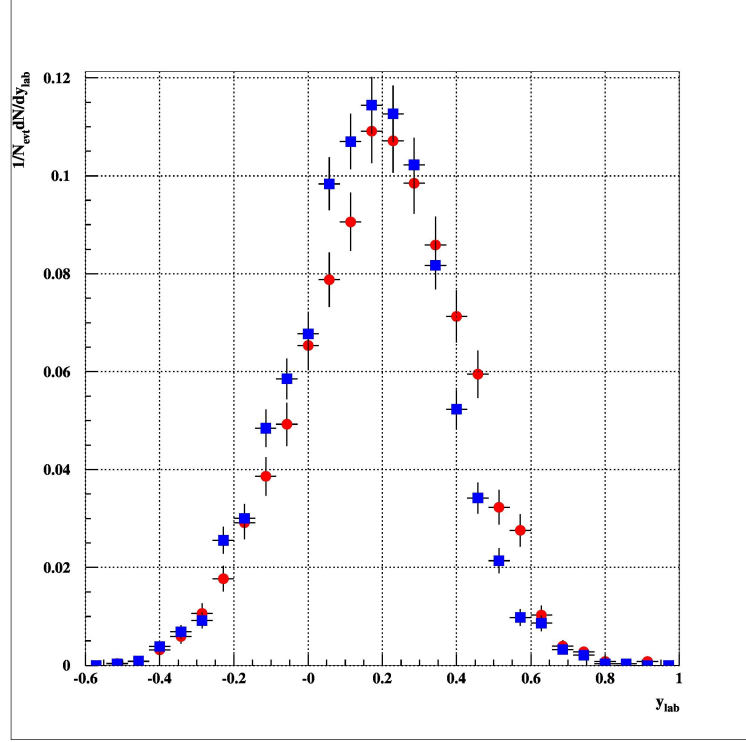


Figure 5.12: Rapidity distributions of the  $\Lambda$  particle compared between the results obtained from the  $\pi^- + C$  (red circles) and  $\pi^- + Pb$  (blue squares) reactions, both at  $\sqrt{s} = 1.75$  GeV. The displayed plot is not efficiency corrected.

### 5.3 $\Lambda$ Inclusive Cross Section

One of the main goals of this study was to determine  $\Lambda$  inclusive cross section in the  $\pi^- + A \rightarrow \Lambda + K$  reaction for the five nuclei used in the S273 experiment. To investigate that phenomenon for the different system sizes, five targets from carbon ( $A = 12$ ) to lead ( $A = 208$ ) have been used.

As it was mentioned previously, two different approaches for the efficiency evaluation and consequently the cross section determination have been applied within this analysis. For the first method, the transport model (GiBUU) is used in the TYPE1 simulations. This provides the global efficiency which is used to correct the experimental data and to calculate the cross section.

The relation for the cross section calculation, together with all explained quantities used inside, has been already presented in Section 2.5, but now the correction evaluated in the previous chapter ( $\varepsilon$ ), together with the number of the reconstructed strange particles ( $N_{rec}$ ) should be included:

$$\sigma_R = \sigma_{tot} = \frac{N_{rec}}{\varepsilon N_{beam} n_{targ}} \sum_{trig} \frac{N_{trig}}{ds_{tot} ds_{trig}}, \quad (5.1)$$

where  $\sigma_R$  is the inclusive reaction cross section.

Prior to the analysis performed for the  $\Lambda$  particle, this approach was tested on the  $K^0$  analysis, since the results could be compared with the results presented in [1] and published in [63]. The obtained cross sections for all five targets are displayed in Table 5.2.

Table 5.2: Calculated cross sections of the  $K^0$  meson in the  $\pi^-$  reactions with all targets used in the experiment. The obtained values are compared with previously published results presented in [1].

target	$\sigma_R[\text{mb}]$	$\sigma_R[\text{mb}]$ from [1]
<b>C</b>	$3.68 \pm 1.51$	$4.14 \pm 0.26$
<b>Al</b>	$6.20 \pm 3.91$	$7.08 \pm 0.88$
<b>Cu</b>	$11.95 \pm 5.38$	$13.60 \pm 1.29$
<b>Sn</b>	$17.00 \pm 6.46$	$20.41 \pm 2.44$
<b>Pb</b>	$29.89 \pm 8.67$	$27.25 \pm 1.68$

The values calculated in this analysis match relatively well with the previously published results. The largest deviation is found for the tin target where the difference is however still within  $2\sigma$ .

The obtained  $\Lambda$  efficiency values for the reactions with carbon and lead targets have been given in Table 4.2. Since the presented results were obtained from the TYPE1 simulation for C and Pb targets only, the efficiency corrections for the middle mass targets (Al, Cu and Sn) were approximated using the linear interpolation between determined C and Pb values and they have also been presented in the last section of Chapter 4.

Table 5.3: Number of reconstructed  $\Lambda$  particles and calculated cross sections of the  $\Lambda$  hyperon from the  $\pi^-$  reactions on the five targets used in the experiment.

target	$N_{rec}(\Lambda)$	$\sigma_R[\text{mb}]$
<b>C</b>	861	$14.93 \pm 9.26$
<b>Al</b>	84	$25.45 \pm 10.94$
<b>Cu</b>	251	$60.24 \pm 27.11$
<b>Sn</b>	99	$52.89 \pm 19.04$
<b>Pb</b>	1457	$137.56 \pm 55.02$

Number of reconstructed  $\Lambda$  particles and corresponding cross sections are given in Table 5.3. As it has been already observed from the  $\Lambda$  invariant mass spectra (Section 5.1) the order of



magnitude for the lambdas reconstructed in the  $C$  and  $Pb$  reactions is equal, while for the other three targets the number of reconstructed lambdas is one order of magnitude smaller. From the results obtained for the cross section values it is observed that the result of the Sn target does not follow the ordering of the other targets, which should be further investigated.

### 5.3.1 Cross Section as a Function of the System Size

The systematics of five different nuclear targets used in this experiment provides the possibility for mutual comparisons and size dependence investigations for different quantities. One of those investigations concerns the inclusive cross section dependence on a system size. The motivation for this inspection is the possibility to obtain the information whether a strange particle is produced in the nucleus interior or on its surface. For that purpose, the obtained cross section dependence on volume ( $A$ ) and surface ( $A^{2/3}$ ) terms is explored. The results are presented in Fig. 5.13.

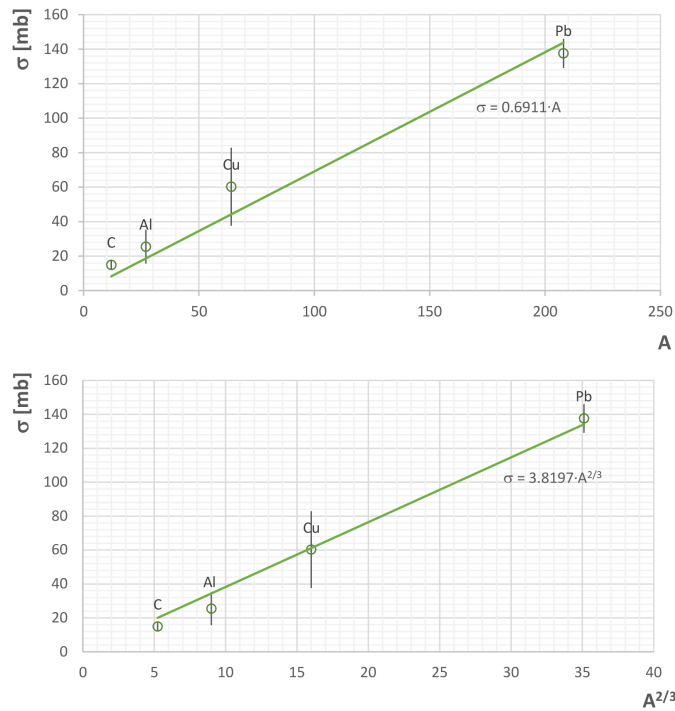


Figure 5.13:  $\Lambda$  production cross section as a function of mass number  $A$  (upper panel) and as a function of  $A^{2/3}$  (lower panel). The  $\Lambda$  particles are produced in the  $\pi^-$  induced reactions at  $\sqrt{s} = 1.75$  GeV.

It is observed that the  $A^{2/3}$  dependence (the  $\chi^2$  quality of the fit is 1.92) slightly better fits the cross sections than the  $A$  dependence (the  $\chi^2$  quality of the fit is 3.31), which would suggest the preferred production of the  $\Lambda$  particles at the nucleus surface.

The further investigation of the cross section behaviour in the dependence on the mass number  $A$  is performed by fitting the data points to a function which includes both, volume and surface, contributions. That function can be written as:

$$\sigma = P_1 \cdot A + P_2 \cdot A^{2/3}, \quad (5.2)$$

where  $P_1$  stands for a parameter describing volume contribution and  $P_2$  stands for a parameter presenting surface contribution to the total  $\sigma$ . The value of  $P_1$  can be understood as an effective cross section for lambdas produced inside a nuclear volume while the  $P_2$  value then represents the effective cross section of lambdas produced at the nucleus surface. The  $\chi^2$  value in this case is 0.33, which would indicate the combined production of  $\Lambda$ , both in a nucleus volume and its surface, but with a greater surface contribution implied by the compared parameters  $P_1$  and  $P_2$ .

The other possibility to check the cross section dependence on  $A$  is to fit the data points to a power law function, as following:

$$\sigma = \sigma_{eff} \cdot A^\alpha. \quad (5.3)$$

If the computed  $\alpha$  value is close to one, it can be concluded that the cross section is proportional to the volume of the target and if the obtained  $\alpha$  value is closer to  $2/3$ , then the computed cross section is proportional to  $A^{2/3}$  (surface) term. The  $\chi^2$  value for this fitting is 0.18. The results of the two explained fittings are shown in Fig. 5.14. The upper plot of the figure represents the results fitted to a combined function and in the lower panel the results fitted to a power law function are presented.

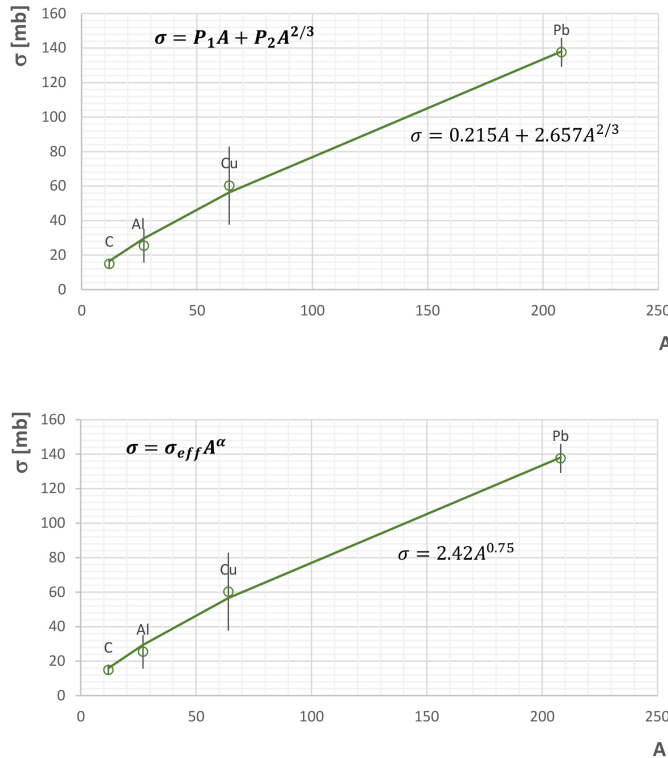


Figure 5.14:  $\Lambda$  production cross section as a function of mass number  $A$ . The results shown in the upper panel are fitted to a function including volume and surface terms. The green line in the lower panel indicates the fitting of the data results to a power law function. The  $\Lambda$  particles, in both cases, are produced in the  $\pi^-$  induced reactions at  $\sqrt{s} = 1.75$  GeV.

The obtained parameter values indicated in each plot show the better agreement with the surface term as well. The value for the  $\alpha$  factor obtained by the fit to a power law function is  $\alpha = 0.75 \pm 0.01$ , which is closer to  $2/3 \approx 0.667$  than to 1. The effective cross section  $\sigma_{eff} = 2.422 \pm 0.050$  obtained by the fit to a power law function should have approximately

the same value as the parameter  $P_2$  from Eq. 5.2,  $P_2 = 2.657 \pm 0.067$ . In comparison with the  $A$  term, the surface contribution dominates in all cases. In all plots, the obtained cross section value for the tin target is omitted because it does not follow the trend of other data points, as already mentioned. This fact needs further investigation.

## 5.4 Differential Cross Section Distributions

After the phase space distribution for  $\Lambda$  particles has been inspected and the results obtained for the reactions with the carbon and lead targets have been compared, one can proceed to investigate the behaviour of  $\Lambda$  yield in  $(p_t, y)$  bins. That is done by studying the invariant production cross section  $d^2\sigma/(2\pi dp_t dy)$  described in Appendix C. For this purpose, the rapidity distribution of the invariant production cross section in different transverse momentum bins is investigated.

The double differential cross section  $d^2\sigma/(dp_t dy)$  as a function of  $y$  for the  $\Lambda$  particle (rapidity distributions in mb/(GeV/c)) is presented for three  $p_t$  bins:  $p_t \in (0.18, 0.38)$ ,  $p_t \in (0.38, 0.58)$  and  $p_t \in (0.58, 0.78)$ . The results are plotted in Fig. 5.15, Fig. 5.16 and Fig. 5.17 for the C (left panels) and Pb (right panels) targets.

Even though the efficiency correction has been determined for the five rapidity bins, not all the results are presented in each plot as it is explained in the following lines. Since the number of reconstructed and/or produced lambdas is found to be zero or close to zero in the "border bins" (especially the lowest rapidity bin for each  $p_t$  bin), large uncertainties are found when the cross sections are computed due to very low ( $\sim 0.0001$ ) efficiencies.

The results for the  $p_t \in (0.18, 0.38)$  bin are shown in Fig. 5.15. For the carbon target the yield increase toward higher rapidity values is observed. The values for the first rapidity bin of the carbon data are omitted because there were no lambdas found in that bin. For the lead target the maximum yield is observed for  $y$  from 0 to 0.2 and then the calculated cross sections decrease toward the higher rapidity values.

In Fig. 5.16 the results for the  $p_t \in (0.38, 0.58)$  bin are presented. The first bin value is here omitted for the Pb target for the same reason explained above. The rapidity distribution for the lead target in the left panel of the figure shows the clear maximum for the rapidity values around 0.3 - 0.4, while the carbon target results show the greater yield for the maximum value in the higher rapidity range (from 0.4 to 0.5). That result is in accordance with the rapidity distribution shown in Fig. 5.12 where the greater values achieved for the carbon target than for the lead target reactions are observed for the rapidities  $y > 0.35$ .

The rapidity distribution for the  $p_t \in (0.58, 0.78)$  bin is displayed in Fig. 5.17. As in the previous figure, for the Pb target the maximum value is observed for the rapidities around 0.3, but the results for the C target show increase toward higher rapidity values as in the first  $p_t$  bin.

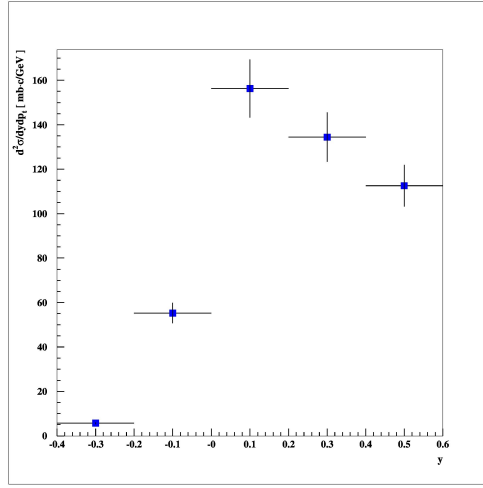
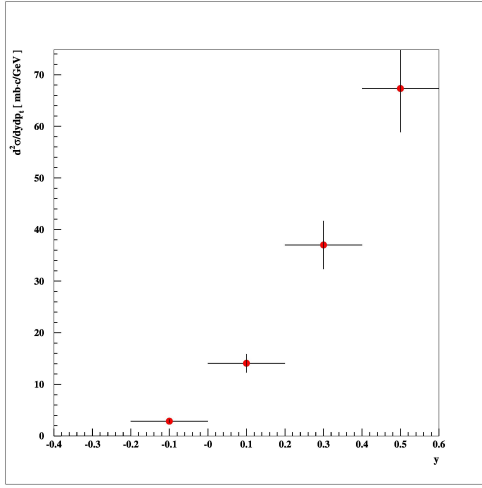


Figure 5.15:  
Differential cross section dependence on rapidity for  $p_T \in (0.18, 0.38)$ . The results for the  $\pi^- + C$  (left panel) and  $\pi^- + Pb$  (right panel) reactions at  $\sqrt{s} = 1.75$  GeV.

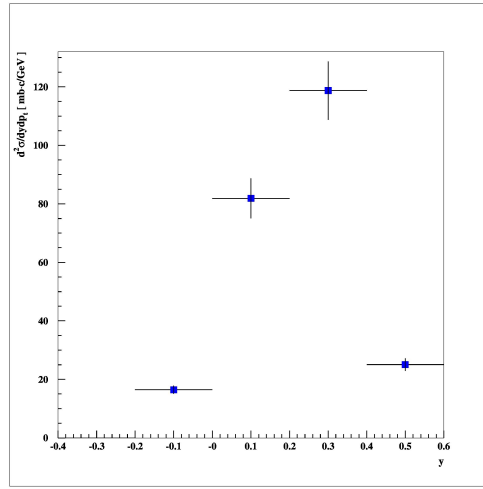
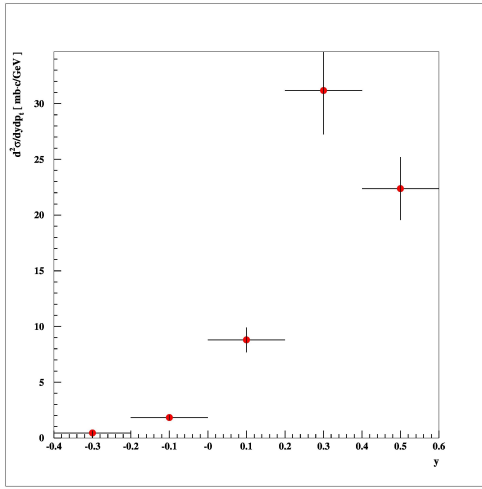


Figure 5.16:  
Differential cross section dependence on rapidity for  $p_T \in (0.38, 0.58)$ . The results for the  $\pi^- + C$  (left panel) and  $\pi^- + Pb$  (right panel) reactions at  $\sqrt{s} = 1.75$  GeV.

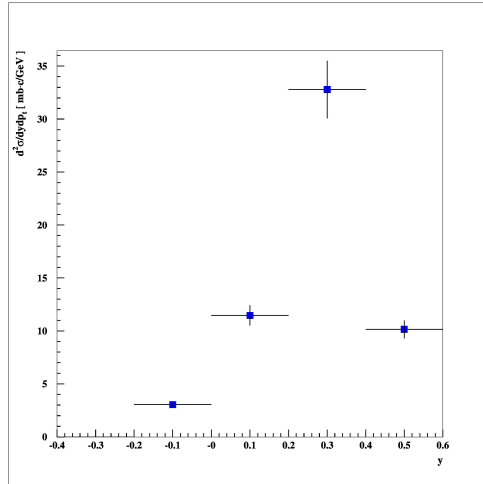
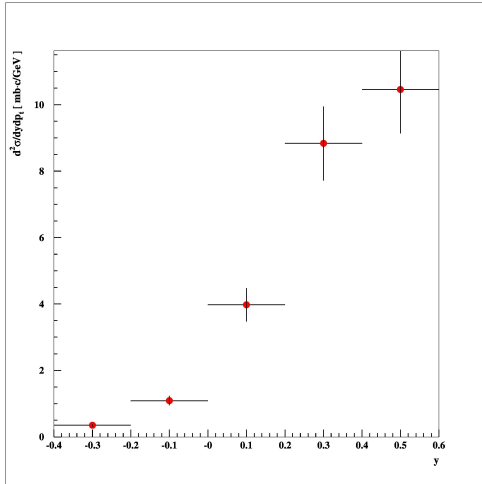


Figure 5.17:  
Differential cross section dependence on rapidity for  $p_T \in (0.58, 0.78)$ . The results for the  $\pi^- + C$  (left panel) and  $\pi^- + Pb$  (right panel) reactions at  $\sqrt{s} = 1.75$  GeV.

To conclude, all presented rapidity distributions show that most of the  $\Lambda$  particles are found in the forward hemisphere. This result confirmed theoretical prediction [28] explained in Section 3.2.

In addition, a rapidity distribution  $d\sigma/dy$  given by:

$$\frac{d\sigma}{dy} = \int_0^\infty \frac{d^2\sigma}{2\pi p_t dp_t dy} dp_t \quad (5.4)$$

is inspected, more precisely, the normalized rapidity distributions  $((1/\sigma) \cdot d\sigma/dy)$  of the carbon and lead target results are compared and displayed in Fig. 5.18.

The presented distributions are obtained by integration over the considered  $p_t$  range and then are normalized. Only the results for the target and forward rapidity range are presented since no lambdas were found in some lower rapidity bins, as emphasised before. The carbon data is indicated by the red circles and the lead data is indicated by the blue squares. The results are in good agreement with the rapidity distribution shown in Fig. 5.12.

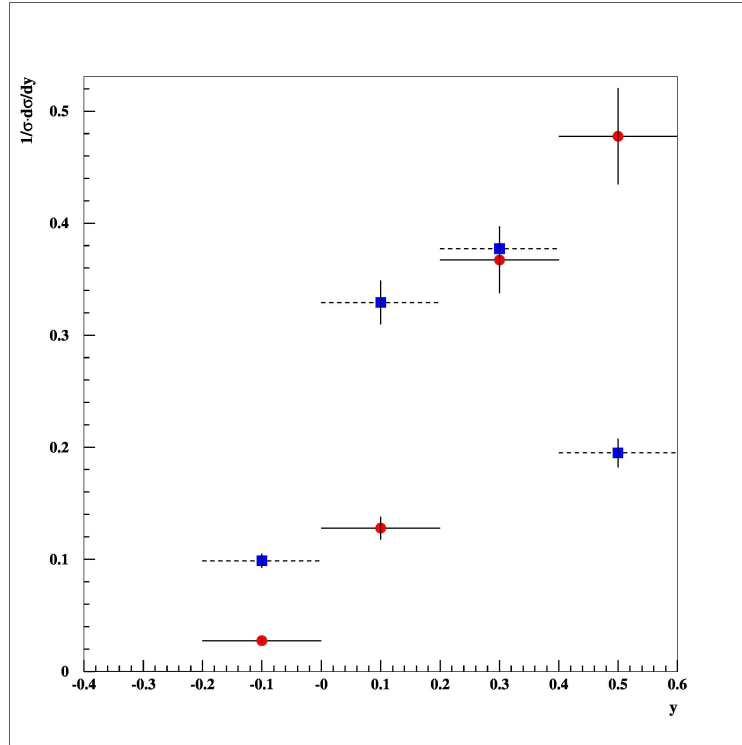


Figure 5.18: Normalized rapidity distribution for  $p_t \in (0.18, 0.78)$  in the target and forward rapidity range. The results obtained for the  $\pi^- + C$  (red circles) and  $\pi^- + Pb$  (blue squares) reactions at  $\sqrt{s} = 1.75$  GeV are compared.

## 5.5 Systematic Error Estimation

There are several factors that affect the systematic errors within the general analysis of this experiment:

- the large ( $2 \times 2$  cm<sup>2</sup>) beam spot,
- the method used for particle identification and reconstruction, i.e. signal retrieving,

- trigger counting of the beam particles,
- the method used for the efficiency correction evaluation and
- the approximation taken for the efficiency of intermediate mass targets (Al, Cu and Sn) which only affects the errors of the invariant cross section determination for the reactions on these targets, of course.

All of these contributions are discussed below.

The size of the pion beam and, consequently, the relatively large geometrical cross sections of the targets used in the S273 experiment have been explained in the second chapter. There are two possibilities for the vertex reconstruction from obtained experimental data. One way, by using the CDC only, has been presented in Chapter 3. The other way includes the silicon strip detectors. The comparison of the reconstructed vertices, more precisely their  $x$  and  $y$  components, using the two methods is presented in Fig. 5.19.

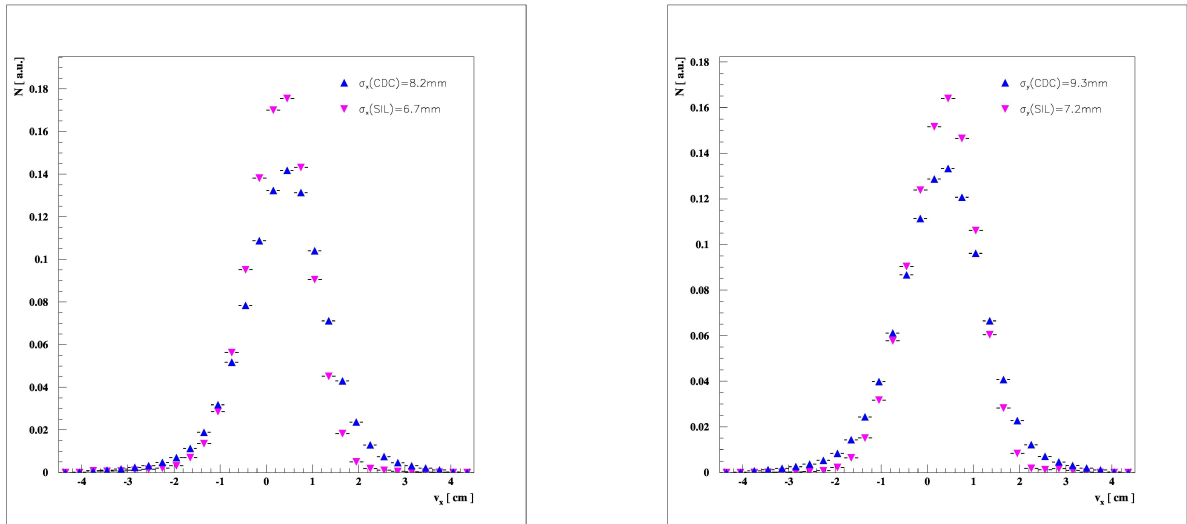


Figure 5.19: The comparison of vertex distributions in  $xy$  plane between the results obtained from the CDC (blue triangles) and silicon (pink triangles) detectors. The vertex reconstructed along  $x$  axis ( $v_x$ ) is shown in the left panel and the vertex reconstructed along the  $y$  axis ( $v_y$ ) is presented in the right panel. Presented results are obtained from  $\pi^- + Pb$  reactions at  $\sqrt{s} = 1.75$  GeV.

The CDC data is shown in the blue colour and the data obtained from the silicon detectors is indicated by the pink colour. The left plot represents the  $v_x$  and the one on the right side of the figure, shows the  $v_y$  distribution. The obtained spatial resolutions for the silicon detector are:  $\sigma_x(SIL) = 6.732 \pm 0.001$  mm and  $\sigma_y(SIL) = 7.1937 \pm 0.0001$  mm, while the corresponding resolutions for the CDC are:  $\sigma_x(CDC) = 8.2368 \pm 0.0003$  mm and  $\sigma_y(CDC) = 9.2910 \pm 0.0003$  mm.

The size of the beam spot and the particle tracking are the two main factors which determine the vertex resolution. For the silicon detectors the resolution is the result of the beam spot contribution only, while the second (tracking) part can be neglected. The reason for that assumption is that the beam particles have to pass 300  $\mu\text{m}$  inside the silicon where they can possible experience multiple scattering, but the deviation due to that effect is small compared to the spatial resolution in the  $xy$  plane, and therefore can be omitted. For the CDC detector the tracking term of the resolution cannot be neglected, moreover it is not possible to separate it from the beam spot size term. The smearing of the vertex, i.e. the variation of the efficiency with the beam spot size has to be done in the simulation since not all possible distortions are included in GEANT. In the simulation input the vertex in the  $xy$  plane is smeared and after tracking the obtained vertex resolution is compared to the vertex resolution gained from real data. The simulation resolution has to agree with the data resolution in order to get the valid efficiency.

The efficiency variation is approximately a linear function of the vertex resolution. Simulations show, that there is a difference about 6% between the efficiencies obtained with the  $\sigma_{SIL}$  and the  $\sigma_{CDC}$  resolution. This leads to a maximum relative difference in the calculated numbers of produced particles of approximately 10%. The value of 10% can be considered as systematic error coming from the beam spot size contribution.

As an example, the results of the compared efficiencies gained using  $\sigma_{SIL}$  and  $\sigma_{CDC}$  are presented in Fig 5.20. The shown results are obtained in the TYPE2 $\Lambda$  simulation for the reactions with carbon target in 15 bin phase space division analysis. Hence, presented values are the elements of the efficiency  $\Phi$  matrix for  $p_t \in (0.38, 0.58)$ . The efficiency estimates obtained from the simulation by using the  $\sigma_{SIL}$  resolution are indicated by the pink circles, while the simulation results obtained by using the  $\sigma_{CDC}$  resolution are indicated by the blue stars.

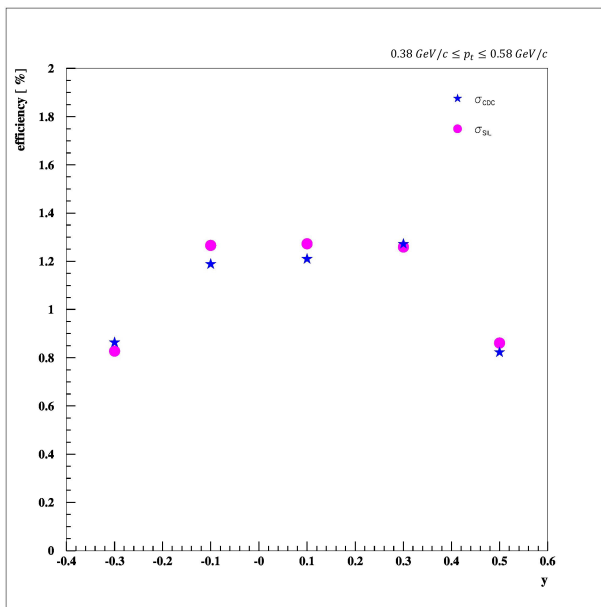


Figure 5.20: Efficiency dependence on vertex resolution: the blue stars indicate efficiencies determined by using  $\sigma_{CDC}$  and the pink circles indicate efficiencies determined by using  $\sigma_{SIL}$  resolution of the vertex in the TYPE2 $\Lambda$  simulation analysis.

To estimate the error due to the method used for the reconstruction of particles, the results obtained by using the three set of cuts (CUT<sub>1</sub>, CUT<sub>2</sub> and CUT<sub>3</sub>) are compared. The presented sets of cuts in Table 5.4 are chosen in the way that the ratio between signal-to-background values is  $\approx 1 : 2 : 0.5$ . Hence, CUT<sub>3</sub> is the most open and CUT<sub>2</sub>, the most restrictive set of cuts. CUT<sub>1</sub> is the set of cuts which were used to obtain the results presented in this and previous chapter and was already presented in Table 3.2.

Table 5.4: Sets of cuts used for  $\Lambda$  particle analysis. The quantities varied for systematic error evaluation are marked bold.

category	quantity [unit]	CUT <sub>1</sub>	CUT <sub>2</sub>	CUT <sub>3</sub>
global	$v_x$ [cm]	$< 4.5$	$< 4.5$	$< 4.5$
	$v_y$ [cm]	$< 4.5$	$< 4.5$	$< 4.5$
	$v_z$ [cm]	$< 12.0$	$< 12.0$	$< 12.0$
	$t_s$ [ns]	$-0.5 < \dots < 0.5$	$-0.5 < \dots < 0.5$	$-0.5 < \dots < 0.5$
	$e_s$ [a.u.]	$-1.5 < \dots < 5.0$	$-1.5 < \dots < 5.0$	$-1.5 < \dots < 5.0$
$\pi^-$	$ d_0 $ [cm]	<b><math>1.2 &lt; \dots &lt; 9.5</math></b>	<b><math>1.5 &lt; \dots &lt; 9.5</math></b>	<b><math>1. &lt; \dots &lt; 9.5</math></b>
	$m$ [GeV/c <sup>2</sup> ]	$0.05 < \dots < 0.50$	$0.05 < \dots < 0.50$	$0.05 < \dots < 0.50$
	$p_t$ [GeV/c]	$> 0.08$	$> 0.08$	$> 0.08$
	$ z_0 $ [cm]	$< 20$	$< 20$	$< 20$
	$N_{hit}$	$> 24$	$> 24$	$> 24$
<i>proton</i>	$ d_0 $ [cm]	<b><math>0.80 &lt; \dots &lt; 5.50</math></b>	<b><math>1.00 &lt; \dots &lt; 5.50</math></b>	<b><math>0.65 &lt; \dots &lt; 5.50</math></b>
	$m$ [GeV/c <sup>2</sup> ]	$0.5 < \dots < 1.3$	$0.5 < \dots < 1.3$	$0.5 < \dots < 1.3$
	$p_t$ [GeV/c]	$> 0.1$	$> 0.1$	$> 0.1$
	$ z_0 $ [cm]	$< 20$	$< 20$	$< 20$
	$N_{hit}$	$> 24$	$> 24$	$> 24$
$\Lambda$	$ d_0 $ [cm]	<b><math>&lt; 5</math></b>	<b><math>&lt; 1</math></b>	<b><math>&lt; 5</math></b>
	$m$ [GeV/c <sup>2</sup> ]	$1.00 < \dots < 1.25$	$1.00 < \dots < 1.25$	$1.00 < \dots < 1.25$
	$p_t$ [GeV/c]	$> 0.18$	$> 0.18$	$> 0.18$
	$r_t$ [cm]	<b><math>1 &lt; \dots &lt; 10</math></b>	<b><math>1 &lt; \dots &lt; 10</math></b>	<b><math>1 &lt; \dots &lt; 20</math></b>
	$ \Delta\Phi  [^\circ]$	<b><math>&lt; 15.0</math></b>	<b><math>&lt; 7.5</math></b>	<b><math>&lt; 25.0</math></b>

The  $\Lambda$  particle reconstruction procedure is done with each set of cuts and the results are summarized inside Table 5.5. The determined mass of the  $\Lambda$  particle with corresponding width, the signal to background ratio, significance and the number of reconstructed lambdas are presented.



It can be noted that the calculated masses (peak positions) and their widths remain almost the same for each set of cuts, while the  $S/B$ , the significance and the number of reconstructed lambdas differ considerably.

Similar to the experimental data, the analysis with the three sets of cuts was applied to the TYPE2 $\Lambda$  simulated data and the corresponding efficiency matrices have been computed. It turns out, that with different cuts, in some cases the local efficiency value changes by up to 50%.

Table 5.5:  $\Lambda$  particle reconstruction with three different sets of cuts applied on experimental data. Mass, width, signal-to-background ratio, significance and number of reconstructed  $\Lambda$  particles are presented for each set of cuts.

set of cuts	mass [MeV/c <sup>2</sup> ]	width [MeV/c <sup>2</sup> ]	S/B	signif.	N <sub>rec</sub>
<b>CUT<sub>1</sub></b>	1116.7 $\pm$ 0.1	2.8 $\pm$ 0.1	8.92	33.95	1457
<b>CUT<sub>2</sub></b>	1116.5 $\pm$ 0.1	2.7 $\pm$ 0.1	23.23	26.67	865
<b>CUT<sub>3</sub></b>	1116.7 $\pm$ 0.1	3.0 $\pm$ 0.1	5.13	39.92	2854

As a potential reason for the systematic error the counting of the beam particles by using different scalers (three in the case of this analysis) was listed. It has been calculated that the difference between these numbers is about 0.1%, thus compared to other influencing factors can be omitted from the total systematic error estimation.

In order to estimate the uncertainty of the global efficiency correction, which has been determined from the TYPE1 simulations with the GiBUU model, the inclusive cross section results are compared with the values published in [1]. The results presented in Table 5.2 give the maximum relative error of 18 % for the Sn target result and all other relative errors are below 13 %. Furthermore, the reconstruction efficiency approximation used for the middle mass targets, additionally contribute to the systematic error for those targets. If it is assumed that the efficiency values for Al, Cu and Sn targets are between the computed efficiency values of the C and Pb targets, the maximum relative error for the obtained cross sections is  $0.23 = 23$  %. The overall systematic error calculated for the total cross section analysis is summarized in Table 5.6.

Table 5.6: Calculated cross sections with corresponding estimated systematic errors.

target	$\sigma_R$ [mb]
<b>C</b>	14.93 $\pm$ 1.76
<b>Al</b>	25.45 $\pm$ 9.34
<b>Cu</b>	60.24 $\pm$ 22.18
<b>Sn</b>	52.89 $\pm$ 21.96
<b>Pb</b>	137.56 $\pm$ 8.04

# Chapter 6

## Summary and Outlook

The main goal of this study was to investigate the  $\Lambda$  particle inclusive production in pion-induced reactions at normal nuclear matter density. For the first time a negative pion beam with momentum of 1.15 GeV/c and intensity of 5000 pions per second was provided at the GSI to Cave B where the FOPI experiment was carried out in 2004. During the FOPI beam time of two weeks in August, the S273 experiment was performed on five nuclear targets (carbon, aluminium, copper, tin and lead). The majority of data was recorded in the reactions of negative pions on the lightest (C) and the heaviest (Pb) target, while the statistics for middle mass targets was significantly more scarce.

Prior to this measurement, properties of strange particles produced inside the nuclear matter had been studied by diverse theoretical approaches, as well as in the experiments performed in different energy ranges. Most of those studies were done for  $K$  mesons, whereas for lambda baryons there is still a lack of similar investigations. Some of the relevant and motivating results were summarized in the first chapter.

The FOPI detector, made primarily for heavy ion experiments, has been developed over the last few decades depending on new investigation needs and current collaboration interests. Several changes in the detector system were made due to the FOPI S273 experiment and a new silicon detector was implemented into the existing setup in order to improve the momentum resolution and reconstruction of secondary vertices. Some of the benefits of the new silicon detector have been examined within this study.

Furthermore, some new approaches and extensions to the FOPI analysis, including the software parts development, were necessary in order to achieve the goals of this work. Although the main part of the analysis was done only with the data collected by the CDC subdetector, it has been shown that a clear  $\Lambda$  signal was also observed when the forward part of the FOPI detector is included (proton detected in Helitron and pion detected in the CDC). This result has allowed further surveys of the  $\Lambda$  particle kinematic and dynamic properties in that part of the phase space.

The analysis of experimental data revealed a clear signal in the invariant mass spectra for all targets used in the experiment. The masses for the  $\Lambda$  particle have been obtained within 0.1%

of the  $\Lambda$  nominal mass value ( $m_\Lambda = 1.116$ ) MeV/c<sup>2</sup>. The number of reconstructed  $\Lambda$  particles is of the same order of magnitude ( $\sim 10^3$ ) for C and Pb targets, while for the other three targets that number is smaller by one order of magnitude ( $\sim 10^2$ ).

Compared phase space distributions between results gained from the reactions with the carbon and the lead target have shown small differences in the  $\Lambda$  particle yields, which could be explained with more scatterings that  $\Lambda$  would experience when produced in the lead target than in the carbon target due to a larger mass number of lead nucleus, i.e. a larger number of nucleons.

A detailed comparison of the experimental data and simulation results has been done in order to achieve the corrections needed to obtain cross sections from the measured distributions. Two approaches to physics simulation have been adopted in this study.

Within the first approach to the global efficiency evaluation, the GiBUU transport model was used in the TYPE1 simulation. The analysis has been provided for reactions with the carbon and lead targets, and it has resulted in the following efficiency estimates:  $\varepsilon_C = (0.370 \pm 0.010)\%$  and  $\varepsilon_{Pb} = (0.291 \pm 0.008)\%$ . Linear interpolation was used to approximate the efficiency corrections for middle mass targets. The evaluated efficiency correction has been included in the cross section calculation and the values for all five targets have been obtained.

The results for  $K^0$  meson have been compared with the results of another FOPI study [1] conducted with the same experimental data, but achieved by means of different methods. This comparison was done using the TYPE1 simulation and it has shown quite good agreement between the calculated cross sections from both studies (within the statistical error ranges), except for the tin target. The possible reason for this discrepancy requires further investigation.

In order to determine differential cross sections, the other approach for the efficiency correction has been applied. TYPE2 simulation has been performed within a subspace analysis, with pion beam incident particle defined together with the starting point in front of the target, in which  $\Lambda$  particles were added in the second phase of the simulation (TYPE2 $\Lambda$ ) to increase the statistics required for the reconstruction efficiency evaluation. The reconstruction efficiency results, which are presented in this work, have been obtained for 15 subspaces of the  $\Lambda$  phase space and the computation of the  $15 \times 15$  efficiency matrix  $\Phi$  was done. The obtained local efficiency corrections were used to calculate the number of produced  $\Lambda$  particles and to inspect differential cross section distributions in different bins of the phase space. Those distributions confirmed the preferential production of  $\Lambda$  hyperon in the forward hemisphere.

The systematics of the five nuclear targets used in this experiment allows mutual comparisons and size dependence investigations for different quantity distributions. The relation between target mass number  $A$  and  $\Lambda$  inclusive cross section has been inspected. The results obtained for the five nuclear targets' cross sections have been presented in dependence on  $A$  which is proportional to the target volume and in dependence on  $A^{2/3}$  which is proportional to the target surface. In both cases, fitting to a linear function was performed and the resulting points have shown slightly better linear dependence for the  $\Lambda$  invariant cross section behaviour

as a function of  $A^{2/3}$ . In addition, the results are fitted to a combined function which includes volume and surface terms  $P_1 \cdot A + P_2 \cdot A^{2/3}$  and to the power law function  $\sigma_{eff} \cdot A^\alpha$ . Both additional tests have shown the  $\Lambda$  production is more preferred at the nucleus surface than in its interior.

This type of analysis is planned to be extended onto the data acquired in a more recent FOPI pion-induced experiment, which took place in June 2011, at a momentum of 1.7 GeV/c on three nuclear targets (C, Cu and Pb). Hence, along with diverse target comparisons, the outcome obtained due to energy differences of the two experiments will also be explored. Although the original intention of this study was to provide a determination of the statistical limit for co-produced  $\Lambda - K^0$  pairs as well, the statistic was ultimately not sufficient enough for such a measurement [1]. That investigation is planned to be done with the results of the new pion experiment. In addition, the exclusive measurement of the production cross section of neutral strange particles can also be performed with the FOPI detector in pion-induced reactions.



# Appendix A

## The Bethe-Bloch Formula

The energy loss per length of a charged particle passing through the medium, measured in MeV/(gcm<sup>-2</sup>) is given by the Bethe-Bloch formula:

$$-\frac{dE}{dx} = 2\pi N_A r_e^2 m_e c^2 \rho \frac{Z}{A} \frac{z^2}{\beta^2} \left[ \ln \left( \frac{2m_e c^2 \gamma^2 \beta^2 W_{max}}{I^2} \right) - 2\beta^2 - \delta \right]. \quad (\text{A.1})$$

Constants, parameters and variables used in the formula are explained below:

- $N_A = 6.022 \cdot 10^{23} \text{mol}^{-1}$  is Avogadro's number,
- $r_e \approx 2.818 \text{ fm}$  is the classical electron radius,
- $m_e c^2 = 511 \text{ keV}$  is the electron mass,
- $z$  is the atomic number of an incident particle,
- $Z$  is the atomic number of the absorbing medium,
- $A$  is the mass number of the absorbing medium,
- $\beta$  is the velocity ( $v/c$ ) of an incident particle,
- $\gamma = 1/\sqrt{1 - \beta^2}$  is the relativity Lorentz factor,
- $\rho$  is the density of the absorbing medium,
- $W_{max}$  is the maximal kinetic energy transfer to an electron in a single collision,
- $I$  is the ionization constant (the characteristic of the absorbing medium) whose approximated value is  $I \approx 16Z^{0.9} \text{ eV}$  and
- $\delta$  is an added correction factor used due to the density of the medium.

If the mass of the incident particle is large enough, i.e.  $M \gg m_e$ , the maximum energy transfer for a single collision can be approximated by  $2m_e c^2 \gamma^2 \beta^2$ . Hence, the Bethe-Bloch formula becomes:

$$-\frac{dE}{dx} = 4\pi N_A r_e^2 m_e c^2 \rho \frac{Z}{A} \frac{z^2}{\beta^2} \left[ \ln \left( \frac{2m_e c^2 \gamma^2 \beta^2}{I^2} \right) - \beta^2 - \frac{\delta}{2} \right]. \quad (\text{A.2})$$

As it can be seen from the relation, the energy loss depends on a velocity  $\beta$  of charged incident particles, but there is no mass dependency. At low velocities  $dE/dx$  decreases with  $1/\beta^2$  till the minimum value for  $\beta\gamma \approx 4$ . At relativistic velocities  $dE/dx$  increases as  $\beta\gamma \rightarrow \infty$ .

The relation used for the charge identification of particles after the energy loss and the velocity were measured with FOPI subdetectors:

$$-\frac{dE}{dx} \propto \frac{z^2}{\beta^2}. \quad (\text{A.3})$$

As the CDC measures the momentum of the particle, the above equation may be transformed:

$$-\frac{dE}{dx} \propto z^2 \left( \frac{\gamma^2}{\gamma^2 - 1} \right) = z^2 \cdot \left( 1 + \frac{1}{\gamma^2 - 1} \right) = z^2 + \frac{(m \cdot c)^2}{\left( \frac{p}{z} \right)^2}. \quad (\text{A.4})$$

and then it is possible to calculate the mass of the detected particle if its charge is an integer value equal or larger than 1.

# Appendix B

## Kinematic Variables

In majority of investigations in heavy-ion and particle physics it is very useful to operate with kinematic variables which can easily be transformed from one reference frame to another (e.g. from laboratory to centre-of-mass frame and vice versa). The rapidity  $y$  is one of those variables which simplifies the calculations involving particle motion in longitudinal direction. It can be written as:

$$y = \frac{1}{2} \ln \left( \frac{E + p_z}{E - p_z} \right) = \operatorname{artanh} \frac{p_z}{E} = \operatorname{artanh} \beta_z, \quad (\text{B.1})$$

where  $E$  is the total energy of a particle,  $\beta_z = v_z/c$  stands for the longitudinal component of the velocity  $\beta = v/c$ ,  $c$  is the light velocity in vacuum and  $p_z$  is the momentum component parallel to the beam direction. For small velocities the rapidity can be replaced with the  $\beta_z$ .

Although rapidity is not reference frame independent, it shows a very convenient behaviour under a Lorentz transformation. Hence, the rapidity in the centre-of-mass system  $y'$  which is moving with velocity  $\beta_{cm}$  with respect to laboratory frame is calculated from the simple relation:

$$y' = y - \frac{1}{2} \ln \left( \frac{1 + \beta_{cm}}{1 - \beta_{cm}} \right) = y - y_{cm}, \quad (\text{B.2})$$

where  $y_{cm}$  is centre-of-mass rapidity.

Or more general, if a particle in the reference frame  $R_1$  has the rapidity  $y_1$  and  $y$  is the rapidity of the reference frame  $R_1$  in the reference frame  $R_2$ , then  $y_2 = y_1 + y$  is the rapidity of the particle in the reference frame  $R_2$ .

The transverse momentum  $p_t$  is determined with

$$p_t = \sqrt{p_x^2 + p_y^2} = \beta_t \gamma m_0 = \frac{\beta_t}{1 - \beta^2} m_0 \quad (\text{B.3})$$

and it is invariant under Lorentz transformations in beam direction. In the equation above  $m_0$  is the rest mass of a particle and  $\beta_t$  is transverse component of  $\beta$ .

Alternatively, since the phase space is defined with rapidity  $y$  and transverse momentum ( $p_t$ ) it is convenient to relate these two variables with formula:



$$p_t = \frac{m \cdot \sin \theta}{\sqrt{\left(\frac{e^{2y}+1}{e^{2y}-1}\right)^2 \cdot \cos^2 \theta - 1}} , \quad (\text{B.4})$$

$\theta$  is polar angle in the laboratory frame.

The transverse mass is defined using a rest mass  $m_0$  and a transverse momentum  $p_t$  of a particle as:

$$m_t = \sqrt{p_t^2 + m_0^2} . \quad (\text{B.5})$$

Using the form of the transverse mass the energy and longitudinal momentum can be simply calculated:

$$E = m_t \cdot \text{ch}(y) , \quad (\text{B.6})$$

$$p_z = m_t \cdot \text{sh}(y) . \quad (\text{B.7})$$

# Appendix C

## Invariant Cross Section

There are several approaches to define the invariant cross section. Here the one explicitly including particles momenta and energies is presented [107], because, written in the form given below it was suitable for this inquiry.

If it is assumed that particles 1 and 2 collide producing particles 3, 4, ...,  $n$ , the cross section of the reaction  $1 + 2 \rightarrow 3 + 4 + \dots + n$  can be determined from:

$$d\sigma = |\mathcal{M}|^2 \cdot \frac{\hbar^2 S}{4\sqrt{(p_1 \cdot p_2)^2 - (m_1 m_2 c^2)^2}} \cdot \left[ \left( \frac{c \cdot d^3 \vec{p}_3}{(2\pi)^3 \cdot 2E_3} \right) \left( \frac{c \cdot d^3 \vec{p}_4}{(2\pi)^3 \cdot 2E_4} \right) \cdots \left( \frac{c \cdot d^3 \vec{p}_n}{(2\pi)^3 \cdot 2E_n} \right) \right] \cdot (2\pi)^4 \cdot \delta^4(p_1 + p_2 - p_3 - p_4 - \dots - p_n) . \quad (\text{C.1})$$

The Lorentz-invariant matrix element  $\mathcal{M}$  represents the amplitude which, together with the phase space factor, defines the transition rate for the observed process:

$$d\Gamma = |\mathcal{M}|^2 \cdot \frac{S}{2\hbar \cdot m_1} \cdot \left[ \left( \frac{c \cdot d^3 \vec{p}_2}{(2\pi)^3 \cdot 2E_2} \right) \left( \frac{c \cdot d^3 \vec{p}_3}{(2\pi)^3 \cdot 2E_3} \right) \cdots \left( \frac{c \cdot d^3 \vec{p}_n}{(2\pi)^3 \cdot 2E_n} \right) \right] \cdot (2\pi)^4 \cdot \delta^4(p_1 - p_2 - \dots - p_n) . \quad (\text{C.2})$$

The formula above is known as *Fermi's golden rule*, where  $p_i = (E_i/c, \vec{p}_i)$  is the four-momentum of the particle  $i$  and  $S$  is the product of statistical factors (for the group of  $j$  identical particles in the final state its value is  $1/j!$ ). It is assumed that particle 1 decays into particles 2, 3, ...,  $n$ . The total decay rate  $\Gamma$  is the result of the integration of Eq. (C.2) over momenta of all outgoing particles.

For the inclusive reactions like  $1 + 2 \rightarrow 3 + X$  the cross section is given by:

$$d\sigma = \frac{\hbar c}{8\pi} |\mathcal{M}|^2 \cdot \frac{S}{(E_1 + E_2) \cdot |\vec{p}_1|} \cdot \frac{\delta(E_1 + E_2) - \sqrt{m_3^2 c^2 + \vec{p}_3^2} - \sqrt{m_X^2 c^2 + \vec{p}_3^2}}{\sqrt{m_3^2 c^2 + \vec{p}_3^2} \cdot \sqrt{m_X^2 c^2 + \vec{p}_3^2}} \cdot d^3 \vec{p}_3. \quad (\text{C.3})$$

The amplitude  $\mathcal{M}$  depends on magnitude and direction of  $\vec{p}_3$ , so the direct angular integration is not possible, but if  $d^3 \vec{p}_3$  is written as:

$$d^3 \vec{p}_3 = p_3^2 dp_3 d\Omega, \quad d\Omega = \sin \theta d\theta d\phi, \quad (\text{C.4})$$

then it is possible to integrate the Eq. (C.3) over  $p_3$  from 0 to  $\infty$  and to obtain the differential cross section:

$$\frac{d\sigma}{d\Omega} = \left( \frac{\hbar c}{8\pi} \right)^2 \cdot |\mathcal{M}|^2 \cdot \frac{S}{(E_1 + E_2)^2} \cdot \frac{|\vec{p}_f|}{|\vec{p}_i|}, \quad (\text{C.5})$$

where  $|\vec{p}_f|$  and  $|\vec{p}_i|$  are the magnitudes of outgoing and ingoing particles respectively.

In the cylindrical symmetry system, the invariant cross section  $E \cdot \frac{d^3 \sigma}{dp^3}$  can be determined as:

$$E \cdot \frac{d^3 \sigma}{dp^3} = E \cdot \frac{d^3 \sigma}{dp_x dp_y dp_z} = E \cdot \frac{d^3 \sigma}{p_t dp_t dp_z d\phi} = E \cdot \frac{d^2 \sigma}{2\pi p_t dp_t dp_z}, \quad (\text{C.6})$$

where after the last equality sign the partial integration over  $\phi$  is performed. The invariant cross section can be written using the phase space variables ( $p_t$  and  $y$ ) as:

$$E \cdot \frac{d^3 \sigma}{dp^3} = \frac{1}{2\pi} \cdot \frac{d^2 \sigma}{p_t dp_t dy}, \quad (\text{C.7})$$

where the relation between  $y$ ,  $p_z$  and  $E$  is gained from Eq. (B.6) and Eq. (B.7) for the fixed  $m_t$ :

$$\left( \frac{dp_z}{dy} \right)_{m_t} = m_t \cdot \text{ch}(y) = E. \quad (\text{C.8})$$

More about invariant cross section and rapidity correlations can be found in e.g. [108].

# Appendix D

## BUU Transport Model Equation

As it was mentioned in the section 4.2, the BUU model uses the Boltzmann-Uehling-Uhlenbeck transport equation to describe collisions under the influence of a mean field [109]. The mean field is a consequence of the surrounding nuclear matter and it can be written using so-called Skyrme parametrization:

$$U(\rho) = A \cdot \left( \frac{\rho}{\rho_0} \right) + B \cdot \left( \frac{\rho}{\rho_0} \right)^\sigma, \quad \sigma > 1, \quad (\text{D.1})$$

where  $A$  stands for the attractive ( $A < 0$ ) and  $B$  for the repulsive part ( $B > 0$ ) of the field.

The non-relativistic equation which describes the time evolution of the single particle phase space density  $f = f(\vec{r}, \vec{p}, t)$  within the mean field  $U$  is:

$$\begin{aligned} \frac{\partial f}{\partial t} + \vec{v} \cdot \vec{\nabla}_r f - \vec{\nabla}_r U \cdot \vec{\nabla}_p f = & - \frac{1}{(2\pi)^6} \int d^3 p_2 d^3 p_{2'} \cdot d\Omega \frac{d\sigma}{d\Omega} \cdot v_{12} \\ & \cdot \left\{ [f f_2 (1 - f_{1'}) (1 - f_{2'}) - f_{1'} f_{2'} (1 - f) (1 - f_2)] \cdot (2\pi)^3 \delta^3(\vec{p} + \vec{p}_2 - \vec{p}_{1'} - \vec{p}_{2'}) \right\}. \end{aligned} \quad (\text{D.2})$$

The evolution is determined with two-body collisions, where  $v_{12}$  is the relative velocity of the colliding particles. Factor  $\delta^3(\vec{p} + \vec{p}_2 - \vec{p}_{1'} - \vec{p}_{2'})$  ensures the momentum conservation. The Pauli principle is included within the factor inside square brackets, where  $f_i$  are one-body distribution functions for the incoming and outgoing particles. The first term represents the scattering from the observed to the final state ( $1', 2'$ ) and the second term describes the scattering from the final into the observed state.

Equation (D.2) is solved numerically by Monte-Carlo method using test particles. After the initialization, the phase space density is given by a set of  $n(A_P + A_T)$  point-like test particles, where  $A_P$  stands for the number of nucleons in projectile and  $A_T$  is the number of nucleons in target nuclei. The motion of these particles is considered classically and it can be expressed

through Hamilton's equations:

$$\dot{\vec{p}}_i = -\vec{\nabla}_r U(\rho(\vec{r}_i)), \quad \dot{\vec{r}}_i = \vec{v}_i . \quad (\text{D.3})$$

The velocity  $\vec{v}_i$  can be either relativistic or non-relativistic.

# Bibliography

- [1] M. L. Benabderrahmane, *PhD thesis*, University of Heidelberg, (2007).
- [2] R. Stock, *Phys. Rept.* **135**, 259 (1986).
- [3] T. Hatsuda, *Nucl. Phys. A* **544**, 27 (1992).
- [4] M. Merschmeyer, *PhD thesis*, University of Heidelberg, (2004).
- [5] J. Pochodzalla et al., *Phys. Rev. Lett.*, **75**, 1040 (1995).
- [6] M. Pichon et al., *Nucl. Phys. A* **779**, 267 (2006).
- [7] H. Stöcker and W. Greiner, *Phys. Rept.* **137**, 277 (1986).
- [8] R. F. Sawyer, *Phys. Rev. Lett.* **29**, 382 (1972).
- [9] A. B. Migdal, *Zh. Eksp. Teor. Fiz.* **61**, 2209 (1971).
- [10] D. B. Kaplan and A. E. Nelson, *Phys. Lett. B* **175**, 57 (1986).
- [11] G. E. Brown and H. Bethe, *Astrophys. J.* **423**, 658 (1994).
- [12] P. Braun-Munzinger and J. Stachel, *J. Phys. G* **28**, 1971 (2002).
- [13] P. Braun-Munzinger, J. Stachel, J.P. Wessels, and N. Xu, *Phys. Lett. B* **344**, 43 (1995).
- [14] P. Braun-Munzinger, J. Stachel, J.P. Wessels, and N. Xu, *Phys. Lett. B* **365**, 1 (1995).
- [15] P. Braun-Munzinger, D. Magestro, K. Redlich, and J. Stachel, *Phys. Lett. B* **518**, 41 (2001).
- [16] G.E. Brown and M. Rho, *Phys. Rept.* **269**, 333 (1996).
- [17] V. Koch, *Int. J. Mod. Phys. E* **6**, 203 (1997).
- [18] F. Rami et al., *Phys. Rev. Lett.* **84**, 1120 (2000).
- [19] J. P. Blaizot, *Phys. Rept.* **64**, 171 (1980).
- [20] D. H. Youngblood, H. L. Clark, and Y.-W. Lui, *Phys. Rev. Lett.* **82(4)**, 691 (1999).

- [21] Pawel Danielewicz, Roy Lacey, and William G. Lynch, *Science* **298(5598)**, 1592 (2002).
- [22] A. Andronic et al., *Phys. Lett. B* **612**, 173 (2005).
- [23] J. Aichelin and C. M. Ko, *Phys. Rev. Lett.* **55**, 2661 (1985).
- [24] C. Sturm et al., *Phys. Rev. Lett.* **86**, 39 (2001).
- [25] C. Fuchs, Amand Faessler, S. El-Basaouny, and E. Zabrodin, *J. Phys. G* **28**, 1615 (2002).
- [26] W. Cassing and E.L. Bratkovskaya, *Phys. Rep.* **308**, 65 (1999).
- [27] R. Hayano and T. Hatsuda, *Rev. Mod. Phys.* **82**, 2949 (2010).
- [28] K. Tsushima et al., *Phys. Rev. C* **62**, 0649904 (2000).
- [29] C. Adami and G. E. Brown, *Phys. Rept.* **234**, 1 (1993).
- [30] Michael C. Birse, *J. Phys. G* **20**, 1537 (1994).
- [31] W. Weise, *Nucl. Phys. A* **553**, 59c (1993).
- [32] J. Gasser and H. Leutwyler, *Phys. Rept.*, **87**, 77 (1982).
- [33] W. Weise, *Prog. Theor. Phys. Suppl.* **149**, 1 (2003).
- [34] Che. Ming Ko et al., *Annual Review of Nuclear and Particle Science* **47(1)**, 505 (1997).
- [35] M. Gell-Mann, R.J. Oakes, and B. Renner, *Phys. Rev.* **175**, 2195 (1968).
- [36] K. Suzuki et al., *Phys. Rev. Lett.* **92**, 072302 (2004).
- [37] Y. Nambu and G. Jona-Lasinio, *Phys. Rev.* **122**, 345 (1961).
- [38] Y. Nambu and G. Jona-Lasinio, *Phys. Rev.* **124**, 246 (1961).
- [39] T. Hatsuda and S.H. Lee, *Phys. Rev. C* **46**, 34 (1992).
- [40] F. Klingl, N. Kaiser, and W. Weise, *Nucl. Phys. A* **624**, 527 (1997).
- [41] W. Weise, *Nucl. Phys. A* **610**, 35c (1996).
- [42] J. Schaffner, A. Gal, I.N. Mishustin, H. Stöcker and W. Greiner, *Phys. Lett. B* **334**, 268 (1994).
- [43] C.H. Lee, *Phys. Rept.* **275**, 255 (1996).
- [44] G.E. Brown, C.-H. Lee, Mannque Rho, and V. Thorsson, *Nucl. Phys. A* **567**, 937 (1994).
- [45] G.-Q. Li, C.-H. Lee, and G.E. Brown, *Nucl. Phys. A* **625**, 372 (1997).

- [46] N. Herrmann for the FOPI collaboration, *Prog. Part. Nucl. Phys.* **42**, 187 (1999).
- [47] P. Senger for the KaoS collaboration. *Prog. Part. Nucl. Phys.* **42**, 209 (1999).
- [48] F. Laue et al., *Phys. Rev. Lett.* **82**, 1640 (1999).
- [49] R. Barth et al., *Phys. Rev. Lett.* **78**, 4007 (1997).
- [50] M. Menzel et al., *Phys. Lett. B* **495**, 26 (2000).
- [51] D. Best et al., *Nucl. Phys. A* **625**, 307 (1997).
- [52] C. Hartnack et al., *Eur. Phys. J. A* **1**, 151 (1998).
- [53] B. Blättel, V. Koch, and U. Mosel, *Rept. Prog. Phys.* **56**, 1 (1993).
- [54] C. Hartnack and J. Aichelin, *J. Phys. G* **28**, 1649 (2002).
- [55] P. Crochet et al., *Phys. Lett. B* **486**, 6 (2000).
- [56] P. Chung et al., *Phys. Rev. Lett.* **91**, 202301 (2003).
- [57] D. Elia et al., *Nucl. Phys. A* **734**, 57 (2004).
- [58] P. A.M. Guichon, *Phys. Lett. B* **200**, 235 (1988).
- [59] K. Tsushima, S. W. Huang, and A. Faessler, *Phys. Lett. B* **337**, 245 (1994).
- [60] K. Tsushima, S. W. Huang, and A. Faessler, *J. Phys. G* **21**, 33 (1995).
- [61] K. Tsushima, A. Sibirtsev, and Anthony W. Thomas, *Phys. Lett. B* **390**, 29 (1997).
- [62] A. Baldini, V. Flaminio, W.G. Moorhead, and D.R.O. Morrison, *Springer-Verlag, Berlin*, (1988).
- [63] M. L. Benabderrahmane et al., *Phys. Rev. Lett.* **102**, 182501 (2009).
- [64] J. Geiss, W. Cassing and C. Greiner, *Nucl. Phys. A* **644**, 107 (1998).
- [65] The FOPI experiment website: <http://www-fopi.gsi.de/>
- [66] P. Crochet et al., *Nucl. Phys. A* **624**, 755 (1997).
- [67] A. Andronic et al., *Nucl. Phys. A* **679**, 765 (2001).
- [68] D. Pelte et al., *Z. Phys. A* **359**, 55 (1997).
- [69] B. Hong et al., *Phys. Lett. B* **407**, 115 (1997).
- [70] D. Pelte et al., *Z. Phys. A* **357**, 215 (1997).



- [71] A. Mangiarotti et al., *Nucl. Phys. A* **714**, 89 (2003).
- [72] K. Wisniewski et al., *Eur. Phys. J. A* **9**, 515 (2000).
- [73] M. Merschmeyer et al., *Phys. Rev. C* **76**, 024906 (2007).
- [74] O. Hartmann, *Int. J. Mod. Phys. A* **24**, 271 (2009).
- [75] X. Lopez et al., *Phys. Rev. C* **81**, 061902 (2010).
- [76] N. Herrmann for the FOPI collaboration. *Nucl. Phys. A* **610**, 49c (1996).
- [77] A. Andronic et al., *Phys. Rev. C* **64**, 041604 (2001).
- [78] A. Andronic et al., *Phys. Rev. C* **67**, 034907 (2003).
- [79] J. Diaz et al., *Nucl. Instr. Meth. A* **478**, 511 (2002).
- [80] A. Gobbi et al., *Nucl. Instrum. Meth. A* **324**, 156 (1993).
- [81] H. Drumm et al., *Nucl. Instrum. Meth.* **176**, 333 (1980).
- [82] R.D. Heuer and A. Wagner. *Nucl. Instrum. Meth. A* **265**, 11 (1988).
- [83] H.M. Fischer et al. *Nucl. Instrum. Meth. A* **283**, 492-501 (1989).
- [84] R. Veenhof. Garfield - Simulation of gaseous detectors. CERN, <http://consult.cern.ch/writeup/garfield>, (2001).
- [85] Edmund Häfele, *PhD thesis*, University of Heidelberg, (1995).
- [86] Tarek Kreß, *PhD thesis*, Technische Universität Darmstadt, (2002).
- [87] G. Goebels, *PhD thesis*, University of Heidelberg, (1995).
- [88] Christopher H. Pinkenburg, *PhD thesis*, University of Heidelberg, (1995).
- [89] H. Foeth et al., *Nucl. Instr. Meth.* **109**, 521 (1973).
- [90] J. Ritman. *Nucl. Phys. Proc. Suppl.* **44**, 708 (1995).
- [91] B. Hyams et al., *Nucl. Instr. Meth.* **205**, 99 (1983).
- [92] J. Hoffmann. *Technical report*, Gesellschaft für Schwerionenforschung mbH, (2002).
- [93] CES Creative Electronic Systems S.A. RIO3 8064, *A PowerPC-Based VME Real-Time Processor Board*. <http://www.ces.ch/>.
- [94] I. Carević, O. Hartmann, M. Dželalija, *Hyperfine Interactions Journal* **203**, 1 (2011).

- [95] L. Montanet et al., *Phys. Rev. D* **50**, 1173 (1994)
- [96] D. Drijard, H.G. Fischer and T. Nakada, *Nucl. Instrum. Meth.* **225**, 367 (1984).
- [97] D. L'Hôte, *Nucl. Instrum. Meth. A* **337**, 544 (1994).
- [98] GEANT Team, *GEANT - Detector Description and Simulation Tool*. CERN, <http://consult.cern.ch/writeup/geant> (1995).
- [99] A. Fassò, A. Ferrari, J. Ranft, P.R. Sala, *World Scientific, Proc. IV Int. Conf. on Calorimetry in High Energy Physics, La Biodola, Italy* 493 (1993).
- [100] P.A.Aarnio et al., *Technical Report TIS-RP-190*, CERN (1987, 1990).
- [101] A.Fassò, A.Ferrari, J.Ranft, P.R.Sala, G.R.Stevenson and J.M.Zazula, *FLUKA92, In Proceedings of the Workshop on Simulating Accelerator Radiation Environments, Santa Fe, USA*, (1993).
- [102] S. Agostinelli et al., *Nucl. Instrum. Meth. A* **506**, 250 (2003).
- [103] O. Buss, T. Gaitanos, K. Gallmeister, H. van Hees, M. Kaskulov, O. Lalakulich, A. B. Larionov, T. Leitner, J. Weil, U. Mosel, *Phys. Rept.* **512**, 1 (2012).
- [104] L. L. Salcedo, E. Oset, M. J. Vicente Vacas, C. Garcia-Recio, *Nucl. Phys. A* **484**, 557 (1988).
- [105] A. Hombach, A. Engel, S. Teis, U. Mosel, *Z. Phys. AA* **352**, 223 (1995).
- [106] GiBUU website, <http://gibuu.physik.uni-giessen.de/GiBUU/>, (2011).
- [107] D. Griffiths, *John Wiley and Sons Inc.*, Introduction to elementary particles, (1987).
- [108] T. Abbott, L. Kowalski, and L.P. Remsberg, Rapidity and invariant cross sections, <http://www.phenix.bnl.gov/WWW/publish/erichard/tutorials/abbotkinematics.pdf>
- [109] G.F. Bertsch and S. Das Gupta, *Phys. Rept.* **160**, 189 (1988).



## Curriculum Vitae

Ivana Weber (born Carević) was born on September 7<sup>th</sup> 1979 in Split. She has been married since 2013 and has one child.

After elementary and secondary grammar school, she started her graduate study at the Faculty of Science of the University of Split in 1998. In 2000 she received Rector's award for her excellent academic success. In November 2004 she defended her diploma thesis and completed her Master's degree in Mathematics and Physics Education. In March 2005 she began her doctoral study in Physics, Nuclear Physics, at the Faculty of Science of the University of Zagreb.

Since January 2005 she has been working as a research and teaching assistant at the Department of Physics at the Faculty of Science in Split. In the past several years she has taught more than ten different courses in the form of auditory and practical exercises and seminars.

She has conducted her scientific research within several national and international projects. In 2005 she started her work at Higher Energy Physics and Application of Grid project, lead by her supervisor Prof Dr. Mile Dželalija. Another project important for her scientific career has been the bilateral project between Croatia (project leader: Prof. Mile Dželalija) and Austria (project leader: Dr. Olaf Hartmann in 2012, Dr. Paul Bühler in 2013), Studying the In-medium Properties of Strange Particles, whose preparation and implementation she worked on in 2012 and 2013.

Ivana Weber is a member of two international collaborations: FOPI and CBM, both based at the GSI, Darmstadt, Germany, where she has attended several scientific trainings and has participated a number of experimental activities since 2006. As a member of the FOPI collaboration, she started to work on her PhD thesis on the topic of Neutral Strange Particles Correlations at SIS Energies, but at the end of 2010, due to priorities and needs of the collaboration, she continued her work on the analysis of the S273 experiment, primarily investigating in-medium strange particle production in pion-induced reactions. The said topic launched her cooperation with Dr. Olaf Hartmann from the Stefan Meyer Institute (SMI) in Vienna in 2011. Since September 2011 she has been on several PhD research study sojourns at the SMI. In 2011 she won the Ernst Mach scholarship by the Austrian Federal Ministry of Science, Research and Economy (BMWFW), and spent one semester in 2012 working at the SMI. There she met her other supervisor, Dr. Paul Bühler who she started to work with in September 2012.

Apart from her research and teaching activities, she has participated in several trainings and seminars in physics and computation, assisted in the work of different committees and societies in the fields of physics and education, worked with students on their projects and participated in the organization and support of several scientific events.

So far she has presented her scientific work at several international and national conferences and has published three scientific papers in CC journals and one more (submitted in December 2015) is waiting for acceptance. These and other public presentations of her work are listed

below.

#### **Scientific publications in Current Contents journals:**

1. Piasecki, K; Herrmann, K; ... ; Weber, Ivana; ..., Influence of Phi mesons on negative kaons in Ni + Ni collisions at 1.91A GeV beam energy, Physical Review C. 91 (2015).
2. Münzer, R; ...; Carević, I.; ..., (The FOPI Collaboration ), SiΛvio: A trigger for Λ-hyperons, Nuclear Instruments and Methods A 745:38-49 (2014) .
3. Zinyuk, V.; Kang, T.I.; Leifels, Y.; Herrmann, N.; Hong, B.; ... ; Carević, Ivana; (The FOPI Collaboration ), Azimuthal emission patterns of K<sup>+</sup> and of K<sup>-</sup> mesons in Ni plus Ni collisions near the strangeness production threshold. Physical review C. 90 (2014).

#### **Other publications in Current Contents journals:**

1. Abel, N.; ... ; Carević, Ivana; et al. (CBM collaboration), The CBM Collaboration., Nuclear physics. A. 830 (2009).

#### **Scientific publications in conference proceedings with international review:**

1. Carević, I.; Hartmann, O.; Dželalija, M., Investigating In-medium Lambda Production in Pion Induced Reactions, Hyperfine Interactions Journal, Vol. 203 Nos. 1-3, (2011).

#### **Posters and presentations:**

1. Carević, I.; Bühler, P.; Dželalija, M.; Čaplar, R.; Istraživanje in-medium stvaranja Lambda hiperona u pionski induciranim reakcijama, poster, 8th Scientific Meeting of Croatian Physical Society, Primošten, October 2013
2. Carević, I.; Hartmann, O.; Dželalija, M., Investigating In-medium Lambda Production in Pion Induced Reactions, poster at EXA conference, Vienna, September 2011
3. Carević, I.; Anđelić, M.; Dželailja, M.; Čaplar, R.; Neutral strange particle decay-plane correlations in heavy-ion reactions, poster at Nuclear Cluster Conference: Clusters '07, Stratford upon Avon, September 2007
4. Anđelić, M.; Carević, I.; Dželailja, M.; Čaplar, R.; Strange Particles Entropy Production in Heavy-ion Reactions, poster at Nuclear Cluster Conference: Clusters '07, Stratford upon Avon, September 2007
5. Carević, I.; Dželalija, M.; Study of K<sup>0</sup> and Lambda Decay-Plane Correlations, talk at the FOPI collaboration meeting, GSI-Darmstadt, February 2007